The Molecular Dynamics of Hydrogen-Bonding Explored with Broadband Two Dimensional Infrared Spectroscopy

by

Luigi De Marco

MASSACHUSETTS INSTITUTE OF TECHNOLOGY
JUN 23 2016
LIBRARIES
ARCHIVES

B.S. Chemistry
McGill University, Montreal, 2010

Submitted to the Department of Chemistry
in partial fulfillment of the requirements for the degree of

Doctor of Philosophy
in Physical Chemistry

at the

Massachusetts Institute of Technology
June 2016

© 2016 Massachusetts Institute of Technology. All rights reserved.

Signature of Author: Signature redacted
Luigi De Marco
May 16, 2016

Certified by: Signature redacted
Andrei Tokmakoff
Professor of Chemistry, The University of Chicago
Thesis Supervisor

Accepted by: Signature redacted
Robert W. Field
Haslam and Dewey Professor of Chemistry
Chairman, Department Committee on Graduate Theses

This doctoral thesis has been examined by a committee of the Department of Chemistry that included:

Signature redacted

Professor Robert W. Field
Thesis Committee Chair

Signature redacted

Professor Keith A. Nelson

Signature redacted

Professor Andrei Tokmakoff
Thesis Supervisor

The Molecular Dynamics of Hydrogen-Bonding Explored with Broadband Two Dimensional Infrared Spectroscopy

by

Luigi De Marco

Submitted to the Department of Chemistry on May 16, 2016
in partial fulfillment of the requirements for the degree of
Doctor of Philosophy in Physical Chemistry

Abstract

It is no overstatement to claim that hydrogen bonding is the most important intermolecular interaction. On a day-to-day basis, we encounter the peculiar effects of hydrogen bonding in liquid water; however, it is well appreciated that hydrogen bonding is immensely important in many contexts and, in particular, in biological ones. Despite this apparent significance, a general molecular picture of the dynamics of hydrogen-bonding systems is lacking.

Over the last two decades, ultrafast multidimensional infrared spectroscopy has emerged as powerful technique for studying molecular dynamics in the condensed phase. By taking advantage of the complex relationship between a molecular oscillator's frequency and its environmental structure, we may understand molecular dynamics from an experimental perspective.

However, the study of hydrogen bonding poses a significant technical challenge in that the interaction gives rise to broad resonances in the mid-infrared absorption spectrum. Traditional methods for generating short pulses of mid-infrared light are fundamentally limited in the bandwidth they can produce. Oftentimes, the width of a hydrogen-bonded oscillator's absorption resonance exceeds the broadest bandwidth mid-infrared laser pulse.

In this thesis, I describe our development and use of a novel source of short, broadband mid-infrared light pulses that span the entire region of high-frequency molecular vibrations. We use this source as a probe in two-dimensional infrared spectroscopy experiments to study a wide variety hydrogen-bonding systems, including hydrogen-bonded dimers and protein films, with a particular emphasis on liquid water.

Across these systems, we observe fascinating trends in the changes in molecular dynamics with increasing complexity of hydrogen bonding. In particular, we find experimental evidence for large deformations of the nuclear potential energy surface, giving rise to extremely anharmonic and collective dynamics. The effect is most dramatic in liquid water, where the rapidly fluctuating hydrogen-bond network results in vibrational excitons wherein O—H stretching motion is delocalized over multiple molecules. In this case, the nuclear potential energy surface is so complex that even simple changes in the mass of the oscillators result in qualitatively different dynamics.

Thesis Supervisor: Andrei Tokmakoff
Title: Henry G. Gale Distinguished Service Professor, The University of Chicago

My family

Acknowledgments

Over the past six years, I have been so fortunate as to cross paths with some of the most wonderful people I will ever meet. Some of them have contributed directly to this thesis, while some have contributed by teaching me something. Others offered their friendship and support and pushed me to do my best. These people have had a profound impact on me, not only as a scientist, but as a person. I thank you all.

I will be forever grateful to my advisor, Andrei Tokmakoff, for an incredible graduate school experience. Andrei's curiosity-driven love of science fostered an atmosphere that allowed me to learn more than I could have ever hoped to. His support and understanding has gotten me through some of the toughest days in the lab; even through the most despairing times, I knew Andrei had my back. He has always pushed me to think big and take on the toughest scientific challenges, and as a result, I am a better scientist for it. After seeing how invested he was in securing me the postdoctoral position I wanted, it became clear that Andrei cares about his students more than anyone I have ever met. At places like MIT and UChicago, good scientists are a dime a dozen, but finding someone who is also as good a person as Andrei, is truly rare.

In all the excellent people I have worked with, I have been lucky enough to call some my friends. Mike Reppert and I started in the group together, and we have been through the good, the bad, and everything in between together. Throughout graduate school, Mike's friendship has been a constant source of happiness for me, both on a personal and intellectual level. These past six years would have certainly been far less enjoyable if he was not around to offer his advice and support. I will always very much consider him my partner in spectroscopic crime. I have cherished my friendship with Bad Paul (Stevenson) and Good Paul (Sanstead) immensely. Over the years, I have learned a great deal from them, both in the lab and at the Pub. Their brilliance and hard work has been a constant source of inspiration for me. I will miss them and our long conversations over a glass of whisky, often lasting well into the early morning, more than I can fathom at the moment. On many occasions, I sought out Kevin Jones and Sam Peng for advice, and they always gave the best. They helped show me the way through graduate school, and when I thought all was hopeless, they assured me that it was not. Sadly, I was never able to out-prank Kevin who was usually a few steps ahead of me, but I am grateful for all of the laughter, confusion, and foam packing peanuts. I also have to thank Ann and Sean Fitzpatrick for showing me that there is life outside of the lab, for finding me an apartment, and for many a song played at the Cove.

This thesis would not exist without Team Water. I started out working with Krupa Ramasesha, and I am forever indebted to her for what she has taught me. She patiently addressed the endless stream of questions I had for her, and she took the time to teach me as much as she could about infrared spectroscopy. We worked well together, and I am sad that I did not have the chance to overlap with her longer. For the entire year of 2011, she and I worked tirelessly on timing up our then-brand-new broadband infrared pulses with the pulses from our optical parametric amplifier. There were bad times; in particular, I am remembering Krupa and I walking around the lab with Kim Wipes attached to long poles trying to find the source of the air currents that plagued us and subsequently installing a pink foam ceiling above the laser table to protect our delicate experiment. Of course, there were good times. On Tuesday, December 6, 2011, just after 4:00 p.m., we finally accomplished what we had been working so hard to do, and we found timing. So far, that is the greatest experience of my scientific career, and I am happy that I was able to share it with Krupa. Aritra Mandal taught me that patience was a virtue when it came to dealing with the experiment and that you can usually get a little more out of the laser if you just try a little longer. When it came time to move the labs, I was fortunate to have Martin Thämer to work with. His dedication and attention to detail played no small part in making the transition so smooth. I thank him for valuable lessons in perseverance and for allowing me to win one out of many tennis matches. I thank Andy Haky IV for his hard work on the protein film project (as well as for being the chief whiteboard specialist, shakeday coordinator, and director of human resources). I am certain that his curiosity and unbridled enthusiasm will take him far in life. I thank Rajib Biswas for interesting discussions of water and acid in computers, the incredible food he made and shared with me, and his great sense of humor. The office was a brighter place with Rajib around. After having rebuilt the experiment from scratch not once, but twice, I am very much attached to it. I am happy to be leaving it in the very capable hands of Joe Fournier and Memo Carpenter. I know that their big ideas are going to take the experiment in new and exciting directions. I cannot wait to see what they, in addition to the newest member of Team Water, Lukas Whaley-Mayda, invent, innovate, and discover.

I thank Memo, Paul, Paul, and Rajib for carefully reading through parts of this thesis and giving useful comments. I owe special thanks to Joe, who painstakingly read through the entire thesis and gave many insightful comments and corrections.

The work described in this thesis was performed at two separate locations: the Massachusetts Institute of Technology and the University of Chicago. The initial development of the broadband 2D IR experiment, as well as the HOD experiments and the initial H_2O experiments were performed in room 2-041, in the basement of Building 2, at MIT. The second generation of the broadband 2D IR experiment, as well as the experiments on organic dimers, light and heavy water, and protein films were performed in room E018, in the basement of the Gordon Center for Integrative Science, at UChicago. The move provided me with an experience that few graduate students get to have, and I am grateful for the opportunity to oversee the construction of our labs from the ground up. Everything from the height of the ceilings to the placement of each electrical outlet to the grade of the vapor barrier to be used on the drywall was a decision that needed to be made. Often, a consensus would only be reached after laborious discussions and planning. As difficult as designing the lab was, it gave me a new appreciation for how scientific experiments are done and how the room that these experiments are conducted in are as much a part of the experiments as the lasers themselves.

Along the way, there were people who were instrumental in making the move a possibility. Above all, John Phillips, the building manager of the GCIS, made the move a breeze. He not only makes the building run, but he makes sure that the research gets done. I have never seen someone do their job with such care and passion, and I hope that one day I can emulate John in whatever I end up doing. I thank him for taking a genuine interest in my research, useful life advice, and many discussions about our common interest in fishkeeping. I am grateful to Helmut Krebs, a true master of his craft, for his patience in teaching me how to machine. At MIT, I am thankful to Peter Giunta, Jennifer Weisman, and the late Danielle Guichard-Ashbrook for their dedication. Without it, I would not have been able to move to Chicago, and my unique graduate experience would not have been possible.

Finally, I want to thank Evan for his love and encouragement from the day we met. Somehow, during one of the most stressful periods of my life, he managed to keep me grounded and continually pushed me to continue working hard. He brings a warmth to my heart that made it easy to keep going, even in the toughest hours. My sister, Daniela, has been my best friend for as long as I can remember. Throughout my entire life, I have looked to her for approval and advice, and I do not know what I would have done without her. Over the last six years, we have grown closer despite being further apart than ever. I am immensely proud of her and I thank her for always being there for me. Lastly, I thank my parents, Franca and John. I do not even know how to go about describing all that they have done for me. I thank them for placing such a strong importance on education since I was young and for fostering my interest in science throughout my entire life. I thank them for talking to me for hours when times were worst, and I called them at odd hours in the morning. I thank them for showing me that no obstacle is too big to overcome. Most of all, I thank them for their unconditional love and support and their undeterrable belief that I can do anything I set my mind to.

Scientific research is a challenge that requires a great deal of commitment and passion. I thank all those I mentioned and all those I missed for strengthening that commitment and fueling that passion.

April 2016 Luigi De Marco

Funding

I would like to thank the Natural Sciences and Engineering Research Council of Canada for an A. G. Bell Canada Graduate Scholarship (CGSM-394287-2010) and a Postgraduate Scholarship (PGSD3-420409-2012). In addition, I thank the US Department of Energy for funding the research described in this thesis through Grant Nos. DE-FG02-99ER14988 and DE-SC0014305.

Contents

List of Figures 15

List of Tables 19

1 Introduction 21
- 1.1 Hydrogen Bonding & Liquid Water 21
- 1.2 Molecules in Motion 26
- 1.3 Dynamics of Water Molecules 32
- 1.4 Overview 36

2 Multidimensional IR Spectroscopy in Theory 39
- 2.1 The Interaction of Light and Matter 39
  - 2.1.1 A Respectable Discussion of Spectroscopy 39
  - 2.1.2 Mechanics of Light-Matter Interactions 41
  - 2.1.3 Generation of a Signal Field 43
- 2.2 Response Theory 46
  - 2.2.1 Introduction 46
  - 2.2.2 Linear Response 49
- 2.3 Third-Order Spectroscopy 52
  - 2.3.1 Third-Order Response 52
  - 2.3.2 Driving Fields and the Rotating Wave Approximation 55
  - 2.3.3 Wavevector Matching 60
- 2.4 Rotational Averaging 62
  - 2.4.1 The Electric Polarization Density 62
  - 2.4.2 Averaging the Molecular Frame Transformation 63
  - 2.4.3 Orientational Diffusion 69
- 2.5 Third-Order IR Spectroscopy 71
  - 2.5.1 Detection of Signal 72
  - 2.5.2 Rephasing and Non-Rephasing 74
  - 2.5.3 Two-Dimensional Infrared Spectroscopy 78
  - 2.5.4 Transient Absorption 85
  - 2.5.5 Polarization Anisotropy 87
- 2.A Tables of Orientational Factors for Third-Order Polarization Spectroscopy . 91

3 **Multidimensional IR Spectroscopy in Practice** **93**
- 3.1 The Nuts and Bolts of the 2D IR Experiment 93
  - 3.1.1 Overview of the Experiment 95
- 3.2 OPA-Based Generation of IR Pulses 97
  - 3.2.1 Generation of Short Pulses of Visible Light 97
  - 3.2.2 OPA and DFG 99
  - 3.2.3 Generation of 3 μm Pulses 101
  - 3.2.4 Generation of Tunable Mid-IR Pulses 103
- 3.3 Broadband Mid-IR Continuum 106
  - 3.3.1 The Need for Broadband Pulses 106
  - 3.3.2 Generation of Broadband Mid-IR Pulses 107
  - 3.3.3 Characterization of Broadband Mid-IR Pulses 111
- 3.4 The Mach-Zehnder Interferometer 119
  - 3.4.1 Principles of Operation 119
  - 3.4.2 Extraction of Spectrum and Phase: The Mertz Method 124
  - 3.4.3 Continuous Scanning of τ_1 127
  - 3.4.4 Interferometric Autocorrelation 129
  - 3.4.5 Fourier Detection of Nonlinear Signal 132
- 3.5 Acquisition and Processing of 2D IR Spectra 134
  - 3.5.1 Sample Area and Detection 134
  - 3.5.2 Transient Absorption Spectroscopy 136
  - 3.5.3 The 2D IR Experiment 139
  - 3.5.4 Scatter 142

4 **Intermolecular Hydrogen Bonds Probed with Broadband 2D IR** **147**
- 4.1 The Significance of NMA 147
  - 4.1.1 The Smallest Protein 147
  - 4.1.2 The Molecular Structure of NMA 149
  - 4.1.3 Thermodynamics of Cooperative Aggregation 150
- 4.2 Vibrations of the NMA Monomer and Dimer 154
  - 4.2.1 Linear Absorption Spectroscopy 154
  - 4.2.2 Simplified Notation 156
- 4.3 The Short-Time 2D IR Spectrum of NMA 156
  - 4.3.1 Amide A and Amide I 156
  - 4.3.2 Amide II and Amide B 161
  - 4.3.3 Fermi Resonances 163
  - 4.3.4 Intermolecular Cross Peaks in 2D IR 166
  - 4.3.5 Vibrational Couplings of NMA Molecules 168
- 4.4 Transition Dipole Orientations in the NMA 172
  - 4.4.1 A Practical Note about Polarization Anisotropy 172
  - 4.4.2 Polarization Dependence of the NMA Cross Peaks 173
- 4.5 Dynamics of the NMA Dimer 175
  - 4.5.1 Peak Dynamics in the 2D IR Spectrum 176
  - 4.5.2 Relaxation of the NMA Monomer 181
  - 4.5.3 Relaxation of the NMA Dimer 182

5 Resonances and Relaxation in Isotopically Dilute Water **185**
5.1 Isotopically Dilute Water 185
  5.1.1 Why Isotopically Dilute? 185
  5.1.2 What has been done? 187
  5.1.3 Sample Preparation 190
5.2 The Linear Absorption Spectrum of HOD 191
5.3 Nonlinear Spectroscopy of HOD in D_2O 193
  5.3.1 Diagonal Features in the Early-Time Spectrum 193
  5.3.2 The Stretch-Bend Cross Peak and Off-Diagonal Features 196
5.4 Relaxation Dynamics of the O—H Stretch 199
  5.4.1 Dispersive Relaxation 201
  5.4.2 Relaxation Pathways 202

6 Molecular Dynamics of Liquid Water **205**
6.1 A Liquid Like No Other 205
  6.1.1 A Field Divided 207
  6.1.2 Notation 208
6.2 Linear Infrared Spectroscopy of H_2O 209
6.3 The 2D IR Spectrum of Liquid Water 212
  6.3.1 The Early-Time Spectra 212
  6.3.2 The Late-Time Spectrum 217
6.4 Vibrational Dynamics in H_2O 218
  6.4.1 Transient Absorption 218
  6.4.2 Dynamics of the 2D IR Spectrum 220
  6.4.3 Decay of Polarization Anisotropy 224
  6.4.4 Vibrational Excitons in H_2O 226
  6.4.5 2D Depolarization 230
  6.4.6 Temperature Effects on Water's Dynamics 231
6.5 The Hot Ground State 234
  6.5.1 Temperature Changes in the Linear Spectrum 234
  6.5.2 Temperature Changes in Nonlinear Spectroscopy 236
  6.5.3 Formation of the Hot Ground State 237
6.6 Summary & Outlook 241
  6.6.1 Water in a Nutshell 241
  6.6.2 Outlook on Water 242
6.A Vibrational Dynamics of Alcohols 245
6.B Waiting Time Series of H_2O 248
6.C Temperature Dependent 2D IR Spectra 249

7 Molecular Dynamics of Heavy Water **251**
7.1 A Predictable Experiment? 251
7.2 Linear Spectroscopy of D_2O 253
7.3 Nonlinear Spectroscopy of D_2O 254
  7.3.1 Early and Late Time Spectra 254
  7.3.2 Polarization Anisotropy 257

7.4 Relaxation Dynamics of Heavy Water 266
7.4.1 Transient Absorption of D_2O 266
7.4.2 Changes in the Integrated 2D IR Spectrum 268
7.5 The Difference between Light and Heavy Water 272
7.5.1 A Toy Model 273

8 Water at the Protein Interface 277
8.1 Looking at Water–Protein Interactions 277
8.1.1 Sample Preparation 281
8.2 Linear IR Spectra of Protein Films 283
8.3 Water Dynamics on Poly-L-Proline 287
8.3.1 Water Structure at the Protein Interface 288
8.3.2 Water Dynamics at the Protein Interface 293
8.4 Water Dynamics on a Hydrophobic Protein 297
8.4.1 Water Structure at a Hydrophobic Interface 298
8.4.2 Dynamics at the Hydrophobic Interface 302
8.5 The Effect of Water on Protein Structure 308
8.5.1 Robust Protein Structure under Hydration 311

Bibliography 317

Curriculum Vitae 353

List of Figures

1.1 Geometry of a hydrogen bond. 23
1.2 Schematic potential energy surfaces for hydrogen bonding 28
1.3 Frequency–geometry correlations for the O—H stretch of HOD in D_2O. . . 30
1.4 Characteristic timescales of molecular motion in water. 33
1.5 Mid-IR absorption spectra of liquid and gaseous water. 35

2.1 The eight Liouville pathways for third-order response 54
2.2 The eight Liouville pathways for the rephasing wavevector-matching condition 58
2.3 Wavevector-matching directions for two common experimental geometries . 59
2.4 The molecular frame transformation 64
2.5 Example 2D IR spectrum for a two-level system 80
2.6 Example 2D IR spectrum for a three-level system 81
2.7 Example 2D IR spectrum for a six-level system 83
2.8 Example transient absorption spectra for two, three, and six-level systems . 86
2.9 Depolarization ratio for cross peaks 87

3.1 Schematic overview of the experimental setup 95
3.2 Pump spectra produced by OPA and DFG sources 104
3.3 Overview of the bradband mid-IR continuum generation 106
3.4 Spectra of broadband mid-IR pumping light 108
3.5 Spectrum of the broadband mid-IR continuum 112
3.6 Polarization characteristics of the broadband mid-IR source 114
3.7 Pulse length measurements of the broadband mid-IR continuum 116
3.8 Chirp calculations of the broadband mid-IR source 118
3.9 Schematic illustration of a Mach-Zehnder interferometer 120
3.10 Interferometric measurement of a pulse spectrum 126
3.11 Interferometric autocorrelation measurement of pulse length 131
3.12 Representative spectra illustrating data collection and processing 141

4.1 Resonance structures of N-methylacetamide monomer and dimer 149
4.2 Concentration-dependent absorption spectra of N-methylacetamide 155
4.3 Early-time 2D IR spectrum of N-methylacetamide 157
4.4 2D IR spectra of isotopically dilute N-methylacetamide 159
4.5 Chain-length dependent 2D IR spectra of N-methylacetamide 160
4.6 Cross-peak region of N-methylacetamide for ZZZZ and ZZYY polarizations 173

4.7 2D IR waiting-time spectra of N-methylacetamide 174
4.8 Dynamics of the amide A and I features of N-methylacetamide 177
4.9 Dynamics of the amide II feature of N-methylacetamide 179

5.1 Absorption spectrum of isotopically dilute HOD in D_2O 191
5.2 Energy levels of HOD in D_2O as a function of hydrogen-bond strength . . . 192
5.3 Transient absorption spectra of isotopically dilute HOD in D_2O 194
5.4 Early-time 2D IR spectrum of isotopically dilute HOD in D_2O 195
5.5 Slices through the 2D IR spectrum of HOD 197
5.6 Dispersive relaxation of the isotopically dilute O—H stretch 200
5.7 Relaxation pathway of the isotopically dilute O—H stretch 203

6.1 Linear IR absorption spectrum of liquid water 209
6.2 2D IR spectra of liquid H_2O at early and late waiting times 213
6.3 Vibrational transitions of H_2O in linear and nonlinear spectroscopy 214
6.4 Transient absorption spectrum of liquid water 218
6.5 Slices through the transient absorption spectrum of H_2O 219
6.6 2D IR waiting-time series of liquid water 223
6.7 Polarization anisotropy decay for the O—H stretch and HOH bend 225
6.8 2D depolarization ratio of the O—H stretching band 230
6.9 Dynamic timescales in H_2O as a function of temperature 232
6.10 Comparison of dynamics in HOD and H_2O as a function of temperature . . 233
6.11 Characterization of temperature changes in the linear spectroscopy of H_2O 234
6.12 Non-adiabatic relaxation of the O—H stretch in H_2O 240
6.13 2D IR spectra of short-chain alcohols 245
6.14 CLS decay timescale as a function of viscosity for hydrogen-bonding liquids 246
6.15 2D IR waiting time series of H_2O in ZZZZ polarization 248
6.16 2D IR waiting time series of H_2O in ZZYY polarization 248
6.17 Temperature-dependent 2D IR spectra of H_2O for several waiting times . . 249

7.1 Linear absorption spectra of D_2O and H_2O 254
7.2 Comparison of 2D IR spectra of D_2O and H_2O 255
7.3 Hot ground state spectra for D_2O and H_2O 256
7.4 Slices through the 2D IR spectrum of D_2O 258
7.5 2D depolarization surface for D_2O and H_2O 259
7.6 Calculated transition-dipole angeles in D_2O 262
7.7 Calculated spectra for collective modes 264
7.8 Transient absorption spectrum of D_2O 266
7.9 Slices through the transient absorption spectrum of D_2O 267
7.10 Dynamic evolution of the 2D IR spectrum of D_2O 269
7.11 2D IR waiting-time series for D_2O in parallel and perpendicular polarizations 270
7.12 Illustration of mass effects in anharmonic potentials 275

8.1 Schematic of humidity-controlled sample cell 280
8.2 Overview of the linear IR spectra of protein films 284
8.3 The sequence of poly-L-proline 287

8.4 The O—H stretching region of hydrated poly-L-proline film 289
8.5 The C=O stretching region of hydrated poly-L-proline film 290
8.6 2D IR spectra of poly-L-proline film 291
8.7 Hot ground state of water's O—H stretch on poly-L-proline 294
8.8 Dyanmics associated with water hydrogen bonded to poly-L-proline film . . 295
8.9 The sequence of the elastin-like polymer GVG(VPGVG)$_{251}$ 296
8.10 Absorption spectra of the amide A region of hydrated GVG(VPGVG)$_{251}$ film 297
8.11 IR spectra of the amide I and II region of hydrated GVG(VPGVG)$_{251}$ film 299
8.12 2D IR spectra of hydrated GVG(VPGVG)$_{251}$ film at various levels of hydration 300
8.13 2D IR waiting time series of 20% RH hydrated GVG(VPGVG)$_{251}$ film . . . 301
8.14 Dynamics of the hydrated GVG(VPGVG)$_{251}$ film 303
8.15 Absorption spectra of the amide A region of hydrated lysozyme film 312
8.16 Center-line slope decay of hydrated lysozyme film 313

List of Tables

2.1 Summary of wavevector-matching conditions 56
2.2 Non-zero orientational tensors in third-order spectroscopy 67
2.3 Non-zero orientational tensors including diffusion of a spherical rotor 71
2.4 ZZZZ orientational factors for a two-oscillator system 91
2.5 ZZYY orientational factors for a two-oscillator system 92

4.1 Timescales associated with the N-methylacetamide monomer and dimer . . 180

6.1 Dynamic timescales for various hydrogen-bonding liquids 227

8.1 Timescales associated with 2D IR spectra of hydrated GVG(VPGVG)$_{251}$ film 305
8.2 Timescales associated with 2D IR difference spectra of GVG(VPGVG)$_{251}$ film 306

Chapter 1

Introduction

1.1 Hydrogen Bonding & Liquid Water

Early on, the aspiring chemist learns of the various forces that one molecule can exert on another. With little effort, a general chemistry student can rattle off the intermolecular forces in order of decreasing strength: ion–ion, ion–dipole, hydrogen bonds, dipole–dipole, ion–induced dipole, dipole–induced dipole, and dispersion. From the get-go, it is clear that one of these things is not quite like the others. While most of the list consists of electrostatic forces, that do not require atoms at all and are fully described in introductory physics, the hydrogen bond is specific to chemistry. The hydrogen bond is unique; unlike the electrostatic interactions, it is highly directional and has covalent character, giving it some chemical bond properties.

We then quickly learn about the unique properties of hydrogen bonding and, in particular, the wondrous liquid that so evidently exhibits hydrogen bonding: water. In fact, almost an entire century has passed since the hydrogen-bonding interaction was proposed and used to explain the properties of liquid water. In their seminal paper entitled *Polarity and Ionization from the Standpoint of the Lewis Thoery of Valence*, W. M. Latimer and W. H. Rodebush first put forth the concrete notion of the hydrogen bond [1] (though others had previously proposed similar interactions [2], and the term 'hydrogen bond' would only be coined a decade later [3]). In particular, they identified that the hydrogen atom, having only one electron, is effectively stripped bare when it participates in chemical bonding and, as such, it can approach the valence electrons of another atom more easily than any other. In their original paper, they write:

> Then, in terms of the Lewis theory, a free pair of electrons on one water molecule might be able to exert sufficient force on a hydrogen held by a pair of electrons on another water molecule to bind the two molecules together. Structurally this may be represented as
>
> 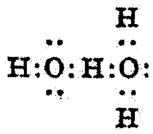
>
> $$\mathrm{H}:\overset{\cdot\cdot}{\underset{\cdot\cdot}{\mathrm{O}}}:\mathrm{H}:\overset{\overset{\mathrm{H}}{\cdot\cdot}}{\underset{\underset{\mathrm{H}}{\cdot\cdot}}{\mathrm{O}}}:$$
>
> Such combination need not be limited to the formation of double or triple molecules. Indeed the liquid may be made up of large aggregates of molecules, continually breaking up and reforming under the influence of thermal agitation.
>
> Such an explanation amounts to saying that the hydrogen nucleus held between 2 octets constitutes a weak "bond."

In just a few pages, the authors put forth an idea that would form the basis for understanding various phenomena in the world around us for years to come.

Since then, our understanding of hydrogen bonding has matured significantly. Figure 1.1 shows a more realistic schematic of a hydrogen bond between two water molecules and defines important geometric parameters that characterize the hydrogen bond [4]. In the case of the water dimer these parameters are: the O—H bond vector, $\boldsymbol{r}_{\mathrm{OH}}$; the oxygen–oxygen distance, $\boldsymbol{R}_{OO}$; and the angle between these two, $\cos\alpha = \hat{\boldsymbol{r}}_{\mathrm{OH}} \cdot \hat{\boldsymbol{R}}_{\mathrm{OO}}$. We speak of strong hydrogen bonds when R_{OO} is small and α is such that the hydrogen bond is linear with respect of the oxygen's lone electron pairs. Weak hydrogen bonds are those that do not meet these criteria. For example, in the water dimer shown in Fig. 1.1, the equilibirum values are $R_{\mathrm{OO}} = 2.96$ Å, and $\alpha = 55°$ [5]. The molecules participating in the hydrogen bond are called the hydrogen-bond acceptor and donor; the latter is the molecule that possesses the O—H group forming the hydrogen bond, and the former is that which possesses the electronegative oxygen atom.

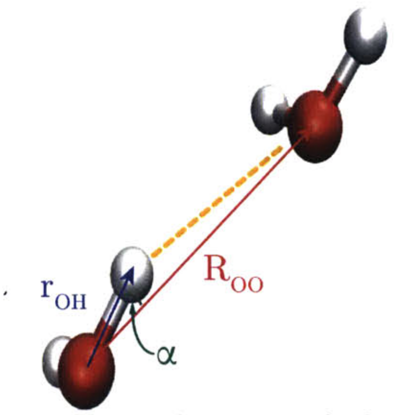

Figure 1.1: Geometry of a hydrogen bond between two water molecules. The hydrogen bond is characterized by the O—H bond vector of the donor, the O ··· O distance vector, and the angle between these two vectors.

Indeed, the properties of water that (much to my annoyance) are dubbed "anomalous" can be understood entirely in terms of hydrogen bonding. As the temperature of a sample of liquid water is lowered, the structure of the liquid evolves to the lowest energy state in which each water molecule can form four hydrogen bonds. The simplest way of doing this is by arranging hydrogen-bonded water molecules in sheets of "chair-form" hexamers, with adjacent sheets held together by hydrogen bonds [6]. The result is a loose-packed crystal with empty shafts running parallel and perpendicular to the unique crystal axis. This structure, designated ice I_h, is the common form of ice, and since the density of the solid is smaller than that of the liquid, ice floats on water.

Other properties of water can be explained in similar ways. For example, the well-known density maximum at 4°C arises due to the interplay between thermal fluctuations and satisfying hydrogen-bonding interactions. As with the formation of ice, as temperature is lowered in the liquid, there is a thermodynamic driving force for an ice-like structure. The competition between structuring and thermal fluctuations results in a non-monotonic behavior of the density, with the density decreasing as the temperature is raised or lowered from 4°C. Similarly, the strong intermolecular hydrogen-bonding forces tends to pull molecules from the surface of the liquid into the bulk, where it's possible to readily satisfy the four hydrogen bonds a water molecule can make. This gives water its low vapor pressure, high boiling point, and high surface tension [6].

The ubiquity of water means that these properties have a significant impact on daily life. When lakes and rivers freeze over, the ice formed stays afloat. What is more, the densest water, that at 4°C, sinks to the bottom providing a habitable zone for aquatic life through even the roughest winters. If hydrogen bonding did not exist, the ice would simply sink and take with it the freshwater aquatic life beneath the surface. Hydrogen bonding provides the force necessary to propel water upwards, against the force of gravity, through the xylem of vascular plants –a feat that would be an impossibility if not for the high surface tension of the liquid, which is the driving mechanism of capillary action. The density difference between the solid and the liquid means that increasing the pressure on the solid drives it to the liquid phase; though this is not what makes ice skating possible! Hydrogen bonding is the reason water from our leaky faucet comes down in droplets and why wet sand is sticky, but dry sand is not. How amazing it is that hydrogen bonding, such a simple concept in principle, ensures that we can build sand castles and that life itself is not wiped out in the winter!

The properties of hydrogen bonding are not limited to liquid water alone. Hydrogen bonding plays a central role in biology and biological processes [2] as well as other fields, such as material design [7]. One would have difficulty finding a molecular biology paper that does not refer to hydrogen bonding or some effect thereof. Hydrogen bonds are the glue that hold proteins in their well-defined secondary structure that, in part, enables them to carry out their precisely honed function [8,9]. The famous DNA double helix, the genetic instruction manual for all living organisms, is but a zipper with hydrogen bonds for teeth [10]. Of course, biology takes place in aqueous media, and water is an active component of any biological machine [11]. Water effects and enables the processes that turn the biological crank; it is as much a biological molecule as any protein or strand of DNA.

With all its amazing properties, one eventually asks the inevitable question: What is a hydrogen bond? As with all such questions regarding definitions, we turn to the standards committees [12], and we receive the following answer:

> The hydrogen bond is an attractive interaction between a hydrogen atom from a molecule or a molecular fragment X—H in which X is more electronegative than H, and an atom or a group of atoms in the same or a different molecule, in which there is evidence of bond formation.

The answer, being almost circular, is somewhat disappointing and does not give a truly clear description of what a hydrogen bond is; rather, we are left looking for "evidence of bond formation." Of course, I do not mean to imply that the International Union of Pure and Applied Chemistry has done a poor job in defining the hydrogen bond –in fact, this is the best definition that we have. Other definitions, based on geometry or energetics, for example, simply fall flat. Perhaps, it is simply best to abandon the notion of a rigorous definition of a hydrogen bond, and be contented with the idea that you know a hydrogen bond when you see it.

If we agree that we may identify a hydrogen bond when we encounter one, we may wonder how the formation of a hydrogen bond affects the motion of molecules. What is the general picture of how a molecule's dynamics are changed when it is participating in a hydrogen bond? As of yet, this question has no answer. The goal of this dissertation is to make an attempt at addressing this question. There are many reasons for this void of information, ranging from technical to scientific, but they can be categorized into two major challenges, in my opinion.

Firstly, there are an enormous variety of hydrogen bonds [2]. Hydrogen bonds vary in strength, geometry, character, and form. Hydrogen bonds can be almost negligibly weak or almost covalent in character. They can be intermolecular, free to fluctuate about a particular geometry, or they can be intramolecular and possibly strained at some large angle. While all hydrogen bonds have the same physical origin, these differences make an experimental approach that addresses hydrogen bonding, as a whole, difficult. Certainly one would be remiss to assume that the hydrogen bonding to an Eigen or Zundel complex in aqueous acids is the same as that of that between a glycine residue and a leucine residue in a β–sheet. Hydrogen bonding in liquid water, where every covalent bond is the same, is different still. Even within a sample of liquid water, there are a variety of hydrogen bonds: some are strong and some are weak. Therefore, the study of hydrogen-bonding systems necessitates techniques that can accurately discriminate between the range of hydrogen bonds observed, even within one system.

If the first issue is, in some sense, scientific, the second issue is technical: hydrogen bonds move fast. Even Latimer and Rodebush, in their original paper [1], were aware that hydrogen bonds would be continuously breaking and forming, in constant motion, due to thermal fluctuations. In fact, it is now known that hydrogen bonds in liquid water fluctuate on a 10^{-14}–10^{-11} s timescale [13–15]. Furthermore, hydrogen bonds in water have an average dissociation energy of 10.6 kJ/mol [16,17] which is not too much larger than the thermal energy available at room temperature, and stronger and weaker hydrogen bonds fluctuate on slower and faster timescales, respectively. Therefore, in addition to being able to discriminate between hydrogen bonds, any experiment that wishes to study the dynamics of a hydrogen bonding system needs a time resolution better than 10^{-13} s. (I will spare you the story of Leland Stanford, Eadweard Muybridge, and the photographs of the horse.)

The motivation for understanding hydrogen-bond dynamics, in particular in liquid water, is almost endless; a knowledge of these molecular motions provides insight that range from fundamental chemistry and physics to problems in molecular and structural biology. Despite strides being made, whether or not an intricate molecule will dissolve in water often cannot be predicted. This originates in the complex interplay between energetics and dynamics that accompany dissolution. The energetics are relatively well understood; the dynamics of water molecules around a solute are not. Another good example of the importance of understanding water's hydrogen bonding dynamics arises in protein–ligand binding. If some ligand is to bind to the active site of, say, an enzyme, it cannot do so unless the site is empty. Therefore, the fastest that such a ligand can bind is limited by how quickly water molecules can vacate the site. These are but some phenomena where hydrogen-bond dynamics are important, but the list is virtually endless.

1.2 Molecules in Motion

If it seems as though a technique that boasts high time resolution as well as structural sensitivity is a tall order, that is because it is. Currently, there is no technique that can unambiguously measure molecular dynamics in hydrogen-bonding systems. However, enormous progress has been made in the field of infrared (IR) spectroscopy and, in particular, the ability to produce short pulses of IR light has enabled the pursuit of hydrogen-bond dynamics in recent years. IR spectroscopy is sensitive to the nuclear potential energy surface that fundamentally governs the dynamics of any molecular system. All nuclear motions, ranging from high-frequency local oscillations to low-frequency collective modes are determined by the nuclear potential energy surface, and in principle, IR spectroscopy can probe it directly. Therefore, before discussing what we can (and cannot) measure with IR spectroscopy, we consider the the nuclear potential energy surface for a hydrogen-bonded oscillator.

Shortly after the hydrogen bond became a widely accepted concept, it was appreciated that the motion of hydrogen bonds was necessarily a multidimensional problem [18]. At the very least, in a X—H $\cdots$ Y hydrogen bond, the high-frequency X—H coordinate and the low-frequency X $\cdots$ Y coordinate must be considered. Hydrogen bonds are, of course, three dimensional, and it is necessary to consider that the hydrogen bond may not be linear, but oriented at an angle. We again refer to Fig. 1.1 for a definition of the coordinates relevant to a simple one hydrogen-bond problem between two water molecules. As discussed in the previous section, there is no universally accepted definition for the geometry of a typical hydrogen bond though some geometric definitions have been proposed for specific systems. For example, a common definition for liquid water states that $R_{\mathrm{OO}} < 3.5$ Å and $\alpha < 30°$ [19].

What does the potential look like in the simplest hydrogen-bonding situation? While "typical" molecular vibrations are thought of as having a potential that resembles a Morse potential, a brief glance at Fig. 1.1 shows that this cannot be possible for an oscillator engaging in hydrogen bonding. If we stretch the X—H bond, we eventually run into the Y atom! We must therefore have strong repulsion at both long and short extensions of the X—H bond. Furthermore, we must remember that oftentimes there may be some propensity for a proton to transfer or sit by the accepting molecule, and so the potential cannot be parabolic at the basin. From the earliest considerations of the potential of a hydrogen bonding oscillator [18], it became clear that the potential can have a relatively flat or even double-welled minimum.

Figure 1.2A shows examples of a O—H potential energy surface for several O$\cdots$O dis-

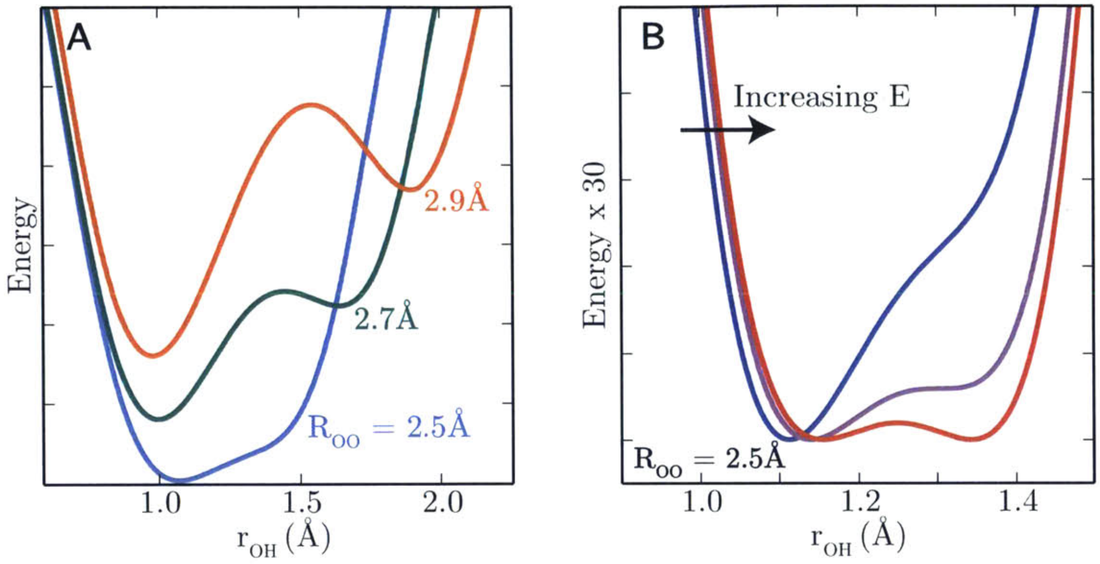

Figure 1.2: (A) Lippincott–Schroder potentials for the O—H bond of a water dimer for several values of R_{OO} at zero electric field. As the R_{OO} distance is decreased, the basin of the well deviates from harmonicity. (B) Lippincott–Schroder potential with an electric field added along the O—H bond. The potential shifts from a single to double well with increasing magnitude of electric field.

tances in the water dimer. These potential energy curves were calculated from the empirical Lippincott-Schroeder model [20, 21] which was originally developed to describe hydrogen bonding in molecular crystals. These curves are meant to be illustrative, and they in no way reflect quantitatively accurate surfaces for the water dimer. While the changes in the $O \cdots O$ distance between the three curves may appear small, we recall that the difference between neutral water at $R_{OO} = 2.8$ Å and an equally shared proton in a Zundel configuration is just 0.4 Å. Even these surfaces neglect one of the three coordinates that parametrize a simple hydrogen bond, α. The potential of a hydrogen-bonded oscillator does not look at all harmonic, and this bestows hydrogen-bonding molecules with the dynamics that both makes them so interesting and complex. Indeed, this notion of extreme anharmonicity is central to all of the studies contained within this thesis.

The energetics of a hydrogen-bonding system is not determined by geometry only. In fact, the electric field exerted by one molecule on another plays a central role in hydrogen-bonding systems as this can dramatically shift the equilibrium position of a hydrogen-bond-forming proton as well as the overall shape of the potential. Figure 1.2B shows a schematic O—H stretching potential energy surface, which would be characteristic of an excess proton in water, for example, at several different electric field strengths for a given value of R_{OO}. For strong enough fields, the potential becomes a true double well. Clearly, the nature of the dynamics in this system and even the very species involved is going to depend strongly on the rapidly fluctuating electric field in the liquid. These fluctuations play no small part in the role of fast proton transfer in liquid water and the rapid interchange between protonated water structures [22,23].

The power of infrared spectroscopy lies in its ability to distinguish between different hydrogen bond geometries based on the frequency of X—H oscillator [15,24–26]. Figure 1.3 shows joint probability distributions for the O—H stretching frequency of dilute HOD in D_2O, adapted from Ref. [26]. In particular, Fig. 1.3A shows an almost perfect correlation of the O—H stretching frequency with total electric field projected along the O—H bond. Put another way, if the frequency of an O—H oscillator is known, the electric field along that bond is known. Going one step further, Fig. 1.3B shows the joint probability distribution for the frequency of the O—H stretch as a function of the electric field due only to its hydrogen-bonding partner. While the degree of correlation has decreased somewhat, it remains relatively high; this shows that the frequency of a hydrogen-bond donor is almost entirely determined by the electric field generated by its hydrogen-bonding partner, which is essentially related to the strength of the hydrogen bond. Strong hydrogen bonds give rise to large, negative electric fields thus shifting the frequency of the oscillator lower. Weak hydrogen bonds give rise to small fields and a higher frequency of oscillation.

On a more fundamental level, when a covalent bond participates in a hydrogen bond, electron density from the former is donated to form the latter [27–29]. This weakens the covalent bond, effectively lowering its "spring constant." A lower spring constant implies a lower frequency and results in a vibration that is redshifted relative to a non-hydrogen-bonded oscillator. Typically, the electron density comes from both the accepting and donating moiety, and so both tend to weaken. For example, upon a local hydroxyl stretch forming a hydrogen bond with a local carbonyl stretch, both will decrease in frequency. For more complex normal modes, that is, vibrations involving more than just a local stretch, the frequency shift with hydrogen bonding is not so obvious. For example, the X—H bending or wagging mode will often tend to blueshift due to a stiffening of the potential upon hydrogen bonding.

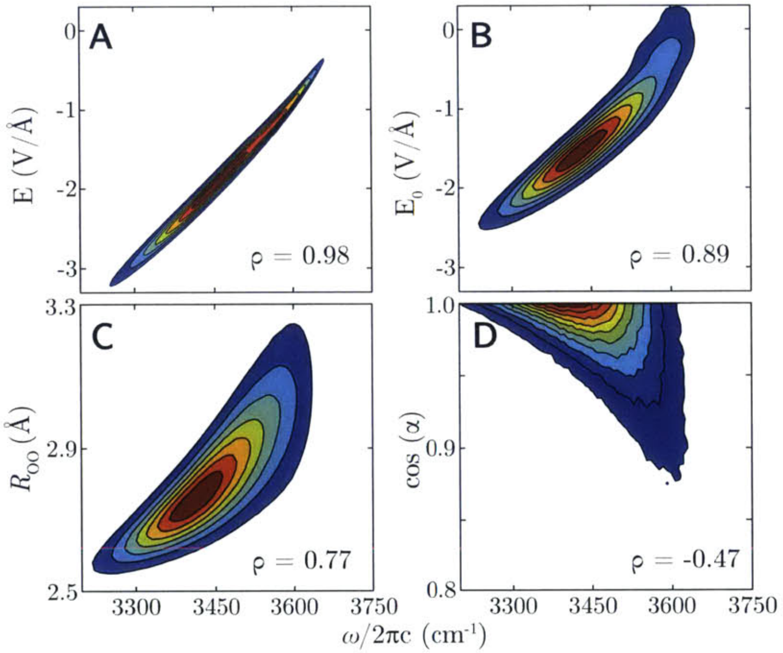

Figure 1.3: Joint probability distributions for the frequency of the O—H stretching mode of dilute HOD in D_2O and (A) the total electric field projected along the O—H bond, (B) the electric field due solely to the hydrogen-bond acceptor, (C) the R_{OO} distance, (D) the cosine of the hydrogen-bond angle, $\cos\alpha$. Correlation coefficients shown in lower-right corner. Adapted from Ref. [26].

The correlation between frequency and electric field is immensely useful, but it is not quite the desired result. If we want to understand how molecules move, it is necessary to be able to relate the electric field to the local geometry of the hydrogen bond. Figures 1.3C and 1.3D show the correlation between frequency and R_{OO} and frequency and hydrogen-bond angle, α, respectively, for the isotopically dilute O—H stretch of HOD in D_2O. Unsurprisingly, the degree of correlation has gone down significantly because a wide range of geometries can give rise to the same local electric field [26]. For example, while a decrease in angle would, in principle, increase the electric field along the O—H bond, it can be compensated for by an increase in R_{OO}. In particular, there are a large range of geometries that give rise to high-frequency stretching modes, but the geometries that give rise to the most redshifted oscillations are fairly restricted. Despite the fact that the correlation between structure and frequency is not perfect, however, it is certainly enough to learn a great deal about hydrogen bonding.

Of course, structural sensitivity is only half of what is necessary to study hydrogen bonding; it is impossible to observe molecular dynamics if the system is probed on timescales longer than those on which the structure evolves. In this sense, the ability to produce pulses of IR light that are shorter than the timescales on which thermal fluctuations occur has truly revolutionized our perspective on hydrogen bonds [30,31]. The ability to follow the frequency evolution of a hydrogen-bonded oscillator on molecular timescales has enabled us to infer how geometric changes occur and has given us insight into phenomena such as hydrogen-bond fluctuations [32,33], switching [34], and breaking and forming [35–37]. This simply would not be possible if a technique with greater structural resolution, such as nuclear magnetic resonance or X-ray diffraction, were used (the former because of the timescale of the precession of the magnetic moment of the proton [38] and the latter because of current technical limitations in the ability to produce short X-ray pulses, though progress is quickly being made in this regard [39]). Figure 1.4 shows the operating timescales for several techniques that are commonly used to study hydrogen bonding.

How, then, do we "follow" the frequency evolution of a hydrogen bond? In linear IR spectroscopy, where there is a single interaction with the electromagnetic field,[1] this is not possible. Namely, this is because there is no way to know what geometry an oscillator originated in once it is probed. "Following" necessarily requires multiple observations –an initial observation and another after some time has elapsed. Nonlinear IR spectroscopy provides us with exactly this capability. By using multiple short pulses of infrared light, separated by experimentally controlled time delays, it is possible to track the frequency evolution, and therefore the structural evolution, of the system as a function of real time.

In principle, we have all the tools required to study hydrogen-bonding dynamics. In practice, reality is never so simple, and any study of hydrogen-bonding dynamics typically requires accompaniment by computational methods. Over the years, numerous theoretical methods have been developed that heavily rely on molecular dynamics simulations to explore hydrogen bonding. However, even then, it is not straightforward to relate any particular dynamics to an infrared spectrum. In fact, this remains an active area of research.

---

[1] It is worth pointing out that the notion of "a single interaction" is rooted in perturbation theory and is somewhat artificial. The real system simply evolves under the total Hamiltonian.

1.3 Dynamics of Water Molecules

Thus far, we have turned to liquid water for most of our examples of hydrogen bonding. This is somewhat logical given water's ubiquity. However, this is probably the poorest example when it comes to typical systems since water is anything but typical [40].

The water molecule is such that each molecule can both accept two hydrogen bonds and donate two in a structure that is, on average, tetrahedral [6,41]. This geometry makes it possible for liquid water to form extended hydrogen-bond networks that span enormous volumes and severely complicate the study of the liquid. Indeed, the very notion of structure when it comes to liquid water is intimately tied to the timescale of observation of the liquid [6]. While we often pretend as though ultrafast spectroscopy provides us with an instantaneous snapshot of the liquid at any given time, the enormous range of molecular dynamics induced by hydrogen bonding means that even under the span of the shortest pulses, there will be some averaging over molecular motions. Figure 1.4 shows the molecular motions undergone by water, the characteristic timescales of these motions, and the timescales of operation of techniques used to probe water.

Each of these modes is associated with some sort of resonance in the electromagnetic spectrum of water. Figure 1.4 also shows the imaginary part of the index of refraction, κ, of water over several decades of energy. The most prominent peak corresponds to the O—H stretching mode, but the spectrum shows features arising due to high and low-frequency modes as well as motions corresponding to collective hydrogen-bond reorganization. As we shall see, these modes of motion are not independent, and are strongly coupled. By this, we mean that the excitation of a vibration has a profound impact on the other modes of vibration. This impact can be as simple as changing the frequency or amplitude of a

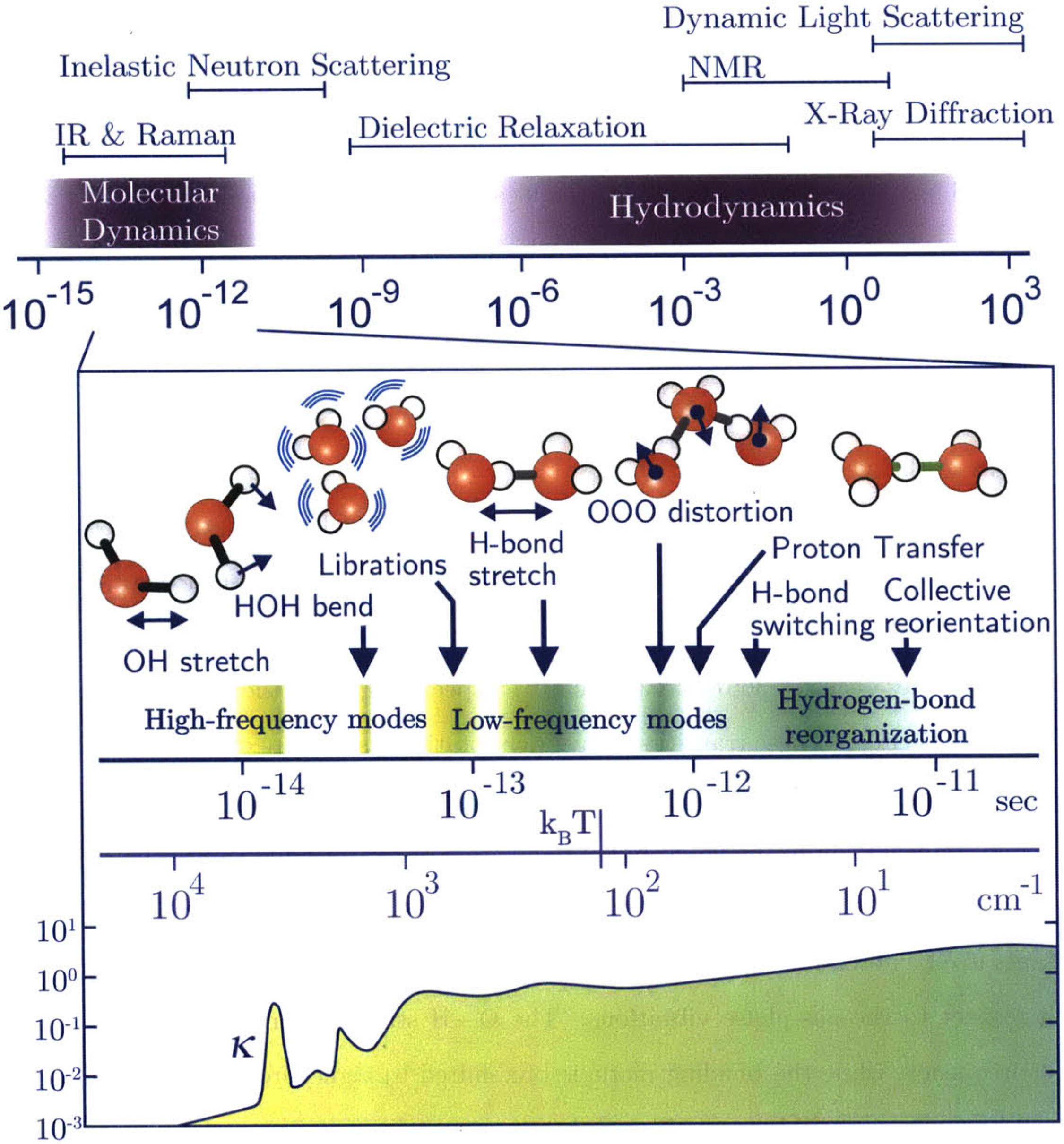
Dynamic Light Scattering
Inelastic Neutron Scattering
NMR
X-Ray Diffraction
IR & Raman
Dielectric Relaxation
Molecular Dynamics
Hydrodynamics
10^{-15}
10^{-12}
10^{-9}
10^{-6}
10^{-3}
10^{0}
10^{3}
OOO distortion
Proton Transfer
H-bond stretch
Librations
HOH bend
H-bond switching
Collective reorientation
OH stretch
High-frequency modes
Low-frequency modes
Hydrogen-bond reorganization
10^{-14}
10^{-13}
10^{-12}
10^{-11}
sec
k_BT
10^{4}
10^{3}
10^{2}
10^{1}
cm^{-1}
10^{1}
10^{0}
10^{-1}
10^{-2}
10^{-3}
κ

Figure 1.4: Timescales associated with molecular motion in water ranging from the period of the O—H stretching mode (10 fs) to collective reorientation of the hydrogen-bond network (10 ps). The upper portion of the figure shows the operation timescale for common experiments along with the types of motion probed. The lower portion shows the imaginary part of the index of refraction over the range of molecular motions. Adapted from Ref. [42].

vibration, but may be as complicated as changing the very nature of the other vibrations.

The main scientific challenge in studying the molecular dynamics of water is the strong, fluctuating coupling induced by the hydrogen-bonding interaction. This interaction, which results in a large density of low-frequency modes [14,43], gives rise to an interplay between inter and intramolecular degrees of freedom. In fact, it has been shown that that magnitude of inter and intramolecular coupling between local O—H stretching modes in liquid water is comparable [44]. That is, both have a value which is on the order of -30 cm^{-1}.[2] This value, when compared to the characteristic spread of O—H stretching frequencies of $\sim$200 cm^{-1}, shows that coupling is going to significantly impact the eigenstates of the O—H stretching vibrations. That is, vibrations in the liquid phase are not at all going to be reflective of vibrations in the gas phase.

This is particularly evident in the comparison of the linear IR absorption spectra of the two phases, shown in Fig. 1.5. In the gas phase spectrum, resonances can be observed for the three well-known normal modes of vibration. The symmetric and antisymmetric O—H stretching modes occur at 3657 and 3757 cm^{-1}, respectively, while the HOH bending mode occurs at 1595 cm^{-1}. These transitions have rich rotational structure owing to the fact that the water molecule is an asymmetric top.

Upon condensation to the liquid phase there are both obvious and subtle changes to the IR spectrum. Most obviously, the sharp rotational structure is lost, and the IR spectrum presents itself as broad absorption bands. In addition, these bands are shifted in frequency with respect to the gas-phase vibrations. The O—H stretching modes are redshifted to lower frequency, while the bending mode is blueshifted to higher frequency. Furthermore, it now becomes impossible to distinguish between stretching modes, and we simplistically refer to the O—H stretching band at 3400 cm^{-1}. In fact, the very nature of the O—H stretching mode in the liquid is an active topic of debate. More subtle effects arise as well. For example, whereas the bending mode has a larger oscillator strength than the stretching modes in the gas phase, the stretching mode is about four times more intense than the bend in the liquid phase. All of these differences are due to the strong, anisotropic hydrogen-bonding interaction, which fundamentally changes the character of the vibrations.

---

[2] The wavenumber unit, cm^{-1}, is used most extensively throughout this thesis. For comparison to other energy scales, we note that 1000 cm^{-1} = 30.0 THz = 1440 K = 124 meV = 12.0 kJ/mol.

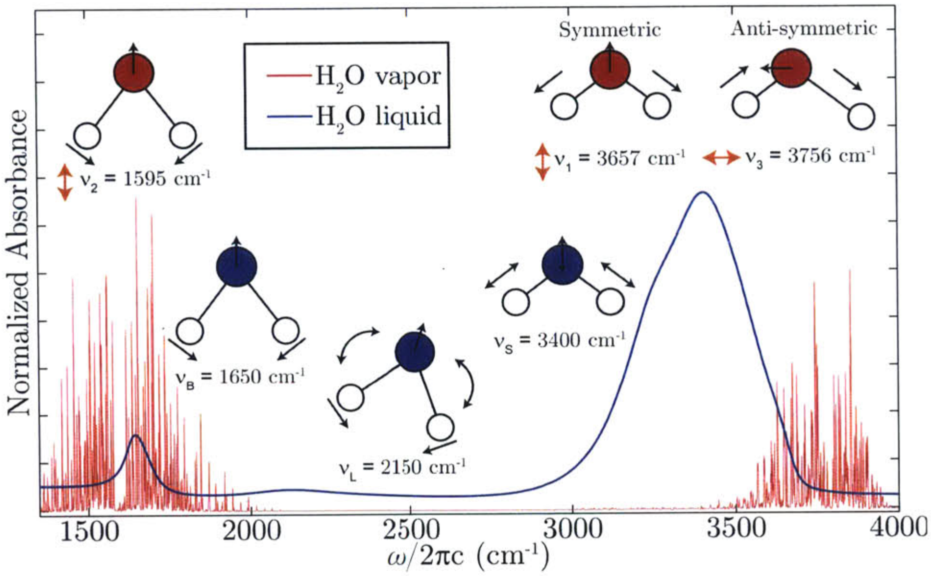

Figure 1.5: Normalized mid-IR absorption spectra of liquid (blue curve) and gaseous (red curve) water. Cartoon molecules show schematic bond displacements and center frequencies of the modes.

In addition to changes in the mid-IR region of the spectrum, liquid water shows a large absorption in the low-frequency part of the spectrum. This can be clearly seen in the imaginary part of the refractive index in Fig. 1.4. These resonances are due to intermolecular modes, which arise entirely due to the strong hydrogen-bonding interaction [14, 43]. In the frequency range of 500–800 cm^{-1} the spectrum shows absorption corresponding to hindered rotations [45–47], which we often call *librations* after the astrophysical phenomenon. When a water molecule is strongly interacting with nearby water molecules, there is a large potential energy barrier to rotation, since that would require the breaking of hydrogen bonds. This gives rise to motion with frequencies much higher than the rotation of a free water molecule, which typically occurs in the range of 9–28 cm^{-1} (278–836 GHz) [48]. In fact, these librations have a direct impact on the mid-IR spectrum as well. A weak, broad absorption band at 2150 cm^{-1} is evident, which is attributed to a combination of bending and librational motion.

At even lower frequencies, a prominent resonance corresponding to hydrogen-bond stretching motion can be observed [45–47]. These occur at a frequency of about 200 cm^{-1}. In analogy with librations, these can be thought of as hindered translations. That is, there is a barrier in the relative motion of two water molecules since separation of the two would require the breaking of a hydrogen bond. At frequencies lower still, are absorption resonances that arise due to less well-defined modes such as hydrogen-bond bending modes and highly delocalized collective motion.

The low-frequency modes complicate the dynamics of water significantly in that they are, in a sense, able to dress the higher frequency vibrations as well as provide an enormous energy sink for excess energy in the system. The strong interplay between high and low-frequency modes makes efforts to decouple the two pointless, and it forces us to reconsider, in a fundamental way, how we interpret spectra and discuss molecular dynamics of liquid water.

1.4 Overview

The study of hydrogen-bonding systems has a storied history that is almost as old as the study of chemical bonding itself. Of course, one cannot possibly conduct an exhaustive study of this topic in any reasonable time frame. Rather, we are forced to work on a small subset of examples in the hope that a more general picture of hydrogen bonding emerges. We conclude this introduction with a brief summary of the content in this thesis.

In **Chapter 2**, we discuss the theoretical basis for the experiments carried out in this thesis. Certainly, this chapter is not comprehensive –the theory of multidimensional spectroscopy is rich and complex, and it is not possible to give a full account here. Rather the intention is to provide a basic foundation through which the experiments that follow can be interpreted.

We go on to discuss the practical implementation of these experiments in **Chapter 3**. The development of broadband two-dimensional IR spectroscopy has been a central endeavor that continues to progress today. As such, the chapter is rather detailed, and contains an in depth discussion of the development and characterization of a plasma-based broadband mid-IR continuum source, as well as its use in 2D IR experiments.

Chapter 4 puts the experimental and theoretical development to use in a study of a simple hydrogen-bonded dimer of N-methylacetamide. Despite the fact that only one hydrogen bond is formed in this system, it shows rich dynamics due to an interplay between electronic and nuclear structure. We show that the vibrations delocalize over the entire dimer, and we characterize the timescales for the fluctuations of the interactions.

In **Chapter 5**, we take our first look at liquid water, which is largely the system that is studied in this thesis. In this chapter, experiments are carried out on isotopically dilute HOD in D_2O, and we focus on understanding the relaxation pathway of the dilute O—H stretch. We show that the relaxation is primarily through the HOD bending mode, and we characterize the dispersive relaxation of the solvent modes.

Neat liquid H_2O is taken on in **Chapter 6**. Here, the focus is on understanding the vibrational structure of the liquid and its dynamics. We find that the vibrations are excitonic in nature, and they are delocalzied over multiple molecules. These excitonic vibrations give rise to unusual dynamical properties and ultrafast relaxation of the O—H stretching mode. We explore the consequences of these dynamics, and, in particular, we thoroughly investigate the non-equilibrium state that is generated immediately after excitation of the O—H stretching mode with a short laser pulse. The phenomena observed in water are related back to the changes in the nuclear potential energy surface that arise due to hydrogen bonding.

In **Chapter 7** we continue to explore liquid water and conduct studies on heavy water, D_2O. Here, we find that the behavior of D_2O is qualitatively different from that of H_2O. In particular, D_2O behaves in a manner that is more consistent with a weakly anharmonic system. This is evidenced by the fact that D_2O shows signatures of symmetric and antisymmetric stretching that are made evident through the polarization-dependent 2D IR spectra. The results are interpreted with the aid of Local Monomer calculations of the transition dipole angles spectrum of D_2O.

Finally, we explore an application of the study of these systems in **Chapter 8**. We consider the hydration-dependent dynamics of water on protein films to try and understand the dynamics of water–protein interactions. The interpretation of these experiments is strongly guided by the results of Chapters 4 and 6, where the amide unit and liquid water are studied, respectively. By investigating several different protein systems, we identify two regimes of water–protein interactions, and, in particular, a regime at low hydration where the water–protein interaction dominates the system's dynamics.

Chapter 2

Multidimensional IR Spectroscopy in Theory

2.1 The Interaction of Light and Matter

2.1.1 A Respectable Discussion of Spectroscopy

As an undergraduate, I attended a seminar on two-dimensional electronic spectroscopy in which the speaker opened with the statement that “all respectable discussions of spectroscopy begin with the equations for light

$$\nabla \cdot \boldsymbol{E} = 4\pi\sigma, \tag{2.1a}$$

$$\nabla \cdot \boldsymbol{B} = 0, \tag{2.1b}$$

$$\nabla \times \boldsymbol{E} + \frac{1}{c}\frac{\partial \boldsymbol{B}}{\partial t} = 0 \tag{2.1c}$$

$$\nabla \times \boldsymbol{B} - \frac{1}{c}\frac{\partial \boldsymbol{E}}{\partial t} = \frac{4\pi}{c}\boldsymbol{J}, \tag{2.1d}$$

and the equation for matter

$$i\hbar\frac{\partial \rho}{\partial t} = [H, \rho]. \tag{2.2}$$

It is very simple," he concluded. This has stuck with me ever since. I certainly do not believe that all respectable discussions of spectroscopy begin with Maxwell's equations and the quantum Liouville equation, but in my opinion, most of the interesting ones do. The theory underlying multidimensional IR spectroscopy is rich and complex and it demands a thorough understanding of both electrodynamics and quantum mechanics, as well as some physical intuition as to what the equations actually mean. While little of the work in this thesis requires a particularly high level of theory to understand, I believe that a thorough understanding of the theory is necessary to truly appreciate the results. It would be impossible to include a complete treatment of the theory in this chapter (or any volume of a reasonable size, for that matter). What I hope to do instead, is give a reasonable overview of the fundamental concepts needed to interpret and understand the data contained in this thesis, with details elaborated elsewhere where necessary.

In a spectroscopic experiment, some matter (usually referred to as the sample or system) is exposed to some electromagnetic field (usually in the form of laser light). The field generates an electric polarization density in the matter, which subsequently radiates an electromagnetic field (usually referred to as the signal field). This field is detected and used to infer molecular details about the system. In a time-resolved spectroscopy, short pulses of light are used as opposed to continuous-wave radiation to force the matter–field interactions to occur at a particular time. At its most fundamental level, the theory of spectroscopy basically amounts to combining Eqs. 2.1 and 2.2 along with the Lorentz force and determining what is radiated by the matter.

It is simple in principle but rather involved in practice. Part of the difficulty lies in the myriad of approximations that form the foundation for most calculations and interpretations of data. Some of these approximations are rather simple to make and have far reaching consequences, while others are far more involved and somewhat more subtle. Oftentimes, the dipole approximation, the rotating-wave approximation, the slow-varying-envelope approximation, the quasi-monochromatic approximation, and the short-pulse approximation, being so indispensable, are implicit. One of the goals of this chapter will be to make clear which approximations are being made and when they apply.

Finally, I would like make a comment on notation. Despite the field of multidimensional optical spectroscopy being around for some 20 years now, it has not seemed to settle on a consistent notation convention. Part of this, I believe, has to do with the depth of the theory, and how large the equations quickly become. Here, I use the notation that I have found most convenient, both in terms of representing the theory and understanding it; though it is by no means a standard or the best. Furthermore, the equations in this chapter (and throughout the thesis wherever possible) are centimeter-gram-second units, which are particularly useful in problems involving electrodynamics. However, this convention will not be strictly adhered to throughout the thesis, and units will be specified whenever unclear.

2.1.2 Mechanics of Light-Matter Interactions

The interaction between light and matter is determined entirely by the Lorentz force exerted on charged particles by the electromagnetic field. In the case of an external electromagnetic field applied to a system of N particles (such as a molecule), the Lagrangian that gives rise to the Lorentz force in a Cartesian coordinate system is [49, 50]

$$L = L_0 + \sum_{i=1}^{N} \left(\frac{q_i}{c} \boldsymbol{v}_i \cdot \boldsymbol{A}(\boldsymbol{r}_i, t) - q_i \phi(\boldsymbol{r}_i, t) \right), \tag{2.3}$$

where L_0 is the Lagrangian of the system in the absence of the field and q_i, $\boldsymbol{r}_i$, and $\boldsymbol{v}_i$ are the charge, position, and velocity of the i^{th} particle, respectively. Here, $\boldsymbol{A}$ and ϕ are respectively the vector and scalar potentials of *external* electromagnetic fields; that is, they are the potentials which are due to charges which are not under consideration in the system. Along with Maxwell's equations, Eqs. 2.1, the Lorentz force provides all the information necessary to determine all there is to know about the system at the classical level. In practice, however, it is impossible to solve the dynamics of the system containing even a small number of particles due to the nonlinearity of the Lorentz force. To that end, it is necessary to linearize the Lorentz force to make the resulting equations of motion tractable.

If the charges in the system are centered on some position $\boldsymbol{R}_0$, and deviate from this position by amounts much smaller than the characteristic length scale on which $\boldsymbol{A}$ and ϕ change, the Lorentz force can be expanded to first order in the relative positions $\delta\boldsymbol{r}_i = \boldsymbol{r}_i - \boldsymbol{R}_0$ [51]. This is the typical case for a molecule interacting with visible or IR light though not for X-rays. We therefore expand the Lagrangian of Eq. 2.3, and rearrange terms to give

$$L = L_0 - \sum_{i=1}^{N} q_i \delta\boldsymbol{r}_i \cdot \left[\frac{1}{c}\dot{\boldsymbol{A}}(\boldsymbol{R}_0,t) + \nabla\phi(\boldsymbol{R}_0,t)\right] + \frac{\mathrm{d}}{\mathrm{d}t}\sum_{i=1}^{N}\frac{q_i}{c}\left(\delta\boldsymbol{r}_i \cdot \boldsymbol{A}_i(\boldsymbol{R}_0,t)\right).$$

The third term is a total time derivative, and therefore, it does not contribute to the variation of the action [50]. It has no effect on the equations of motion. The term in square brackets is simply the external electric field [49], while the sum over $q_i\delta\boldsymbol{r}_i$ is the electric dipole moment of the system. Therefore, the linearized Lorentz force is given by

$$L = L_0 + \boldsymbol{\mu} \cdot \boldsymbol{E}(\boldsymbol{R}_0,t). \tag{2.4}$$

For obvious reasons, this is known as the dipole approximation, and it is perhaps the most fundamental approximation underlying typical treatments of light–matter interactions. Indeed it even shapes the language used to discuss spectra (for example, "selection rules" are only accurate within the dipole approximation). While this approximation is sufficient for interpreting almost all IR spectra, it is worth noting that expanding the Lagrangian Eq. 2.3 to higher order would have resulted in higher-order interaction terms such as electric-quadrupole interactions and magnetic-dipole interactions [51].

In what follows, the field is treated classically, but the matter is treated quantum mechanically. For a quantum mechanical treatment, it is convenient to use the Hamiltonian of the system instead of the Lagrangian. It is straightforward to convert between the two [50], and the result is

$$H = H_0 - \boldsymbol{\mu} \cdot \boldsymbol{E}(\boldsymbol{R}_0,t), \tag{2.5}$$

where H_0 is the Hamiltonian of the unperturbed system.

2.1.3 Generation of a Signal Field

In nonlinear time-resolved spectroscopies, some number of laser pulses create an electric polarization density in a sample [52–54]. If this was the entire story, nothing would be learned since it is not possible to measure an electric polarization density directly. However, an electric polarization density that changes in time necessarily radiates an electromagnetic field [49], and this field carries with it information about the sample. Therefore, much of the theory of nonlinear spectroscopy is concerned with calculating the electric polarization density after interaction with an electromagnetic field given the interaction Lagrangian Eq. 2.3.

For electric fields whose magnitudes are much smaller than the magnitude of the internal electric fields of molecules, the induced electric polarization density is linear in the field. This gives rise to the linear optical phenomena experienced in everyday life, such as absorption, reflection, and refraction. However, if the electric fields incident on matter are comparable to the internal molecular fields, the electric polarization density is no longer linear in the field amplitude. Intuitively, this arises because the field can interact with the system multiple times; that is, the field can modify the system before interacting with it. This gives rise to a whole new set of nonlinear optical phenomena such as frequency doubling.

From Maxwell's equations (Eqs. 2.1) it is possible to show that for nonmagnetic media, the electric field is related to the nonlinear electric polarization density via the inhomogeneous wave equation [55, 56]

$$\nabla \times \nabla \times \boldsymbol{E}(\boldsymbol{x}, \omega) - \frac{\omega^2}{c^2}\varepsilon(\omega)\boldsymbol{E}(\boldsymbol{x}, \omega) = \frac{4\pi\omega^2}{c^2}\boldsymbol{P}^{(\mathrm{NL})}(\boldsymbol{x}, \omega), \tag{2.6}$$

where $\varepsilon(\omega)$ is the dielectric constant of the medium (which arises due to the linear electric polarization density) and $\boldsymbol{P}^{(\mathrm{NL})}$ is the nonlinear electric polarization density.[1] In general, Eq. 2.6 is impossible to solve since the nonlinear electric polarization density depends in a complex way on the electric field $\boldsymbol{E}$. It is therefore necessary to make a number of approximations to actually solve Eq. 2.6.

---

[1] In ordered media, such as crystals, $\varepsilon(\omega)$ is a tensor that couples the different components of the field. However, a change of coordinates to diagonalize $\varepsilon(\omega)$ is usually possible [57], and as such, we treat it as a scalar.

In what follows, we are only considered with the transverse field, since the longitudinal part of the field does not propagate.[2] Using the identity for the curl of the curl of a vector field, and separating the longitudinal and transverse parts, gives

$$\nabla^2 \boldsymbol{E}_\perp(\boldsymbol{x},\omega) + k^2(\omega)\boldsymbol{E}_\perp(\boldsymbol{x},\omega) = -4\pi k_0^2(\omega)\boldsymbol{P}_\perp^{(\mathrm{NL})}(\boldsymbol{x},\omega), \tag{2.7}$$

where $k_0^2 = \omega^2/c^2$ and $k^2 = \omega^2\varepsilon(\omega)/c^2$. It should be noted that the longitudinal part of the field can be significant in that it can contribute to $\boldsymbol{P}_\perp^{(\mathrm{NL})}$, though this is a subtle point which is largely ignored. From hereon out, we only work with the transverse electric field and so we drop the $\perp$ subscript.

To solve Eq. 2.7, we assume that the electric field has the form $\boldsymbol{E} = \boldsymbol{\mathcal{E}}(\boldsymbol{x})\mathrm{e}^{\mathrm{i}kz}$ and we take the real part at the end of any *linear* calculation.[3] If the field primarily propagates along z, then $\boldsymbol{\mathcal{E}}(\boldsymbol{x})$ is a slowly varying function of z since the rapid optical oscillations have been factored out. With this form, working through the Laplacian operator in Eq. 2.7 gives

$$\nabla_\perp^2 \boldsymbol{\mathcal{E}}(\boldsymbol{x},\omega) + \left(\frac{\partial^2 \boldsymbol{\mathcal{E}}(\boldsymbol{x},\omega)}{\partial z^2} + \mathrm{i}2k\frac{\partial \boldsymbol{\mathcal{E}}(\boldsymbol{x},\omega)}{\partial z}\right) = -4\pi k_0^2 \boldsymbol{P}_\perp^{(\mathrm{NL})}(\boldsymbol{x},\omega)\mathrm{e}^{-\mathrm{i}kz}. \tag{2.8}$$

Solution of this equation is all but hopeless unless some approximation is made. We make two rather draconian, but nonetheless standard, approximations. First, we assume that the field does not vary appreciably in x and y (plane-wave approximation). This implies that $\nabla_\perp^2 \boldsymbol{\mathcal{E}} \approx 0$. Next, we assume that the complex envelope of the field varies slowly over the characteristic wavelength of the light (slow-varying envelope approximation) [55,56,58].

---

[2] The equation for the longitudinal field is simply $\boldsymbol{E}_\parallel(\boldsymbol{x},\omega) = \frac{4\pi}{\varepsilon(\omega)}\boldsymbol{P}_\parallel^{(\mathrm{NL})}(\boldsymbol{x},\omega)$, and as such, does not propagate. Rather, it is non-zero wherever $\boldsymbol{P}_\parallel^{(\mathrm{NL})}$ is non-zero.

[3] It is important to note that in a nonlinear calculation, the real part of the field must be used throughout to allow for mixing between the complex field amplitude and its complex conjugate. This is not an issue in linear electrodynamics since all the operations are linear in that case.

This is true if

$$\left|\frac{\partial^2 \mathcal{E}(\boldsymbol{x},\omega)}{\partial z^2}\right| \ll \left|2k\frac{\partial \mathcal{E}(\boldsymbol{x},\omega)}{\partial z}\right| \tag{2.9}$$

is satisfied. These approximations are good barring extremely short pulses (one the order of a single cycle) or highly focused beams. With these approximations, the wave equation becomes

$$\frac{\partial \mathcal{E}(\boldsymbol{x},\omega)}{\partial z} = \mathrm{i}\frac{2\pi\omega}{c\hat{n}(\omega)}\boldsymbol{P}_{\perp}^{(\mathrm{NL})}(\boldsymbol{x},\omega)\mathrm{e}^{-\mathrm{i}kz} \tag{2.10}$$

where we have introduced the index of refraction, $\hat{n}(\omega) = \sqrt{\varepsilon(\omega)}$. Equation 2.10 is the starting point for many discussions of nonlinear optics and spectroscopy. We note that Eq. 2.10 holds at each value of ω, though the nonlinear polarization will serve to mix different frequencies.[4]

Oftentimes, the nonlinear polarization can be written as $\boldsymbol{P}_{\perp}^{(\mathrm{NL})} = \mathcal{P}^{(\mathrm{NL})}\mathrm{e}^{\mathrm{i}k_{\mathrm{p}}z}$, where $\mathcal{P}^{(\mathrm{NL})}$ does not depend on z and k_{p} depends on the fields that generate the electric polarization density. Neglecting the spatial dependence of the electric polarization density amounts to neglecting the depletion of the fields that generate it (usually referred to as neglecting pump depletion). In this case, Eq. 2.10 is easily integrated to give [52, 56, 59]

$$\mathcal{E}(\boldsymbol{x},\omega) = \mathcal{E}(x,y,z=0,\omega) + \mathrm{i}\frac{4\pi\omega}{c\hat{n}(\omega)}\mathcal{P}^{(\mathrm{NL})}\mathrm{e}^{\mathrm{i}\Delta kz/2}\frac{\sin(\Delta kz/2)}{\Delta k}, \tag{2.11}$$

where $\Delta k = k_{\mathrm{p}} - k$ is the so-called phase-matching condition.

The phase-matching condition determines whether a nonlinear process effectively produces an electric field or not. If Δk is large, then the nonlinear field rapidly drops as a function of z and no field is produced; that is, $\mathcal{E}(\boldsymbol{x},\omega) = \mathcal{E}(x,y,z=0,\omega)$. If the phase-matching condition is met perfectly, then $k_{\mathrm{p}} = k$, and after traversing a length of the sample

---

[4] If there are a discreet number of frequencies of interest in a problem (e.g. frequency doubling is concerned with ω_0 and $2\omega_0$) an equation of the form of Eq. 2.10 can be written down for each of those frequencies. For an n^{th} order polarization, this gives $n+1$ differential equations and gives rise to the so-called coupled-wave formalism [55].

ℓ, the field is given by

$$\boldsymbol{E}(\boldsymbol{x},\omega) = \boldsymbol{\mathscr{E}}(x,y,z=0,\omega)\mathrm{e}^{\mathrm{i}k_{\mathrm{P}}z} + \mathrm{i}\frac{2\pi\omega\ell}{c\hat{n}(\omega)}\boldsymbol{P}^{(\mathrm{NL})}. \tag{2.12}$$

We see then that the field after the sample consists of the initial field, propagated as though unaffected by the sample, and a signal field, radiated by the sample.

The remainder of this chapter is dedicated to calculating the nonlinear polarization density generated by input fields and how this relates to the structure and dynamics of the sample under study.

2.2 Response Theory

2.2.1 Introduction

To understand the signal emitted by a sample in a nonlinear spectroscopy experiment, it is necessary to calculate the electric polarization density of a system after interaction with an electromagnetic field. However, even for a relatively simple Hamiltonian, the quantum Liouville equation, Eq. 2.2, is not readily solvable. It is therefore necessary to devise a scheme to determine the approximate evolution of the density matrix under a particular Hamiltonian. Such a scheme for calculating the dynamics of a system taken out of equilibrium was developed with great success by Ryogo Kubo in the late 1950s [60,61]. The response theory formalism provides a straightforward method of calculating the density matrix to various orders of interaction with the perturbation. A linearization in the "complicated" part of the Hamiltonian is the most straightforward approach, but this fails as the perturbation strength is increased. It then is necessary to include the nonlinear response. The nonlinear response encodes in it information about the system in the form of time-correlation functions that cannot be extracted from the linear response.

An expansion for the density matrix in some perturbation can be reached in a fairly straightforward manner. We separate the Hamiltonian into a sum of a solvable or simple part

H_0 and a time-dependent interaction term $V(t)$. The Liouville equation can be iteratively solved to different orders in the interaction term. In the interaction picture representation, the result is

$$\rho(t) = \sum_{n=0}^{\infty} \left(\frac{-\mathrm{i}}{\hbar}\right)^n \int_{t_0}^{t} \mathrm{d}t_n \cdots \int_{t_0}^{t_3} \mathrm{d}t_2 \int_{t_0}^{t_2} \mathrm{d}t_1 [V(t_n), \ldots [V(t_2), [V(t_1), \rho(t_0)]] \ldots], \tag{2.13}$$

where all operators are in the interaction picture representation. Therefore, given knowledge of the initial density matrix, it is possible to determine the density matrix at some later time if the sum can be computed. In practice, the series converges quickly and only the lowest terms must be retained.

The density matrix cannot be measured directly; only the expectation value of certain Hermitian operators can be measured [62]. The expectation value of an interaction picture operator $A(t)$ is given by

$$\langle A(t)\rangle = \sum_{n=0}^{\infty} \left(\frac{\mathrm{i}}{\hbar}\right)^n \int_{t_0}^{t} \mathrm{d}t_n \cdots \int_{t_0}^{t_3} \mathrm{d}t_2 \int_{t_0}^{t_2} \mathrm{d}t_1 \left\langle [V(t_1), [V(t_2), \ldots [V(t_n), A(t)] \ldots]] \right\rangle, \tag{2.14}$$

where the fact that the trace is invariant under cyclic permutation has been used. The expectation value is taken with respect to the density matrix evaluated at time t_0, which is taken to be the *equilibrium* density matrix. Likewise, the limit $t_0 \to -\infty$ is often taken.

It is convenient to work with time intervals as opposed to absolute times. That is, we may define intervals τ_n such that $\tau_n = t_{n+1} - t_n$; a simple change of variables gives

$$\begin{aligned} \langle A(t)\rangle = \sum_{n=0}^{\infty} \left(\frac{\mathrm{i}}{\hbar}\right)^n \int_{0}^{\infty} \mathrm{d}\tau_n \cdots \int_{0}^{\infty} \mathrm{d}\tau_2 \int_{0}^{\infty} \mathrm{d}\tau_1 \\ \left\langle [V(t-\tau_n-\ldots-\tau_2-\tau_1), [V(t-\tau_n-\ldots-\tau_2), \ldots [V(t-\tau_n), A(t)] \ldots]] \right\rangle . \end{aligned} \tag{2.15}$$

The dipole interaction, given by Eq. 2.5, is of the form $-\boldsymbol{F}(t)\cdot\boldsymbol{B}$, where $\boldsymbol{B}$ is a operator which only has time-dependence due to the interaction picture representation and $\boldsymbol{F}(t)$ is a classical vector. Since the field $\boldsymbol{F}(t)$ is a classical function, it may simply be pulled out of the nested commutator. If we recall that an interaction picture operator is related to the

Schrödinger picture operator via $A_I(t) = U_0^\dagger(t) A_S U_0(t)$, where $U_0(t)$ is the time evolution operator for the unperturbed Hamiltonian, the terms can be permuted such that the nested commutator is greatly simplified. If we insert the interaction term $-\boldsymbol{F}(t)\cdot\boldsymbol{B}$, a tedious but straightforward proof by induction shows that the expectation value reduces to

$$\begin{aligned}\langle A(t)\rangle = \sum_{n=0}^{\infty}\int_{-\infty}^{\infty}\mathrm{d}\tau_n\cdots\int_{-\infty}^{\infty}\mathrm{d}\tau_2\int_{-\infty}^{\infty}\mathrm{d}\tau_1 \\ F_{\alpha_1}(t-\tau_n-\ldots-\tau_2-\tau_1)F_{\alpha_2}(t-\tau_n-\ldots-\tau_2)\ldots F_{\alpha_n}(t-\tau_n)R^{(n)}_{\alpha_1\alpha_2\ldots\alpha_n},\end{aligned} \tag{2.16}$$

where α_n indexes the three spatial dimensions for the n$^{\text{th}}$ interaction and are always to be implicitly summed over. In Eq. 2.16, we have introduced the n$^{\text{th}}$ order response function

$$\begin{aligned}R^{(n)}_{\alpha_1\alpha_2\ldots\alpha_n} &= \left(\frac{-\mathrm{i}}{\hbar}\right)^n \\ &\times \langle[B_{\alpha_1}(0),[B_{\alpha_2}(\tau_1)),\ldots[B_{\alpha_n}(\tau_1+\tau_2+\ldots+\tau_{n-1}),A((\tau_1+\tau_2+\ldots+\tau_n)]\ldots]]\rangle \\ &\times \theta(\tau_1)\theta(\tau_2)\ldots\theta(\tau_n),\end{aligned} \tag{2.17}$$

where $\theta(t)$ is the Heavyside step function. In general, the response function depends on the spatial coordinates as well; however, for spatially homogeneous systems, which is exclusively what we will consider here, it does not. In the types of experiments we most often consider, the $\boldsymbol{F}$ fields are external fields controlled by the experimenter. Therefore, all of the information regarding the system under study is contained in the response function and the goal of any spectroscopic experiment is, in some sense, to determine all or part of a response function of a particular order.

In what follows, we briefly consider the linear response, which is relevant to linear infrared absorption spectroscopy. Though this is not the focus of this thesis, the theory of linear response is an invaluable stepping stone to understand nonlinear response. The rest of the chapter will be dedicated to developing the theory of third order spectroscopy, which is what the bulk of the experiments in this thesis are based on.

2.2.2 Linear Response

For perturbations $V(t)$ which are substantially smaller than the unperturbed Hamiltonian, H_0, it is sufficient to only consider the first term in the expansion of Eq. 2.16. For the interaction Hamiltonian of Eq. 2.5, the expectation value of the α^{th} component of the dipole moment operator is

$$\left\langle \mu_\alpha^{(1)}(t) \right\rangle = \int_{-\infty}^{\infty} \mathrm{d}\tau_1 E_{\alpha_1}(t-\tau_1) R_{\alpha_1,\alpha}^{(1)}(\tau_1). \tag{2.18}$$

At linear order, the expectation value of the dipole moment operator is simply given by the convolution of the external electric field and the linear response function, which is given by

$$R_{\alpha_1,\alpha}^{(1)}(\tau_1) = \left(\frac{-\mathrm{i}}{\hbar}\right) \langle [\mu_{\alpha_1}(0), \mu_\alpha(\tau_1)] \rangle \, \theta(\tau_1). \tag{2.19}$$

Therefore, the linear response is basically determined by the dipole–dipole correlation function. Since the operators in Eq. 2.19 are in the interaction picture representation, evaluation of the matrix elements depends on the matrix elements of H_0 through the time-evolution operator.

At this point, it becomes necessary to adopt a model for H_0 in order to develop the theory further. A fairly general model is one in which we split the Hamiltonian into a "system" part, which is the part of interest, and an "environment" part which interacts with the system [52,63]. To that end, we write $H_0 = H_\text{S}(P,Q) + \hat{H}_\text{E}(\hat{p},\hat{q}) + \hat{H}_\text{SE}(Q,\hat{q})$, where P and Q are operators in the system subspace and $\hat{p}$ and $\hat{q}$ are operators in the bath subspace. $\hat{H}_\text{SE}(Q,\hat{q})$ is the interaction between the system and the environment. Henceforth, a carat above an operator designates that it is an operator in the environment subspace (though it may or may not be an operator in the system subspace). To simplify the treatment, we assume that the system–environment interaction is diagonal in the system eigenstates (i.e. the eigenstates of H_S, denoted $|a\rangle$) so that it cannot induce transitions between states of the system but it is not diagonal in the environment's eigenstates (i.e. those of $\hat{H}_\text{E}$, denoted

$|\nu\rangle$). This results in what is known as pure dephasing [63] which is a decent approximation for many systems.

In this model, the linear response function is given by

$$\begin{aligned} R^{(1)}_{\alpha_1,\alpha} = {} & \left(\frac{2}{\hbar}\right)\theta(\tau_1)\Im\sum_{a,b}\rho_{\mathrm{S}}^{aa}\mathrm{e}^{-\mathrm{i}\omega_{ab}\tau_1} \\ & \times\left\langle\hat{\mu}^{ab}_{\alpha_1}\exp_+\left[\frac{\mathrm{i}}{\hbar}\int_{-\infty}^{\tau_1}\mathrm{d}\tau\,\delta\hat{H}_b(\tau)\right]\hat{\mu}^{ba}_{\alpha}\exp_+\left[\frac{-\mathrm{i}}{\hbar}\int_{-\infty}^{\tau_1}\mathrm{d}\tau\,\delta\hat{H}_a(\tau)\right]\right\rangle_E, \end{aligned} \tag{2.20}$$

where the dipole moment matrix elements are operators in the environment subspace, $\delta\hat{H}_x = \langle x|\hat{H}_{\mathrm{E}}(\hat{p},\hat{q}) + \hat{H}_{\mathrm{SE}}(Q,\hat{q})|x\rangle$, ρ_{S}^{aa} the the a^{th} element of the system density matrix, and the subscript E on the angular brackets denotes an average over the equilibrium environment density matrix. The notation $\exp_+$ denotes the usual time-ordered exponential function. We have also implicitly made the assumption that the equilibrium system and environment density matricies are separable.

The fact that the dipole moment matrix elements in Eq. 2.20 depend on the environment degrees of freedom implies that transitions between the system states are accompanied by environment state transitions. Often, the environment degrees of freedom evolve on timescales much slower than those of the system[5] and transitions of the system occur without transitions of the environment. In this case, the dipole moment matrix elements can be approximated as not being functions of the environment degrees of freedom and they can be removed from the average over the environment degrees of freedom. This is known as the Condon approximation. With this, the linear response function is given by

$$R^{(1)}_{\alpha_1,\alpha}(\tau_1) = \left(\frac{2}{\hbar}\right)\Im\sum_{a,b}\rho_{\mathrm{S}}^{aa}\mathrm{e}^{\mathrm{i}\omega_{ba}\tau_1}\mu^{ab}_{\alpha_1}\mu^{ba}_{\alpha}f_{ab}(\tau_1), \tag{2.21}$$

---

[5] In electronic spectroscopy, separation of the electronic coordinates (system) and nuclear coordinates (environment) is rather straightforward, except at certain special configurations of the nuclei. In vibrational spectroscopy, however, the situation is rarely so clear cut and the separation of system and environment is more ambiguous. Nonetheless, discussions of vibrational spectroscopy usually proceed as though this separation has been made successfully.

where we have introduced the lineshape function

$$f_{ab}(\tau_1) = \theta(\tau_1)\left\langle \exp_+\left[\frac{-\mathrm{i}}{\hbar}\int_{-\infty}^{\tau_1} \mathrm{d}\tau\delta\hat{H}_{ab}(\tau)\right]\right\rangle_{\mathrm{E}} \tag{2.22}$$

with $\delta\hat{H}_{ab}(\tau) = \delta\hat{H}_a(\tau) - \delta\hat{H}_b(\tau)$. Therefore, the linear response function has four essential ingredients: 1) the equilibrium distribution of the system degrees of freedom, ρ_{S}^{aa}, 2) the transition frequencies of the system, ω_{ab}, 3) the transition dipole moment matrix elements of the system,[6] $\boldsymbol{\mu}^{ab}$, and 4) the correlations of the bath degrees of freedom, $\delta\hat{H}_{ab}(t)$. In the absence of a bath, $f_{ab}(\tau_1) = \theta(\tau_1)$, and the system response is to simply oscillate at the frequencies ω_{ab}, that characterize the transitions between eigenstates, with an amplitude determined by the transition dipole moment. Including a bath results in the response deviating from pure oscillatory behavior through the complex lineshape function. This generally has the effect of damping the oscillations (resulting in a finite linewidth in the frequency domain) as well as shifting frequencies.

Typically the formalism of §2.1.3 is not used for linear response since it can be incorporated analytically in the solution of the wave equation via the dielectric constant. However, the approximate treatment is illustrative. In the frequency domain, the linear electric polarization density is given by $E_\alpha(\omega)\chi_{\alpha_1,\alpha}(\omega)$ with

$$\chi^{(1)}_{\alpha_1,\alpha}(\omega) = \left(-\frac{\mathrm{i}}{\hbar}\right)\sum_{a,b}\rho_S^{aa}\mu_{\alpha_1}^{ab}\mu_\alpha^{ba}\left[f_{ab}(\omega+\omega_{ba}) - f^*_{ab}(\omega_{ba}-\omega)\right], \tag{2.23}$$

being the linear susceptibility. The real part of $\chi^{(1)}$ results in the radiation of a $\pi/2$ phase-shifted field due to the factor of i in Eq. 2.12. On the other hand, the imaginary part of $\chi^{(1)}$ results in a field that is π phase-shifted with respect to the driving field, and as such, results in a loss of field amplitude. Therefore, it is the real and imaginary parts of $\chi^{(1)}$ that are responsible for dispersion and absorption, respectively.

---

[6] At this point, it is worth mentioning that if the Hamiltonian, H_0, posses time-reversal symmetry then a basis can always be constructed in which the matrix elements of Hermitian operators (in particular, the transition dipole moment operator) are real. This can be seen by considering the fact that if ϕ_m is an eigenvector of H_0 with eigenvalue ϵ_m, time-reversal symmetry will ensure that so too is ϕ_m^* an eigenvector of H_0 with the same eigenvalue ϵ_m. Then, a purely real basis can be constructed by $\psi_m = (\phi_m + \phi_m^*)/2$; in such a real basis, all Hermitian operators will have real matrix elements. [64]

2.3 Third-Order Spectroscopy

2.3.1 Third-Order Response

If the fields incident on a sample are comparable to the internal fields of molecules, the system does not respond linearly to the perturbation. However, the calculation of the third-order response closely follows the development of the linear response outlined in §2.2.2. In practice, the equations describing the response are significantly more cumbersome due to the fact that there are three interactions (and thus four operators to deal with) between the sample and the field. For the dipole-interaction Hamiltonian of Eq. 2.5, the α^{th} component of the expectation value of the dipole moment operator to third order is given by

$$\left\langle \mu_\alpha^{(3)}(t) \right\rangle = \iiint \mathrm{d}\tau_3 \mathrm{d}\tau_2 \mathrm{d}\tau_1 E_{\alpha_1}(t-\tau_3-\tau_2-\tau_1) E_{\alpha_2}(t-\tau_3-\tau_2) E_{\alpha_1}(t-\tau_3) R^{(3)}_{\alpha_1,\alpha_2,\alpha_3,\alpha}. \tag{2.24}$$

The equations become somewhat more tractable if the third-order response function, given by Eq 2.17, is split into four different terms called Liouville pathways. To that end, we write

$$R^{(3)}_{\alpha_1,\alpha_2,\alpha_3,\alpha} = \left(\frac{-\mathrm{i}}{\hbar}\right)^3 \sum_{j=0}^{3} \mathcal{R}^{(3,j)}_{\alpha_1,\alpha_2,\alpha_3,\alpha} - \mathcal{R}^{(3,j)*}_{\alpha_1,\alpha_2,\alpha_3,\alpha} = -\frac{2}{\hbar^3} \sum_{j=0}^{3} \Im \mathcal{R}^{(3,j)}_{\alpha_1,\alpha_2,\alpha_3,\alpha}, \tag{2.25}$$

with the Liouville pathways being

$$\mathcal{R}^{(3,0)}_{\alpha_1,\alpha_2,\alpha_3,\alpha} = \theta(\tau_1,\tau_2,\tau_3) \left\langle \mu_{\alpha_2}(\tau_1) \mu_{\alpha_3}(\tau_1+\tau_2) \mu_\alpha(\tau_1+\tau_2+\tau_3) \mu_{\alpha_1}(0) \right\rangle \tag{2.26a}$$

$$\mathcal{R}^{(3,1)}_{\alpha_1,\alpha_2,\alpha_3,\alpha} = \theta(\tau_1,\tau_2,\tau_3) \left\langle \mu_{\alpha_1}(0) \mu_{\alpha_3}(\tau_1+\tau_2) \mu_\alpha(\tau_1+\tau_2+\tau_3) \mu_{\alpha_2}(\tau_1) \right\rangle \tag{2.26b}$$

$$\mathcal{R}^{(3,2)}_{\alpha_1,\alpha_2,\alpha_3,\alpha} = \theta(\tau_1,\tau_2,\tau_3) \left\langle \mu_{\alpha_1}(0) \mu_{\alpha_2}(\tau_1) \mu_\alpha(\tau_1+\tau_2+\tau_3) \mu_{\alpha_3}(\tau_1+\tau_2) \right\rangle \tag{2.26c}$$

$$\mathcal{R}^{(3,3)}_{\alpha_1,\alpha_2,\alpha_3,\alpha} = \theta(\tau_1,\tau_2,\tau_3) \left\langle \mu_\alpha(\tau_1+\tau_2+\tau_3) \mu_{\alpha_3}(\tau_1+\tau_2) \mu_{\alpha_2}(\tau_1) \mu_{\alpha_1}(0) \right\rangle. \tag{2.26d}$$

In the above equations, the multi-variable Heavyside function is simply shorthand for the product of Heavyside functions for the individual variables. This shows that the third-order response is essentially determined by the four-point dipole correlation function; it is the fact that the response depends on multiple points in time, that makes third-order spectroscopy so powerful at elucidating molecular correlations in a time-resolved manner. The response functions can be evaluated in the same manner as the linear response function in §2.2.2 and we do so here within the same system–environment model for H_0. The result is

$$\mathcal{R}^{(3,0)}_{\alpha_1,\alpha_2,\alpha_3,\alpha} = \sum_{a,b,c,d} \mu^{cb}_{\alpha}\mu^{cd*}_{\alpha_3}\mu^{da*}_{\alpha_2}\mu^{ba}_{\alpha_1}\rho^{aa}_0 \mathrm{e}^{-\mathrm{i}(\omega_{ba}\tau_1+\omega_{bd}\tau_2+\omega_{bc}\tau_3)}\mathcal{F}_{da,cd,bc}(\tau_1,\tau_2,\tau_3) \tag{2.27a}$$

$$\mathcal{R}^{(3,1)}_{\alpha_1,\alpha_2,\alpha_3,\alpha} = \sum_{a,b,c,d} \mu^{cb}_{\alpha}\mu^{cd*}_{\alpha_3}\mu^{ba}_{\alpha_2}\mu^{da*}_{\alpha_1}\rho^{aa}_0 \mathrm{e}^{-\mathrm{i}(\omega_{ad}\tau_1+\omega_{bd}\tau_2+\omega_{bc}\tau_3)}\mathcal{F}_{ab,cd,bc}(\tau_1,\tau_2,\tau_3) \tag{2.27b}$$

$$\mathcal{R}^{(3,2)}_{\alpha_1,\alpha_2,\alpha_3,\alpha} = \sum_{a,b,c,d} \mu^{cb}_{\alpha}\mu^{ba}_{\alpha_3}\mu^{cd*}_{\alpha_2}\mu^{da*}_{\alpha_1}\rho^{aa}_0 \mathrm{e}^{-\mathrm{i}(\omega_{ad}\tau_1+\omega_{ac}\tau_2+\omega_{bc}\tau_3)}\mathcal{F}_{cd,ab,bc}(\tau_1,\tau_2,\tau_3) \tag{2.27c}$$

$$\mathcal{R}^{(3,3)}_{\alpha_1,\alpha_2,\alpha_3,\alpha} = \sum_{a,b,c,d} \mu^{ad}_{\alpha}\mu^{dc}_{\alpha_3}\mu^{cb}_{\alpha_2}\mu^{ba}_{\alpha_1}\rho^{aa}_0 \mathrm{e}^{\mathrm{i}(\omega_{ba}\tau_1+\omega_{ca}\tau_2+\omega_{da}\tau_3)}\mathcal{F}_{bc,cd,da}(\tau_1,\tau_2,\tau_3), \tag{2.27d}$$

where we have introduced the third-order lineshape function

$$\begin{aligned}\mathcal{F}_{ab,cd,ef}(\tau_1,\tau_2,\tau_3) = \theta(\tau_1,\tau_2,\tau_3)\Big\langle &\exp_+\left[\frac{-\mathrm{i}}{\hbar}\int_{-\infty}^{\tau_1}\mathrm{d}\tau\delta\hat{H}_{ab}(\tau)\right] \\ &\times\exp_+\left[\frac{-\mathrm{i}}{\hbar}\int_{-\infty}^{\tau_1+\tau_2}\mathrm{d}\tau\delta\hat{H}_{cd}(\tau)\right]\exp_+\left[\frac{-\mathrm{i}}{\hbar}\int_{-\infty}^{\tau_1+\tau_2+\tau_3}\mathrm{d}\tau\delta\hat{H}_{ef}(\tau)\right]\Big\rangle_E .\end{aligned} \tag{2.28}$$

The third-order lineshape function is analogous to the one encountered in the treatment of linear response except that it depends on all three time intervals in the experiment. In the absence of a bath, the third-order response function oscillates at many transition frequencies of the system during the three intervals. Through interactions with the environement, the third-order lineshape function modifies these oscillations, changing their frequency and phase and causes them to decay.

Considering the discussion of the reality of the dipole moment matrix elements in the footnote of §2.2.2, it seems pointless to keep track of dipole complex conjugates in Eqs. 2.27. This is not without purpose. It is evident that keeping track of these terms becomes cumbersome rather quickly; however, the use of complex conjugates prompts a somewhat more intuitive interpretation of the response functions. We may interpret each dipole matrix element as being due to a transition of either the ket or bra side of the density matrix. Unconjugated elements represent a transition on the ket side while conjugated ones represent a transition on the bra side. For example, in Eq. 2.27a, be may consider that the density matrix "begins" in the $|a\rangle\langle a|$ state, "transitions" to the $|b\rangle\langle a|$, then to $|b\rangle\langle d|$, then to $|b\rangle\langle d|$, and finally to $|b\rangle\langle c|$. We must remember that this is not actually the state of the system, but rather a convenient way of keeping track of terms in the density matrix.

In fact, for greater convenience still, we may represent the Liouville pathways diagrammatically in what is called a ladder diagram. Each rung of the ladder represents an interaction with the electromagnetic field while the density matrix term is written in between the rungs. The eight Liouville paths (including complex conjugates) are shown in Fig. 2.1 and provide a powerful method for keeping track of the multitude of terms as well as the interpretation of experiments.

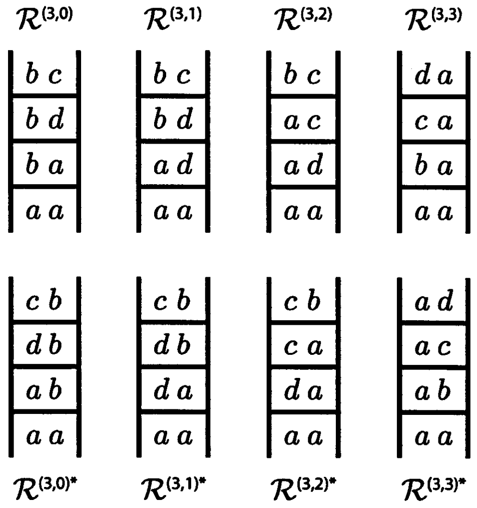

Figure 2.1: The eight Liouville pathways for third-order response.

Of course, the expectation value of the dipole moment operator is not determined solely by the third-order response function, but also by the fields that drive the transitions. In the following sections, we consider the effect of the electromagnetic fields and complete the development for calculating the expectation value of the dipole moment.

2.3.2 Driving Fields and the Rotating Wave Approximation

In most time-resolved third-order spectroscopy experiments, either two or three short pulses of light interact with a sample. The use of short pulses is what provides time resolution since it forces the interaction between the field and the matter to occur at specific times, uncertain to within the pulse length. A fairly general form of the electric field is given by

$$\boldsymbol{E}(\boldsymbol{x},t) = \sum_i \boldsymbol{e}_i E_i(\boldsymbol{x},t) \sum_{z_i} \mathrm{e}^{z_i \mathrm{i}(\omega_i t - \boldsymbol{k}_i \cdot \boldsymbol{x} + \phi_i)}, \tag{2.29}$$

where $\boldsymbol{e}_i$, $E_i(\boldsymbol{x},t)$, ω_i, $\boldsymbol{k}_i$, and ϕ_i are the polarization, amplitude, center frequency, wavevector, and phase of the i^{th} pulse, respectively. The index z takes on values of 1 and -1, and ensures that the field is a real quantity. The wavevector is given by $\boldsymbol{k}_i = (\omega_i \tilde{n}(\omega_i)/c)\hat{\boldsymbol{k}}_i$ and determines the principle direction of pulse propagation. The polarization vector is a real-valued unit vector. The amplitude, $E_i(\boldsymbol{x},t)$ is a slow-varying (slow relative to the optical period, $2\pi/\omega_i$, and optical wavelength $2\pi/k_i$) function of space and time and is also real valued and, for a short pulse, it is sharply peaked in time at $t = s_i$. For a chirped pulse, the phase, ϕ_i, is a function of time as well; however, we will consider pulses with a constant phase.

To calculate the expectation value of the dipole moment, we must plug the field, Eq. 2.29, into Eq. 2.24. For a three-pulse experiment, this results in $3^3 \times 2 = 54$ terms. The additional 8 terms in the response function means that the expectation value of the dipole moment operator contains a sum over all system eigenstates of 432 terms. Certainly the equations become overwhelming incredibly quickly. Fortunately, there are a number of simplifications that can be made. Even for short, well-separated pulses, the full 432 term expression contains terms where interactions occur out of order. For example, it is possible for the third pulse to interact before the first one even though the latter arrives earlier. Certainly, such terms will be small and they can be ignored. This is known as the pulse-ordering approximation and reduces the number of terms to 144 since there are only 9 well-ordered field terms.

Table 2.1: Summary of wavevector-matching conditions.

Z index	Sign Ordering	Total Wavevector	Frequency
0	$+++$	$\boldsymbol{k}_i + \boldsymbol{k}_j + \boldsymbol{k}_k$	$3\omega_0$
1	$-++$	$-\boldsymbol{k}_i + \boldsymbol{k}_j + \boldsymbol{k}_k$	ω_0
2	$+-+$	$\boldsymbol{k}_i - \boldsymbol{k}_j + \boldsymbol{k}_k$	ω_0
3	$++-$	$\boldsymbol{k}_i + \boldsymbol{k}_j - \boldsymbol{k}_k$	ω_0

Let us consider only the field part of Eq. 2.24, which we denote $\sum_{ijk} \mathcal{E}_{ijk}^{\alpha_1,\alpha_2,\alpha_3}$. The roman letters index the pulse ordering for the particular term. For example, $\mathcal{E}_{123}^{\alpha_1,\alpha_2,\alpha_3}$ corresponds to a field interaction with each of the three pulses, while $\mathcal{E}_{113}^{\alpha_1,\alpha_2,\alpha_3}$ corresponds to two interactions with the first pulse, and one with the third. Explicitly, the field tensor is given by

$$\begin{aligned}\mathcal{E}_{ijk}^{\alpha_1,\alpha_2,\alpha_3} &= e_i^{\alpha_1} e_j^{\alpha_2} e_k^{\alpha_3} E_i(\boldsymbol{x}, t-\tau_3-\tau_2-\tau_1) E_j(\boldsymbol{x}, t-\tau_3-\tau_2) E_k(\boldsymbol{x}, t-\tau_3) \\ &\times \sum_{z_i,z_j,z_k} \mathrm{e}^{-\mathrm{i}(z_i \boldsymbol{k}_i + z_j \boldsymbol{k}_j + z_k \boldsymbol{k}_k)\cdot \boldsymbol{x}} \mathrm{e}^{\mathrm{i}(z_i \phi_i + z_j \phi_j + z_k \phi_k)} \\ &\times \mathrm{e}^{-\mathrm{i} z_i \omega_i \tau_1} \mathrm{e}^{-\mathrm{i}(z_i \omega_i + z_j \omega_j)\tau_2} \mathrm{e}^{-\mathrm{i}(z_i \omega_i + z_j \omega_j + z_k \omega_k)\tau_3} \\ &\times \mathrm{e}^{\mathrm{i}(z_i \omega_i + z_j \omega_j + z_k \omega_k) t}.\end{aligned} \tag{2.30}$$

The sums over $\{z\}$ produce $2^3 = 8$ terms, however only four of these are independent and the other four are simply their complex conjugates. To that end, we split them into the $+++$ term, $-++$ term, $+-+$ term, and $++-$ term, such that the overall wavevector is positive. We give these terms the names third harmonic generation, rephasing, non-rephasing, and double quantum coherence, respectively, and are collectively referred to as wavevector-matching conditions. We can then write

$$\mathcal{E}_{ijk}^{\alpha_1,\alpha_2,\alpha_3} = \sum_{Z=0}^{3} \mathcal{E}_{ijk,Z}^{\alpha_1,\alpha_2,\alpha_3} + \mathcal{E}_{ijk,Z}^{\alpha_1,\alpha_2,\alpha_3 *}, \tag{2.31}$$

where the Z index determines the wavevector matching condition, with 0 corresponding to third harmonic generation, 1 to rephasing, 2 to non-rephasing, and 3 to double quantum coherence. The wavevector matching conditions are summarized in Table 2.1. For example, the rephasing term is explicitly given by

$$\begin{aligned}\mathcal{E}^{\alpha_1,\alpha_2,\alpha_3}_{ijk,1} &= e_i^{\alpha_1} e_j^{\alpha_2} e_k^{\alpha_3} E_i(\boldsymbol{x}, t-\tau_3-\tau_2-\tau_1) E_j(\boldsymbol{x}, t-\tau_3-\tau_2) E_k(\boldsymbol{x}, t-\tau_3) \\ &\times \mathrm{e}^{\mathrm{i}(\boldsymbol{k}_i-\boldsymbol{k}_j-\boldsymbol{k}_k)\cdot\boldsymbol{x}} \mathrm{e}^{-\mathrm{i}(\phi_i-\phi_j-\phi_k)} \\ &\times \mathrm{e}^{\mathrm{i}\omega_i\tau_1} \mathrm{e}^{\mathrm{i}(\omega_i-\omega_j)\tau_2} \mathrm{e}^{\mathrm{i}(\omega_i-\omega_j-\omega_k)\tau_3} \\ &\times \mathrm{e}^{-\mathrm{i}(\omega_i-\omega_j-\omega_k)t}.\end{aligned}$$

The last line of Eq. 2.30 shows that the expectation value of the dipole moment oscillates as a function of time at frequencies that are combinations of $\pm\omega_i \pm \omega_j \pm \omega_k$. If all pulses have the same center frequency, ω_0, the dipole moment can only oscillate at $\pm 3\omega_0$ for third harmonic generation (thus the name) and $\pm\omega_0$ for the other three terms. We also note that each term has a unique wavevector given by one of $\pm\boldsymbol{k}_i \pm \boldsymbol{k}_j \pm \boldsymbol{k}_k$. This dependence transfers directly to the electric polarization density, which in turn radiates in one of the four possible directions. Depending on the wavevectors of the input pulses, these four directions can be unique or not.

With the notation we have introduced, the third order dipole moment is given by

$$\left\langle \mu_\alpha^{(3)}(t) \right\rangle = -\frac{2}{\hbar^3} \sum_{ijk} \sum_{n=0}^{3} \sum_{Z=0}^{3} \iiint \mathrm{d}\tau_3 \mathrm{d}\tau_2 \mathrm{d}\tau_1 \Im \left[\mathcal{E}^{\alpha_1,\alpha_2,\alpha_3}_{ijk,Z} \left(\mathcal{R}^{(3,n)}_{\alpha_1,\alpha_2,\alpha_3,\alpha} - \mathcal{R}^{(3,n)*}_{\alpha_1,\alpha_2,\alpha_3,\alpha} \right) \right]. \tag{2.32}$$

There are many terms in Eq. 2.32 and the question naturally arises whether it is possible to determine if certain terms are small. The integrals in Eq. 2.32 are over functions that oscillate as a function of integration variable. If the oscillation frequencies are large, than the integral will produce a small value. Therefore, it suffices to consider only terms for which the integrand does not oscillate rapidly as a function of the three τ's. This is known as the rotating-wave approximation. Since the field term oscillates at non-zero frequencies, it is necessary for the oscillation of the response function to cancel the field oscillation.

As an example, we consider the oscillatory part of the product of the rephasing term with the first Liouville path

$$\mathcal{E}_{ijk,1}^{\alpha_1,\alpha_2,\alpha_3}\mathcal{R}^{(3,0)}_{\alpha_1,\alpha_2,\alpha_3,\alpha} \propto \mathrm{e}^{\mathrm{i}(\omega_i-\omega_{ba})\tau_1}\,\mathrm{e}^{\mathrm{i}(\omega_i-\omega_j-\omega_{bd})\tau_2}\,\mathrm{e}^{\mathrm{i}(\omega_i-\omega_j-\omega_k-\omega_{bc})\tau_3}.$$

In the case that the center frequencies of the three pulses are the same ω_0, we can immediately see that such terms can only contribute significantly if $\omega_{ba} \approx \omega_0$, $\omega_{bd} \approx 0$, and $\omega_{bc} \approx -\omega_0$. In other words, the first interaction must be an upwards transition on the ket side, the second interaction an upwards transition on the bra side to the same state as the first interaction, and finally, another upwards transition on the ket side so that state b is smaller in energy than state c.

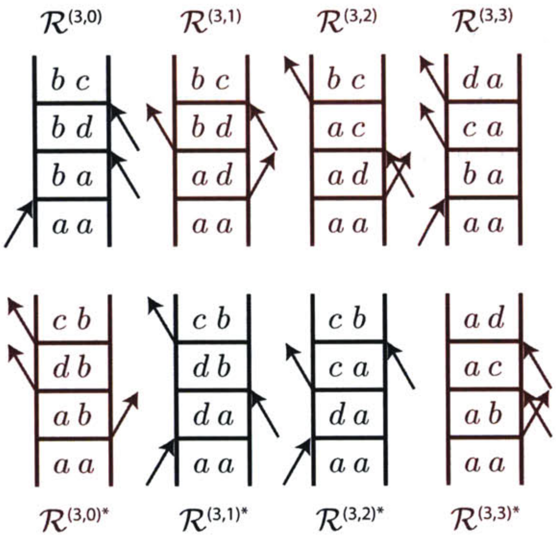

Figure 2.2: The eight Liouville pathways for the rephasing wavevector-matching condition.

Being so powerful, it is extremely convenient to incorporate the rotating-wave approximation into the diagrammatic representation of the response function. To that end, we add to the Liouville pathways of Fig. 2.1 arrows that correspond to the wavevector-matching condition. A right-pointing arrow corresponds to an upward (downward) transition on the ket (bra) side of the Liouville diagram. A left-pointing arrow corresponds to a downward (upward) transition on the ket (bra) side of the diagram. The directions of all three arrows is determined by Z.

For example, the rephasing pathway $(-++)$ corresponds to right, left, left. Transitions must be up-down-down on the ket side, or down-up-up on the bra side for the rotating wave approximation to be satisfied. Figure 2.2 shows the eight Liouville diagrams for the rephasing pathway. Each diagram corresponds to a term in the expansion of the third-order dipole moment, Eq. 2.32. In the typical interpretation of an experiment, one writes down all possible diagrams for a particular wavevector-matching condition, and associates with each one a term in the expression for the third order dipole moment.

One further approximation that can be made, known as the low-temperature approximation, further simplifies the expression for the third-order dipole moment. The response functions, given by Eq. 2.27, contain a sum over the diagonal elements of the equilibrium density matrix. However, if the transitions under study are much larger than $k_\mathrm{B}T$, then only the ground state will be significantly populated. In other words, the diagonal elements of the equilibrium density matrix will look like $\rho_0^{aa} \approx \delta_{a0}$ and a will be the ground state. (For high-frequency vibrations $\omega \gg k_\mathrm{B}T$, this is usually a good approximation.) Therefore, any terms which require a downward transition from the a state will necessarily violate the rotating wave approximation. Such terms are shown in maroon in Fig. 2.2.[7] Within the low-temperature approximation, only three Liouville paths survive for the rephasing wavevector-matching condition. Three pathways survive for the non-rephasing wavevector-matching condition, two for the double quantum coherence condition, and one for the third-harmonic generation condition. In the following section, we explore what consequence the wavevector-matching condition has for the radiated light.

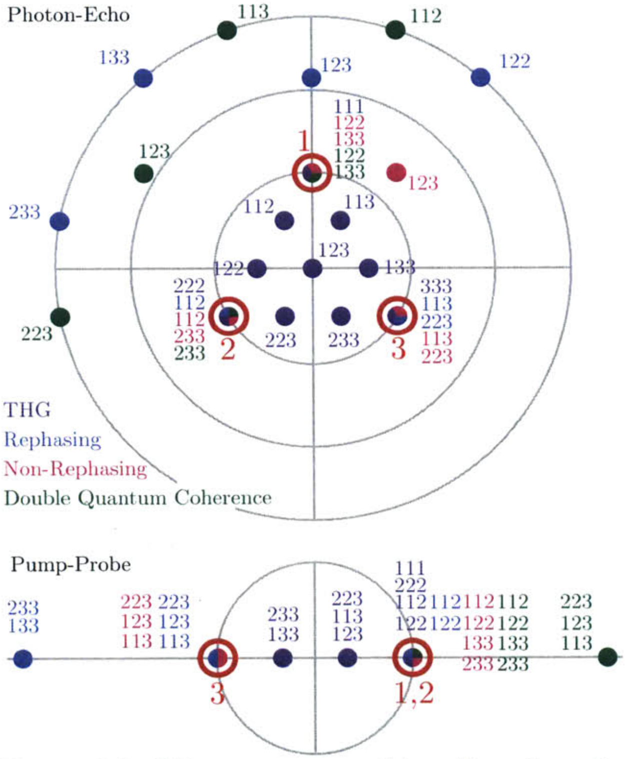
Photon-Echo
113
112
133
123
122
111
122
133
122
133
1
123
123
233
112
113
123
122
133
222
112
112
233
233
2
223
233
3
333
113
223
113
223
223
THG
Rephasing
Non-Rephasing
Double Quantum Coherence
Pump-Probe
233
133
223 223
123 123
113 113
3
233
133
223
113
123
111
222
112 112 112 112
122 122 122 122
133 133
233 233
1,2
223
123
113

Figure 2.3: Wavevector-matching directions for two common experimental geometries.

---

[7] The $\mathcal{R}^{(3,3)}$ term does not necessarily vanish in the low temperature approximation if b is not the first excited state. However, experimental considerations or selection rules often ensure that this is the case.

2.3.3 Wavevector Matching

As mentioned in §2.3.2, the wavevector-matching condition determines the sign and magnitude of both the wavevector and the frequency of the the third-order dipole moment. In the following section, we relate the expectation value of the third-order dipole moment to the macroscopic electric polarization density (Eq. 2.34). In obtaining the expression for the macroscopic polarization, the $\boldsymbol{x}$ dependence is unaffected, and the macroscopic polarization can be written as a sum over terms that have the form

$$\mathrm{e}^{\mathrm{i}(\pm\boldsymbol{k}_i\pm\boldsymbol{k}_j\pm\boldsymbol{k}_k)\cdot\boldsymbol{x}}\mathscr{P}^{(3)}(\boldsymbol{x},t),$$

where the sign on the wavevectors is determined by the wavevector-matching condition. In §2.1.3, it was shown that a polarization of this form will only generate a signal field if the phase-matching condition is met. That is, for the radiated signal field,

$$\Delta\boldsymbol{k} = \boldsymbol{k}_{\mathrm{P}} - \boldsymbol{k} = \pm\boldsymbol{k}_i \pm \boldsymbol{k}_j \pm \boldsymbol{k}_k - \boldsymbol{k} \approx 0. \tag{2.33}$$

Therefore, the direction of the radiated signal field is determined by the wavevector-matching condition, and the four different conditions will in general radiate in different directions.

Of course, in the consideration of phase-matching, we must also take into account the linear index of refraction. That is, the wavevectors in Eq. 2.33 are those in the medium, and this has profound effect on the actual phase-matching condition. As an example, we consider third harmonic generation of a single field of frequency ω_0, which occurs at $3\omega_0$. Then, $\boldsymbol{k} = 3\omega_0\hat{n}(3\omega_0)/c\hat{\boldsymbol{k}}$ and $\boldsymbol{k}_i = \boldsymbol{k}_j = \boldsymbol{k}_k = \omega_0\hat{n}(\omega_0)/c\hat{\boldsymbol{k}}_{\mathrm{in}}$. The phase-matching condition Eq. 2.33 then comes down to

$$\Delta\boldsymbol{k} = \frac{3\omega_0}{c}(\hat{n}(3\omega_0)\hat{\boldsymbol{k}} - \hat{n}(\omega_0)\hat{\boldsymbol{k}}_{\mathrm{in}}),$$

which can only be approximately zero if $\hat{n}(3\omega_0) = \hat{n}(\omega_0)$ and if $\hat{\boldsymbol{k}} = \hat{\boldsymbol{k}}_{\mathrm{in}}$. The former condition is not usually met in liquids (although can be met in appropriately cut crystals) and so third-harmonic generation does not usually occur in liquids.

On the other hand, the rephasing wavevector-matching condition generates a signal at ω_0 if a single frequency is input. Then, with three unique input fields, the phase-matching condition is given by

$$\Delta\boldsymbol{k} = \frac{\omega_0}{c}\hat{n}(\omega_0)(\hat{\boldsymbol{k}} + \hat{\boldsymbol{k}}_1 - \hat{\boldsymbol{k}}_2 - \hat{\boldsymbol{k}}_3),$$

which is only non-zero if the signal field is radiated in the $\hat{\boldsymbol{k}} = -\hat{\boldsymbol{k}}_1 + \hat{\boldsymbol{k}}_2 + \hat{\boldsymbol{k}}_3$ direction. Furthermore, there is no frequency-matching condition imposed by the index of refraction, and so a rephasing electric polarization density can be generated in a liquid. The same is true for the non-rephasing and double quantum coherence pathways.

Researchers typically draw from a handful of geometries when designing an experiment to most conveniently acquire the signal of interest. Figure 2.3 shows two common geometries: the photon-echo geometry [65–67] and the pump-probe geometry [68, 69]. In the former, three beams have unique wavevectors that point to the corners of an equilateral triangle. In spherical coordinates, $\boldsymbol{k}_1 = (0, \sin\theta, \cos\theta)$, $\boldsymbol{k}_2 = (-\sqrt{3/4}\sin\theta, -1/2\sin\theta, \cos\theta)$, and $\boldsymbol{k}_3 = (\sqrt{3/4}\sin\theta, -1/2\sin\theta, \cos\theta)$, where θ is the angle between the wavevector and the axis of propagation. The use of a small value of θ increases time resolution (due to a smaller region of overlap in the sample) at the expense of angular resolution; that is, all of the wavevector matching conditions point along the z axis as $\theta \to 0$.

In the pump–probe geometry, all beams lie in a plane, with $\boldsymbol{k}_1 = \boldsymbol{k}_2 = (\sin\theta, \cos\theta)$ and $\boldsymbol{k}_3 = (-\sin\theta, \cos\theta)$. As is evident from Fig. 2.3, this results in fewer unique signal directions and as such, has the added benefit of not having to collect multiple signals. This is also a drawback in that it is not possible to collect the individual signals separately. In this geometry, the rephasing and non-rephasing signals involving one interaction with $\boldsymbol{k}_3$ are emitted in the same direction as $\boldsymbol{k}_3$. As such, the $\boldsymbol{k}_3$ field also necessarily heterodynes the emitted signals (see §2.5.1). This again has the advantage of being simple, in that no external field is needed to heterodyne the emitted signal. On the other hand, this can be disadvantageous since it is not possible to independently control the heterodyning field.

Finally, it is worth briefly discussing the physical origin of phase matching. When the macroscopic polarization is generated, individual transition dipoles are excited in a spatial pattern dictated by the wavevector matching condition. Each individual dipole proceeds to radiate with a fixed phase relation relative to the other dipoles. However, the spatial excitation pattern imprinted by the input fields results in destructive interference of the dipole radiation in all but a few unique directions. In a third-order experiment, we often say that the first two interactions pattern a diffraction grating on the sample and the signal is a result of the third beam being diffracted off this grating. While this is an oversimplification of reality, it captures the basic idea. What is important to note, however, is that *phase matching is not due to conservation of momentum* as is commonly, but mistakenly, stated. Of course, momentum is conserved in phase matching the signal, as it must be, but it is not the reason there is phase matching. In other words, momentum is conserved in all spectroscopic experiments (e.g. in fluorescence experiments, photon momentum is balanced by recoil of the emitting molecule) but only experiments that generate a coherent spatially varying electric polarization density result in a phase-matched signal.

2.4 Rotational Averaging

2.4.1 The Electric Polarization Density

So far, we have calculated the expectation value of the dipole moment of the system after one or multiple interactions with the electric field. However, we must calculate the electric polarization density since it radiates the signal we actually measure. According to classical electrodynamics, the electric polarization density is the coarse-grained dipole moment per unit volume [49]. As such, the electric polarization density is given by

$$\boldsymbol{P}(\boldsymbol{x},t) = n_0 \overline{\langle \boldsymbol{\mu}(t) \rangle}, \tag{2.34}$$

where n_0 is the number density of molecules in the sample and the overbar represents a classical averaging of the expectation value of the dipole moment. In some sense, we have already implicitly done some coarse-graining by assuming the sample is spatially homogeneous. That is, we have assumed that an averaging over the "roughness" due to the individual molecules can be carried out, resulting in a uniform number density, n_0.

On the other hand, we have not yet taken into account the distributions of orientations of the molecules. Individual dipoles will radiate in different directions and reduce somewhat the overall signal compared to uniformly oriented dipoles. For our purposes, the overbar essentially represents a classical average over the orientation of the dipole moment vector. In a crystalline solid, the dipoles are fixed and there is no need to due such averaging. In a liquid or amorphous solid, however, it is necessary to average over an isotropic distribution. It is also possible to have other situations; for example, for a liquid near a surface, it is necessary to average over a non-isotropic distribution.

The averaging procedure is somewhat complicated by the fact that the expectation value of the dipole moment is actually determined by a tensor of rank two or four for linear and third-order spectroscopy, respectively. Therefore, it is in reality necessary to perform a rotational average over a tensor. In this section, we perform this average and show how signal intensities are affected due to it. In addition, we show how the angle between two transition dipole moments affects the intensity of the measured signal.

2.4.2 Averaging the Molecular Frame Transformation

Consider a vector $\boldsymbol{\mu}$ in the lab frame, whose indices we denote by some α_n, as in the previous sections, which takes on values of X, Y, and Z. There is a transformation parametrized by a continuous set of variable Ω such that the transformation $T(\Omega)$ takes the vector $\boldsymbol{\mu}$ from the lab frame to the molecular frame

$$\boldsymbol{m} = T(\Omega)\boldsymbol{\mu}, \tag{2.35}$$

where $\boldsymbol{m}$ is the vector $\boldsymbol{\mu}$ in the molecular frame. The molecular frame indicies are denoted with some a_n, and they take on values of $1, 2, 3$. For convenience, we express vectors in the molecular frame in spherical coordinates with the vector 3 corresponding to $\theta = 0$ and the vector 1 corresponding to $(\theta, \phi) = (\pi/2, 0)$. Vectors in the molecular frame are illustrated schematically in the left-hand side Fig. 2.4. It is convenient to write the transformation in using the summation convention

$$m_a = T_{a\alpha}(\Omega)\mu_\alpha, \tag{2.36}$$

with the summation over the index α implied.

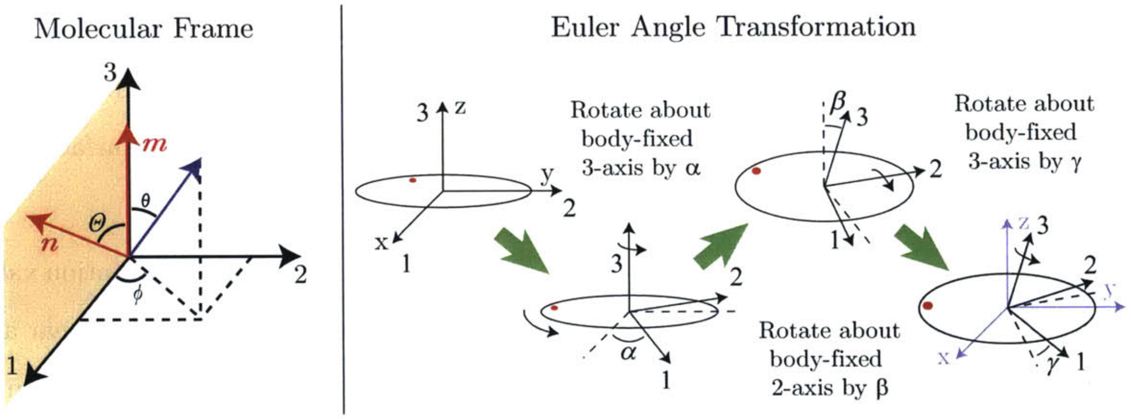
Molecular Frame
3
m
θ
Θ
n
ϕ
2
1
Euler Angle Transformation
3 z
y
2
x
1
Rotate about body-fixed 3-axis by α
3
2
α
1
β
3
2
1
Rotate about body-fixed 2-axis by β
Rotate about body-fixed 3-axis by γ
z 3
2
y
x
γ
1

Figure 2.4: (Left) Illustration of the vectors $\boldsymbol{m}$ and $\boldsymbol{n}$ in the molecular frame. (Right) Euler angle transformation carried out on a disc with a dot on it.

As per the discussion of the previous sections, we are concerned with averaging terms which look like $\overline{\mu_{\alpha_1}\nu_{\alpha_2}\rho_{\alpha_3}\sigma_{\alpha_4}\cdots}$, where again the overbar denotes an average over the possible orientations of the molecule and the greek letters denote different lab-frame vectors. This amounts to averaging over the set of transformation variables Ω since each different set of variables connects the lab frame to a molecular frame with a different orientation. In third-order spectroscopy, we have to deal with terms that are the product of four vectors only. In the summation notation, we may write such terms as

$$\overline{\mu_{\alpha_1}\nu_{\alpha_2}\rho_{\alpha_3}\sigma_{\alpha_4}} = \overline{T_{\alpha_1 a_1}(\Omega)m_{a_1}T_{\alpha_2 a_2}(\Omega)n_{a_2}T_{\alpha_3 a_3}(\Omega)r_{a_3}T_{\alpha_4 a_4}(\Omega)s_{a_4}}. \tag{2.37}$$

However, the vectors are fixed in the molecular frame and therefore may be removed from the averaging. This allows us to write

$$\overline{\mu_{\alpha_1}\nu_{\alpha_2}\rho_{\alpha_3}\sigma_{\alpha_4}} = m_{a_1}n_{a_2}r_{a_3}s_{a_4}Y^{a_1a_2a_3a_4}_{\alpha_1\alpha_2\alpha_3\alpha_4}, \tag{2.38}$$

where we have introduced the orientational tensor

$$\begin{aligned} Y^{a_1a_2a_3a_4}_{\alpha_1\alpha_2\alpha_3\alpha_4} &= \overline{T_{\alpha_1a_1}(\Omega)T_{\alpha_2a_2}(\Omega)T_{\alpha_3a_3}(\Omega)T_{\alpha_4a_4}(\Omega)} \\ &= \int \mathrm{d}\Omega P(\Omega)T_{\alpha_1a_1}(\Omega)T_{\alpha_2a_2}(\Omega)T_{\alpha_3a_3}(\Omega)T_{\alpha_4a_4}(\Omega), \end{aligned} \tag{2.39}$$

where $P(\Omega)\mathrm{d}\Omega$ is the probability of finding the molecule within the orientation limits Ω and $\Omega + \mathrm{d}\Omega$.

Before we begin evaluating such terms explicitly, we may use the symmetry of the response function, which has the symmetry of the system, to decide which terms will be zero or non-zero. In an isotropic system, the response function will have inversion symmetry. Therefore, under the transformation X → −X, the response function must be unchanged [55,56]. This can only happen if the indices (X,Y,Z) appear in pairs. Therefore, terms which look like $\mu_{\alpha_1}\nu_{\alpha_1}\rho_{\alpha_1}\sigma_{\alpha_2}$ (with $\alpha_1 \neq \alpha_2$) will necessarily average to zero. For linear spectroscopy, this implies that the linear response function of a liquid, $R^{(1)}_{\alpha_1,\alpha}(\tau)$, is a diagonal tensor and only components in which $\alpha_1 = \alpha$ are non-zero. Physically this implies that an isotropic liquid cannot change the polarization of the excitation field; an interaction polarized along one laboratory direction cannot stimulate radiation polarized along another. Furthermore, an isotropic system is invariant under rotations, which implies that switching any of the axes leaves the response function unchanged. Therefore, we find that only four configurations will survive the averaging process: ZZZZ, ZZYY, ZYZY, and ZYYZ, with other permutations being equivalent.

Thus far, we haven't mentioned what the transformation actually is. While this transformation may be any suitable transformation which maps the lab frame into the molecular frame, the transformation using Euler angles is by far the most convenient. In the y-convention [50, 70, 71], the Euler transformation matrix reads

$$T(\alpha,\beta,\gamma)=\begin{array}{c c}
\begin{array}{ccc} X & Y & Z \end{array} & \\
\begin{pmatrix} c_\alpha c_\beta c_\gamma - s_\alpha s_\gamma & -c_\gamma s_\alpha - c_\alpha c_\beta s_\gamma & c_\alpha s_\beta \\ c_\alpha s_\gamma + c_\beta c_\gamma s_\alpha & c_\alpha c_\gamma - c_\beta s_\alpha s_\gamma & s_\alpha s_\beta \\ -c_\gamma s_\beta & s_\beta s_\gamma & c_\beta \end{pmatrix} & \begin{array}{c} 1 \\ 2 \\ 3 \end{array}
\end{array}, \tag{2.40}$$

where we have used the notation $c_\alpha = \cos\alpha$ and $s_\alpha = \sin\alpha$. As written, the transformation carries out a rotation about the body-fixed 3–axis (i.e. in the molecular frame) by an angle α, then a rotation about the body-fixed 2–axis by an angle β, and finally another rotation about the body-fixed 3–axis by an angle γ. The Euler transformation is illustrated in the right-hand side of Fig 2.4. The volume element of Euler angles is given by

$$\int \mathrm{d}\Omega = \int_0^{2\pi} \mathrm{d}\alpha \int_{-1}^{1} \mathrm{d}c_\beta \int_0^{2\pi} \mathrm{d}\gamma. \tag{2.41}$$

We note that the integral over all angles is equal to $8\pi^2$, so that the probability density for an isotropic distribution is $P(\Omega) = (8\pi^2)^{-1}$.

It is instructional at this point to evaluate some orientational tensors explicitly. We begin by considering dipoles which all point along the 3-axis in the molecular frame. There are four such orientational tensors. The first one is given by

$$Y^{3333}_{\mathrm{ZZZZ}} = \overline{T^4_{3Z}(\Omega)} = \frac{1}{8\pi^2}\int_0^{2\pi} \mathrm{d}\alpha \int_{-1}^{1} \mathrm{d}c_\beta \int_0^{2\pi} \mathrm{d}\gamma c^4_\beta = \frac{1}{5}.$$

Other terms are equally straightforward to calculate

$$Y^{3333}_{\mathrm{ZZYY}} = \overline{T^2_{3Z}(\Omega)T^2_{3Y}(\Omega)} = \frac{1}{8\pi^2}\int_0^{2\pi} \mathrm{d}\alpha \int_{-1}^{1} \mathrm{d}c_\beta \int_0^{2\pi} \mathrm{d}\gamma s^2_\gamma s^2_\beta c^2_\beta = \frac{1}{15}.$$

$$Y^{3333}_{\mathrm{ZYYZ}} = Y^{3333}_{\mathrm{ZYZY}} = Y^{3333}_{\mathrm{ZZYY}}.$$

In reality, all dipoles do not point in the same direction in the molecular frame. In most cases, however, we will only be dealing with two dipole moments in the molecular frame. We can always choose one to lie along the 3 direction and the other to be in the 1-3 plane (see Fig. 2.4). We explicitly consider one such element before listing off all the others

$$Y^{3311}_{\mathrm{ZZZZ}} = \overline{T^2_{1Z}(\Omega)T^2_{3Z}(\Omega)} = \frac{1}{15} = Y^{3333}_{\mathrm{ZZYY}}.$$

The fact that $Y^{3311}_{\mathrm{ZZZZ}} = Y^{3333}_{\mathrm{ZZYY}}$ is not a coincidence. It reflects the symmetry to exchange the axes in the lab and molecular frames [72]. That is, the orientational tensor is invariant under the exchnage 1 → 3, Y → Z or vice versa. In the simplest example of this is $Y^{3333}_{\mathrm{ZZZZ}} = Y^{1111}_{\mathrm{YYYY}}$. The list of orientational tensors required for third-order spectroscopy are summarized in Table 2.2. For linear spectroscopy of an isotropic liquid, the only orientational tensor to consider is Y^{33}_{ZZ} since all others are either equivalent or vanish by symmetry. The value of the orientational tensor relevant to linear spectroscopy is $Y^{33}_{\mathrm{ZZ}} = 1/3$.

Table 2.2: Value of non-zero orientational tensors relevant to third-order spectroscopy.

Orientational Tensor	Value
Y^{3333}_{ZZZZ}	1/5
$Y^{3333}_{\mathrm{ZYYZ}} = Y^{3333}_{\mathrm{ZYZY}} = Y^{3333}_{\mathrm{ZZYY}}$	1/15
$Y^{3311}_{\mathrm{ZZZZ}} = Y^{3131}_{\mathrm{ZZZZ}} = Y^{3113}_{\mathrm{ZZZZ}}$	1/15
$Y^{3311}_{\mathrm{ZZYY}} = Y^{3131}_{\mathrm{ZYZY}} = Y^{3113}_{\mathrm{ZYYZ}}$	2/15
$Y^{3131}_{\mathrm{ZZYY}} = Y^{3113}_{\mathrm{ZZYY}} = Y^{3311}_{\mathrm{ZYZY}} = Y^{1331}_{\mathrm{ZYZY}} = Y^{3311}_{\mathrm{ZYYZ}} = Y^{3131}_{\mathrm{ZYZY}}$	-1/30

To determine what factor the orientational averaging is going to impart on the spectrum, we must sum the factors corresponding to all the Liouville pathways that contribute to a particular feature. We will explore these more thoroughly in §2.5.5.

Before closing this section, let us consider dipoles $\boldsymbol{m}$ and $\boldsymbol{n}$ in the molecular frame, which we choose to have be $\boldsymbol{m} = m(0,0,1)$ and $\boldsymbol{n} = n(\sin\Theta, 0, \cos\Theta)$ consistent with our discussion above. These vectors are explicitly shown in the left-hand side of Fig. 2.4. The two interaction orderings that will turn out to be relevant to the experiments presented in later chapters are $\mu\mu\nu\nu$ and $\mu\nu\mu\nu$. For the ZZZZ polarization scheme, these will be the same. For the first term in the ZZZZ polarization scheme, using Eq 2.38

$$\begin{aligned}\overline{\mu_Z\mu_Z\nu_Z\nu_Z} &= m^2n^2\left(Y^{1133}_{\mathrm{ZZZZ}}\sin^2\Theta + 2\cancelto{0}{Y^{1333}_{\mathrm{ZZZZ}}}\sin\Theta\cos\Theta + Y^{3333}_{\mathrm{ZZZZ}}\cos^2\Theta\right)\\ &= m^2n^2\frac{1}{15}\left(1+2\cos^2\Theta\right)\end{aligned} \tag{2.42}$$

The orientational tensor where the index 1 appears once (the second term) vanishes. This is easy to verify explicitly or simply by symmetry. Again, the other term for this polarization scheme is the same; that is, $\overline{\mu_Z\mu_Z\nu_Z\nu_Z} = \overline{\mu_Z\nu_Z\mu_Z\nu_Z}$. Remarkably, the intensity of this particular pathway is in fact determined by the angle between the transition dipoles in the molecular frame. While this will be elaborated further in §2.5.5, we note here that this provides a direct route, in principle, to determine these angles.

For the ZZYY polarization scheme, these terms will not be the same since in one term each polarization interacts with only one dipole, while in the other, each polarization interacts with both. For the $\boldsymbol{\mu\mu\nu\nu}$ interaction order in the ZZYY polarization scheme, we have

$$\begin{aligned}\overline{\mu_Z\mu_Z\nu_Y\nu_Y} &= m^2n^2(Y^{1133}_{\mathrm{ZZYY}}\sin^2\Theta + 2\cancelto{0}{Y^{1333}_{\mathrm{ZZYY}}}\sin\Theta\cos\Theta + Y^{3333}_{\mathrm{ZZYY}}\cos^2\Theta)\\ &= m^2n^2\frac{1}{15}\left(2-\cos^2\Theta\right)\end{aligned} \tag{2.43}$$

On the other hand, for the $\boldsymbol{\mu\nu\mu\nu}$ interaction order in the ZZYY polarization scheme, we have

$$\begin{aligned}\overline{\mu_Z\nu_Z\mu_Y\nu_Y} &= m^2n^2(Y^{1313}_{\mathrm{ZZYY}}\sin^2\Theta + 2\cancelto{0}{Y^{1333}_{\mathrm{ZZYY}}}\sin\Theta\cos\Theta + Y^{3333}_{\mathrm{ZZYY}}\cos^2\Theta)\\ &= m^2n^2\frac{1}{30}\left(3\cos^2\Theta-1\right)\end{aligned} \tag{2.44}$$

It is interesting to point out that unlike Eqs. 2.42 and 2.43, Eq. 2.44 actually vanishes if the transition dipoles form an angle between them which is equal to 54.7°.

The factors arising from the rotational averaging are summarized in Appendix 2.A for the Liouville pathways relevant to a two-oscillator system.

2.4.3 Orientational Diffusion

The discussion so far has not included the possibility that the excited molecules can reorient during the experiment. Over the course of the delay between pulses in an experiment, excited molecules reorient their transition dipoles, resulting in a drop in signal with increasing waiting time. We must therefore consider that the molecular frame transformation necessarily changes as a function of time due to the rotational diffusion of the vibrational excitation. In this case, it is necessary to modify Eq. 2.39 to allow for diffusion to a new molecular orientation [73–76].

$$\begin{aligned} Y^{a_1a_2a_3a_4}_{\alpha_1\alpha_2\alpha_3\alpha_4} = \int \mathrm{d}\Omega_3 \int \mathrm{d}\Omega_2 \int \mathrm{d}\Omega_1 \int \mathrm{d}\Omega_0 P(\Omega_0) T_{\alpha_1 a_1}(\Omega_0) G(\Omega_1, \tau_1 | \Omega_0) \\ \times T_{\alpha_2 a_2}(\Omega_1) G(\Omega_2, \tau_2 | \Omega_1) T_{\alpha_3 a_3}(\Omega_2) G(\Omega_3, \tau_3 | \Omega_2) T_{\alpha_3 a_3}, \end{aligned} \tag{2.45}$$

where $P(\Omega)$ is still the initial probability distribution, and G is a conditional probability distribution that describes the diffusional reorientation of the molecule. That is, $G(\Omega_1, \tau_1|\Omega_0)$ gives the probability of the molecular frame having oriented itself to Ω_1 after a time τ_1 given that it was initially oriented at Ω_0. The specific form of $G(\Omega_1, \tau_1|\Omega_0)$ depends on the details of the molecule; that is, it will have a different form for differently shaped molecules. For a molecule exhibiting no particular symmetry, arriving at the form of $G(\Omega_1, \tau_1|\Omega_0)$ is incredibly complex [73]. However, for a molecule that is spherically symmetric (or approximately so), $G(\Omega_1, \tau_1|\Omega_0)$ is given by [76]

$$G(\Omega_1, \tau_1|\Omega_0) = \frac{1}{8\pi^2} \sum_{jmk} (2j+1) D^{j*}_{mk}(\Omega_1) D^{j}_{mk}(\Omega_0) c_j(\tau_1), \tag{2.46}$$

where

$$c_j(\tau_1) = \mathrm{e}^{-j(j+1)\tau/\tau_r}. \tag{2.47}$$

Here, τ_r is the timescale for rotational diffusion, and

$$D^{j}_{mk}(\Omega) = \mathrm{e}^{-i(\alpha m + \gamma k)} \langle jm | \mathrm{e}^{-iJ_y\beta} | jk \rangle \tag{2.48}$$

is the Wigner rotation matrix, where J_y is the y–component of the angular momentum operator. The Wigner rotation matrices have the following useful properties [70, 71]

$$D^{j*}_{mk} = (-1)^{m-k} D^{j}_{-m-k} \tag{2.49a}$$

$$\int \mathrm{d}\Omega D^{j}_{mk}(\Omega) D^{j'}_{m'k'}(\Omega) = \frac{8\pi^2}{2j+1}\delta_{jj'}\delta_{mm'}\delta_{kk'} \tag{2.49b}$$

$$\int \mathrm{d}\Omega D^{J}_{MK}(\Omega) D^{j}_{mk}(\Omega) D^{j'}_{m'k'}(\Omega) = \frac{8\pi^2}{2J+1}\langle jmj'm'|JM\rangle\langle jkj'k'|JK\rangle, \tag{2.49c}$$

and the functional form of the matrix elements can be found in several textbooks. The $\langle jmj'm'|JM\rangle$ appearing in Eq. 2.49 are Clebsh-Gordon coefficients which are also commonly tabulated (in the Appendix of Ref. [71], for example). These orthogonality conditions make it possible to calculate the orientational tensor without explicitly carrying out the integral of Eq. 2.45. To that end, we rewrite the elements of the Euler transformation as elements of the Wigner rotation matricies (e.g. $T_{Z3}(\Omega) = \cos\beta = D^{1}_{00}(\Omega)$). Once this is done, it is straightforward albeit incredibly tedious to evaluate the various orientational tensors. Two particularly useful relations for doing this are

$$\int \mathrm{d}\Omega_0 G(\Omega_1, \tau_1|\Omega_0) D^{j}_{mk}(\Omega_0) = c_j(\tau_1) D^{j*}_{mk}(\Omega_1) \tag{2.50a}$$

$$\int \mathrm{d}\Omega_0 G(\Omega_1, \tau_1|\Omega_0) D^{j}_{km}(\Omega_0) D^{j'}_{m'k'}(\Omega_0) = \sum_{JMK} c_J(\tau_1) D^{J*}_{MK}(\Omega_1)\langle jmj'm'|JM\rangle\langle jkj'k'|JK\rangle, \tag{2.50b}$$

which follow from Eqs. 2.49.

Finally, we can calculate the orientational tensors including molecular diffusion. The results are given in Table 2.3 [72]. In the limit that $\tau_1 = \tau_2 = \tau_3 = 0$, the values of the orientational tensors reduce to their static ones given in Table 2.2. In many cases, molecular diffusion is slow enough (that is, slow compared to the lifetime) that it can be neglected entirely. However, for smaller molecules orientational diffusion can contribute significantly to the decay of the measured signal.

We conclude by noting that "orientational diffusion" can occur without reorientation

Table 2.3: Value of non-zero orientational tensors including diffusion of a spherical rotor.

Orientational Tensor	Value
Y^{3333}_{ZZZZ}	$\frac{1}{9}c_1(\tau_1)\left[1+\frac{4}{5}c_2(\tau_2)\right]c_1(\tau_3)$
$Y^{3333}_{\mathrm{ZZYY}} = Y^{3311}_{\mathrm{ZZZZ}}$	$\frac{1}{9}c_1(\tau_1)\left[1-\frac{2}{5}c_2(\tau_2)\right]c_1(\tau_3)$
$Y^{3333}_{\mathrm{ZYYZ}} = Y^{3333}_{\mathrm{ZYZY}} = Y^{3131}_{\mathrm{ZZZZ}} = Y^{3113}_{\mathrm{ZZZZ}}$	$\frac{1}{15}c_1(\tau_1)c_2(\tau_2)c_1(\tau_3)$
Y^{3311}_{ZZYY}	$\frac{1}{9}c_1(\tau_1)\left[1+\frac{1}{5}c_2(\tau_2)\right]c_1(\tau_3)$
$Y^{3311}_{\mathrm{ZYZY}} = Y^{3311}_{\mathrm{ZYYZ}} = Y^{3131}_{\mathrm{ZZYY}} = Y^{3113}_{\mathrm{ZZYY}}$	$-\frac{1}{30}c_1(\tau_1)c_2(\tau_2)c_1(\tau_3)$
$Y^{3131}_{\mathrm{ZYZY}} = Y^{3113}_{\mathrm{ZYYZ}}$	$\frac{1}{4}c_1(\tau_1)\left[\frac{1}{5}c_2(\tau_2)+\frac{1}{3}c_1(\tau_2)\right]c_1(\tau_3)$
$Y^{3131}_{\mathrm{ZYYZ}} = Y^{3113}_{\mathrm{ZYZY}}$	$\frac{1}{4}c_1(\tau_1)\left[\frac{1}{5}c_2(\tau_2)-\frac{1}{3}c_1(\tau_2)\right]c_1(\tau_3)$

of the molecules. Rather, the measurement is sensitive to the orientation of the excited transition dipoles. Excitation may transfer to modes oriented along different directions, resulting in a loss of orientational correlations without a reorientation of a molecule. In this case, the exact rate at which orientational correlations are lost depends intimately on the details of the transfer. While this type of diffusion is far more difficult to model than a spherical rotor, the formalism developed here is, in principle, still applicable, though the experiments must be interpreted differently.

2.5 Third-Order IR Spectroscopy

We are finally in a position to put the concepts of the preceding sections together and calculate the results of an experiment. In this section we describe two experiments and how they can be used to extract molecular information from a system of interest. The first, two-dimensional infrared spectroscopy (2D IR) [77–79], is the most general third-order IR spectroscopy in that it in principle measures the full response function. The second experiment, transient absorption (TA), is a special case of a 2D IR experiment, and it provides less information. However, oftentimes this is sufficient especially considering how much easier the TA experiment is in practice.

2.5.1 Detection of Signal

Before describing the experiments, we consider the method of detection. As described in §2.1.3, the generated electric polarization density radiates a signal field, $\boldsymbol{E}_{\mathrm{s}}(\boldsymbol{x},t)$, in a phase-matched direction according to Eq. 2.10. Depending on the method of detection, the way in which data is processed and interpreted can change fairly dramatically. In a typical 2D IR experiment, the optical density of the sample is kept low enough that pump depletion is insignificant, and Eq. 2.11 is a good approximation for the radiated field (or Eq. 2.12 in the case of perfect phase matching).

In experiments, the signal field is heterodyned with a local oscillator, which is simply a pulse of known amplitude and phase. Therefore, the field measured at the detector is

$$\boldsymbol{E}(\boldsymbol{x},t) = \boldsymbol{E}_{\mathrm{LO}} + \boldsymbol{E}_{\mathrm{s}}. \tag{2.51}$$

Before measurement, the field is frequency dispersed by a diffraction grating, and imaged by an array of detector elements. Each element can be thought of as measuring a small range in the frequency domain. This can be obtained by applying a box filter in the frequency domain. If a particular detector element has a center frequency ω_n and accepts a bandwidth of 2δ, the field falling on any one detector element is

$$\boldsymbol{E}_{\omega_n}(t) = \frac{1}{\pi}\int_{-\infty}^{\infty} \mathrm{d}s\boldsymbol{E}(s)\cos(\omega_n(s-t))\frac{\sin(\delta(s-t))}{(s-t)}, \tag{2.52}$$

where the real part has been taken to ensure that the field is not complex (an artifact of applying an asymmetric window in the frequency domain). Furthermore, the $\boldsymbol{x}$ dependence has been dropped since the detector is fixed in space and integrates the field over the entire element. Equation 2.52 is simplified considerably in the limit of good resolution. That is, if δ is small so that the detector elements do not accept too much bandwidth, the sin function can be approximated as its argument. Writing the field under the integral as its Fourier transform shows that the field incident on any detector element is

$$\boldsymbol{E}_{\omega_n}(t) \approx \frac{\delta}{\pi} A(\omega_n) \cos(\omega_n t - \phi(\omega_n)), \tag{2.53}$$

where $A(\omega)$ and $\phi(\omega)$ are the amplitude and phase of the input field respectively. Therefore, the detected field can be approximated as being a cosine at the frequency of the detector element, with an amplitude and phase dictated by the input pulse. For the heterodyned signal in Eq. 2.51, the total field at each detector element is given by the form of Eq. 2.53 except as the sum of the signal and local oscillator fields. Using the trigonometric identities for the sum of two cosines, the total signal is given by $A\cos(\omega t - \phi)$, with the amplitude and phase at a particular detector element being given by

$$A^2(\omega_n) = A_{\mathrm{LO}}^2(\omega_n) + A_{\mathrm{s}}^2(\omega_n) + 2A_{\mathrm{s}}(\omega_n)A_{\mathrm{LO}}(\omega_n)\cos(\phi_{\mathrm{s}}(\omega_n) - \phi_{\mathrm{LO}}(\omega_n)) \tag{2.54a}$$

$$\tan\phi = \frac{A_{\mathrm{s}}(\omega_n)\sin(\phi_{\mathrm{s}}(\omega_n)) + A_{\mathrm{LO}}(\omega_n)\sin(\phi_{\mathrm{LO}}(\omega_n))}{A_{\mathrm{s}}(\omega_n)\cos(\phi_{\mathrm{s}}(\omega_n)) + A_{\mathrm{LO}}(\omega_n)\cos(\phi_{\mathrm{LO}}(\omega_n))}. \tag{2.54b}$$

The importance of heterodyne detection is thus made clear in Eq. 2.54a. The squared amplitude of the measured field depends linearly on the amplitude of the signal and on the phase difference between the signal and the local oscillator; as such, the heterodyne measurement gives a full characterization of the signal field if the local oscillator field is known. The detector elements give rise to a voltage proportional to the time-averaged intensity of the field. That is, it measures

$$I_{\mathrm{det}} = \lim_{T\to\infty} \frac{1}{2T} \int_{-T}^{T} \mathrm{d}t E^2(t). \tag{2.55}$$

Here, $2T$ is the integration time of the detector, though for short pulses this window can be taken to infinity as is done in the above equation. The $\cos^2(\omega t - \phi)$ part of the measured signal averages to 1/2, and so the quantity detected in the experiment is $A^2(\omega_n)/2$.

Typically, $A_{\mathrm{s}}(\omega_n) \ll A_{\mathrm{LO}}(\omega_n)$, and so the homodyne term in Eq. 2.54a, $A_{\mathrm{s}}^2(\omega_n)$, can be neglected. Furthermore, an independent measurement of $A_{\mathrm{LO}}^2(\omega_n)$ can always be made by removing the fields that generate the third-order signal. If care is taken to ensure that $\phi_{\mathrm{LO}}(\omega_n) = 0$ (by adjusting the timing between the local oscillator and signal field, for example) and dividing through by $A_{\mathrm{LO}}(\omega_n)$, it is possible to measure the full signal field as $A_{\mathrm{s}}(\omega_n)\cos\phi_{\mathrm{s}}(\omega_n)$. The take home message then, is that the heterodyne measurement allows us to essentially measure a signal $S(\omega)$ given by

$$S(\omega) = \Re E(\boldsymbol{x}, \omega) = A(\omega)\cos\phi(\omega). \tag{2.56}$$

2.5.2 Rephasing and Non-Rephasing

Two-dimensional IR spectroscopy and TA spectroscopy are heterodyned third-order spectroscopies that measure the rephasing and non-rephasing pathways as a function of the time delay between three or two different pulses. To that end, the nonlinear polarization generated in a 2D IR experiment is (Eq. 2.32)

$$\begin{aligned} P_{\alpha}^{(\mathrm{2DIR})}(\boldsymbol{x}, t) = -\frac{2}{\hbar^3} n_0 \sum_{n=0}^{3} \iiint \mathrm{d}\tau_3 \mathrm{d}\tau_2 \mathrm{d}\tau_1 \\ \Im\left[\left(\mathcal{E}_{ijk,1}^{\alpha_1,\alpha_2,\alpha_3} + \mathcal{E}_{ijk,2}^{\alpha_1,\alpha_2,\alpha_3}\right)\left(\overline{\mathcal{R}_{\alpha_1,\alpha_2,\alpha_3,\alpha}^{(3,n)}} - \overline{\mathcal{R}_{\alpha_1,\alpha_2,\alpha_3,\alpha}^{(3,n)*}}\right)\right]. \end{aligned} \tag{2.57}$$

Unfortunately, it is now necessary to fully expand the electric polarization density in order to understand the 2D IR signal. To simplify matters somewhat, we consider the rephasing pathway explicitly and simply state the result for the non-rephasing pathway. We consider only the Liouville paths consistent with the low-temperature approximation (that is, the diagrams not in maroon in Fig. 2.2). With this, the rephasing part of the polarization is given by

$$\begin{aligned} P_{\alpha}^{(\mathrm{R})}(\boldsymbol{x}, t) = -\frac{2}{\hbar^3} n_0 \iiint \mathrm{d}\tau_3 \mathrm{d}\tau_2 \mathrm{d}\tau_1 \\ \Im\left[\mathcal{E}_{ijk,1}^{\alpha_1,\alpha_2,\alpha_3}\left(\overline{\mathcal{R}_{\alpha_1,\alpha_2,\alpha_3,\alpha}^{(3,0)}} - \overline{\mathcal{R}_{\alpha_1,\alpha_2,\alpha_3,\alpha}^{(3,1)*}} - \overline{\mathcal{R}_{\alpha_1,\alpha_2,\alpha_3,\alpha}^{(3,2)*}}\right)\right]. \end{aligned} \tag{2.58}$$

Using the definition for the field tensor (Eq. 2.30) as well as the response function (Eq. 2.27), the electric polarization density for the rephasing pathway is given explicitly given by

$$
\begin{aligned}
P_{\alpha}^{(\mathrm{R})}(\boldsymbol{x},t) = -\frac{2}{\hbar^3}n_0 \iiint \mathrm{d}\tau_3\mathrm{d}\tau_2\mathrm{d}\tau_1 \Im \sum_{a,b,c,d} e_i^{\alpha_1} e_j^{\alpha_2} e_k^{\alpha_3} \\
&\times E_i(\boldsymbol{x}, t-\tau_3-\tau_2-\tau_1) E_j(\boldsymbol{x}, t-\tau_3-\tau_2) E_k(\boldsymbol{x}, t-\tau_3) \\
&\times \mathrm{e}^{\mathrm{i}(\boldsymbol{k}_i-\boldsymbol{k}_j-\boldsymbol{k}_k)\cdot\boldsymbol{x}} \mathrm{e}^{-\mathrm{i}(\phi_i-\phi_j-\phi_k)} \mathrm{e}^{-\mathrm{i}(\omega_i-\omega_j-\omega_k)t} \rho_0^{aa} \\
&\times \Big(\overline{\mu_{\alpha}^{cb} \mu_{\alpha_3}^{cd*} \mu_{\alpha_2}^{da*} \mu_{\alpha_1}^{ba}} \mathrm{e}^{-\mathrm{i}(\omega_{ba}-\omega_i)\tau_1 - \mathrm{i}(\omega_{bd}-\omega_i+\omega_j)\tau_2 - \mathrm{i}(\omega_{bc}-\omega_i+\omega_j+\omega_k)\tau_3} \mathcal{F}_{da,cd,bc}(\tau_1,\tau_2,\tau_3) \\
&- \overline{\mu_{\alpha}^{cb*} \mu_{\alpha_3}^{cd} \mu_{\alpha_2}^{ba*} \mu_{\alpha_1}^{da}} \mathrm{e}^{\mathrm{i}(\omega_{ad}+\omega_i)\tau_1 + \mathrm{i}(\omega_{bd}+\omega_i-\omega_j)\tau_2 + \mathrm{i}(\omega_{bc}+\omega_i-\omega_j-\omega_k)\tau_3)} \mathcal{F}^{*}_{ab,cd,bc}(\tau_1,\tau_2,\tau_3) \\
&- \overline{\mu_{\alpha}^{cb*} \mu_{\alpha_3}^{ba*} \mu_{\alpha_2}^{cd} \mu_{\alpha_1}^{da}} \mathrm{e}^{\mathrm{i}(\omega_{ad}+\omega_i)\tau_1 + \mathrm{i}(\omega_{ac}+\omega_i-\omega_j)\tau_2 + \mathrm{i}(\omega_{bc}+\omega_i-\omega_j-\omega_k)\tau_3} \mathcal{F}^{*}_{cd,ab,bc}(\tau_1,\tau_2,\tau_3) \Big) .
\end{aligned}
\tag{2.59}
$$

The goal is to understand how this expression behaves as a function of the time delay between the three pulses. For general pulse envelopes, the integrals are not possible to evaluate analytically; however, we may invoke the notion that the pulses are sharply peaked at some particular time to do so. The exponentials in the integrand oscillate at a frequency that is determined by the detuning between the system frequency and the driving field. In typical experiments, it is the case that the detuning is kept small. Therefore, pulses that are much shorter in time than the inverse of the detuning (which are readily generated in the lab) will effectively behave as a delta function under the integral.

To that end, we make the short-pulse approximation, and we set $E_i(\boldsymbol{x},t) \propto \delta(t-s_i)$. In the lab, however, pulses peaked at a particular time are commonly generated by introducing a delay in the optical pathlength; as such, the pulses accrue an additional phase proportional to the time delay s [80]. The fields envelopes are therefore given by $E_i(\boldsymbol{x},t) = E_i(\boldsymbol{x})\delta(t - s_i)\mathrm{e}^{-\mathrm{i}z_i\omega_i s_i}$. With this approximation, $\tau_1 \to s_j - s_i$, $\tau_2 \to s_k - s_j$, and $\tau_3 \to t - s_k$.

Since the zero of time is arbitrary, we can, without loss of generality, set it to be at the final interaction point. This fixes $s_k = 0$. Furthermore, we want to continue working with the interval between pulses. Unfortunately, the interval between pulses is typically denoted by τ as well as the integration variable. Keeping in mind that we are no longer integrating over τ variables (since theses are now the experimentally fixed intervals between pulses), we can set $s_i = -\tau_1 - \tau_2$, $s_j = -\tau_2$, and $s_k = 0$.

The rephasing electric polarization density then becomes

$$\begin{aligned} P^{(\mathrm{R})}_{\alpha}(\boldsymbol{x},t) \approx -\frac{2}{\hbar^3} n_0 \Im \sum_{a,b,c,d} & e^{\alpha_1}_i e^{\alpha_2}_j e^{\alpha_3}_k E_i(\boldsymbol{x}) E_j(\boldsymbol{x}) E_k(\boldsymbol{x}) \mathrm{e}^{\mathrm{i}(\boldsymbol{k}_i - \boldsymbol{k}_j - \boldsymbol{k}_k)\cdot \boldsymbol{x}} \mathrm{e}^{-\mathrm{i}(\phi_i - \phi_j - \phi_k)} \rho^{aa}_0 \\ & \times \Big(\overline{\mu^{cb}_{\alpha} \mu^{cd*}_{\alpha_3} \mu^{da*}_{\alpha_2} \mu^{ba}_{\alpha_1}} \mathrm{e}^{-\mathrm{i}\omega_{ba}\tau_1 - \mathrm{i}\omega_{bd}\tau_2 - \mathrm{i}\omega_{bc} t} \mathcal{F}_{da,cd,bc}(\tau_1, \tau_2, t) \\ & - \overline{\mu^{cb*}_{\alpha} \mu^{cd}_{\alpha_3} \mu^{ba*}_{\alpha_2} \mu^{da}_{\alpha_1}} \mathrm{e}^{\mathrm{i}\omega_{ad}\tau_1 + \mathrm{i}\omega_{bd}\tau_2 + \mathrm{i}\omega_{bc} t} \mathcal{F}^{*}_{ab,cd,bc}(\tau_1, \tau_2, t) \\ & - \overline{\mu^{cb*}_{\alpha} \mu^{ba*}_{\alpha_3} \mu^{cd}_{\alpha_2} \mu^{da}_{\alpha_1}} \mathrm{e}^{\mathrm{i}\omega_{ad}\tau_1 + \mathrm{i}\omega_{ac}\tau_2 + \mathrm{i}\omega_{bc} t} \mathcal{F}^{*}_{cd,ab,bc}(\tau_1, \tau_2, t) \Big) . \end{aligned} \tag{2.60}$$

In this expression, the laser frequencies have dropped out entirely because we have assumed that the pulse is short relative to the timescale set by the detuning. In other words, the spectrum of the laser fields was approximated as being broad relative to the linewidth of the transition.

If this condition is not met and there are non-resonant terms, they must be treat with the full Eq. 2.59. Such non-resonant terms will usually be small, but can be significant if there are many of them. Equation 2.60 is the simplest form that the rephasing electric polarization density can be reduced to without making assumptions about the lineshape. We remind ourselves that the lineshape function is proportional to $\theta(\tau_1)\theta(\tau_2)\theta(t)$ so that the electric polarization density is non-zero only for $t > 0$.

As a function of the two time delays, or as a function of time the electric polarization density oscillates at the transition frequencies of the system. The lineshape function modifies these frequencies somewhat via its imaginary part and causes the electric polarization density to decay via its real part. The time-dependence of the electric polarization density is further modified via the rotational average over the dipole orientations with the expressions given in Table 2.3. To proceed with this expression, it is necessary to assume a lineshape function, which we consider shortly.

The non-rephasing electric polarization density is given by

$$\begin{aligned} P_{\alpha}^{(\mathrm{NR})}(\boldsymbol{x},t) = -\frac{2}{\hbar^3}n_0 \iiint \mathrm{d}\tau_3\mathrm{d}\tau_2\mathrm{d}\tau_1 \\ \Im\left[\mathcal{E}_{ijk,2}^{\alpha_1,\alpha_2,\alpha_3}\left(\overline{\mathcal{R}_{\alpha_1,\alpha_2,\alpha_3,\alpha}^{(3,1)}} - \overline{\mathcal{R}_{\alpha_1,\alpha_2,\alpha_3,\alpha}^{(3,0)*}} - \overline{\mathcal{R}_{\alpha_1,\alpha_2,\alpha_3,\alpha}^{(3,3)*}}\right)\right], \end{aligned} \tag{2.61}$$

which, within the short-pulse approximation, becomes

$$\begin{aligned} P_{\alpha}^{(\mathrm{NR})}(\boldsymbol{x},t) \approx -\frac{2}{\hbar^3}n_0\Im\sum_{a,b,c,d} e_i^{\alpha_1}e_j^{\alpha_2}e_k^{\alpha_3}E_i(\boldsymbol{x})E_j(\boldsymbol{x})E_k(\boldsymbol{x})\mathrm{e}^{-\mathrm{i}(\boldsymbol{k}_i-\boldsymbol{k}_j+\boldsymbol{k}_k)\cdot\boldsymbol{x}}\mathrm{e}^{\mathrm{i}(\phi_i-\phi_j+\phi_k)}\rho_0^{aa} \\ \times\left(\overline{\mu_{\alpha}^{cb}\mu_{\alpha_3}^{cd*}\mu_{\alpha_2}^{ba}\mu_{\alpha_1}^{da*}}\mathrm{e}^{-\mathrm{i}\omega_{ad}\tau_1-\mathrm{i}\omega_{bd}\tau_2-\mathrm{i}\omega_{bc}t}\mathcal{F}_{ab,cd,bc}(\tau_1,\tau_2,t)\right. \\ -\overline{\mu_{\alpha}^{cb*}\mu_{\alpha_3}^{cd}\mu_{\alpha_2}^{da}\mu_{\alpha_1}^{ba*}}\mathrm{e}^{\mathrm{i}\omega_{ba}\tau_1+\mathrm{i}\omega_{bd}\tau_2+\mathrm{i}\omega_{bc}t}\mathcal{F}_{da,dc,bc}^{*}(\tau_1,\tau_2,t) \\ \left.-\overline{\mu_{\alpha}^{ad*}\mu_{\alpha_3}^{dc*}\mu_{\alpha_2}^{cb*}\mu_{\alpha_1}^{ba*}}\mathrm{e}^{\mathrm{i}\omega_{ba}\tau_1+\mathrm{i}\omega_{ca}\tau_2+\mathrm{i}\omega_{da}t}\mathcal{F}_{bc,cd,da}^{*}(\tau_1,\tau_2,t)\right). \end{aligned} \tag{2.62}$$

The non-rephasing electric polarization density shows qualitatively similar behavior.

We now calculate the detected field using Eq. 2.11. Since the frequency-domain field is what is detected (§2.5.1), we must calculate the frequency-domain electric polarization density. As per the discussion of §2.3.3, we can assume that the phase matching is perfect ($\Delta k = 0$) for rephasing and non-rephasing pathways since the resultant frequency is approximately the same as the input frequency. As such, Eq. 2.12 describes the radiated field for a sample of pathlength ℓ. Calling the Fourier transform frequency variable of t ω_3, the frequency domain fields as measured on the detector are

$$\begin{aligned} E_{\alpha}^{(\mathrm{R})}(\omega_3) = -\Re\mathrm{i}\frac{4\pi\omega_3\ell n_0}{c\hbar^3\hat{n}(\omega_3)}\int \mathrm{d}t\mathrm{e}^{\mathrm{i}\omega_3 t} \\ \Im\sum_{a,b,c,d} e_i^{\alpha_1}e_j^{\alpha_2}e_k^{\alpha_3}E_iE_jE_k\mathrm{e}^{-\mathrm{i}(\phi_i-\phi_j-\phi_k)}\rho_0^{aa} \\ \times\left(\overline{\mu_{\alpha}^{cb}\mu_{\alpha_3}^{cd*}\mu_{\alpha_2}^{da*}\mu_{\alpha_1}^{ba}}\mathrm{e}^{-\mathrm{i}\omega_{ba}\tau_1-\mathrm{i}\omega_{bd}\tau_2-\mathrm{i}\omega_{bc}t}\mathcal{F}_{da,cd,bc}(\tau_1,\tau_2,t)\right. \\ -\overline{\mu_{\alpha}^{cb*}\mu_{\alpha_3}^{cd}\mu_{\alpha_2}^{ba*}\mu_{\alpha_1}^{da}}\mathrm{e}^{\mathrm{i}\omega_{ad}\tau_1+\mathrm{i}\omega_{bd}\tau_2+\mathrm{i}\omega_{bc}t}\mathcal{F}_{ab,cd,bc}^{*}(\tau_1,\tau_2,t) \\ \left.-\overline{\mu_{\alpha}^{cb*}\mu_{\alpha_3}^{ba*}\mu_{\alpha_2}^{cd}\mu_{\alpha_1}^{da}}\mathrm{e}^{\mathrm{i}\omega_{ad}\tau_1+\mathrm{i}\omega_{ac}\tau_2+\mathrm{i}\omega_{bc}t}\mathcal{F}_{cd,ab,bc}^{*}(\tau_1,\tau_2,t)\right). \end{aligned} \tag{2.63}$$

and

$$
\begin{aligned}
E_\alpha^{(\mathrm{NR})}(\omega_3) = -\Re \mathrm{i} \frac{4\pi\omega_3 \ell n_0}{c\hbar^3 \hat{n}(\omega_3)} \int \mathrm{d}t \mathrm{e}^{\mathrm{i}\omega_3 t} \\
\Im \sum_{a,b,c,d} e_i^{\alpha_1} e_j^{\alpha_2} e_k^{\alpha_3} E_i E_j E_k \mathrm{e}^{\mathrm{i}(\phi_i - \phi_j + \phi_k)} \rho_0^{aa} \\
\times \Big(\overline{\mu_\alpha^{cb} \mu_{\alpha_3}^{cd*} \mu_{\alpha_2}^{ba} \mu_{\alpha_1}^{da*}} \mathrm{e}^{-\mathrm{i}\omega_{ad}\tau_1 - \mathrm{i}\omega_{bd}\tau_2 - \mathrm{i}\omega_{bc} t} \mathcal{F}_{ab,cd,bc}(\tau_1, \tau_2, t) \\
- \overline{\mu_\alpha^{cb*} \mu_{\alpha_3}^{cd} \mu_{\alpha_2}^{da} \mu_{\alpha_1}^{ba*}} \mathrm{e}^{\mathrm{i}\omega_{ba}\tau_1 + \mathrm{i}\omega_{bd}\tau_2 + \mathrm{i}\omega_{bc} t} \mathcal{F}^*_{da,dc,bc}(\tau_1, \tau_2, t) \\
- \overline{\mu_\alpha^{ad*} \mu_{\alpha_3}^{dc*} \mu_{\alpha_2}^{cb*} \mu_{\alpha_1}^{ba*}} \mathrm{e}^{\mathrm{i}\omega_{ba}\tau_1 + \mathrm{i}\omega_{ca}\tau_2 + \mathrm{i}\omega_{da} t} \mathcal{F}^*_{bc,cd,da}(\tau_1, \tau_2, t) \Big) .
\end{aligned}
\tag{2.64}
$$

Where the spatial dependence of the fields is understood to have been integrated out by the detector elements. Equations 2.63 and 2.64 contain everything one needs for third-order spectroscopies involving only the rephasing and non-rephasing pathways. The expressions are not particularly aesthetically pleasing, but they are an accurate representation of what is actually measured within the approximations we have made. In the sections that follow, we discuss these expressions in a simplified way in the context of particular experiments.

2.5.3 Two-Dimensional Infrared Spectroscopy

We begin by considering a 2D IR experiment. The experiments in this thesis are performed in the pump–probe geometry (§2.3.3) and as such, we limit the discussion to this geometry. We set $(i, j, k) = (1, 2, 3)$, $\boldsymbol{k}_1 = \boldsymbol{k}_2$, and $\phi_1 = \phi_2 = \phi_3 = 0$. The time dependence in the integrands of Eqs. 2.63 and 2.64 comes from both the lineshape function and the decay of rotational correlations associated with the rotational diffusion. The dependence of rotational correlations on τ_1 and t is simply multiplicative, and as such we lump it in with the lineshape function. For illustrative purposes, we assume a simplified lineshape function given by

$$
\mathcal{F}_{ab,cd,ef}(\tau_1, \tau_2, t) = \theta(\tau_1)\theta(\tau_2)\theta(t) e^{-\gamma_{ab}\tau_1 - k_{cd}\tau_2 - \gamma_{ef} t}. \tag{2.65}
$$

The γ's contain the decay due to rotational diffusion, while k_{ab} is decay rate for the ab coherence and k_{aa} is the population relaxation rate for the a state.

At this point, it is not instructive to retain the entire term since its evaluation quickly becomes opaque due to the plethora of terms. Furthermore, a 2D IR spectrum is typically interpreted on a feature-by-feature basis, and so isolating the terms is, in some sense, a natural way to proceed. To that end, we focus on a single term. Consider the Liouville pathway, $\mathcal{R}^{(3,1)*}_{\alpha_1,\alpha_2,\alpha_3,\alpha}$ shown in the upper part of Fig. 2.5 for a two-level system, with a ground state denoted by 0 and an excited state denoted by 1. This corresponds to the second term in Eq. 2.63. In the case that, $a = 0, b = 1, c = 0, d = 1$ and we can easily carry out the integrals in Eq. 2.63. Under the conditions for the pump–probe geometry discussed above, this signal term becomes

$$\begin{aligned} S^{(\mathrm{R})}(\tau_1, \tau_2, \omega_3) = -&\frac{2\pi\omega_3 \ell n_0}{c\hbar^3 \hat{n}(\omega_3)} e_1^{\alpha_1} e_2^{\alpha_2} e_3^{\alpha_3} E_1 E_2 E_3 \overline{\mu_{\alpha}^{01*} \mu_{\alpha_3}^{01} \mu_{\alpha_2}^{10} \mu_{\alpha_1}^{10*}} \rho_0^{00} \mathrm{e}^{-\gamma_{01}\tau_1 - k_{11}\tau_2} \\ &\left[\frac{\gamma_{01} \cos\omega_{10}\tau_1 + \Omega_{01} \sin\omega_{10}\tau_1}{\Omega_{01}^2 + \gamma_{01}^2} - \frac{\gamma_{01} \cos\omega_{10}\tau_1 - \Omega_{10} \sin\omega_{10}\tau_1}{\Omega_{10}^2 + \gamma_{01}^2} \right], \end{aligned} \tag{2.66}$$

where we have defined $\Omega_{ab} = \omega_3 - \omega_{ab}$. The first term is peaked strongly at negative frequencies ($\omega_3 \approx \omega_{01}$), while the second is peak at positive frequencies ($\omega_3 \approx \omega_{10}$). To that end, we may discard the first term since the detector only measures positive frequencies. The signal for this particular pathway then oscillates at the initial interaction frequency and decays away as a function of τ_1. It is sharply peaked at the final frequency in ω_3, with its width being determined by the decay of the lineshape function. As a function of τ_2, this feature decays away with the population lifetime of the 1 state.

Normally 2D IR spectra are represented in the freqeuncy domain for τ_1 as well, and by definition we take the real part of this Fourier transformed spectrum. To that end, neglecting the features peaked at negative frequencies, we Fourier transform the expression in τ_1 to give

$$\begin{aligned} S^{(\mathrm{R})}(\omega_1, \tau_2, \omega_3) = &\frac{2\pi\omega_3 \ell n_0}{c\hbar^3 \hat{n}(\omega_3)} e_1^{\alpha_1} e_2^{\alpha_2} e_3^{\alpha_3} E_1 E_2 E_3 \overline{\mu_{\alpha}^{01*} \mu_{\alpha_3}^{01} \mu_{\alpha_2}^{10} \mu_{\alpha_1}^{10*}} \rho_0^{00} \\ \times &\frac{\gamma_{01}^2 + \Omega_{10}\Delta_{10}}{(\Delta_{10}^2 + \gamma_{01}^2)(\Omega_{10}^2 + \gamma_{01}^2)} \mathrm{e}^{-k_{11}\tau_2}, \end{aligned} \tag{2.67}$$

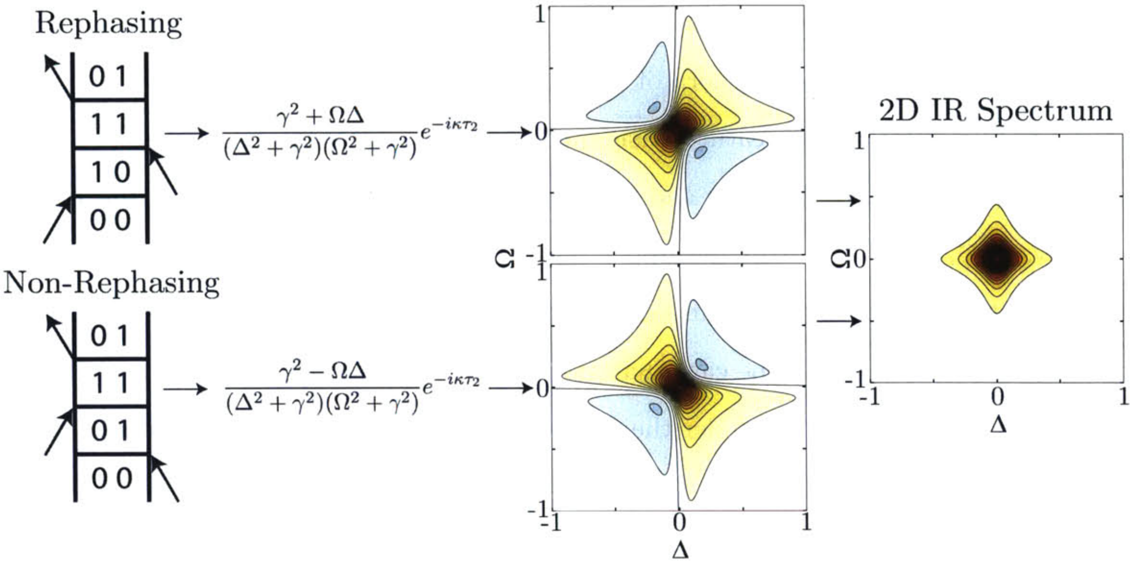

Figure 2.5: Example rephasing, non-rephasing, and 2D IR spectra for a two-level system. In a multi-level system, each Liouville pathway is associated with a twisted Lorentzian in the spectrum.

where $\Delta_{ab} = \omega_1 - \omega_{ab}$. We therefore see that the 2D IR spectrum has a peak in the spectrum at the intial interaction frequency in ω_1 and the final frequency in ω_3. In addition, the spectrum is not a perfect two-dimensional Lorentzian; rather, the spectrum has a twisted component, with the twist being given by $\Omega_{10}\Delta_{10}$. An example of the rephasing spectrum is shown in Fig. 2.5.

In addition to this term, there is a *corresponding* non-rephasing term which has interactions at the same freqeuncies. In a similar way, it is straightforward to show that the signal derived from the non-rephasing pathway is given by

$$\begin{aligned} S^{(\mathrm{NR})}(\omega_1,\tau_2,\omega_3) = {} & \frac{2\pi\omega_3\ell n_0}{c\hbar^3\hat{n}(\omega_3)} e_1^{\alpha_1} e_2^{\alpha_2} e_3^{\alpha_3} E_1 E_2 E_3 \overline{\mu_{\alpha}^{01*}\mu_{\alpha_3}^{01}\mu_{\alpha_2}^{10}\mu_{\alpha_1}^{10*}}\rho_0^{00} \\ & \times \frac{\gamma_{01}^2 - \Omega_{10}\Delta_{10}}{(\Delta_{10}^2+\gamma_{01}^2)(\Omega_{10}^2+\gamma_{01}^2)} \mathrm{e}^{-k_{11}\tau_2}, \end{aligned} \tag{2.68}$$

This signal is almost identical to the rephasing pathway except that the twist, $-\Omega_{10}\Delta_{10}$ is in the opposite sense, as seen in Fig. 2.5. Therefore, by adding the rephasing and non-rephasing pathways, this phase twist can be eliminated entirely resulting in a Lorentzian peak. This results in a 2D IR spectrum that is sharply peaking at the initial excitation frequency in ω_1 and at the final frequency in ω_3, whose magnitude is dependent on the value of $e^{-k_{11}\tau_2}$. The result of adding a rephasing and non-rephasing spectrum for a two-level system is shown in Fig. 2.5.

In the pump–probe geometry, repahsing and non-rephasing signals are emitted in the same direction as the third pulse, which serves as the local oscillator. As such, it is not possible to measure the rephasing or non-rephasing separately (unless a phase cycling scheme is employed [81, 82]). However, this comes with the advantage that a full 2D IR spectrum is measured without having to measure the two wavevector-matching conditions separately.

Real vibrations are not two-level systems, and as such it is necessary to include other states. For a single oscillator, the minimum number of states that will contribute to the signal is three: the ground state and first two excited states. With such a system, there are only three rephasing pathways and three non-rephasing pathways that will contribute; these are shown in the upper part of Fig. 2.6. We note that not all of the pathways have the same sign: the two which have the same initial and final frequency ω_{10} have a net positive sign while the pathway that has ω_{10} as its initial freqeuncy and ω_{21} as its final frequency has a net negative sign (as per Eqs. 2.63 and 2.64). This results in a 2D IR spectrum with both positive and negative features as shown in Fig. 2.6.

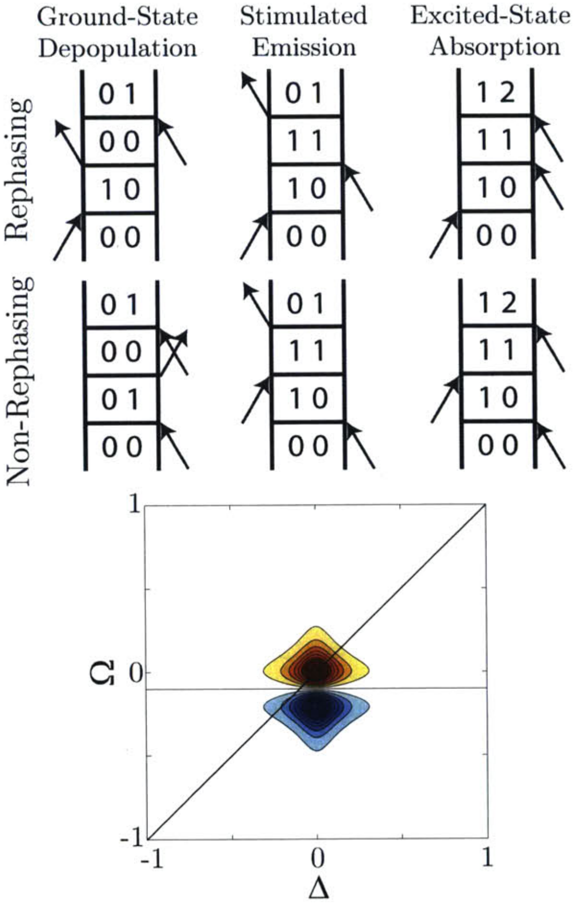

Figure 2.6: Pathways contributing the the 2D IR spectrum of a three-level system. Excited-state absorption pathways contribute a negative peak to the spectrum.

The Liouville paths for the three level system have simple interpretation. The first, shown in Fig. 2.6, corresponds to depletion of the ground state. The excitation field generates some population in the excited state and thus depletes the ground state. This results in less absorption of the third pulse which results in a larger field being transmitted (thus the net positive sign). The second pathway corresponds to stimulated emission from the first excited state, and as such also results in a larger field being transmitted through the sample. These two terms together are often called a "ground-state bleach" and are associated with less absorption of the sample at its fundamental frequency. The final path corresponds to an absorption from the first excited state to the second excited state. This results in less light being transmitted at the ω_{21} and as such appears negative in the spectrum due to the reduction in transmitted field. This term is called excited-state absorption.

For molecular vibrations, the nuclear potential is typically such that $\omega_{21} < \omega_{10}$ [83], and so the excited-state absorption pathway results in a negative peak below the diagonal, as shown in Fig. 2.6. If the system were harmonic, that is the transitions would be such that $\omega_{10} = \omega_{21}$ and $\mu^{21} = \sqrt{2}\mu^{10}$, the two features would overlap perfectly and the amplitude of the third term would be exactly the sum of the amplitudes of the first two terms. The three paths would therefore destructively interfere and no 2D IR signal would be observed. This is a general feature of nonlinear spectroscopy and signal is only observed for anharmonic systems.

Finally, we consider how the 2D IR spectrum changes with multiple oscillators. Each oscillator can be thought of as a three-level system since the first three levels are the only ones to contribute to the 2D IR spectrum. If the oscillators are independent (i.e. non-interacting) then the 2D IR spectrum is simply the sum of the individual oscillator spectra at their respective frequencies. However, if the oscillators are coupled (interacting) the situation is quite different. In this case, the excitation of one oscillator leads to a change in frequency (and possibly oscillator strength) of the others due to a shifting of the eigenstates. For example, in an uncoupled two-oscillator system, the $|00\rangle \rightarrow |01\rangle$ necessarily has the same frequency as the $|10\rangle \rightarrow |11\rangle$ since the second oscillator is independent of the first. This is

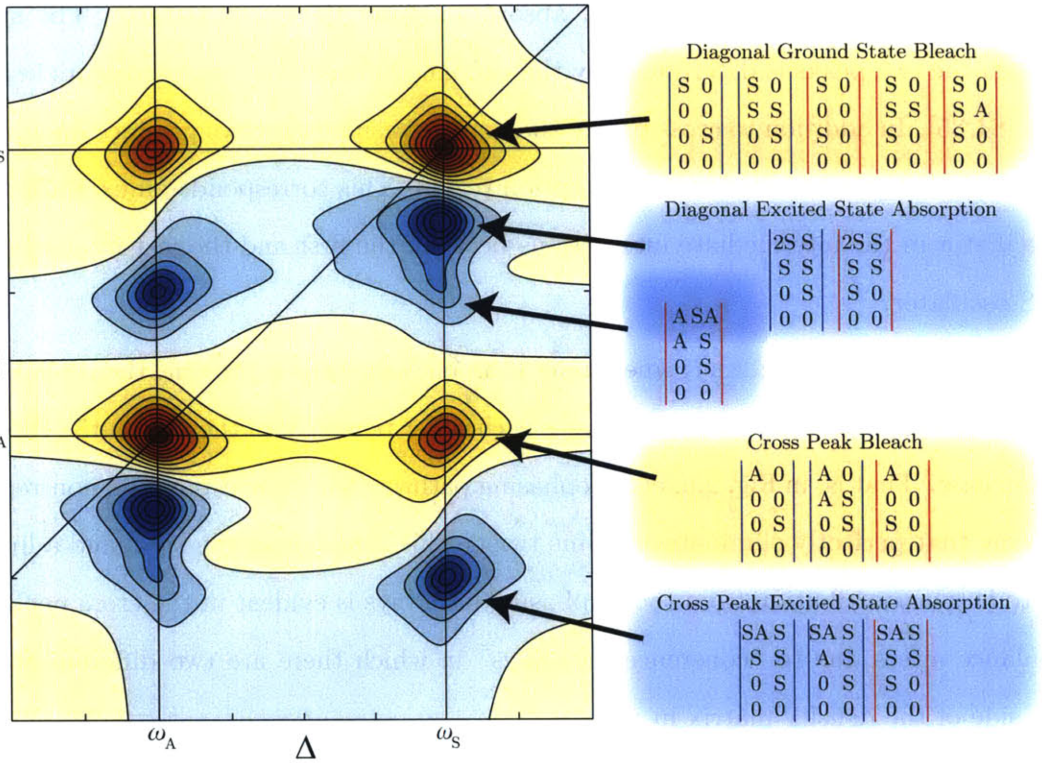

Figure 2.7: Schematic 2D IR spectrum of a two-oscillator (six-level) system with 14 of the 28 pathways shown. Rephasing pathways are shown with blue bars while non-rephasing pathways are shown with red bars.

not the case that if the oscillators are coupled. This implies that excitation at a particular ω_1 value can result in a response at the frequency of another oscillator. Such features appear off the diagonal and are aptly called cross-peaks.

To illustrate this concept more clearly, Fig. 2.7 shows the 2D IR spectrum for a coupled two-oscillator (six-level) system and 14 of the 28 associated rephasing and non-rephasing pathways [78]. The oscillator states are labeled S and A for the two oscillators, with second excited states being labeled 2S, 2A, and SA. As expected, the 2D IR spectrum shows two features on the diagonal corresponding to the ground-state bleach and excited-state absorption of the two individual oscillators. In addition, cross peaks between the two vibrations are evident corresponding to an initial interaction with one oscillator and a final interaction with the other. These two come in a doublet corresponding to the bleaching of the ground state and an absorption from the excited state. The splitting between the two peaks is determined by the coupling between the two oscillators in the site basis [84,85]. In addition to cross peaks, the non-rephasing pathways produce an additional peak in the diagonal excited-state absorption region. This corresponds an excitation of the A oscillator in the intermediate interactions between the first and the last interaction with the S oscillator.

It is interesting to note that when more than one oscillator is present, the rephasing and non-rephasing pathways no longer balance each other perfectly as they do in the three-level system case. That is, in Fig. 2.6, each rephasing pathway has a corresponding non-rephasing pathway that perfectly eliminates the line twist. This is no longer the case, and a line twist due to larger contribution from the resphasing pathways is evident in the cross peaks. This imbalance arises due to "coherence pathways" in which there are two different states on each side of the density matrix in τ_2.

In the experiments performed in this thesis, however, the first two pulses are narrow in spectrum while the third is broad. In this situation, cross peaks that are not in the bandwidth of the first pulse have fewer pathways. For example, if the narrowband pulse is resonant with the S mode, it is impossible to have an interaction with the A mode until the third pulse (within the rotating-wave approximation). As such, any pathway that has an "A" below the third rung of the ladder does not contribute. In this case, rephasing and non-rephasing once again compensate each other perfectly, and there is no line twist in the cross peaks. The total number of pathways for the excitation of a single oscillator in a two-oscillator system is reduced to 10 from 14 if coherence pathways are not measured.

Finally, we note that the results contained within this section are entirely contingent on the simple lineshape function that we assumed. If the lineshape function is different, the rephasing and non-rephasing spectra will have different functional forms, but the 2D IR spectrum is always the sum of the two. In fact, the lineshape that we have chosen is unrealistic for most systems since it does not include the possibility of spectral diffusion. A transition frequency of the system will evolve in time due to the evolution of the bath; as such, the lineshape function must be of a form that captures this behavior. For example, the Kubo lineshape function [86] captures the motional narrowing that occurs as a function of time, resulting in the evolution of the lineshape with τ_2. Accurate formalisms for a lineshape are difficult to develop due to the form of Eq. 2.28. However, much success has been had in using a cumulant expansion for the lineshape function since this reduces the three-point lineshape function to a sum of one-point lineshape functions [52].

Qualitatively, the lineshape in a 2D IR experiment can be thought of as reflecting frequency correlations as a function of τ_2. Initially, the lineshape is elongated along the diagonal. As time τ_2 is increased, frequency memory is lost and the lineshape becomes a symmetric function about its center. The rate at which the lineshape changes is related to the decay of the freqeuncy–frequency correlation function [87,88], and as such provides a straightforward method for extracting environmental fluctuations. While there are several metrics to characterize such frequency correlations [33, 89], the center-line slope (CLS) method is used most frequently in this thesis. In the CLS method, the first moment of the peak in ω_3 is found as a function of ω_1. This is usually approximately linear and has a slope whose magnitude reflects the degree of frequency correlation. This slope decays to zero as a function of τ_2 and the decay timescale can be associated with the decay of the frequency–frequency correlation function.

2.5.4 Transient Absorption

In the pump–probe geometry, a transient absorption (TA) experiment is identical to a 2D IR experiment except that τ_1 is fixed at zero. Experimentally, this is accomplished by using a single pulse instead of a pulse pair. The advantage of this experiment over 2D IR is purely experimental in that there is one fewer variable to change and so the experiment is significantly faster and less noisy to perform. This technique is particularly useful for measuring the relaxation rates of the population terms generated in τ_2.

Since $\tau_1 = 0$, the rephasing and non-rephasing pathways are identical. We can therefore use Eq. 2.66 as an example of a typical term measured in a TA. Setting $\tau_1 = 0$ in this equation gives

$$S^{(\mathrm{R})}(0,\tau_2,\omega_3) = \frac{2\pi\omega_3\ell n_0}{c\hbar^3\hat{n}(\omega_3)} e_1^{\alpha_1} e_2^{\alpha_2} e_3^{\alpha_3} E_1 E_2 E_3 \overline{\mu_{\alpha}^{01*}\mu_{\alpha_3}^{01}\mu_{\alpha_2}^{10}\mu_{\alpha_1}^{10*}} \rho_0^{00} \mathrm{e}^{-\kappa_{11}\tau_2} \frac{\gamma_{01}}{\Omega_{10}^2+\gamma_{01}^2}, \quad (2.69)$$

This signal is therefore a Lorentzian peaked in ω_3 at ω_{10}, and it decays on a timescale of κ_{11} as a function of τ_2. Therefore, if a population-relaxation timescale needs to be measured, TA is often preferable due to its relative ease.

When the 2D IR spectrum is initially collected, it is a function of τ_1, τ_2, and ω_3 and it is subsequently transformed to the ω_1 domain. The transformation can be inverted, of course, such that the 2D IR spectrum is related to the time domain spectrum by

$$S(\tau_1,\tau_2,\omega_3) = \frac{1}{2\pi}\int \mathrm{d}\omega_1 \mathrm{e}^{-\mathrm{i}\omega_1\tau_1} S(\omega_1,\tau_2,\omega_3). \quad (2.70)$$

Therefore, the TA spectrum is related to the 2D IR spectrum by

$$S(0,\tau_2,\omega_3) = \frac{1}{2\pi}\int \mathrm{d}\omega_1 S(\omega_1,\tau_2,\omega_3). \quad (2.71)$$

That is, the TA spectrum is simply proportional to the 2D IR spectrum integrated over the initial excitation frequency, ω_1, a consequence of the projection–slice theorem of Fourier transforms. Herein also lies the disadvantage of TA spectroscopy in that it is not possible to gain any information about the initial excitation frequency.

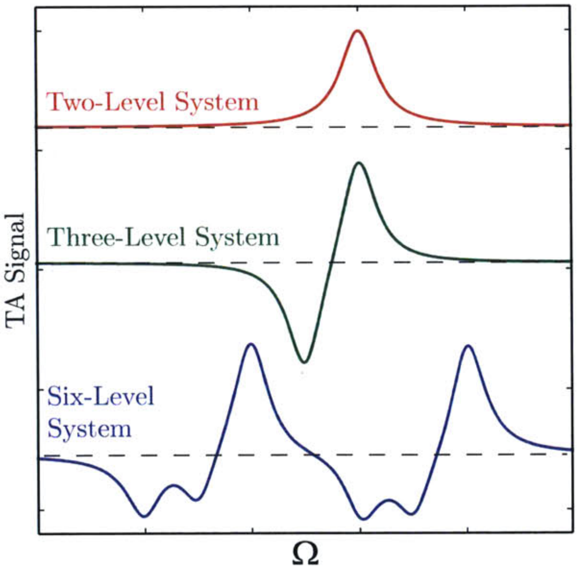

Figure 2.8: Schematic TA spectra for two-, three-, and six-level systems.

Figure 2.8 shows TA spectrum for two-level, three-level, and six-level systems that can be directly compared to the 2D IR spectra of Figs. 2.5, 2.6, and 2.7, respectively. The complexity associated with projecting the 2D IR spectrum onto a single axis is evident from the

TA spectrum for the six-level system. It is impossible here to determine whether there is any coupling associated with these features or whether they arise due to two independent oscillators. As such, while TA spectra are useful for rapidly and accurately extracting timescales and excited-state absorption frequencies, great care must be taken when interpreting them due to the lack of resolution in the excitation frequency. Hence, the interpretation of a TA spectrum is typically accompanied by the analysis of 2D IR spectra at several values of τ_2.

2.5.5 Polarization Anisotropy

We now continue to develop the ideas initially put forth in §2.4, and describe how the various rotational correlations come into play in 2D IR and TA spectroscopy. As discussed in §2.4.2, when multiple transitions are involved in a particular pathway, the rotational averaging result is dependent on the angle between the transition dipoles. As such, polarization-dependent experiments can be used to determine the angle between transition dipoles. Appendix 2.A tabulates the dependence on transition dipole angle for the 14 pathways shown in Fig. 2.7 for ZZZZ and ZZYY polarization schemes.

Each of the orientational tensors in Table 2.3 are proportional to $c_1(\tau_1)$ and $c_1(\tau_3)$; as such, these contribute directly to the lineshape in ω_1 and ω_3, respectively. Depending on the orientational diffusion constant, orientational dynamics can either have a significant or negligible effect on the lineshape. The dependence in τ_2 is somewhat more complex, and we may take advantage of this complexity to either determine the rotational dynamics or eliminate them completely in τ_2.

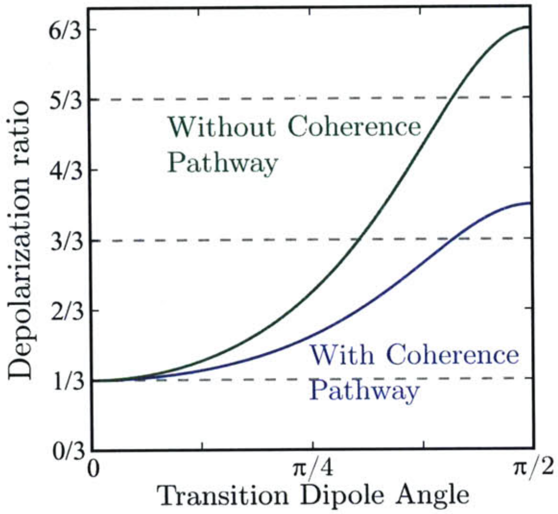

Figure 2.9: Depolarization ratio for cross peaks with and without coherence pathways.

We begin by considering the orientational tensors for $\tau_2 = 0$. The pathways are proportional to the various orientational tensor elements, but the overall magnitude of the features is determined by the magnitude of the transition dipoles. Therefore, to extract angular information, it is necessary to measure ratios of the intensity of the various features. If we consider a diagonal peak and neglect coherence pathways, the tables in Appendix 2.A show that the signal in the ZZZZ polarization scheme, $S_{\parallel}$, is proportional to a factor of $4Y^{3333}_{ZZZZ}$, which is equal to 4/5 at $\tau_2 = 0$. In the ZZYY Polarization scheme, the signal, $S_{\perp}$, is proportional $4Y^{3333}_{ZZYY}$, which is 4/15 at $\tau_2 = 0$. Therefore, the depolarization ratio for a diagonal peak, which is defined as $S_{\perp}/S_{\parallel}$, is 1/3. That is, the height of a diagonal signal in the parallel scheme is three times that in the perpendicular scheme.

The situation is not so simple if the coherence pathway is included. Then, this term is not proportional to the same overall factor. As such, its magnitude is not simply divided out and the depolarization ratio can deviate from 1/3 for diagonal peaks. In addition, the magnitude of the deviation depends on the angle between the transition dipole of the two oscillators.

Cross peaks are somewhat more complex, but certainly more interesting. If we consider the bleach of the cross-peak, there are three paths to consider, one of which is a coherence path. All pathways depend on the same dipoles however, and as such, normalization is not an issue. The ZZZZ signal goes as $S_{\parallel} \propto \sin^2 \Theta(2Y^{3311}_{ZZZZ} + Y^{3131}_{ZZZZ}) + 3\cos^2 \Theta Y^{3333}_{ZZZZ}$ which at $\tau_2 = 0$ is given by $\frac{1}{5}(1 + 2\cos^2 \Theta)$. On the other hand, the ZZYY signal is given by $S_{\perp} \propto \sin^2 \Theta(2Y^{3311}_{ZZYY} + Y^{3131}_{ZZYY}) + 3\cos^2 \Theta Y^{3333}_{ZZZZ}$ which at $\tau_2 = 0$ is given by $\frac{1}{30}(7 - \cos^2 \Theta)$. Therefore, the depolarization ratio for the cross peak, including the coherence pathway, is given by

$$D_{\text{cp}}(\Theta) = \frac{1}{6}\frac{7 - \cos^2 \Theta}{1 + 2\cos^2 \Theta}. \tag{2.72}$$

The depolarization ratio varies from 1/3 at $\Theta = 0$, as expected from the discussion of the previous paragraph to 7/6 at $\Theta = \pi/2$. This shows that for perpendicular dipoles, the ZZYY cross-peak signal is in fact slightly more intense than the ZZZZ signal.

Without the coherence pathway, there are only two pathways to consider, and the depolarization ratio is given by

$$D'_{\mathrm{cp}}(\Theta) = \frac{2 - \cos^2 \Theta}{1 + 2\cos^2 \Theta}, \tag{2.73}$$

which is of course different from the depolarization ratio including coherence pathway. The $\Theta = 0$ and $\Theta = \pi/2$ values are 1/3 and 2, respectively, and thus the depolarization ratio, $D'_{\mathrm{cp}}(\Theta)$ spans a larger range than $D_{\mathrm{cp}}(\Theta)$. Therefore, performing spectroscopy in which the coherence term is not measured can result in a more accurate angle measurement. Figure 2.9 shows how $D_{\mathrm{cp}}(\Theta)$ and $D'_{\mathrm{cp}}(\Theta)$ vary as a function of Θ.

We now consider the orientational dynamics in τ_2, and we begin by focusing on the elimination of these dynamics. If we consider the three-level system, the ground-state bleach has two rephasing and non-rephasing pathways in which each of the interactions is with the same dipole. Therefore, if the fields are all polarized parallel to each other, the amplitude of this peak will be proportional to $S_{\|} \propto 4Y^{3333}_{ZZZZ}$. Similarly, in the perpendicular polarization scheme, the peak will be proportional to $S_{\perp} \propto 4Y^{3333}_{ZZYY}$. From looking up the orientational tensors in Table 2.3, it is evident that the sum

$$S_{\mathrm{iso}} = S_{\|} + 2S_{\perp} \tag{2.74}$$

is independent of rotational dynamics in τ_2. That is, the orientational function $c_2(\tau_2)$ is eliminated, resulting in a signal that is independent of orientational dynamics during τ_2. We refer to this as the isotropic signal.

Since the signals are additive in an experiment, it should be possible to devise a polarization scheme between the first two pulses and the third such that we directly extract the isotropic signal. If we assume that the third pulse is polarized along Z, we desire that the first two pulses have a polarization e such that $(e \cdot \hat{Y})^2 = 2(e \cdot \hat{Z})^2$. The squares are a result of there being two interactions with the first two fields. If $\cos\theta$ is the projection of the polarization vector onto the lab-frame $\hat{Z}$ axis, then the condition reduces to $\sin^2\theta = 2\cos^2\theta$. Therefore, the angle between the first two pulses and the third which produces the isotropic signal is given by

$$\theta_{\mathrm{MA}} = \arctan\sqrt{2} = 54.74^\circ. \tag{2.75}$$

This is known as the "magic angle." Therefore, if the relative polarization between the first two fields and the third and the signal field is set to magic angle, then orientational dynamics will not be observed in τ_2. Since the magic-angle signal is, in effect, "diluted" over three signals, we note that

$$S_{\mathrm{MA}} = \frac{1}{3} S_{\mathrm{iso}}. \tag{2.76}$$

In addition to the four paths contributing to the three-level system, a six-level system will contain an additional coherence pathway (see Fig. 2.7) that is proportional to Y^{3113}_{IJKL}. However, we see that $Y^{3113}_{ZZZZ} = -2Y^{3113}_{ZZYY}$ and as such, this pathway is eliminated entirely in the isotropic signal.

In the same way that we may eliminate orientational dynamics from the τ_2 signal, we may isolate them as well. To that end, we again consider the diagonal ground-state bleach of the three-level system, and note that $S_{\parallel} - S_{\perp} \propto \frac{2}{15} c_1(\tau_1) c_2(\tau_2) c_1(\tau_3)$. On the other hand, $S_{\mathrm{iso}} \propto \frac{1}{3} c_1(\tau_1) c_1(\tau_3)$, and these two terms have *the same proportionality factor*. Therefore, we define the orientational anisotropy function

$$r(\tau_2) = \frac{S_{\parallel} - S_{\perp}}{S_{\parallel} + 2S_{\perp}} = \frac{2}{5} c_2(\tau_2) = \frac{2}{5} \mathrm{e}^{-6\tau_2/\tau_{\mathrm{r}}}. \tag{2.77}$$

This provides a convenient way to experimentally extract the rotational diffusion constant, τ_{r}, though often $\tau_{\mathrm{r}}/6$ is reported.

If the additional pathway from the six-level system is present, the situation is complicated somewhat. Now, the anisotropy contains an additive term due to the extra pathway which is proportional to $\frac{3}{40} c_2(\tau_2)$, but the proportionality factor is not simply divided out by the isotropic signal. This term is a rather small contribution to the anisotropy measurement, however, and it does not significantly contribute to experimental measurements.

2.A Tables of Orientational Factors for Third-Order Polarization Spectroscopy

Table 2.4: Orientational factors for two-oscillator system for the ZZZZ polarization scheme assuming excited-state transitions have the same orientation as ground-state ones.

Pathway	Dipole Factor	Orientational Factor	$\tau_2 = 0$ value
$\left\lvert\begin{array}{cc} \mathrm{S} & 0 \\ 0 & 0 \\ 0 & \mathrm{S} \\ 0 & 0 \end{array}\right\rvert$ $\left\lvert\begin{array}{cc} \mathrm{S} & 0 \\ \mathrm{S} & \mathrm{S} \\ 0 & \mathrm{S} \\ 0 & 0 \end{array}\right\rvert$ $\left\lvert\begin{array}{cc} \mathrm{S} & 0 \\ 0 & 0 \\ \mathrm{S} & 0 \\ 0 & 0 \end{array}\right\rvert$ $\left\lvert\begin{array}{cc} \mathrm{S} & 0 \\ \mathrm{S} & \mathrm{S} \\ \mathrm{S} & 0 \\ 0 & 0 \end{array}\right\rvert$	$\mu^{s,0}\mu^{s,0}\mu^{s,0}\mu^{s,0}$	Y^{3333}_{ZZZZ}	$\frac{1}{5}$
$\left\lvert\begin{array}{cc} \mathrm{S} & 0 \\ \mathrm{S} & \mathrm{A} \\ \mathrm{S} & 0 \\ 0 & 0 \end{array}\right\rvert$	$\mu^{s,0}\mu^{a,0}\mu^{a,0}\mu^{s,0}$	$\sin^2\Theta Y^{3113}_{ZZZZ} + \cos^2\Theta Y^{3333}_{ZZZZ}$	$\frac{1}{15}(1+2\cos^2\Theta)$
$\left\lvert\begin{array}{cc} 2\mathrm{S} & \mathrm{S} \\ \mathrm{S} & \mathrm{S} \\ 0 & \mathrm{S} \\ 0 & 0 \end{array}\right\rvert$ $\left\lvert\begin{array}{cc} 2\mathrm{S} & \mathrm{S} \\ \mathrm{S} & \mathrm{S} \\ \mathrm{S} & 0 \\ 0 & 0 \end{array}\right\rvert$	$\mu^{2s,s}\mu^{2s,s}\mu^{s,0}\mu^{s,0}$	Y^{3333}_{ZZZZ}	$\frac{1}{5}$
$\left\lvert\begin{array}{cc} \mathrm{A} & \mathrm{SA} \\ \mathrm{A} & \mathrm{S} \\ 0 & \mathrm{S} \\ 0 & 0 \end{array}\right\rvert$	$\mu^{a,sa}\mu^{sa,s}\mu^{a,0}\mu^{s,0}$	$\sin^2\Theta Y^{3113}_{ZZZZ} + \cos^2\Theta Y^{3333}_{ZZZZ}$	$\frac{1}{15}(1+2\cos^2\Theta)$
$\left\lvert\begin{array}{cc} \mathrm{A} & 0 \\ 0 & 0 \\ 0 & \mathrm{S} \\ 0 & 0 \end{array}\right\rvert$ $\left\lvert\begin{array}{cc} \mathrm{A} & 0 \\ 0 & 0 \\ \mathrm{S} & 0 \\ 0 & 0 \end{array}\right\rvert$	$\mu^{a,0}\mu^{a,0}\mu^{s,0}\mu^{s,0}$	$\sin^2\Theta Y^{3311}_{ZZZZ} + \cos^2\Theta Y^{3333}_{ZZZZ}$	$\frac{1}{15}(1+2\cos^2\Theta)$
$\left\lvert\begin{array}{cc} \mathrm{A} & 0 \\ \mathrm{A} & \mathrm{S} \\ 0 & \mathrm{S} \\ 0 & 0 \end{array}\right\rvert$	$\mu^{a,0}\mu^{s,0}\mu^{a,0}\mu^{s,0}$	$\sin^2\Theta Y^{3131}_{ZZZZ} + \cos^2\Theta Y^{3333}_{ZZZZ}$	$\frac{1}{15}(1+2\cos^2\Theta)$
$\left\lvert\begin{array}{cc} \mathrm{SA} & \mathrm{S} \\ \mathrm{S} & \mathrm{S} \\ 0 & \mathrm{S} \\ 0 & 0 \end{array}\right\rvert$ $\left\lvert\begin{array}{cc} \mathrm{SA} & \mathrm{S} \\ \mathrm{S} & \mathrm{S} \\ \mathrm{S} & 0 \\ 0 & 0 \end{array}\right\rvert$	$\mu^{sa,s}\mu^{sa,s}\mu^{s,0}\mu^{s,0}$	$\sin^2\Theta Y^{3311}_{ZZZZ} + \cos^2\Theta Y^{3333}_{ZZZZ}$	$\frac{1}{15}(1+2\cos^2\Theta)$
$\left\lvert\begin{array}{cc} \mathrm{SA} & \mathrm{S} \\ \mathrm{A} & \mathrm{S} \\ 0 & \mathrm{S} \\ 0 & 0 \end{array}\right\rvert$	$\mu^{sa,s}\mu^{sa,a}\mu^{a,0}\mu^{s,0}$	$\sin^2\Theta Y^{3131}_{ZZZZ} + \cos^2\Theta Y^{3333}_{ZZZZ}$	$\frac{1}{15}(1+2\cos^2\Theta)$

Table 2.5: Orientational factors for two-oscillator system for the ZZYY polarization scheme assuming excited-state transitions have the same orientation as ground-state ones.

Pathway	Dipole Factor	Orientational Factor	$\tau_2 = 0$ value
$\left\lvert\begin{array}{cc} S & 0 \\ 0 & 0 \\ 0 & S \\ 0 & 0 \end{array}\right\rvert$ $\left\lvert\begin{array}{cc} S & 0 \\ S & S \\ 0 & S \\ 0 & 0 \end{array}\right\rvert$ $\left\lvert\begin{array}{cc} S & 0 \\ 0 & 0 \\ S & 0 \\ 0 & 0 \end{array}\right\rvert$ $\left\lvert\begin{array}{cc} S & 0 \\ S & S \\ S & 0 \\ 0 & 0 \end{array}\right\rvert$	$\mu^{s,0}\mu^{s,0}\mu^{s,0}\mu^{s,0}$	Y^{3333}_{ZZYY}	$\frac{1}{15}$
$\left\lvert\begin{array}{cc} S & 0 \\ S & A \\ S & 0 \\ 0 & 0 \end{array}\right\rvert$	$\mu^{s,0}\mu^{a,0}\mu^{a,0}\mu^{s,0}$	$\sin^2\Theta Y^{3113}_{ZZYY} + \cos^2\Theta Y^{3333}_{ZZYY}$	$\frac{1}{30}(3\cos^2\Theta - 1)$
$\left\lvert\begin{array}{cc} 2S & S \\ S & S \\ 0 & S \\ 0 & 0 \end{array}\right\rvert$ $\left\lvert\begin{array}{cc} 2S & S \\ S & S \\ S & 0 \\ 0 & 0 \end{array}\right\rvert$	$\mu^{2s,s}\mu^{2s,s}\mu^{s,0}\mu^{s,0}$	Y^{3333}_{ZZYY}	$\frac{1}{15}$
$\left\lvert\begin{array}{cc} A & SA \\ A & S \\ 0 & S \\ 0 & 0 \end{array}\right\rvert$	$\mu^{a,sa}\mu^{sa,s}\mu^{a,0}\mu^{s,0}$	$\sin^2\Theta Y^{3113}_{ZZYY} + \cos^2\Theta Y^{3333}_{ZZYY}$	$\frac{1}{30}(3\cos^2\Theta - 1)$
$\left\lvert\begin{array}{cc} A & 0 \\ 0 & 0 \\ 0 & S \\ 0 & 0 \end{array}\right\rvert$ $\left\lvert\begin{array}{cc} A & 0 \\ 0 & 0 \\ S & 0 \\ 0 & 0 \end{array}\right\rvert$	$\mu^{a,0}\mu^{a,0}\mu^{s,0}\mu^{s,0}$	$\sin^2\Theta Y^{3311}_{ZZYY} + \cos^2\Theta Y^{3333}_{ZZYY}$	$\frac{1}{15}(2 - \cos^2\Theta)$
$\left\lvert\begin{array}{cc} A & 0 \\ A & S \\ 0 & S \\ 0 & 0 \end{array}\right\rvert$	$\mu^{a,0}\mu^{s,0}\mu^{a,0}\mu^{s,0}$	$\sin^2\Theta Y^{3131}_{ZZYY} + \cos^2\Theta Y^{3333}_{ZZYY}$	$\frac{1}{30}(3\cos^2\Theta - 1)$
$\left\lvert\begin{array}{cc} SA & S \\ S & S \\ 0 & S \\ 0 & 0 \end{array}\right\rvert$ $\left\lvert\begin{array}{cc} SA & S \\ S & S \\ S & 0 \\ 0 & 0 \end{array}\right\rvert$	$\mu^{sa,s}\mu^{sa,s}\mu^{s,0}\mu^{s,0}$	$\sin^2\Theta Y^{3311}_{ZZYY} + \cos^2\Theta Y^{3333}_{ZZYY}$	$\frac{1}{15}(2 - \cos^2\Theta)$
$\left\lvert\begin{array}{cc} SA & S \\ A & S \\ 0 & S \\ 0 & 0 \end{array}\right\rvert$	$\mu^{sa,s}\mu^{sa,a}\mu^{a,0}\mu^{s,0}$	$\sin^2\Theta Y^{3131}_{ZZYY} + \cos^2\Theta Y^{3333}_{ZZYY}$	$\frac{1}{30}(3\cos^2\Theta - 1)$

Chapter 3

Multidimensional IR Spectroscopy in Practice

3.1 The Nuts and Bolts of the 2D IR Experiment

Two dimensional IR (2D IR) spectroscopy is a technique unlike any other. In a 2D IR experiment, three ultrashort pulses of mid-IR light generate a nonlinear polarization density in a sample which radiates an electromagnetic field [77, 78]. Encoded in that radiation are frequency and dipole correlations between various molecular vibrations. By measuring these correlations with femtosecond time resolution we can infer changes in molecular structure on characteristic timescales of molecular motion since a vibration's frequency is dependent on the molecular structure and the oscillator's environment in the liquid phase [15, 24, 25]. We therefore often talk about "making movies" of molecular dynamics. Reality is far more complex, however, and rarely is the data so clear cut. Rather, in depth interpretation, usually accompanied by extensive computational simulations, is necessary to understand a spectrum and even then, we are often limited to qualitative descriptions of our samples –certainly a far cry from making molecular movies! Despite the intrinsic complexity of 2D IR spectroscopy, however, it has been used successfully to study a wide variety of systems. Ranging from small molecules to complex biological macromolecules, 2D IR has proven to be an indispensable tool for understanding condensed-phase phenomena that other techniques simply do not have access to.

On paper, the experimental implementation of a 2D IR experiment is quite simple. Three short mid-IR pulses, separated by controllable time delays, are focused into a molecular sample. The polarization density induced in the sample radiates light, which is measured in a spectrally resolved manner as a function of the two time delays between the pulses. Just one step into the lab, however, is enough to convince yourself that the experiments are far more involved than such a simple description might indicate. Ultrashort pulses need to be generated, amplified, compressed, down-converted to the mid-IR, and compressed again. Care must be taken to ensure that mid-IR beams possess a good mode, are collimated, and are well-overlapped with visible tracer beams. Special care must be taken to avoid dispersion of the pulses. An interferometer must be used to generate time-separated pulse pairs, with an accuracy on the order of 1 fs –a path-length difference of only 300 nm. Then, three pulses, lasting only a few tens of femtoseconds, must be overlapped in space and time and focused into a region of space no larger than a few tens of microns on any side. The resulting signal must be carefully collected and detected. Of course, the entire experiment is enclosed in purged boxes so that atmospheric water and carbon dioxide do not absorb the IR pulses, and the entire room is maintained at a precise temperature and humidity for stable laser operation. Above the experiment lives a mess of controllers, computers, power supplies, integrators, delay generators, data cables, electrical cables, and hoses carrying scrubbed air or cooling water. There is not a day that goes by where I am not absolutely amazed that so many independent parts can somehow come together and function synchronously to bring such a complex experiment to life.

In this chapter, I hope to provide a thorough but practical introduction to how 2D IR experiments are carried out in the laboratory. Certainly all of the details and "tricks" necessary to run a 2D IR experiment cannot be written down and can only be obtained through a few years of struggling. Rather, I hope to give enough information to serve as a guide to continue operating the current experiments as well as provide notes for future

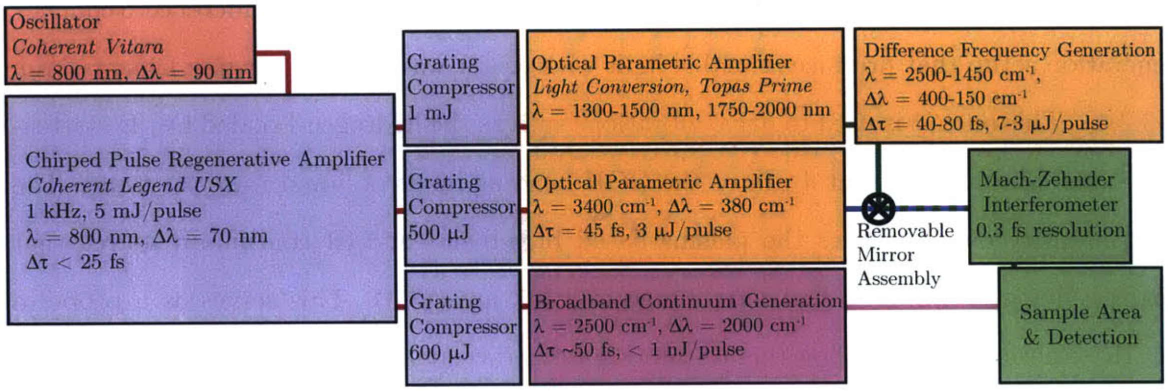
Oscillator
Coherent Vitara
$\lambda = 800$ nm, $\Delta\lambda = 90$ nm
Chirped Pulse Regenerative Amplifier
Coherent Legend USX
1 kHz, 5 mJ/pulse
$\lambda = 800$ nm, $\Delta\lambda = 70$ nm
$\Delta\tau < 25$ fs
Grating Compressor 1 mJ
Grating Compressor 500 μJ
Grating Compressor 600 μJ
Optical Parametric Amplifier
Light Conversion, Topas Prime
$\lambda = 1300$-1500 nm, 1750-2000 nm
Optical Parametric Amplifier
$\lambda = 3400$ cm^{-1}, $\Delta\lambda = 380$ cm^{-1}
$\Delta\tau = 45$ fs, 3 μJ/pulse
Broadband Continuum Generation
$\lambda = 2500$ cm^{-1}, $\Delta\lambda = 2000$ cm^{-1}
$\Delta\tau$ ~50 fs, < 1 nJ/pulse
Difference Frequency Generation
$\lambda = 2500$-1450 cm^{-1},
$\Delta\lambda = 400$-150 cm^{-1}
$\Delta\tau = 40$-80 fs, 7-3 μJ/pulse
Removable Mirror Assembly
Mach-Zehnder Interferometer 0.3 fs resolution
Sample Area & Detection

Figure 3.1: Schematic overview of the experimental setup illustrating pulse generation, manipulation, and detection.

generations of graduate students on what has succeeded, what has failed, what has been done, and what needs to be done.

3.1.1 Overview of the Experiment

Before delving into the details of the 2D IR experiment, it is worth giving an overview of all the components and how they fit together. The different steps necessary to carry out a 2D IR experiment can broadly be categorized into generation, manipulation, and detection. Figure 3.1 shows a schematic layout of the different components of the experiment and how they fit together.

The generation of mid-IR pulses begins with the generation of short pulses of visible light. Short pulses from a mode-locked oscillator are amplified in a chirped-pulse regenerative amplifier (§3.2.1). Pulses are split into three distinct beams and independently compressed in three separate grating-based compressors. The output of each compressor drives a mid-IR-generation source.

The lowest intensity output drives a home-built two stage optical parametric amplifier that outputs a center wavelength of 3 μm (§3.2.3). This output is used to drive hydrogen-bonded X—H stretches in the experiments detailed in this thesis. The highest intensity output drives a commercial optical parametric amplifier that generates a signal and idler beam tunable throughout the entire near-IR. This drives a home-built difference frequency generation setup that produces tunable light with center wavelengths ranging from 4–7 μm (§3.2.4). This output is used to drive vibrations such as the hydrogen-bonded O—D stretching mode of heavy water at 4 μm or the HOH bending mode of liquid water at 6 μm. The mid intensity output drives the plasma-based broadband mid-IR continuum source that spans a detector-limited wavelength range of 2.5–7 μm (§3.3). This serves as a probe in 2D IR experiments that allows us to interrogate and correlate vibrations across the entire mid-IR. A high accuracy translation stage allows us to control the time delay between the probe pulse and the driving fields.

The excitation pulses from the optical parametric amplifier or difference frequency generation source are fed into a removable mirror assembly that allows us to switch between the sources with relative ease. They are subsequently fed into a Mach-Zehnder interferometer (§3.4) that produces a pulse pair with a time delay between them that can be accurately controlled. The driving pulse pair and the broadband mid-IR continuum probe enter a sample area where they are focused into a sample (§3.5.1). A nonlinear electric polarization density is induced in the sample which subsequently radiates a signal field that is heterodyned with a local oscillator.

The signal field is dispersed in a monochromator, imaged onto an array of detectors, and measured as a function of the two time delays between the three pulses. Due to interference between the electric polarization density induced in the sample and the driving fields, the 2D IR signal oscillates as a function of time at the excitation frequencies of the sample. Measuring the signal field as a function of the time delay between the two driving fields and Fourier transforming along this time dimension results in a two-dimensional correlation surface that gives the change in absorption for exciting the system at a particular frequency after waiting the amount of time equal to the delay between the driving fields and the probe (§3.5.3). The details are given in the remainder of this chapter.

3.2 OPA-Based Generation of IR Pulses

3.2.1 Generation of Short Pulses of Visible Light

The plethora of nonlinear time-resolved spectroscopies in the spectral range of mid-IR to UV that have been developed in the last 20 years or so are due, in no small part, to the development of commercially available mode-locked laser oscillators [90]. By stabilizing the relative phase of many longitudinal modes of a laser cavity, it is possible to generate pulses as short as 5 fs [91] through constructive and destructive interference of the different modes [92]. Pulses are generated at a repetition rate determined by the length of the cavity, which is in the MHz range for common cavities. First developed some 25 years ago [93,94], $Ti^{3+}:Al_2O_3$ (commonly Ti:Sapphire) self-mode-locking lasers have found widespread use owing to their simplicity, versatility, and robustness, and to the fact that short pulses are selectively amplified due to the optical Kerr effect. $Ti^{3+}:Al_2O_3$ effectively acts as a four-level lasing medium that is capable of supporting over 100 nm of bandwidth centered at a wavelength of 800 nm [95].

The energy per pulse of a mode-locked laser, typically in the nanojoule range, is too small to carry out the nonlinear processes necessary to convert the 800 nm light from the $Ti^{3+}:Al_2O_3$ mode-locked laser to the mid-IR light for 2D IR experiments. Before the pulses are used, they must therefore be amplified. This is accomplished through chirped pulse amplification (CPA) [96]. In CPA, femtosecond pulses are chirped in an optical stretcher before being amplified in a $Ti^{3+}:Al_2O_3$ crystal that is optically pumped by a nanosecond pulsed Q-switched laser. Such laser amplifiers typically cannot run at the MHz rates of mode-locked lasers, so it is necessary to only amplify a select few of oscillator pulses thus reducing the repetition rate. After the chirped pulses are amplified, they are recompressed in an optical compressor. The gain in the $Ti^{3+}:Al_2O_3$ is not linear in frequency [95], and this has the effect of producing a narrower output spectrum (i.e. a longer pulse) compared to the spectrum of the input pulse.

The laser system used in these experiments is based on a commercial $Ti^{3+}:Al_2O_3$ mode-locked oscillator (*Coherent Vitara-T*) pumped by an optically-pumped semiconductor continuous wave laser (*Coherent Verdi-G*). The oscillator produces pulses centered at 800 nm with 80 nm of bandwidth at a repetition rate of 80 MHz with 470 mW of power, corresponding to about 6 nJ per pulse. Before CPA, a spectral notch filter cuts the intensity of the spectrum by ~80% in the region from 770 to 830 nm. This has the effect of mitigating the bandwidth narrowing in the CPA stage. The CPA is carried out in a commercial Ti^{3+}:Al_2O_3 based regenerative amplifier (*Coherent Legend USX*) which consists of a grating-based optical stretcher, an amplifier, and three separate optical compressors. The Ti^{3+}:Al_2O_3 amplifier is pumped by a frequency doubled Q-switched Nd^{3+}:$LiYF_4$ laser (*Coherent Evolution 30*) which produces 532 nm nanosecond pulses at a repetition rate of $f_{\text{rep}} = 1$ kHz. Seed pulses from the oscillator are injected into the amplifier by rotation of the polarization with a Pockels cell which is synchronously triggered by the Q-switched laser and the oscillator outputs. The pulses make 14 round trips through the cavity before being ejected by a second Pockels cell. At this point, the pulses have an energy of 5–6 mJ per pulse (corresponding to an amplification of $\sim 10^6$) and a bandwidth of 60–70 nm, centered at 800 nm, but are stretched in time. Before compression, the pulse passes through a 33:67 beamsplitter. The more intense beam is then further passed through a 50:50 beamsplitter, resulting in three beams of roughly equal intensity. Each of these beams is fed into its own independent grating compressor which compresses pulses to lengths between 20 and 25 fs; this is somewhat longer than what would be expected for Gaussian pulses, but consistent with a Fourier-limited pulse based on the actual measured spectrum. Attenuation of the pulses after compression is problematic since the length of the pulse ensures that there will be significant dispersion and nonlinear processes occurring in almost any medium. Therefore, the pulses are attenuated in the compressors, on the gratings themselves, by rotating the polarization of the uncompressed pulses with three waveplates placed just after the three beams are split. The three different arms produce similar P-polarized pulses, with ~65 nm of bandwidth at 800 nm, energies up to ~1 mJ, and durations of less than 25 fs.

3.2.2 OPA and DFG

Without a doubt, optical parametric amplification (OPA) followed by difference frequency generation (DFG) is by far the most wide spread method (and for a long time, the only method) of generating short mid-IR pulses. The description of OPA is somewhat different from typical nonlinear processes in that it involves many cascaded second-order processes [55,56]. (In reality, cascading happens in all nonlinear processes and the ability to differentiate between OPA and DFG, for example, really lies within the intensity of the input beams.) In OPA, an intense pump and a weak seed are mixed in a nonlinear medium; DFG between these two results in the creation of an idler at the difference frequency

$$\omega_{\mathrm{I}} = \omega_{\mathrm{P}} - \omega_{\mathrm{S}}. \tag{3.1}$$

The idler then mixes with the intense pump to generate *signal* at the difference frequency which, by energy conservation, is the same frequency as the input seed. The signal and idler continue to mix with the pump so as to deplete intensity from it and increase the intensity at the signal and idler frequencies. Since the signal and idler necessarily have frequencies less than that of the pump (whose sum is precisely that of the pump) OPA provides an effective means of down conversion.

The intensity of signal and idler generated can be determined by solving the coupled wave equations with initial conditions corresponding to an intense pump, weak signal, and no idler [55,56]. This is, in general, not possible and a number of approximations must be made. In the limit that the pump intensity is not significantly depleted and that the envelope of the pulse varies slowly in space compared to the wavelength, the field amplitudes of the signal and idler as a function of depth in the crystal are respectively given by

$$E_{\mathrm{S}}(z) = E_{\mathrm{S}}(0)\left(\cosh(gz/2) + \frac{\Delta k}{g}\sinh(gz/2)\right) \tag{3.2a}$$

$$E_{\mathrm{I}}(z) = E_{\mathrm{S}}(0)\frac{\omega_{\mathrm{I}}}{\omega_{\mathrm{S}}}\left(\frac{k_{\mathrm{S}z}}{k_{\mathrm{I}z}}\right)^{1/2}\frac{g_0}{g}\cosh(gz/2). \tag{3.2b}$$

In the above expression,

$$\Delta k = k_{\mathrm{P}z} - k_{\mathrm{S}z} - k_{\mathrm{I}z}, \tag{3.3a}$$

is the phase mismatch for the OPA process which represents the difference in the wavevectors between the pump and the signal plus idler. In vacuum, these are of course the same, however, we must consider the index of refraction of the nonlinear medium. Furthermore,

$$g = \left(g_0^2 - \Delta k^2\right)^{1/2} \tag{3.3b}$$

$$g_0^2 = \frac{16\pi^2 \omega_{\mathrm{S}}^2 \omega_{\mathrm{I}}^2}{c^4 k_{\mathrm{S}z} k_{\mathrm{I}z}} \left(\chi^{(2)} \vdots \hat{e}_{\mathrm{P}} \hat{e}_{\mathrm{S}} \hat{e}_{\mathrm{I}}\right)^2 E_{\mathrm{P}}^2, \tag{3.3c}$$

are the gain parameter and gain parameter for perfect phase matching, respectively. The phase mismatch, Δk, is the most important property determining whether OPA will occur or not. If g is real and nonzero, the amplitude of the signal and idler field grows exponentially and without bound (an artifact of the approximation that pump depletion is negligible). This will be the case if $|\Delta k| < g_0$, which can be achieved if $\chi^{(2)} E_{\mathrm{P}}$ is large enough or if Δk is small enough. In practice, it is easier to minimize the phase mismatch by using a crystal for which $\Delta k \approx 0$ over the bandwidth of interest rather than making E_{P} large or finding a crystal with a large enough $\chi^{(2)}$. This limits the bandwidth which can be produced in OPA. If $|\Delta k| > g_0$, g is imaginary and the field amplitude does not grow. The signal field oscillates with a spatial period of $2/g$, and the real part of the idler field remains zero at all crystal depths.

OPA in and of itself is usually not enough to generate mid-IR pulses with $\lambda \geq 3.5$ μm since most crystals in which OPA is an efficient process will absorb IR light. Therefore, it has become common to use OPA to generate a signal and idler in the near-IR (0.8-2.5 μm) and perform DFG to generate a mid-IR frequency. For a given signal and idler, the difference frequency will be

$$\omega_{\mathrm{DFG}} = \omega_{\mathrm{S}} - \omega_{\mathrm{I}} = 2\omega_{\mathrm{S}} - \omega_{\mathrm{P}}, \tag{3.4}$$

where Eq. 3.1 has been used to eliminate the idler frequency in the second equality. For pump frequencies corresponding to 800 nm (12500 cm^{-1}), generating mid-IR light at frequencies ranging from 4–7 μm (2500–1430 cm^{-1}) requires signal frequencies between 1.33–1.44 μm (7500–6965 cm^{-1}), which is easily achievable with readily available nonlinear crystals.

In principle, the same set of coupled wave equations determining the amplitude of the fields in OPA govern the DFG process. In practice, however, we can assume that neither the signal nor idler are depleted significantly during the DFG process, which simplifies the solution to a great extent [55, 56]. The field amplitude of the generated difference frequency (again within the slowly varying envelope approximation and neglecting depletion of the pump fields) is given by

$$E_{\mathrm{DFG}}(z) = E_{\mathrm{S}}(0)E_{\mathrm{I}}(0)\frac{2\pi\omega_{\mathrm{DFG}}^{2}}{k_{\mathrm{DFG}z}c^{2}}\left(\chi^{(2)}:\hat{e}_{\mathrm{P}}\hat{e}_{\mathrm{S}}\hat{e}_{\mathrm{I}}\right)\mathrm{sinc}\left(\frac{\Delta k z}{2}\right)z, \tag{3.5}$$

where the phase mismatch is now given by

$$\Delta k = k_{\mathrm{S}z} - k_{\mathrm{I}z} - k_{\mathrm{DFG}z}. \tag{3.6}$$

In the limit of perfect phase matching, $\Delta k = 0$, the difference frequency field grows linearly with propagation through the crystal. For non-zero Δk, however, the amplitude of the difference frequency field oscillates with a spatial period of $1/\Delta k$ and falls off inversely as Δk. Therefore, similarly to OPA, the ability to phase match a certain range of frequencies fundamentally limits the bandwidth of mid-IR pulses which can be achieved. Typically, mid-IR pulses produced by DFG are longer than the input signal and idler pulses.

Excitation pulses for the experiments described in this thesis were generated with one of two sources, which are described in the following two sections.

3.2.3 Generation of 3 μm Pulses

Mid-IR pulses, centered at 3 μm, were generated using a home-built two-stage optical parametric amplifier. This amplifier has been described in detail in the literature [97], and so only a brief description is given here. About 500 μJ of P-polarized 800 nm light, at a rough beam size of 8 mm, is used to pump the amplifier. About 1% of this is split off, and focused into a [0001]-cut sapphire plate to generate white light continuum. Before focusing into the sapphire plate, the beam is irised down to a size of 3–4 mm and passed through a $\lambda/2$ waveplate and thin film polarizer (S-polarized, set a Brewster's angle) to rotate the polarization and control the intensity. The size of the iris is *crucial*, as this will determine the mode of the white light and therefore, of the 3 μm light that is ultimately produced. It is typically open to an aperture of ~3–4 mm. The portion of the white light around 1.1 μm serves as the seed in the first OPA stage. To minimize dispersion of the white-light continuum, it is steered and focused using reflective optics. The white light is combined with ~34% of the initial 800 nm light on a custom-made dichroic beamsplitter, which is designed to minimized group velocity dispersion (GVD).

The 800 nm and white light are focused into a 1 mm thick beta barium borate ($\beta-\mathrm{BaB_2O_4}$, BBO) crystal (negative uniaxial) [98] cut at $\theta = 29°$ but rotated in its mount to the phase-matching angle of $\theta = 21.5°$ for a type–I process (800 nm (e) = 1100 nm (o) + 2933 nm (o)). The divergence-matched 800 nm and white light focus ~2.5 cm behind the crystal in order to avoid saturation and damage to the BBO crystal. The OPA processes produces signal at 1.1 μm, but the idler, nominally at 2.93 μm is absorbed by the BBO crystal. This process produces 450–500 nJ of S-polarized light at 1.1 μm with a bandwidth of 400 cm^{-1}. Unfortunately, at this crystal angle, second harmonic generation (SHG) of 1.1 μm is also phase matched, and the pulse energy would be approximately double if this were not the case. This, and other nonlinear processes occurring in the BBO, produce a bright white visible spot in the beam after the crystal; this serves as a visual aid for alignment and timing.

The remaining 65% of 800 nm light is telescoped to a size of ~3 mm and kept fairly collimated in order to reduce the divergence of the generated 3 μm light in the second OPA process. The 1.1 μm generated in the first stage and the remaining 800 nm are passed through a 1 mm thick potassium niobate ($\mathrm{KNbO_3}$, KNB) crystal (negative biaxial) [99] cut at $\theta = 41°$ in the xz plane (where $n_x < n_y < n_z$) to achieve Type–I phase matching, as described above. This results in the production of more signal (~3 μJ) at 1.1 μm and idler at 2.9 μm. After generation, the residual 800 nm light is dumped into a beam block using a high-reflecting dielectric mirror which is essentially transparent to the signal and idler. Finally, the remaining visible and signal are filtered with an anti-reflection (AR) coated germanium wafer which serves as a point of overlap for a visible HeNe tracer. It is crucial that the residual 800 nm is dumped before this, otherwise a significant number of hot carriers are generated in the germanium which readily absorb the idler.

At generation, the beam size of the idler is quite small and rapidly divergent. It is expanded in a telescope made of CaF_2 lenses and collimated at a beam size of 7–9 mm (for a precise definition of beam size, see §3.5.1). By rotating the angle of the KNB slightly, the idler wavelength is mildly tunable in the range 3100–3500 cm^{-1} with a bandwidth that ranges from 400 cm^{-1} on the low-frequency side to 330 cm^{-1} on the high-frequency side. Figure 3.2 shows a typical 3 μm spectrum. Pulse energies range from 4 μJ on the low-energy side to 2.5 μJ on the high-energy side. The power fluctuations are typically on the order of 2%, which is higher than ideal, but sufficient for 2D IR experiments. In the expanding telescope, the pulses propagate through ~14 mm of CaF_2 which has a GVD of -107 fs^2/mm at 3 μm [100]. However, this is largely compensated for by the 1 mm thick Ge wafer which has a GVD of 1524 fs^2/mm at 3 μm [101]. The idler pulses are 40–45 fs long as measured by interferometric autocorrelation (Fig. 3.11 shows a typical measurement), which is described in detail in §3.4.4. This is consistent with Fourier limited Gaussian pulses with ~350 cm^{-1} of bandwidth.

3.2.4 Generation of Tunable Mid-IR Pulses

The method of IR generation detailed above does not readily extend to wavelengths longer than ~3.3 μm principally due to the lack of nonlinear crystals which can effectively phase-match the OPA process while simultaneously transmitting the light [102]. Therefore, we take the DFG approach to generate light between 3.5 and 7 μm.

We use a commercial optical parametric amplifier (*Topas Prime, Light Conversion*) to produce signal and idler pulses in the near-IR and subsequently use a homebuilt DFG setup to produce mid-IR pulses. The function of the optical parametric amplifier is described in detail in the user manual and will not be reproduced here beyond a brief description.

The optical parametric amplifier is pumped with ~1.2 mJ 800 nm pulses which is roughly split in a 1:10:200 ratio inside the amplifier. The small fraction is used to generate white light in a sapphire plate which is non-collinearly combined with the medium fraction in a BBO crystal in a pre-amplification stage. This generates a small amount of signal which is readily separated from the idler and pump beams due to the non-collinear geometry. The generated signal is then combined with the remainder of the pump pulse in a second BBO to generate intense signal and idler. The wavelength of the signal in the pre-amplification stage is tuned by delaying the white light relative to the 800 nm and changing the angle of the pre-amplification crystal. Similarly, the wavelength in the second amplification stage is tuned by adjusting the delay of the pre-amplified signal and crystal angle. Delays and crystal angles are software controlled and readily tuned on a day to day basis to optimize the DFG output.

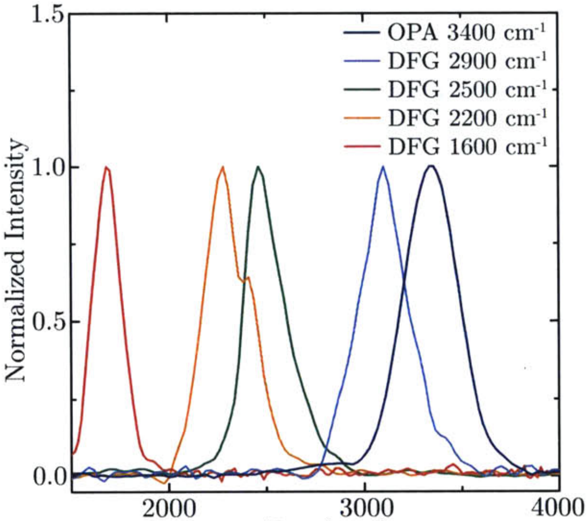

Figure 3.2: Example spectra produced by the OPA and DFG sources.

The optical parametric amplifier produces S-polarized signal at wavelengths ranging from 1200 to 1600 nm, which corresponds to P-polarized idler wavelengths ranging from 2500 to 1600 nm. The energy of the output signal is, on average, ~225 μJ per pulse but drops substantially at the degeneracy point (1600 nm). The energy of the idler is, on average, ~135 μJ per pulse, but also drops at either wavelength extreme. At its peak power, we observed a greater than 30% conversion efficiency from 800 nm to near-IR. The spectrum and pulse length of the near-IR signal and idler were not measured.

The near-IR pulses were then sent into a Michaelson interferometer using a dichroic beamsplitter (high reflection: 1.2-1.46 μm, high transmission: 1.64-2.1 μm) to separate and recombine the two pulses. The ability to adjust the timing between the two pulses (done here with a translation stage driven by a differential micrometer) has been shown to greatly improve the output power and stability of the DFG process [103]. The timed signal and idler are then sent into a silver gallium sulfide ($AgGaS_2$, AGS) crystal [104] which is both highly efficient at DFG and is more than 80% transparent in the mid-IR. The signal and idler are mixed in a type–II process (e.g. 4000 nm (e) = 1333 nm (e) − 1999 nm (o)) to give S-polarized mid-IR. Depending on the wavelength we wish to tune to, we use one of two AGS crystals. For pulses centered between 4 and 5 μm, we use a 1 mm thick AGS crystal (*Eksma*) cut at $\theta = 47.2°$, while for pulses centered between 5 and 7 μm we use a 1 mm thick AGS crystal (*Eksma*) cut at $\theta = 42.0°$. The crystals are titled to match the desired frequency; for example, the phase-matching angle for 4 μm is $\theta = 51.8°$.

The resulting mid-IR is passed through a 2.40 μm long-pass filter (*Edmund Optics*) to remove residual signal and idler; this optic also serves as a point of overlap for a visible HeNe tracer beam. (We note that the bandgap of pure germanium is not large enough to effectively filter the idler at most frequencies of the mid-IR.) The mid-IR beam is then expanded to a final beamsize of 6–8 mm in a Z-folded reflective telescope with a ROC = 2000 mm convex mirror and ROC = −2500 mm concave mirror.

The generated pulses vary considerably in power and pulse length depending on the center wavelength of the pulses; however, at all wavelengths, the stability was exceptional with an energy standard deviation of <1%. At 4 μm, pulses had an energy of ∼8 μJ and a pulses length of 40 fs (measured as described in §3.4.4), while at 6 μm, pulses had an energy of ∼5 μJ and a pulse length of 80 fs and the energy and pulse length varied more or less smoothly between these extremes.

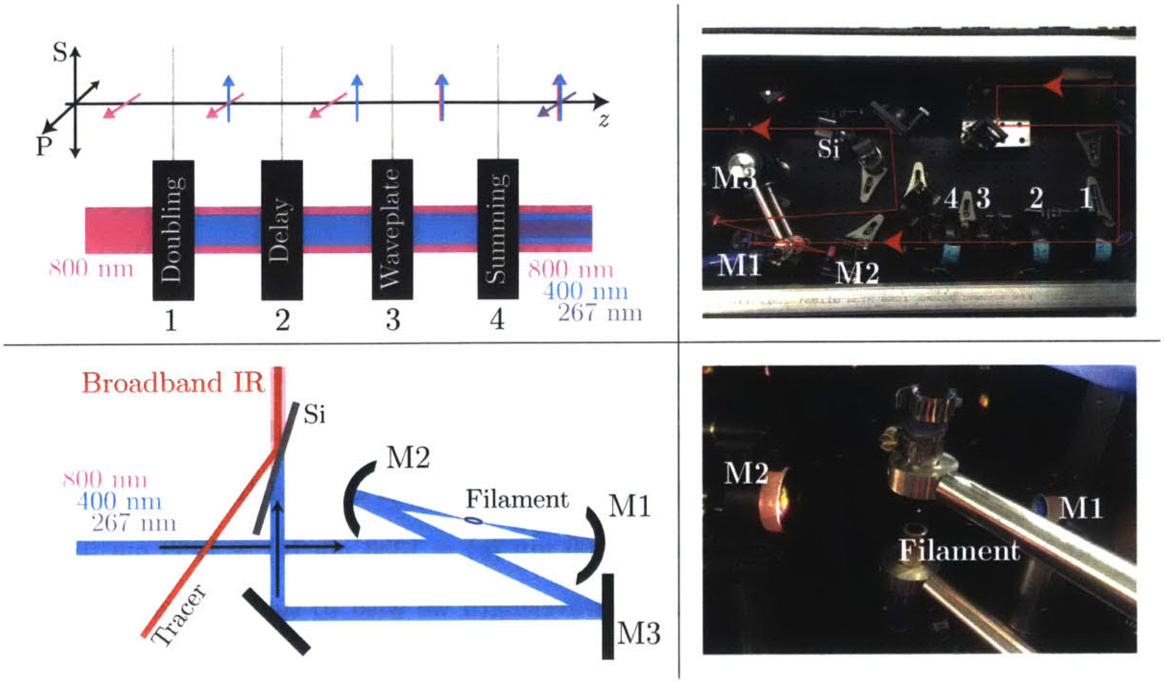
S
P
z
Doubling
Delay
Waveplate
Summing
800 nm
800 nm
400 nm
267 nm
1
2
3
4
Si
M3
4
3
2
1
M1
M2
Broadband IR
Si
M2
800 nm
400 nm
267 nm
Filament
M1
Tracer
M3
M2
M1
Filament

Figure 3.3: Schematic for broadband mid-IR continuum generation (left) photographs of the experimental setup (right).

3.3 Broadband Mid-IR Continuum

3.3.1 The Need for Broadband Pulses

In practice, phase matching limits the bandwidth one can achieve with OPA to typical values of less than 400 cm^{-1}. However, the exceptionally broad absorption resonances in hydrogen-bonding systems can easily have linewidths larger than this. For example, the O—H stretch in liquid H_2O has an absorption profile ranging 3000 to 3600 cm^{-1}. 2D IR Experiments employing pulses with bandwidths less than the width of the feature under study introduce distortions in the measured lineshape in addition to lacking the time-resolution necessary to measure the dephasing of such a broad line. Therefore, a useful study of a hydrogen-bonding system requires, at the very least, a probe which is broad enough to cover the necessary spectral range, although an ideal study would employ a broadband excitation pulse as well. To generate weak broadband probe pulses, we use a technique which borrows heavily on methods developed in the terahertz [105] and high-harmonic generation [106] communities which was extended to the mid-IR region of the spectrum [107]. By focusing visible light in various gases to generate a plasma, it is possible to create pulses whose spectra span the entire mid-IR which can serve as a probe in 2D IR experiments [108–111]. This has enabled us to study a wide variety of systems which could not be analyzed before, in addition to being able to probe vibrational correlations over large frequency ranges. Indeed, the advent of broadband probing has changed the way we carry out experiments.

At this time, the energy of the generated pulses is too weak to carry out a full broadband 2D IR experiment. As such, the filamentation technique seems to be falling out of favor in the literature, and it is being replaced by self-phase modulation techniques. The use of soft-glass ZBLAN fluoride fibers for producing large powers [112], chalcogenide fibers for producing large bandwidths [113, 114], and simple glasses for a combination of the two [115, 116] are becoming increasingly popular, and these are but a few examples to be sure. However, it is my hope that the techniques we have developed to manipulate and characterize broadband IR pulses generated via filamentation will pave the way to the generation of intense broadband IR pulses for performing fully broadband 2D IR measurements.

3.3.2 Generation of Broadband Mid-IR Pulses

To generate broadband mid-IR pulses via filamentation, we use the scheme of Ref. [108] in which pulses of 800 nm light and its first two harmonics are focused in a gas. At the focal point, the electric field is large enough to ionize the molecules resulting in a plasma. From this plasma, a broad spectrum is emitted, including a significant portion of the mid-IR. A schematic of the experimental layout is shown in Fig. 3.3.

In practice, 600 to 800 μJ of S-polarized 800 nm light is rotated on a 90° turning periscope before being frequency doubled in a 200 μm thick BBO crystal cut at 29.2° in a type–I process. Next, the copropagating 800 and 400 nm pulses are passed through a 2 mm thick BBO crystal cut at 66°; this crystal does not phase match any nonlinear processes. Rather, we take advantage of the birefringence of BBO to delay the 800 nm pulses relative to the 400 nm pulses since the two beams, being generated in a type–I process, are orthogonally polarized. This delay is used to precompensate for any temporal walkoff which occurs downstream. The 800 and 400 nm are aligned along the slow and fast axes respectively to compensate for a total of ~200 fs of walkoff. The time delay can be changed modestly (~8 fs/deg) by rotating the crystal in its mount and in practice, it is typically adjusted based on the overall broadband IR intensity. Next, the delayed 800 and 400 nm pulses are sent into a dual waveplate which is 6.5λ at 800 nm and 14λ at 400 nm, which rotates the P-polarized 800 nm light onto the S-polarized 400 nm light. Finally, the 800 and 400 nm are summed in yet another type–I process in a 100 μm thick BBO crystal cut at 44.6° to generate 267 nm light. After the crystal assembly, the 800, 400, and 267 nm pulses copropagate in time and space with polarizations of S, S, and P, respectively. Being entirely collinear and with no moving parts or separation of the beams at any point, the visible generation scheme is quite robust and shows very little drift over long periods of time. Figure 3.4 shows the visible and near-IR portions of the beam after each crystal stage with arbitrary normalization. The fiber spectrometer used to acquire these spectra was not sensitive to wavelengths below 400 nm, however spectral intensity is evident in the 400–550 nm range after passing through the summing crystal (Fig. 3.4, green curve). This presumably arises from self-phase modulation of the 400 nm pulse in the BBO.

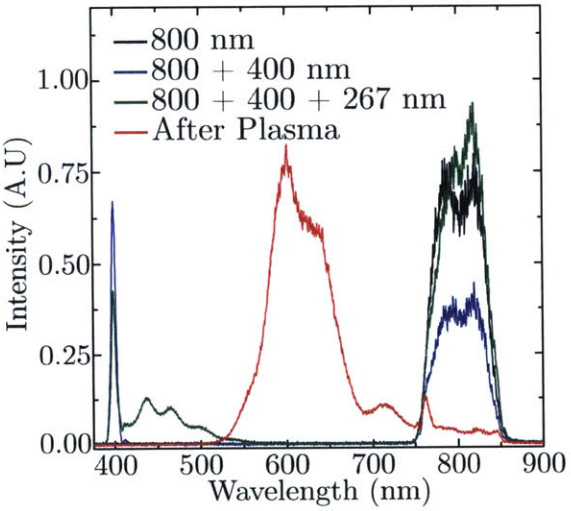

Figure 3.4: Spectra of the broadband IR pumping light as well as that radiated from the plasma.

Next, the 800, 400, and 267 nm pulses are focused into a gentle stream of nitrogen using a ROC = −10 cm dielectric mirror coated for high reflectivity at 800 and 400 nm, which is found to have good reflectivity at 267 nm as well. At the focal point, a plasma is generated, which radiates light across the entire electromagnetic spectrum. The visible spectrum of the light emitted from the plasma is shown as a red curve in Fig. 3.4 as well. The visible frequencies are indicative of how dramatic the frequency mixing really is. The emitted light is collected on an ROC = −10 cm aluminum mirror placed 10 cm away from the focusing mirror in an x−fold geometry. An x−fold angle of ~7°, the smallest achievable given the size of the optics, is used to minimize spherical aberration of the beam at the focal point. The use of a gentle stream of nitrogen instead of air or a static gas is found to both increase the intensity of the generated broadband by about 40% as well as increase its stability. This increase in stability is found whether air or nitrogen is flowed (though the increase in intensity is only observed with nitrogen), suggesting that this arises from having a fresh volume of gas to generate the plasma in. Indeed, studies have shown that the relaxation for a plasma can be longer than $1/f_{\text{rep}}$ [117]. If we assume a focal size of 10 μm (which is significantly larger than the diffraction limit) then the gas needs to flow at a velocity of 1 cm/s to ensure a fresh focal volume at each laser shot. This is easily achieved with modest flow rates given the small aperture of the nitrogen output tube. In practice, the plasma is generated between tubes hooked up to a nitrogen source and a vacuum source so that reaction products generated in the plasma are removed from the experimental setup. It was found that the vacuum is necessary to remove generated ozone which otherwise oxidizes the surrounding optics, including gold mirrors. The increase in intensity is not as well understood and seems to depend intimately on the composition of the gas the plasma is generated in. We never conducted a careful study of how the gas composition affects the generated pulses, although, it was found that using argon increases the intensity of the pulses enormously; however, this also comes with an enormous decrease in stability [118]. The general trends we find in going from air to nitrogen to argon are in agreement with studies conducted in a static gas cell at variable pressure [110].

The generated mid-IR is not collinear with the input visible pulses. Instead, it is typically displaced from the input pulses [111], but travels with some of the generated visible light. However, we find that the actual direction of the generation depends in an incredibly sensitive way on the input pulses. In particular, the mode and divergence of the 800 nm pulses seems to have the largest effect on the emission of the mid-IR. After reflection off a number of steering optics, the light generated in the plasma is filtered using a 400 μm thick high-resistivity silicon wafer. Having a band gap of 1.1 μm [119], the wafer filters the residual 800, 400, and 267 nm pulses as well as the visible which is generated in the filamentation process. Reflection losses are minimized by placing the silicon wafer at Brewster's angle which is about 73° relative to the wavevector of the light (the polarization of the generated broadband IR is discussed in §3.3.3). The mode quality of the generated mid-IR is found to be quite poor having an odd shape and several hotspots. Therefore, a spatial filter is employed and the broadband IR is focused through a 75 μm pinhole using a set of off-axis parabolic mirrors with an effective focal length of 101.6 mm. While these generally result in poorer focusing than lenses, they are necessary to avoid the chromatic aberration and dispersion which plagues such broad bandwidth mid-IR pulses. While 40% of the intensity is lost in this process, the focusing of the light in the experiment is significantly improved. The resulting beam is Gaussian, with a divergence which is easily tuned by adjusting the position of the pinhole relative to the collimating parabola. While it is not expected to have a serious impact on experiments, it is interesting to note that diffraction is such that the long wavelengths will diverge more rapidly than short ones and thus collimate at a larger size. For an octave spanning spectrum such as ours, this implies that the 3 μm portion of the beam will be half as large as the 6 μm portion. At 3500 cm^{-1}, the beam is collimated to a size of about 6 mm and so even at 6 μm, the 2"+ optics used in the experimental setup easily accommodate the entire beam.

While the generation of broadband mid-IR via filamentation of visible pulses is carried out in a relatively simple experimental setup, the physics which governs the actual generation process is incredibly complex. As such, the dominant generation mechanism is not well-understood, though it is thought that rectification by four-wave mixing or the plasma current generated by tunneling ionization are the strongest contenders [120,121]. It is worth noting, however, that a fair amount of success has been had in both the THz [122,123] and

IR [107,110,124,125] with four-wave mixing, though other studies found that plasma generation is a necessity [126]. In the first stages of the generation process, the electric field from the input pulses ionizes the molecules, which means that the force exerted by the peak electric field of the input pulses must exceed the Coulomb force that binds the electrons to the nitrogen molecules. The root-mean-square electric field of a pulse is given by

$$|E| = \left(\frac{2Z_0P_0}{Af_{\text{rep}}\tau_{\text{p}}} \right)^{1/2}, \tag{3.7}$$

where P_0 is the average power of the laser, A is the transverse area of the beam, τ_{p} is the pulse length, and $Z_0 = (c\epsilon_0)^{-1} = 376.73\ \Omega$ is the impedance of free space. At the focal point, if we assume 20 fs pulses with an average power of 0.7 W and a diameter of 10 μm, the field strength is 5.8 GV/cm which is certainly comparable to, if not more than, the field strength in typical molecules. Field intensities this large preclude a perturbative expansion in the field strength that converges quickly and as such has made a theoretical treatment of the process difficult. The situation is further complicated by the fact that once ionized, the charges experience the ponderomotive force which combined with the interparticle Coulomb interactions significantly alters the density of the plasma, especially along its longitudinal axis. Finally, the mechanism of recombination of charges is expected to play a significant role that depends intimately on its details. For example, whether the ionized particles are recombined by the laser pulse itself or whether they recombine once the pulses is gone will significantly change the way we understand the mechanism.

3.3.3 Characterization of Broadband Mid-IR Pulses

Characterization of the broadband mid-IR pulses is difficult since the tools that are generally used to characterize mid-IR pulses are not transferable to such broad spectra. Furthermore, the low intensity of the pulses makes nonlinear processes exceedingly weak. Our characterization is therefore by no means quantitative, but rather puts upper or lower bounds on the quantities we are typically interested in. A full characterization is necessary to understand the generation mechanism, carefully interpret experiments, and develop schemes to amplify the broadband mid-IR. However, it seems as though a full characterization is a doctoral thesis in and of itself.

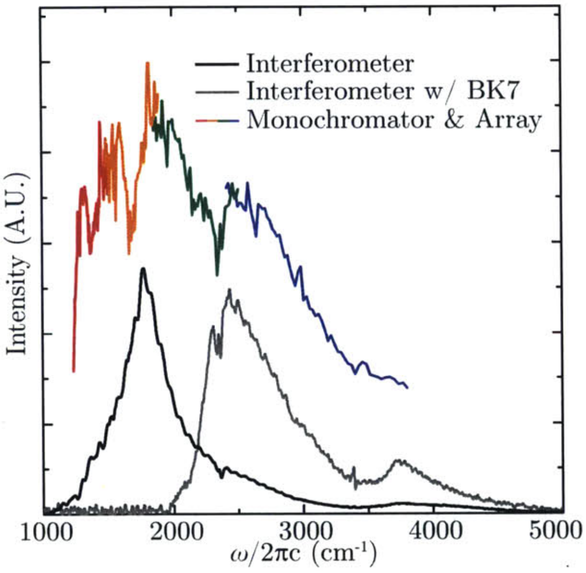

Figure 3.5: Spectra of the broadband IR source measured on different detectors.

Spectrum

The main challenge in measuring a spectrum lies in the detection. Photoconductive mercury-cadmium-telluride (MCT) detectors or photovoltaic indium-antimonide (InSb) detectors have a finite detection bandwidth determined by the doping of the semiconductor, and, in practice, the spectrum of the generated broadband pulses exceeds this bandwidth. Furthermore, grating-based measurements impose additional loss since the maximum efficiency of diffraction occurs only at the blaze wavelength of the grating at a particular order; therefore, the grating itself will change the shape of the spectrum. Finally, the finite dynamic range of a detector makes it difficult to measure parts of the spectrum with vastly different intensities, which can either be due to the actual generated spectrum or spectral modification imposed by the optics used.

With these challenges in mind, Fig. 3.5, shows the broadband mid-IR spectrum measured on a liquid nitrogen cooled 2x64 pixel MCT array detector (*MCT7128, Infrared Associates*) after being dispersed with a Czerny–Turner monochromator (*Triax 190, Horiba Jobin Yvon*) (colored curves) as well as the spectrum measured using a Mach-Zehnder interferometer (see §3.4) with (grey) and without (black) 1 mm of BK7 glass in the beampath. The monochromator-based spectrum must be measured for several grating angles since the 64-pixel stripe is not long enough to capture the entire spectrum; each of these angles is shown as a different color in Fig. 3.5. Furthermore, a long-pass filter with a wavelength cutoff of 4.5 μm must be placed before the monochromator aperture for certain grating positions to avoid the second order diffraction which overlaps with the first order diffraction when the spectrum spans more than an octave. The interferometer-based spectrum is measured differentially (see §3.4.5) on a pair of matched single-channel MCT detectors doped for a band gap of 11 μm. The interferometer spectrum without BK7 (Fig. 3.5, black curve) shows that the spectrum is peaked at 1775 cm^{-1}, but has a long tail to the blue, with some intensity at 4000 cm^{-1}. The spectrum is qualitatively similar to the response of an MCT detector. The cutoff at 1200 cm^{-1} on the red side is due to the onset of absorption of the CaF_2 optics used in the interferometer. Likewise, the detector response drops off on the blue side limiting the spectrum to less than ~5000 cm^{-1}. In order to see the higher frequencies more clearly, 1 mm of BK7 glass was used to strongly absorb light below ~2500 cm^{-1} (Fig. 3.5, gray curve). The monochromator spectrum, taken at four different grating angles dispersed with a 50 grooves/mm grating blazed at 6 μm, shows a fairly different spectrum which appears "flatter" than the interferometer spectrum. This is likely due to the combined spectral response of the grating as well as the MCT pixels. The range shown in Fig. 3.5 accurately represents the range accessible with the monochromator as the broadband intensity drops to undetectable levels beyond the shown limits.

In practice, we observed light at all frequencies with varying intensities. By eye, it is obvious that a large amount of visible is generated in the filamentation process (see also Fig. 3.4). In addition, while we have not measured it directly, the success of this method in generating low frequency pulses suggests that there is a significant amount of terahertz radiation being generated. Using various filters, we have determined that there is intensity at frequencies spanning the near-IR as well, from 2.5 to 1.1 μm. The quantitative measurement of the generated continuum is an interesting and challenging problem, requiring not only a detector which is sensitive from the terahertz to the ultraviolet, but one which possess sufficient dynamic range and whose spectral response is known precisely. In the future, significant effort will be needed to accurately measure the generated spectrum.

Pulse Energy and Stability

The pulse energy is rather low and so its measurement is difficult as well. Pulses generated via OPA or DFG are measured using a commercial pyroelectric detector which produces a voltage due to a change in temperature induced by the pulse. Its lower response limit is ~10 nJ/pulse. Since the broadband IR does not register a response on this detector, 10 nJ is an upper limit for the energy of the broadband pulses. In principle, it is possible to calibrate a single channel semiconductor detector using pulses generated by OPA and extrapolate to approximate the energy of the broadband mid-IR. That is, measure the voltage as a function of incident power and assume that the relation holds as the power approaches zero. This is difficult to do accurately however, since the measured voltage is highly dependent on the focusing of the light into the detector. Furthermore, the calibration would only hold at the frequency of the OPA pulse and would therefore not give a very accurate measure of the total pulse energy. However, it should be possible, in principle, to calibrate the energy at a particular frequency (e.g. by using a notch filter) and, if a sufficiently accurate spectrum is available, estimate the energy of the pulse. This goes to show, however, that the measurement of the energy and spectrum are linked.

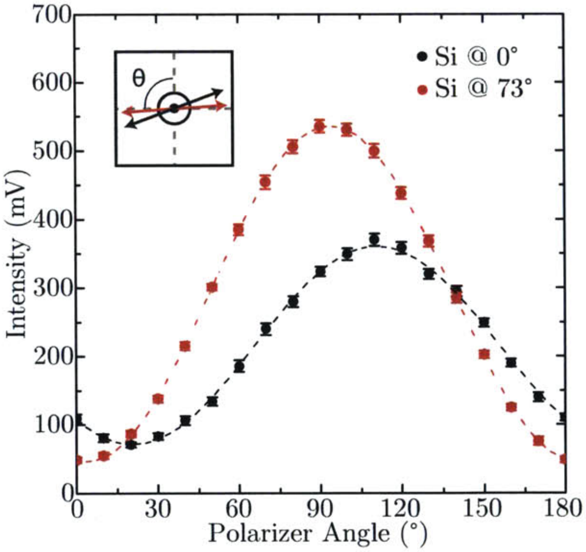

Figure 3.6: Polarization characteristics of the broadband IR source.

Given the method of generation, it is perhaps to be expected that the broadband mid-IR is not a particularly stable source. However, typically, intensity stabilities of ~2% can be achieved by optimizing the generation process. While this value is large compared to the DFG source described above, it is similar to values obtained with the 3 µm OPA source. Furthermore, shot-to-shot normalization of the broadband intensity is performed in all measurements, making the value of 2% workable. Since the broadband mid-IR generation mechanism is poorly understood, it is difficult to exactly determine how to stabilize the source. However, given that the efficiency of the generation relies on having ultrashort pulses, it stands to reason that stabilizing the relative phase between the carrier and the envelope of the pulses could dramatically improve stability.

Polarization

While the bandwidth of the generated pulses makes manipulating the polarization of the broadband difficult, measurement of its polarization is straightforward. In the generation process, vertically polarized ($\theta = 0°$) 800 and 400 nm and horizontally polarized ($\theta = 90°$) 267 nm are mixed and the generated broadband mid-IR continuum is linearly polarized with the semimajor electric field axis at an angle of $\theta = 110°$ with respect to vertical when viewed against the propagation direction of the beam (see Fig. 3.6). The eccentricity of the polarization is $e = 0.980$ ($e = 1$ corresponds to linearly polarized light and $e = 0$ corresponds to circular polarization). However, the polarization is altered significantly by the silicon wafer that filters the visible light. Having an index of refraction of 3.423 at 5 μm, Brewster's angle is 73.7° in silicon. This corresponds to a reflectance of 0.710 of S-polarized light and in that sense, the wafer acts to polarize the broadband along the P direction. After the wafer, the broadband is still linearly polarized (with an increased eccentricity of $e = 0.996$) with the semimajor axis at an angle of $\theta = 94°$ with respect to vertical (see Fig. 3.6, inset).

Normally, a waveplate and polarizer would be used to control the polarization and intensity of the mid-IR pulses. However, the broad bandwidth of the pulses means that a waveplate would not be able to rotate the polarization of the entire pulse; that is, the waveplate is only $\lambda/2$ thick at a particular frequency. Furthermore, adding transmissive CaF_2 optics would result in a dispersion in the broadband pulses which is far too large to cope with. Therefore, in experiments, the pulses are used as they are generated after the silicon wafer and an analyzing polarizer is placed after the sample to pick out the P-polarized component (90° with respect to vertical) of the broadband light and signal.

Pulse Length

Perhaps the most difficult pulse parameter to characterize is the pulse length. Typically, pulse characterization uses nonlinear frequency mixing to extract the pulse envelope and phase which together provide a full characterization of the temporal properties of the pulse [92, 127]. However, the low intensity and broad spectrum of the broadband precludes this method. Instead, we use non-resonant frequency-resolved optical gating (FROG) in silicon to characterize the broadband pulses. In this method, an intense 3 μm pulse induces a non-resonant response in a 400 μm thick silicon wafer which modifies the transmission of the broadband pulse. Multi-photon absorption of the 3 μm pump above the bandgap is avoided by lowering the 3 μm pulse power to 50 nJ/pulse. Since it is a non-resonant interaction the transmission is only modified when the 3 μm pulse is present (i.e. the response is instant) and therefore, the pump pulse serves as a 45 fs gate for the probe pulse. Scanning the time delay between the pump and the probe provides a measure of the arrival time of the different frequencies composing the pulse. In practice, the situation is not so simple since there exists an optical phonon mode at 520 cm^{-1} in pure silicon [128] which can

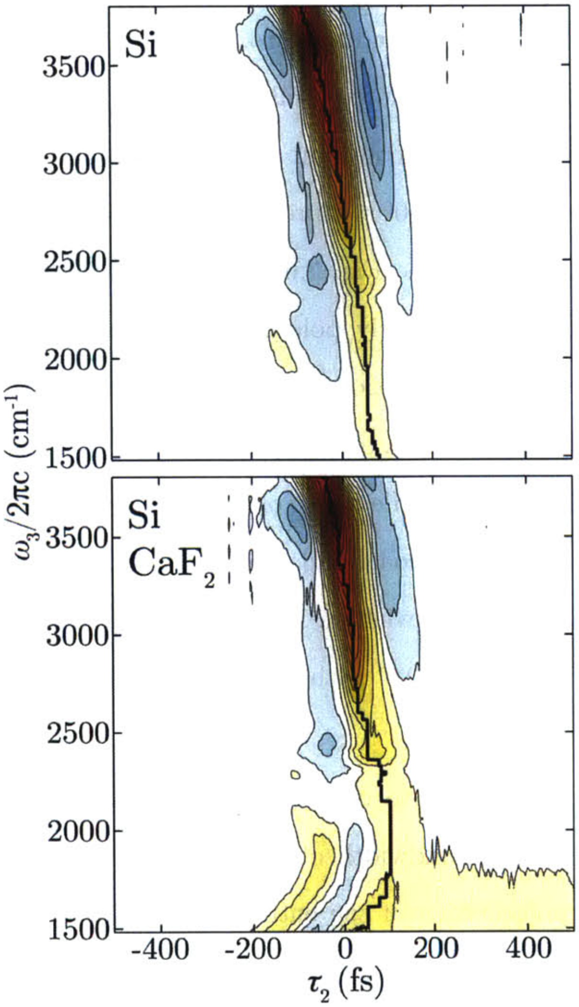

Figure 3.7: FROG measurements for 400 μm of Si (upper) and 400 μm of Si and 1 mm CaF_2 (lower) in the beampath.

be excited in a Raman-type process by the pump pulse. With impurities, the number of modes will increase. Excitation of these modes persist for times beyond the pulse length and so the response is not the idealized instantaneous response we desire. This type of response, however, has been characterized in the literature [129] and can still approximately be considered instantaneous.

In an actual experiment, the broadband IR pulse passes through 400 μm of silicon and 1 mm of CaF_2 before generating the signal in the sample. Any dispersion introduced by transmissive optics after the signal is generated is irrelevant since the spectrum is unaffected, and the phase of the signal and broadband will be changed in the same way such that the relative phase is unchanged. Therefore, when making a FROG measurement we insert a 1 mm thick CaF_2 window in the beam path to measure the pulse length of the broadband as the sample sees it. Figure 3.7 shows the results of the FROG measurement for Si (upper panel) and Si+CaF_2 (lower panel), where the change in transmission is plotted as a function of frequency and time between the pump and probe pulses. Additionally, we extract the arrival time as a function of frequency by taking the maximum of the response. These are overlayed with the data in Fig. 3.7 as a thick black line. Care must be taken when determining the maximum since the signal is modulated due to the phonon response. In this plot, an unchirped pulse would correspond to a straight vertical line; that is, all frequencies would arrive at the same time.

With only the silicon wafer in the beampath, the arrival time between 3 and 6 μm varies by about 130 fs. That is, the portion of the pulse at 1600 cm^{-1} arrives roughly 130 fs later than that at 3400 cm^{-1} corresponding to normal dispersion. If we assume the chirp is linear, we obtain a slope of 0.065 fs/ cm^{-1}; considering the 400 μm thickness of the silicon, this results in a measured GVD of 5417 fs^2/mm, which is significantly larger than the positive GVD of 346 fs^2/mm at 4.5 μm for mid-IR light in silicon [130]. Figure 3.8 shows the chirp of the broadband pulses (black line, left panel) compared to simulations. Using the Sellmeier equations for silicon [130], it is straightforward to calculate the result of a FROG experiment, assuming the broadband is a Fourier limited pulse when it is generated. The

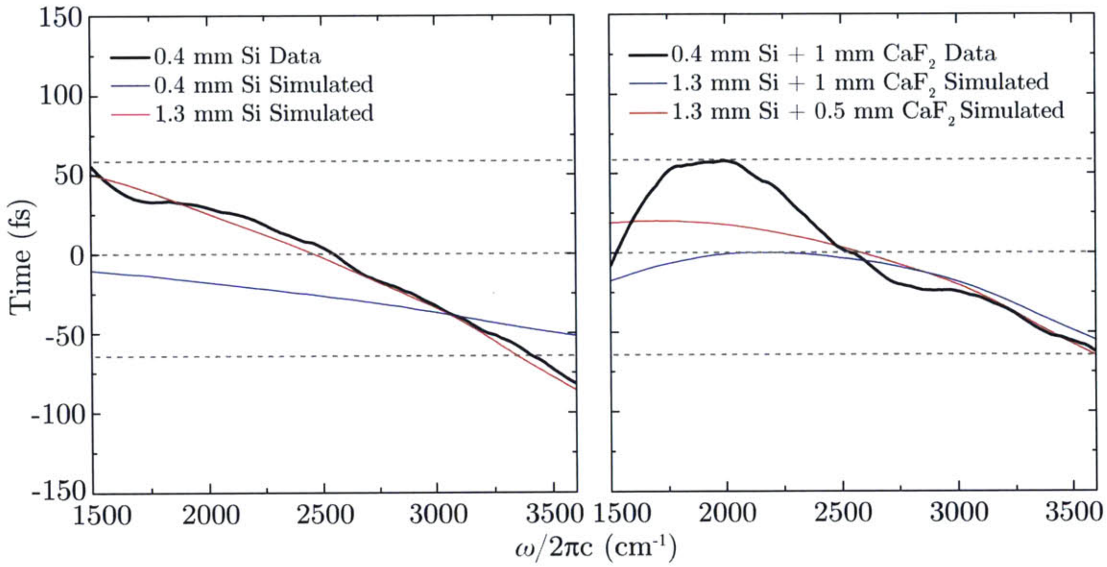

Figure 3.8: Calculations of the chirp for Si (left) and Si + CaF$_2$ (right) compared to experimental data.

blue line corresponds to 400 μm of silicon while the red line, which actually agrees with the measurement quite well, corresponds to 1.3 mm of silicon. The reason for this discrepancy is not clear. It is possible that the initial assumption of a Fourier limited pulse is false; however, it is necessary to consider that there is a large amount of light with a frequency greater than the bandgap of silicon incident on the wafer, and this will certainly modify the index of refraction. Finally, it is also necessary to consider that the FROG measurement is performed in silicon, and this may contribute somewhat to the measured chirp.

Adding a CaF$_2$ window, which has anomalous GVD in the mid-IR (-415 fs^2/mm at 4.5 μm [100]), results in red light travelling faster than blue light and actually compresses the broadband pulse somewhat at low frequencies (Fig. 3.8, right panel). However, the GVD in CaF$_2$ is highly nonlinear so that the arrival time actually curves significantly. This results in 6 μm arriving about 50 fs later than 3 μm, while 5 μm arrives 50 fs after that. Using the Sellmeier equations for CaF$_2$ [100], the full phase after propagation through 1.3 mm of Si and 1 mm of CaF$_2$ and 1.3 mm of Si and 500 μm of CaF$_2$ is calculated and shown in Fig. 3.8, right panel, as the blue and red lines, respectively. The agreement for CaF$_2$ is somewhat better if we assume a thinner window than the wafer, but is nowhere near as accurate as for silicon. This likely stems from neglecting the imaginary part of the index of refraction which becomes significant at low frequencies due to the broad resonance at 10 μm. In experiments, we do no further correction for the dispersion, mostly due to the fact that it is not possible to find a material that will precisely compensate the highly nonlinear dispersion we measure [131]. Rather, we keep the dispersion in mind when analyzing experimental data. A more careful (and perhaps more clever) measurement of pulse length will not only be useful for characterization of the experiment, but may give insight into the generation mechanism.

3.4 The Mach-Zehnder Interferometer

3.4.1 Principles of Operation

Performing 2D IR measurements in the pump-probe geometry [68,69], requires focusing an intense, collinear pulse pair, separated by a time interval τ_1, into a sample. Therefore, the generated OPA and DFG pulses must be split into a pair with an experimentally controlled time delay separating them. This is accomplished in practice through the use of a Mach-Zehnder interferometer (MZI) [132]. While simple in principle, the MZI is the workhorse of the pump-probe geometry 2D IR experiment, and it serves a multitude of different purposes; as such, it merits a detailed discussion. In a MZI, illustrated schematically in Fig. 3.9, a beamsplitter, nominally splits a beam into two equal-intensity beams that travel different paths before being recombined on an ideally identical beamsplitter. The path length traveled by one of the beams is engineered to be variable, so that an accurate time delay can be imparted between the two beams. The phase shift imparted is $\omega\tau_1 = \omega\Delta x/c$, where Δx is the optical path-length difference between the two arms. The linear phase shift imparted on one of the beams is equivalent to a displacement in time by an amount τ_1. When the pulses overlap in time (near $\tau_1 = 0$) they interfere to produce an interferogram which deviates the output power from the sum of the intensity of the two pulses.

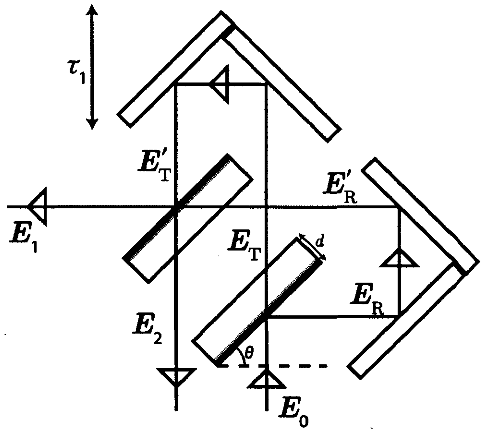

Figure 3.9: Schematic illustration of a MZI.

In calculating the output of a MZI, we will make a number of approximations, which simplify the expressions somewhat without sacrificing important details. To that end, we will assume that the two beamsplitters have the same reflectance, transmittance, index of refraction, and thickness. Taking these into account change the output by a multiplicative factor or constant phase, but the latter can easily be corrected for. On the other hand, there are two approximations which we make which are somewhat more severe. The first is that of perfect alignment, such that the beam does not deviate as the variable path is changed. This imparts a phase on the output which can be corrected for provided that the misalignment is not too dramatic. The other is the neglecting of weak reflections off the non-beamsplitter-coated sides of the beamsplitter; this gives rise to so-called ghost pulses which can be the bane of one's existence if they are mistaken for the intense reflection off the beamsplitter-coated side. The result of including ghost pulses is extra interferograms appearing in τ_1 separated from the main interferogram at $\tau_1 = 0$ by the amount of time it takes for the pulses to travel through the beamsplitters. Typically this is on the order of 10 ps, and provided the signal is measured for the entire τ_1 range, it is usually easy to determine which interferogram corresponds to $\tau_1 = 0$.

At the first beamsplitter, the input pulse $\boldsymbol{E}_0$ is split into two which we denote $\boldsymbol{E}_\mathrm{R}$ and $\boldsymbol{E}_\mathrm{T}$ for the reflected and transmitted pulses, respectively. After the beamsplitter, in addition to reflection and transmission coefficients, the transmitted field will have an additional phase for propagating through the beamsplitter which is given by $kn\ell = knd\sin\theta$, where d is the thickness of the beamsplitter, θ its angle relative to the input beam and k and n are the beam's wavevector and beamsplitter's index of refraction, respectively. Keeping in mind that there is an additional π phase shift upon reflection from a rarer medium off of a denser medium, the reflected and transmitted fields are

$$\boldsymbol{E}_{\mathrm{R}}(t) = -r\boldsymbol{E}_0(t) \tag{3.8a}$$

$$\boldsymbol{E}_{\mathrm{T}}(t) = t\boldsymbol{E}_0(t)\mathrm{e}^{\mathrm{i}kn\ell}, \tag{3.8b}$$

where we have not shown the spatial dependence of the fields explicitly, and where we have introduced the reflection and transmission coefficients, r and t, respectively. We recall that the reflectance and transmittance of a beamsplitter refer to the power and not the field amplitude; therefore, for a 50:50 beamsplitter, we have $r = 1/\sqrt{2}$. The reflected and transmitted beams travel the length of the arms of the interferometer, and before recombining on the second beamsplitter, each has accrued a phase of kL where L is the length of the interferometer path. However, the transmitted beam is shifted in time by an amount τ_1 due to the difference in path length; the field of the reflected and transmitted beams before the second beamsplitter are given by

$$\boldsymbol{E}'_{\mathrm{R}}(t) = -r\boldsymbol{E}_0(t)\mathrm{e}^{\mathrm{i}kL} \tag{3.9a}$$

$$\boldsymbol{E}'_{\mathrm{T}}(t) = t\boldsymbol{E}_0(t-\tau_1)\mathrm{e}^{\mathrm{i}k(n\ell+L)}. \tag{3.9b}$$

Upon recombination on the second beamsplitter, each beam is further split into a reflected and transmitted beam. To ensure that the initially reflected beam, which did not pass through the first beamsplitter, travels through the same amount of material as the initially transmitted beam (and thus accrues the same phase) the second beamsplitter must be oriented such that the reflected beam travels through the substrate before being split. Since each beam is split further into two, there are two outputs of the MZI, labeled 1 and 2 in Fig. 3.9.

We begin by considering output 1, in which the initially reflected beam is transmitted and the initially transmitted beam is reflected. The electric field at this output is given by

$$\boldsymbol{E}_1 = t\boldsymbol{E}'_{\mathrm{R}}\mathrm{e}^{\mathrm{i}kn\ell} - r\boldsymbol{E}'_{\mathrm{T}}(t) = -rt(\boldsymbol{E}_0(t) + \boldsymbol{E}_0(t-\tau_1))\mathrm{e}^{\mathrm{i}k(n\ell+L)}. \tag{3.10}$$

Since each pulse is reflected and transmitted once in this output, the two output pulses have the same intensity, given by r^2t^2. For 50:50 beamsplitters, the product r^2t^2 is 1/4. While the field is the relevant quantity for calculating the 2D IR response, the quantity measured in the lab is the intensity of the field which is given by the time integral of the absolute magnitude squared of the field. For output 1, the intensity is given by

$$I_1(\tau_1) = 2r^2t^2I_0 + 2r^2t^2\frac{c}{4\pi}\Re\int_{-\infty}^{\infty} \mathrm{d}t\boldsymbol{E}_0(t)\cdot\boldsymbol{E}_0^*(t-\tau_1), \tag{3.11}$$

where I_0 is the intensity of the input pulse. Thus the output, as a function of the path length difference, consists of a constant offset determined by the intensity of the input beam and the reflectance and transmittance of the beamsplitters and a term which is the autocorrelation of the pulse. This term is zero for large τ_1 since the pulses are not overlapped, and is large and oscillatory when τ_1 is close to zero giving rise to the pulse interferogram. In §3.4.2, we detail how this is used to extract the pulse spectrum and phase on the interferogram.

We now consider the second output in which the initially reflected pulse is reflected once again and the initially transmitted pulse is again transmitted. Now, we keep in mind that the reflected pulse is reflecting off of a rarer medium so that there is no π phase shift and that the reflected pulse actually passes through the beamsplitter twice. The total field at the second output is therefore

$$\boldsymbol{E}_2 = t\boldsymbol{E}'_{\mathrm{T}}\mathrm{e}^{\mathrm{i}kn\ell} + r\boldsymbol{E}'_{\mathrm{R}}(t)\mathrm{e}^{\mathrm{i}kn2\ell} = (t^2\boldsymbol{E}_0(t-\tau_1) - r^2\boldsymbol{E}_0(t))\mathrm{e}^{\mathrm{i}k(n2\ell+L)}. \tag{3.12}$$

In this output, the two pulses produced have different intensities if the beamsplitters are not precisely 50:50 and there is a π phase shift between the two. This output is therefore not suitable for 2D IR experiments. However, there is utility in the intensity of this output, which is given by

$$I_2(\tau_1) = (r^4+t^4)I_0 - 2r^2t^2\frac{c}{4\pi}\Re\int_{-\infty}^{\infty} dt\boldsymbol{E}_0(t)\cdot\boldsymbol{E}_0^*(t-\tau_1). \tag{3.13}$$

The interferogram is the same as that of the first output with a π phase shift. Therefore, while this output cannot be used for 2D IR experiments, it can be used to monitor the interferogram in real time during such an experiment. Summing the intensity of the two outputs gives $I_1(\tau_1) + I_2(\tau_1) = (r^2 + t^2)^2 I_0 = I_0$ as the case must be in order for energy to be conserved.

In practice, IR pump pulses are split and recombined by 50:50 CaF_2 beamsplitters (*Thin Film Labs*) or ZnSe beamsplitters (*Rocky Mountain Instrument Co.*) for center wavelengths of 3–5 μm and 4–7 μm, respectively. The beamsplitter coated sides provide an average reflectance of 50% ± 5% at 45° for S-polarized light. The other sides have an anti-reflective coating ($R_{\text{avg}} < 2.5\%$) in order to minimize ghost pulses. Path length differences are generated by translating two mirrors placed on a computer-controlled, motorized translation stage (*Aerotech ANT-25L*, 1 nm resolution (6.67 as), ±100 nm reproducibility (0.67 fs)) which can easily produce reproducible path length differences of < 1 fs. Given that the shortest wavelength we typically use for excitation is 3 μm, this corresponds to at least $\lambda/10$. The output used for experiments (output 1 in the schematic above), is passed through a tunable $\lambda/2$ zero-order waveplate (*Alphalas*, MgF_2 on CaF_2) and wire-grid polarizer (*Molectron*, CaF_2) to allow for polarization control of the pump pulses. The other output is focused into a room-temperature mid-IR detector (*Electro-Optical Systems*) to collect the interferogram during experiments. A mechanical chopper (*New Focus*) frequency-locked to the laser chops the fixed arm of the interferometer at half the laser repetition rate (500 Hz).

Alignment of the MZI generally proceeds in three steps: 1) alignment of the variable arm, 2) rough overlap of the tracer in the near-field and the far-field, and 3) fine alignment based on the observed spatial interference in the tracer beam. In the first step, it is necessary that the beam does not translate as the translation stage moves. Even though the stage is only moved ~150 μm in a typical experiment, even a small displacement of the beam can result in significant distortions. The tracer beam of the fixed arm is then overlapped with that of the variable arm using mirrors in the fixed arm as well as the combining beamsplitter. Once the beams are sufficiently well-overlapped, a spatial interference pattern is evident in the tracer beam. Since the spatial interference goes as $\cos(\Delta \boldsymbol{k} \cdot \boldsymbol{x})$, where $\Delta \boldsymbol{k}$ is the difference in wavevectors between the two beams, the goal is to ensure the fringes are as far apart as possible since perfect alignment corresponds to $\Delta \boldsymbol{k} = 0$. This is accomplished by tweaking the combining beamsplitter until the fringes are spaced by a distance larger than the beam itself.

3.4.2 Extraction of Spectrum and Phase: The Mertz Method

Other than generating a pulse pair for 2D IR experiments, the MZI is used to measure the spectrum of the excitation pulses and phase of the interferogram using the detector at output 2. The offset off Eq. 3.13 is a zero-frequency contribution to the spectrum and can therefore be neglected. In practice, this is done by subtracting the mean off the interferogram, since the second term in Eq. 3.13 has zero mean. We therefore, only need to consider the autocorrelation of the input pulse. Ignoring the $-2r^2t^2c/4\pi$ amplitude factor, we can rewrite the second term in Eq. 3.13 by expressing the fields in terms of their Fourier transforms. The result is

$$I_2(\tau_1) = \int_{-\infty}^{\infty} \frac{\mathrm{d}\omega}{2\pi} \left|\tilde{E}(\omega)\right|^2 \cos(\omega\tau_1). \tag{3.14}$$

This shows that the interferogram for the idealized situation described above is a symmetric function of τ_1, which means that its Fourier transform is a purely real function which is simply given by

$$\tilde{I}_2(\omega_1) = \frac{1}{2}\left(\left|\tilde{E}(\omega_1)\right|^2 + \left|\tilde{E}(-\omega_1)\right|^2\right). \tag{3.15}$$

Therefore, the Fourier transform of the interferogram provides us with the power spectrum of the input pulse. Normally, we neglect the negative frequency components and report the spectrum with a normalized amplitude.

Errors in timing, misalignments, beamsplitter imperfections, and laser and electrical noise, however, cause the interferogram to not be a symmetric function of τ_1 and thus its Fourier transform is not the power spectrum of the input field. The simplest such phase error is an error in timing such that τ_1 is replaced by $\tau_1 - \tau_x$ in Eq. 3.14, and the Fourier transformed interferogram comes with a linear phase of $\omega_1\tau_x$. Errors other than timing, result in more complex phases on the transform of the interferogram. Extracting the phase from the Fourier transformed symmetric interferogram (which is first apodized with a Hann window and zero-padded to twice the number of points), $\tilde{I}_2(\omega_1)$, is simple, as it is given by

$$\tan\phi(\omega_1) = \frac{\Im\tilde{I}_2}{\Re\tilde{I}_2}. \tag{3.16}$$

Then, the Fourier transformed interferogram can be made purely real, as it should be, by multiply by the complex conjugate of the phase factor to give the power spectrum

$$\left|\tilde{E}(\omega_1)\right|^2 = \tilde{I}_2(\omega_1)\mathrm{e}^{-\mathrm{i}\phi(\omega_1)}. \tag{3.17}$$

In reality, collection of a symmetric interferogram (or two-sided interferogram) is redundant since both positive and negative τ_1 values contain the same information. So normally, a so-called one-sided interferogram is collected in which data is collected asymmetrically about $\tau_1 = 0$ (e.g. see Fig. 3.10, left panel). This asymmetry results in an additional phase which must be corrected for in a somewhat careful manner.

This is accomplished by the Mertz method [133]. In the Mertz method, we first obtain a low-resolution phase $\phi_{\mathrm{LR}}(\omega_1)$, by generating a two-sided interferogram by truncating the one-sided interferogram symmetrically about $\tau_1 = 0$. Then, $\phi_{\mathrm{LR}}(\omega_1)$ is calculated as in Eq. 3.16. Assuming that the asymmetry in the interferogram is weak, that is, the errors mentioned above are not too large, then the phase is a slowly varying function of frequency and $\phi_{\mathrm{LR}}(\omega_1)$ is a good approximation to the actual phase. It is interpolated to the same number of points as the full phase. We then correct the full Fourier transformed one-sided interferogram (apodized with an asymmetric Hann window and zero-padded to twice the number of points) with $\phi_{\mathrm{LR}}(\omega_1)$ as in Eq. 3.17. The corrected transformed interferogram is then transformed back to the time domain, where the data for $\tau_1 < 0$ is discarded. Finally, the one-sided interferogram is symmetrized and transformed to yield the correct spectrum

$\left|\tilde{E}(\omega_1)\right|^2$. A representative spectrum (black line) and phase (red line) of the 3 μm OPA source, as measured at output 2 of the MZI and corrected by the Mertz method, is shown in the right panel of Fig. 3.10.

It, at first, may seem a bit extreme to go to such lengths to accurately extract the spectrum and phase, but these serve two important purposes. Firstly, and most significantly, the phase error on the spectrum as measured in the interferometer is, of course, also in the pulses which generate the 2D IR signal. As such, the 2D IR signal, which is inherently an asymmetric function of τ_1, has an additional phase, $\phi_{\mathrm{LR}}(\omega_1)$, on it that must be corrected for. Therefore, as τ_1 is scanned in an experiment, the second output of the interferometer is monitored and $I_2(1)$ is collected so that $\phi_{\mathrm{LR}}(\omega_1)$ can be measured. The 2D IR signal is then corrected by the Mertz method as described above to give a spectrum free of phase errors. Secondly, features in the 2D IR spectrum will be weighted by the intensity of the pump spectrum in ω_1. Simultaneous collection of the pump spectrum during an experiment allows us to correct for this in post-processing.

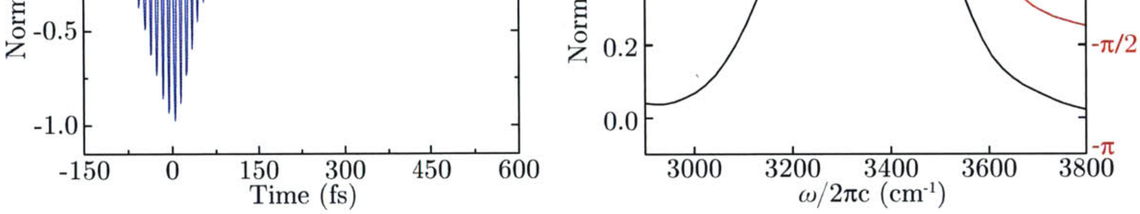

Figure 3.10: Typical one-sided interferogram collected with an MZI (left) and the corresponding spectrum and phase (right).

3.4.3 Continuous Scanning of τ_1

In a typical 2D IR experiment, the generated signal is dispersed on an MCT array and measured at each pixel as a function of τ_1. The signal is then Fourier transformed along the τ_1 axis to generate the excitation axis ω_1. The fact that a Fourier transform will be performed requires equal step sizes to be taken (in principle, it is possible to measure in unequal step sizes and then interpolate, but this is found to introduce artifacts in the data). Then, for a given step in time $\Delta\tau$ and number of points N collected, the frequency resolution (in wavenumbers) of the signal, $\Delta\tilde{\omega}$, is [132]

$$\Delta\tilde{\omega} = \frac{1}{c\Delta\tau N}. \tag{3.18}$$

In practice, there are two ways to measure the signal as a function of τ_1. In the "step-scan" mode the delay stage is stepped incrementally in steps of $\Delta x = c\Delta\tau/2$ (the factor of 1/2 arises because of the double pass geometry of the stages). Once the step is complete, the signal is averaged over a certain number of samples (laser shots). Typically, between 500 and 5000 laser shots are averaged depending on the intensity of the signal being measured and the stability of the laser system at the time of data collection. It is worth noting that only half the shots actually carry signal with them due to the chopping of the fixed arm of the interferometer. After a typical step of $\Delta\tau = 2$ fs (300 nm) the stage takes about 250 ms to settle, corresponding to 250 wasted laser shots. Step-scan is therefore not the most efficient mode of operation.

In the "continuous scanning" mode, the stage is not stepped but rather it is moved at constant velocity and each laser shot is collected as the stage moves [134]. For a given stage velocity v, data is collected at time steps corresponding to

$$\Delta\tau = \frac{2v}{cf_{\text{rep}}}, \tag{3.19}$$

where f_{rep} is the repetition frequency of the laser. From Eq. 3.18, we see that the resolution is given by

$$\Delta\tilde{\omega} = \frac{f_{\text{rep}}}{2vN}. \tag{3.20}$$

In practice, the resolution and the number of points are specified and the velocity is determined based on that input. The collection is limited by the buffer of the electronics integrating the output of the MCT array and so $N \leq 10^4$. In addition, care must be taken to not sweep the stage too quickly, or the signal will have changed substantially between adjacent pulses and the k_1–k_3 background will not subtract between chopped and unchopped laser shots. We therefore limit the velocity of the stage in an experiment to be $v \leq \lambda f_{\text{rep}}/100$, where λ is the shortest wavelength of interest in the experiment. This ensures that the stage does not move by more than $\lambda/100$ between laser shots. This limits the resolution in our experiments to

$$\Delta\tilde{\omega} \geq \frac{100}{2\lambda N}, \tag{3.21}$$

which for $\lambda = 3$ μm and $N = 10^4$, $\Delta\tilde{\omega} \geq 16.67$ cm^{-1}. This limit is not present in step-scan mode since the step size and the number of data points can be changed without constraint (barring the Nyquist frequency), and this is one of the advantages of step-scanning over continuous scanning.

The advantage of the continuous-scanning mode lies in the time it takes to collect a spectrum. Suppose a step-scan spectrum is collected with 250 data points and 2000 samples per point. In this case, there is about 63 seconds of stage settling time and at first, it seems that this is the amount of time that will be saved in the continuous scanning mode. However, this makes the assumption that it is necessary to collect 250x2000 = 5x10^5 points via averaging in the continuous scanning mode; this is not the case. Collecting that many points in step scanning would mean that the 2D IR spectrum is collected over the course of 500 s, neglecting settling time. On the other hand, in continuous scanning, many 2D IR spectra are collected, but each is collected over the course of 10 s. This reduces the effect that long term drift of the laser power has on the signal to noise ratio. That is, over the course of 10 s, the laser power is roughly constant; however, over the course of 500 s, the laser power will drift, and in step-scanning, this drift will be incorporated into the data. In practice, we find that it is sufficient to collect less than a fifth of the number of points in continuous scanning compared to step-scanning to obtain a similar quality of data.

Implementation of continuous scanning is only possible if the Mertz method is used to correct the phase of the spectrum. From scan to scan, the exact same time points are not sampled and so the phase changes slightly between scans. It is therefore necessary to apply the Mertz correction to each scan individually and average phase-corrected data. The improvement in acquisition time over step-scanning is substantial and has enable the collection of enormous amounts of data. In principle, it ought to be possible to speed up the acquisition further. For example, currently scanning is unidirectional with a rapid return to the initial position; bidirectional scanning should decrease acquisition time. Also, if it were possible to collect high fidelity data without chopping one of the pulses, this would both decrease the acquisition time (since then, the time step is only limited by the Nyquist frequency) and remove the resolution constraint (Eq. 3.21). On the other hand, it is possible to remove the resolution constraint by increasing the buffer capacity of the multi-channel integrator.

3.4.4 Interferometric Autocorrelation

The output of the MZI provides us with a convenient method to measure the temporal envelope of a pulse, which we use to measure the length of pulses generated via OPA. Essentially, the pulse pair generated is sent into a nonlinear crystal cut to phase-match the second harmonic generation process. As the timing between the pulses is scanned, there will be second harmonic generated with one interaction occurring with each of the pulses when the pulses are overlapped temporally. By monitoring this, it is possible to extract the pulse envelope [92].

Neglecting proportionality factors, when the pulse pair is sent into the crystal, the generated electric field is

$$E^{(2)}(t;\tau_1) \propto E^2(t;\tau_1) = E^2(t) + E^2(t-\tau_1) + 2E(t)E(t-\tau_1). \tag{3.22}$$

In Eq. 3.22, the third term depends on the product of the two pulse fields, and it is this term that allows us to measure the pulse envelope. The measured intensity of the radiated field is then

$$I^{(2)}(\tau_1) = \int_{-\infty}^{\infty} \mathrm{d}t \left[2E^4(t) + 6E^2(t)E^2(t-\tau_1) + 4E^3(t)(E(t-\tau_1) + E(t+\tau_1))\right] \tag{3.23}$$

The first term is independent of τ_1, and it provides a constant background intensity I_0. The second term is the intensity autocorrelation and the final term is essentially the second harmonic generated from the interference between the initial pulses; both of these terms report on the pulse length, albeit the second in a more straightforward manner. At $\tau_1 = 0$, all of the terms are identical, and the result is $8I_0$; this value turns out to be highly sensitive to the alignment of the interferometer and provides a good metric for the accuracy of the measurement.

Writing the fields in the Fourier domain, the second term is given by

$$\int \mathrm{d}tE^2(t)E^2(t-\tau_1) = \iiint \frac{\mathrm{d}\omega_1\mathrm{d}\omega_2\mathrm{d}\omega_3}{(2\pi)^3}\tilde{E}(\omega_1)\tilde{E}(\omega_2)\tilde{E}(\omega_3)\tilde{E}^*(\omega_1+\omega_2+\omega_3)\mathrm{e}^{-\mathrm{i}(\omega_1+\omega_2)\tau_1} \tag{3.24}$$

Typically, the spectra of the fields are peaked at some ω_0 and fall of rapidly away from this frequency. Therefore, for the integral to be non-zero, it is necessary that all the integration variables are close to ω_0 or $-\omega_0$ and that $\omega_1 + \omega_2 + \omega_3 \approx \pm\omega_0$. This means that the frequency in the exponential will either be close to zero if $\omega_1 \approx -\omega_2$ or close to $2\omega_0$ if $\omega_1 \approx \omega_2$. Therefore, as a function of τ_1, this term oscillates at either the second harmonic or is static. In a similar vein, it is possible to show that the third term in Eq. 3.23, oscillates at the fundamental frequency ω_0. Upon measuring $I^{(2)}(\tau_1)$, we may subtract off the static offset. Subsequent Fourier transformation then allows us to isolate the second term (peaks at 0 and $2\omega_0$) or the third term (at ω_0). Windowing the $2\omega_0$ part of the spectrum and then inverse Fourier transforming essentially gives the amplitude autocorrelation function, and it is equivalent to a noncollinear measurement. For Gaussian pulses, the width of the amplitude autocorrelation function is related to the width of the envelope function by a factor of $\sqrt{2}$.

Figure 3.11 shows an example interferomentric autocorrelation (upper panel) and the corresponding pulse envelope (lower panel) of the 3 μm OPA source. The fundamental frequency has been filtered out in the experiment so that the upper plot is a true normalized representation of the quantity in Eq. 3.23. The wings on either side of the central burst are a reflection of a nonlinear phase (i.e. chirp) on the pulse. The fact that the peak does not reach a numerical value of 8 reflects misalignments in the experiment or inefficient frequency doubling to a certain extent. Sloping baselines, due to chirp, can also reduce the magnitude of the interferometric autocorrelation. Filtering the interferometic autorrelation in the Fourier domain, between the frequencies of 5500 and 8000 cm^{-1} provides access to the autocorrelation of the pulse envelop, Eq. 3.24. A fit (dashed red line) shows that the pulse is not quite Gaussian, and these deviations are reflected in the low-frequency background of the autocorrelation. In partic-

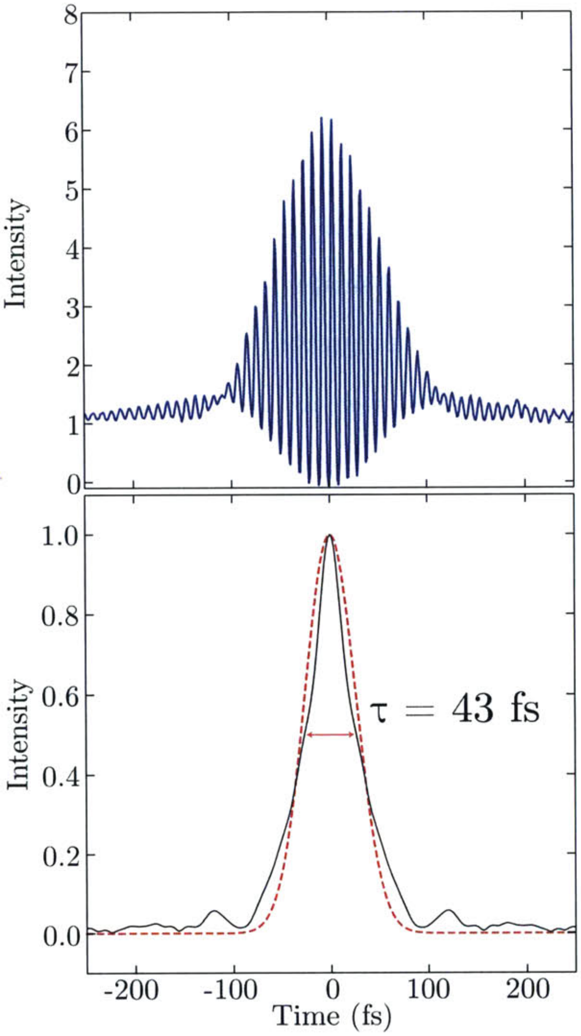

Figure 3.11: Interferometric autocorrelation (upper) and corresponding pulse envelope (lower) of the 3 μm source.

ular, the central part of the pulse is narrower, but has broader wings in time. Nonetheless, the Gaussian fit gives a full width of 43 fs at half maximum, which is consistent with the breadth of the spectrum measured.

3.4.5 Fourier Detection of Nonlinear Signal

Using a monochromator and array for detection has a number of disadvantages when measuring broadband spectra. Notably, to collect an entire spectrum, it is necessary to collect the spectrum multiple times at different grating angles. In addition, gratings are lossy and only about 30% of the light actually makes it to the detector. Thus only a small amount of light actually falls on each pixel making the measurement susceptible to electrical noise. On the practical side, mid-IR arrays are expensive, costing close to \$100k and require large multi-channel integrator systems.

One way to remedy these disadvantages is to measure the pulses in the time domain. In the boxcar geometry, where the nonlinear signal is emitted in a background-free direction [68], this is straightforward: the signal is scanned against a local oscillator and the resulting oscillations are a direct measure of the nonlinear spectrum. In the pump–probe geometry, however, it is not so simple since the field is radiated in the same direction as k_3. That is, the signal field is naturally heterodyned with the probe pulse giving a total field of

$$E(t;\tau_1,\tau_2) = E_{k_3}(t) + E_{\mathrm{S}}(t,\tau_1,\tau_2), \tag{3.25}$$

and there is no possibility to change the relative time delay between them.

One possibility is to measure the spectrum of the total field as is done in an FTIR spectrometer and extract the nonlinear spectrum from that. Essentially, this involves sending the total field into a MZI and scanning a third delay, τ_{F}. However, this will take much longer in principle than dispersing the signal since a new dimension must be scanned. Therefore, to minimize acquisition time, it is necessary to have good signal to noise in the experiment. One method to do this is to use differential detection. To that end, we measure both outputs of the MZI using a pair of balanced MCT single channel detectors and generate the sum and difference signals.

$$I_-(\tau_\mathrm{F}) = I_1 - I_2 = 4r^2t^2\frac{c}{4\pi}\Re\int_{-\infty}^{\infty}\mathrm{d}t\boldsymbol{E}(t)\cdot\boldsymbol{E}^*(t-\tau_\mathrm{F}) \tag{3.26a}$$

$$I_+(\tau_\mathrm{F}) = I_1 + I_2 = I_0 \tag{3.26b}$$

The difference signal suppresses correlated noise in I_1 and I_2 and dramatically improves the quality of the measured interferogram. The interferometric broadband IR spectra shown in Fig. 3.5 was measured in this manner. The sum signal is, in principle, the intensity of the total field and this gives a measure for how well-aligned the interferometer is and how well-balanced the detectors are. It would seem as though the ratio of I_-/I_+ should further suppress noise by cancelling fluctuations in total intensity. In practice, this does not seem to make much difference suggesting that this is not a prominent source of noise. If the beamsplitters are not identical, this mixes the sum and difference signals somewhat.

Given the total field of Eq. 3.25, the measured difference signal (neglecting multiplicative constants) is

$$I_-(\tau_\mathrm{F};\tau_1,\tau_2) = \int \mathrm{d}t\,\left(E_{k_3}(t)E^*_{k_3}(t-\tau_\mathrm{F}) + 2\Re E_{k_3}(t)E^*_\mathrm{S}(t-\tau_\mathrm{F};\tau_1,\tau_2) + E_\mathrm{S}(t)E^*_\mathrm{S}(t-\tau_\mathrm{F})\right). \tag{3.27}$$

The third term is the product of two nonlinear fields and so is typically neglected relative to the other two. The second term is the term of interest, that is, it is linear in the signal field, while the first term is simply the interferogram of the probe pulse. By Fourier transformation in τ_F (of course, correcting the phase via the Mertz method) it is in principle possible to extract the nonlinear signal.

As of yet, however, we have unfortunately been unable to attain the signal to noise ratio necessary to collect reliable nonlinear signal. However, it should be noted that in all of our previous implementations, τ_F, was scanned for fixed values of τ_1. This is not ideal since both the signal and probe interferogram oscillate as a function of τ_F and it is difficult to extract a small AC signal on top of a large AC signal. It is my belief that this method can be improved substantially by scanning τ_1 for fixed values of τ_F so that we measure a small AC signal on top of a large DC signal (since the probe interferogram does not oscillate in τ_1). Furthermore, it seems as though electrical noise is a significant contributor to the total noise and so this scheme would benefit dramatically from low-noise electronics. Finally, it should be noted that the low dynamic range of the MCT detectors is also a serious challenge since the spectrum of the broadband IR is far from flat; the Fourier detection method would benefit greatly from spectral shaping of the probe before being used in the experiment.

3.5 Acquisition and Processing of 2D IR Spectra

3.5.1 Sample Area and Detection

After the spatial filter that cleans the mode of the broadband mid-IR, it is reflected off a 50:50 KBr beamsplitter. The transmitted portion is dispersed onto one stripe of the two-stripe MCT array. This serves as a reference in experiments to correct for fluctuations in spectral intensity. The reflected portion is steered towards the sample which is held on a 3-axis translation stage between two 90° off-axis parabolic (OAP) mirrors. Meanwhile, pump pulses coming out of the MZI are also steered towards the sample area. Before the pump pulses and the probe are focused by the first OAP mirror, they are both reflected off a common mirror. At this point, the alignment is such that the two beams are propagating parallel to each other and vertically displaced by 1". The first OAP mirror (with an effective focal length of 101.6 mm) focuses the two beams in the sample which are then recollimated by the second OAP mirror with the same effective focal length. Immediately after passing through the sample, the probe is sent through an analyzing polarizer to preclude any chance that the polarization of the generated signal is scrambled. This is particularly important in anisotropy measurements (§3.5.2). The pump pulses are usually blocked with an iris shortly after the sample.

At the sample focal point, close to 100% of the broadband mid-IR can be transmitted through a 100 μm pinhole, which is essentially a result of re-imaging the 75 μm spatial filter. On the other hand, pump pulses can transmit anywhere between 50-80% through a 100 μm pinhole depending on the mode being generated by the OPA. To relate these transmission values to a beam size, we assume that the beam is in the TEM_{00} Gaussian mode and use the standard definition [135] for the intensity of a collimated beam or a beam at its focus (that is, a beam with an infinite radius of curvature)

$$I(r) = I_0 \frac{2}{\pi w^2} \mathrm{e}^{-\frac{r^2}{w^2/2}}, \tag{3.28}$$

where w is the beamwaist and is simply the radius at which the field falls to an amplitude of e^{-1}. Correspondingly, the intensity falls to a value of e^{-1} at a radius of $w/\sqrt{2}$. It is straightforward to show that the intensity transmission T through an aperture of size r_c is related to the beamwaist by

$$\frac{1}{w} = \frac{1}{r_c}\sqrt{\frac{1}{2}\ln\left(\frac{1}{1-T}\right)}. \tag{3.29}$$

Therefore, a transmission of 50–80% through a 100 μm pinhole corresponds to beamwaists between 110 and 170 μm, though the errorbars for determining the spot size grow rapidly if a large amount of light is not transmitted through the pinhole. This rather poor focusing at the sample is a result of the poor mode of the light generated in the OPA process as well as misalignments in parabolas.

In principle, the focusing can be improved by introducing a spatial filter for the pump pulses as well. We note that at $T = 0.86466$, $w = r_c$, and this is the number that is reported in previous sections when discussing beam size. The largest pulse energies we typically achieve at the sample position vary between 1.5 and 2.5 μJ. This corresponds to an average pulse electric field strength of 7 MV/cm which is well below typical molecular electric fields, and the excitation pulse really can be considered a weak perturbation.

After the signal is generated, it is focused into a monochromator which images the dispersed spectrum onto the other stripe of the MCT array, generating the ω_3 axis. The monochromator is equipped with three diffraction gratings with 150, 75, and 50 grooves/mm, blazed at wavelengths of 4, 4, and 6 µm, respectively. In the experiments described in this thesis, only the latter two gratings were used. Gratings are calibrated at various angles by dispersing pump light emitted by the MZI, scattered off of a pinhole, on the array and interferometrically scanning the time delay between pulses. Each pixel then oscillates at a frequency corresponding to the center wavelength of the light dispersed on it. The oscillations are Fourier transformed and the center wavelength as a function of pixel number is fit to a line. (It is important to use the wavelength and not frequency since the grating dispersion is linear in wavelength.) These calibrations for grating angles are found to not change significantly (1–3 cm^{-1} changes) over long periods of time, even if the monochromator is moved.

Samples are held in a homemade liquid cell which consists of two CaF_2 windows sandwiching a spacer; the liquid is held between the windows in the pocket formed by the spacer. Depending on the sample under study, the spacer can range from a thickness of 6 to 125 µm and is made of either Mylar, Teflon, or Delrin. For samples of high optical density no spacer is used and the liquid is sandwiched between the windows.

The temperature of the sample can be controlled by flowing water through the jacket which holds the cell. The temperature is maintained with a cooling circulator (*Huber Ministat 125*) which can nominally reach circulating temperatures ranging from -25 to 95°C if a mixture of water and ethylene glycol is used as the circulating fluid. The temperature of the cell is monitored by affixing to it a K-type thermocouple which is brought into thermal contact with the cell with silver compound thermal paste. At temperatures close to room temperature, the temperature of the cell is almost identical to the temperature of the circulating bath. At either temperature extreme (-25° or 95°), however, the magnitude of the temperature of the cell is less than the magnitude of the temperature of the bath.

3.5.2 Transient Absorption Spectroscopy

In a transient absorption (TA) experiment, an intense pump pulse is followed by a broadband probe pulse after a time delay, τ_2. Data is collected as a function of τ_2, typically with unequally spaced data points chosen to sample the dynamics of interest. In this experiment, there is no need for a MZI to generate a pulse pair and typically the MZI is held at a fixed value of $\tau_1 = 0$. When the chopper is open, the intensity of the pump which reaches the sample is I_0; however, when the chopper is closed, it is $I_0/4$. Therefore, in this configuration, the signal is somewhat less than if no MZI was present and the entire pulse was chopped, which is usually what is done. For ease of use however, the MZI is usually kept in place with τ_1 fixed at 0 fs. With the chopper open, the quantity measured is

$$\begin{aligned} I_{\text{open}}(\tau_2, \omega_3) &= \int \mathrm{d}t \left(E_{k_3}(t; \omega_3) + E^{(1)}(t; \omega_3) + E^{(3)}(t; \tau_1 = 0, \tau_2, \omega_3) \right)^2 \\ &\approx I_{k_3}(\omega_3) + 2S^{(1)}(\omega_3) + 2S^{(\text{TA})}(\tau_2, \omega_3), \end{aligned} \tag{3.30}$$

where I_{k_3} is the spectral intensity of the probe, $S^{(1)}$ is the linear absorption signal, and $S^{(TA)}$ is the transient absorption signal. The ω_3 axis is generated as described in detail in §2.5.1. The homodyne terms have been dropped since they are typically much less intense than terms involving the probe field. On the other hand, with the chopper closed (i.e. removing half of the pump field), the signal measured is

$$I_{\text{closed}}(\tau_2, \omega_3) \approx I_{k_3}(\omega_3) + 2S^{(1)}(\omega_3) + S^{(\text{TA})}(\tau_2, \omega_3), \tag{3.31}$$

The quantity reported in experiments is the referenced change in absorption

$$\Delta\text{OD} = -\log_{10}\left(\frac{I_{\text{open}}}{R_{\text{open}}} \cdot \frac{R_{\text{closed}}}{I_{\text{closed}}} \right). \tag{3.32}$$

The R quantities in Eq. 3.32 correspond to the spectral intensity of the reference. The broadband is not chopped and so R is the same whether open or closed except for noise between different laser shots. Therefore, multiplicative noise in I is divided out by the reference and the mean R terms average to 1. Using the expressions for I_{open} and I_{closed} above, and assuming the TA signal is small compared to the probe intensity and linear signal, we obtain

$$\Delta\mathrm{OD} = -\log_{10}\left(1 + \frac{S^{(\mathrm{TA})}(\tau_2,\omega_3)}{I_{k_3}(\omega_3) + 2S^{(1)}(\omega_3) + S^{(\mathrm{TA})}(\tau_2,\omega_3)}\right), \tag{3.33}$$

which for small signals is

$$\Delta\mathrm{OD} \approx -\frac{1}{2.303}\frac{S^{(\mathrm{TA})}(\tau_2,\omega_3)}{I_{k_3}(\omega_3) + 2S^{(1)}(\omega_3)}. \tag{3.34}$$

Normally, we assume that the linear absorption term is small relative to the spectral intensity of the probe pulse as well. However, this is only true of samples with a low optical density. If this is not the case, the linear absorption will result in distortions of the TA signal. It is possible to correct for the linear absorption of samples [136,137]; however, this is not done in the data presented in this thesis. If we assume that the linear absorption is small, then the change in absorption is proportional to the third-order susceptibility integrated against the spectral intensity of the pump (this is because $S^{(\mathrm{TA})}$ is essentially linear in I_{k_3}.)

To collect a broadband TA spectrum, it is necessary to collect spectra at several grating angles and "stitch" them together in postprocessing. This is done by ensuring that the data is collected for grating angles where there are at least ~100 cm^{-1} of overlapping bandwidth between grating positions. In the region of overlap then, each curve (for each value of τ_2) is given an offset which brings the overlap region to a common average value. The two curves are then averaged in this region which generates a smooth continuation between the two grating positions. This is repeated for however many grating positions were collected. The stitching process is not foolproof, however, and sometimes it may introduce small kinks or offsets in the data. It is therefore imperative that subtle features are analyzed in the unstitched data and that the stitched is analyzed carefully.

Transient absorption anisotropy measurements are inherently difficult as they are a double-difference spectroscopy. Ideally, the ZZZZ and ZZYY signals are collected simultaneously; however, our current version of the experiment does not easily allow this and the two signals must be collected separately. Changing the polarization of the pump field is not as benign as it seems: timing, pointing, and intensity change as well. To remedy this, the waveplate following the MZI is set to rotate the pump field to a polarization of 45° and the polarizer, set to 0 or 90°, filters the Z or Y component of the pump. This results in a 50% loss in intensity; however, the upside is that the waveplate can be adjusted so that the Z and Y components have the same intensity, and, furthermore, the pointing of the pump does not change substantially. Timing remains an issue, however, and the timing between the pump and the probe must be adjusted each time the polarizer is changed.

3.5.3 The 2D IR Experiment

The 2D IR experiment proceeds in a similar manner to the TA experiment, except that data is collected for fixed values of τ_2 while continuously scanning τ_1 (§3.4.3). The experiments described in this thesis are done in the pump-probe geometry [68,69], where $\boldsymbol{k}_1 = \boldsymbol{k}_2$. This results in the signal being emitted in the same direction as the probe pulse, $\boldsymbol{k}_3$, which also serves to heterodyne the signal. Since the pulses are no longer fixed to $\tau_1 = 0$, there are more signals which can be generated in this experiment. Neglecting homodyne signals, it is straightforward to show, that with the chopper open and all three pulses impinging on the sample, the measured signal is

$$I_{\text{open}} \approx I_{k_3}(\omega_3) + 2S^{(1)}(\omega_3) + 2S^{(\text{TA})}(\tau_2, \omega_3) + 2S^{(\text{TA})}(\tau_1 + \tau_2, \omega_3) + 2S^{(\text{2D})}(\tau_1, \tau_2, \omega_3), \quad (3.35)$$

where $S^{(\text{2D})}$ is the 2D IR signal. The first TA signal comes from the $(\boldsymbol{k}_2, \boldsymbol{k}_3)$ TA, while the second TA signal is the $(\boldsymbol{k}_1, \boldsymbol{k}_3)$ TA. In the 2D IR experiment, the fixed arm of the MZI is chopped, which corresponds to the second pulse. Therefore, the signal when the chopper is closed is given by

$$I_{\text{closed}} \approx I_{k_3}(\omega_3) + 2S^{(1)}(\omega_3) + 2S^{(\text{TA})}(\tau_1 + \tau_2, \omega_3). \quad (3.36)$$

The reason for chopping the fixed arm of the interferometer is now clear: since the I_{closed} term contains the TA signal between $\boldsymbol{k}_1$ and $\boldsymbol{k}_3$ (which depends on τ_1), it will drop out of the measured change in absorption. This is important since the TA signal between $\boldsymbol{k}_1$ and $\boldsymbol{k}_3$ would change as a function of τ_1. The change in absorption is identical to that measured in the TA experiment (Eq. 3.32) and, making the same assumptions as in the calculation for the TA experiment, is given by

$$\Delta\text{OD} \approx -\frac{1}{2.303}\frac{2S^{(\text{TA})}(\tau_2,\omega_3) + 2S^{(\text{2D})}(\tau_1,\tau_2,\omega_3)}{I_{k_3}(\omega_3) + 2S^{(1)}(\omega_3)}. \tag{3.37}$$

Again, the same considerations for the linear absorption apply in this case.

At first, it seems like the presence of $S^{(\text{TA})}$ in the measured signal may pose a problem. That is, there is a TA signal between the $\boldsymbol{k}_2$ and $\boldsymbol{k}_3$ which rides on top of the 2D IR signal. However, this signal is independent of τ_1 and, as such, as a function of τ_1, provides a constant offset to the 2D IR signal. The 2D IR signal oscillates about zero, so in practice it is sufficient to subtract the mean of the measured signal from the measured signal for each value of ω_3. This is also a useful way of obtaining the TA spectrum simultaneously with the 2D IR spectrum.

The 2D IR signal is then Fourier transformed in τ_1. The phase of the 2D IR spectrum is corrected using the Mertz method (§3.4.2), using the phase spectrum measured from the interferogram of the pump pulses. Then, to a decent approximation (essentially assuming pulses are short compared to the response of the sample), the 2D IR signal is given by

$$S^{(\text{2D})}(\omega_1,\tau_2,\omega_3) \approx I_{\text{P}}(\omega_1)I_{k_3}(\omega_3)\chi^{(3)}(\omega_1,\tau_2,\omega_3) \tag{3.38}$$

where I_{P} is the spectral intensity of the pump pulses. The denominator of Eq. 3.37 then removes the dependence on the spectral intensity of the probe if the linear absorption is small enough. Furthermore, the spectral intensity of the pump can simply be divided out as well. Since this approximation is only true if the pump pulses are much shorter than the response of the system, the division by the pump spectrum only works if the pump spectrum is much broader than the linewidth of the feature under study. If it is not, the correction is formally incorrect, but does an approximate job of correcting the 2D IR signal. In practice, the pump spectrum is measured simultaneously with the 2D IR signal by monitoring the interferogram produced by the MZI. Therefore it is straightforward to perform the correction after data collection. As in the case of the TA signal, to collect a full 2D IR surface it is necessary to collect the data at multiple grating angles and stitch the data together in postprocessing. This is done in the same way as in the TA spectrum, except that ω_3 slices are stitched for each ω_1 value. This results in a 2D IR spectrum which is narrow in ω_1 reflecting the bandwidth of the pump pulses and broad in ω_3, reflecting the bandwidth of the probe pulses.

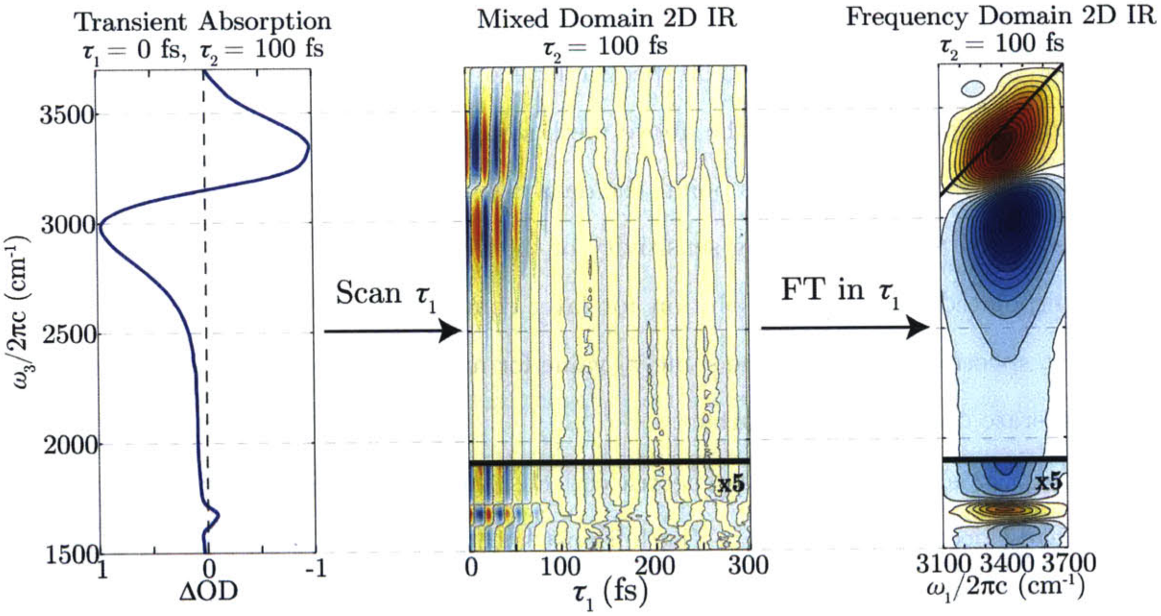

Figure 3.12: Representative TA and 2D IR spectra illustrating data collection and processing steps.

Processing the data proceeds in a straightforward manner, and it is done on the fly as data is collected. From the pump interferogram and set frequency resolution, the phase spectrum of the interferogram is calculated; this serves to correct both the pump interferogram and the 2D IR signal. From the pump interferogram, the pump spectrum is measured. For each value of τ_1, the mean of the 2D IR signal is subtracted to remove the $(\boldsymbol{k}_2, \boldsymbol{k}_3)$ TA signal. The signal is transformed to the frequency domain (after zero-padding and windowing), phase-corrected using the Mertz method, and transformed back to the time domain. At this point, the negative time data points are discarded since these do not contain the desired 2D IR signal, but contain double-quantum coherence signal. The signal is again Fourier transformed, resulting in a 2D IR spectrum.

The result of any single continuous-scanning run is rather noisy, so it is necessary to collect and average between 10 and 60 spectra depending on the desired signal to noise ratio. Each surface is processed using the above method, and the resulting spectra are averaged in the frequency domain. At this point, the data is smoothed in ω_3 over 3 pixels to remove noise associated with the varying sensitivity of the pixels in the MCT array. The data is then interpolated to 1 cm^{-1} resolution for later convenience during analysis. Finally, if necessary, spectra collected at the same τ_2 value for multiple grating angles are stitched in ω_3 to generate one continuous surface.

Figure 3.12 shows the various spectra collected in a typical experiment on H_2O that have already been stitched in ω_3. The leftmost spectrum is the TA spectrum taken at a value of 100 fs, $S^{(\text{TA})}(\tau_2 = 100 \text{ fs}, \omega_3)$. We note that by the properties of Fourier transforms, this is equal to $S^{(\text{2D})}(\tau_1 = 0 \text{ fs}, \tau_2 = 100 \text{ fs}, \omega_3)$. By scanning τ_1, we generate the mixed domain 2D IR signal, $S^{(\text{2D})}(\tau_1, \tau_2 = 100 \text{ fs}, \omega_3)$, which is shown in the center panel of Fig. 3.12. This is representative of the raw data collected after subtraction of the $(\boldsymbol{k}_2, \boldsymbol{k}_3)$ TA signal, $S^{(\text{TA})}(\tau_2 = 100 \text{ fs}, \omega_3)$ (keeping in mind that the $(\boldsymbol{k}_1, \boldsymbol{k}_3)$ TA signal is removed by mechanically chopping the fixed arm of the interferometer). Finally, Fourier transforming the mixed domain 2D IR signal with the methods detailed above results in the 2D IR surface.

3.5.4 Scatter

So far the effect of scatter on the signal has not been considered. In any sample, some amount of light from $\boldsymbol{k}_1$ and $\boldsymbol{k}_2$ is scattered towards the detector due to inhomogeneity in the sample. Scatter can arise for a large number of reasons (e.g. dirty or scratched sample windows, particulate in the solution, back reflection off the windows) and often, it is difficult or impossible to determine the source. Most of the time, scatter can be reduced by taking care to use high quality windows that have been cleaned meticulously or solutions free of dust or bubbles. However, in cases where the sample is solid, scatter is unavoidable unless solids of high optical quality can be made. In these cases, polarizing the pump beams perpendicular to the analyzing polarizer (ZZYY) helps significantly, but the inherent randomness of the scattering process often scrambles the polarization of the pump beams and a certain amount of leak-through still occurs.

In a highly scattering sample, there are, in effect, six fields which make it to the detector: the probe field, $\boldsymbol{k}_3$, (which we assume contains the linear signal field), the 2D IR signal field, the $\boldsymbol{k}_1$–$\boldsymbol{k}_3$ TA signal field, the $\boldsymbol{k}_2$–$\boldsymbol{k}_3$ TA signal field, scatter from $\boldsymbol{k}_1$, and scatter from $\boldsymbol{k}_2$. Typically, the probe field is the largest contributor to the measured intensity by far, but for highly scattering samples, the scatter from $\boldsymbol{k}_1$ and $\boldsymbol{k}_2$ can be significant as well. The measured intensity will therefore have contributions from 36 terms. Not all of these terms are significant however, and they can usually be dealt with depending on whether a TA or 2D IR experiment is performed. The measured intensity, including scatter is given by

$$\begin{aligned}
I_{\mathrm{TOT}} =& 2S^{(\mathrm{2D})}(\tau_1,\tau_2) + A_{12}(\tau_1) \\
&+2S^{(\mathrm{TA})}(\tau_1+\tau_2) + A_{13}(\tau_1+\tau_2) + B_{1,13}(\tau_1+\tau_2) \\
&+2S^{(\mathrm{TA})}(\tau_2) + A_{23}(\tau_2) + B_{2,2D}(\tau_2) + B_{2,23}(\tau_2) \\
&+B_{1,2D}(\tau_1+\tau_2) + B_{2,13}(\tau_1+\tau_2) + B_{1,23}(\tau_1+\tau_2) \\
&+C_{2D,13}(\tau_1,\tau_2) + C_{2D,23}(\tau_1,\tau_2) + C_{13,23}(\tau_1,\tau_2) \\
&+I_{\mathrm{2D}} + I_{13} + I_{23} + I_3 + I_1^{\mathrm{S}} + I_2^{\mathrm{S}}.
\end{aligned} \tag{3.39}$$

Terms designated with an S are signal terms as defined above. Terms designated with an A are scattering terms between the different input fields

$$A_{ij} = 2\int \mathrm{d}t\boldsymbol{E}_i(t)\cdot\boldsymbol{E}_j(t). \tag{3.40}$$

Terms designated with a B are interference terms between the pump fields and the signal fields

$$B_{ij} = 2\int \mathrm{d}t\boldsymbol{E}_i(t)\cdot\boldsymbol{E}_j^{(3)}(t). \tag{3.41}$$

In our notation, $B_{1,13}$, for example, corresponds to the interference between the scatter of the pump pulse and the $\boldsymbol{k}_1$–$\boldsymbol{k}_3$ TA signal. These terms look like the "normal" signal terms, except that they are heterodyned by scattered fields and not $\boldsymbol{k}_3$. Terms designated with a C are interference terms between different signal fields

$$C_{ij} = 2\int dt\boldsymbol{E}_i^{(3)}(t)\cdot\boldsymbol{E}_j^{(3)}(t). \tag{3.42}$$

Generally, these terms are small; that is, they are the same order of magnitude as the homodyne signals.

In a 2D IR experiment, terms on the second line of Eq. 3.39 are removed by chopping. In addition, terms on the third and sixth lines are static in τ_1 and therefore removed in the Fourier transformation process. The C terms on the fifth line are small and may safely be neglected if we are neglecting nonlinear signal homodyne terms. The remaining terms in the 2D IR experiment are therefore

$$I_{\mathrm{TOT}}^{(2\mathrm{D})} = 2S^{(2\mathrm{D})}(\tau_1,\tau_2) + A_{12}(\tau_1) + B_{1,2D}(\tau_1+\tau_2) + B_{2,13}(\tau_1+\tau_2) + B_{1,23}(\tau_1+\tau_2). \tag{3.43}$$

The largest unwanted term in this expression is the A term, the scatter between the two pump fields. This can be minimized by blocking the probe pulse (removing all terms except the A term) and translating the sample to a spot where A_{12} is a minimum. Minimizing this term necessarily minimizes the B terms as well, although it is possible to rigorously remove these terms by modulating τ_2 (see below).

In a TA experiment, τ_1 is fixed at zero and there is no Fourier transform to be done. This results in a larger number of terms contributing to the total measured intensity. Keeping in mind that $\boldsymbol{k}_1$ and $\boldsymbol{k}_2$ are the same pulse, that τ_1 is zero, and which terms are small, the total measured signal is

$$I_{\mathrm{TOT}}^{(\mathrm{TA})} = 6S^{(\mathrm{TA})}(\tau_2) + 2A_{13}(\tau_2) + 6B_{1,13}(\tau_2) + 2I_1^{\mathrm{S}}. \tag{3.44}$$

The last term is static in time, and can be corrected for by measuring a background at values of $\tau_2 \ll 0$, where the first three terms are zero. There is, however, no simple way to correct for the scattering A and B terms. Again, it is possible to try and find a part of the sample where scattering is small, but usually the A term is incredibly large because it arises from heterodyning scatter with the probe pulse. For highly scattering samples, it is therefore sometimes advantageous to collect 2D IR surfaces and integrate over ω_1 to extract the TA spectrum.

Clever methods of suppressing scatter in TA experiments have been used in the literature previously. The A and B terms oscillate with the frequency of the pump light as a function of τ_2 while the S term is usually an exponential, which is centered at zero frequency. Therefore, it is, in principle, possible to filter the signal in the Fourier domain. However, this suffers from the drawback that for rapid decays, the filtering process can drastically alter the decay timescale. Since TA is most often used to measures timescales, this is undesirable. Another method of suppressing the A and B terms is to rapidly modulate τ_2 over the range of a period of the pump light during an experiment and average over the scatter. This has been successfully implemented with pump pulses with a bandwidth of ~100 cm^{-1} [138]. However, for broader pulses, such as those produced by our OPA, the suppression is only effective over a narrow range of frequencies. So while scatter is indeed suppressed by modulating τ_2, it is not sufficient to collect TA spectra of highly scattering samples.

Chapter 4

Intermolecular Hydrogen Bonds Probed with Broadband 2D IR

4.1 The Significance of NMA

4.1.1 The Smallest Protein

Since the seminal papers by Mizushima [139] and Miyazawa [140] on the normal vibrations of the amide unit, N-methylacetamide (NMA) has been one of the IR spectroscopy community's favorite molecules. Indeed, the number of experimental and computational studies on the molecule is staggering, and even today, papers trying to understand the vibrations of NMA are being published.

The interest is two-fold. Firstly, NMA is a small molecule with non-trivial electronic properties that exhibits complex structures in the solution phase. In solution, NMA forms long chains linked by relatively strong hydrogen bonds, whose strength is actually enhanced due to cooperative effects induced by the two electronic resonance structures [141]. Secondly, NMA is an amide unit capped by two methyl groups and is therefore the smallest amide unit. Since proteins are essentially polymers composed of amide units, it is believed that if the vibrational spectroscopy of NMA is well-understood, this will open a window into the understanding of the IR spectroscopy of proteins [142–144]. Thus far, NMA has proven to be more complicated than its simple structure would suggest, showing rich and complex vibrational features, and the "bottom-up" to protein vibrational spectroscopy has not been particularly fruitful [145].

The work in this chapter was actually birthed out of a desire to have a "simple" model system to develop a basic platform on which to use 2D IR to study intermolecular interactions as well as test the newly developed broadband IR source. The study of intermolecular interactions using 2D IR promises to fill a large gap in experimental studies of solvation dynamics. The vast majority of existing experiments study these interactions indirectly by measuring the dynamic influence of the solvent on the properties of the solute. For example, after electronic excitation of a solute chromophore, experiments measuring the evolution of the electronic energy gap [146–149] or the low-frequency vibrational response of the solvent [150, 151] have been carried out. Such experiments provide timescales of the reorganization of solvent molecules, but are limited in their ability to structurally characterize the correlated motions of solute and solvent. On the opposite end of the spectrum, magnetic resonance experiments [152–154] can probe site-specific solute-solvent interactions, but lack the time-resolution required to reveal the ultrafast molecular dynamics of interest. Boasting both structural sensitivity and high time resolution, 2D IR can in principle overcome the disadvantages of these approaches.

The high-frequency N—H stretch vibration and low-frequency C═O stretch vibration interact strongly through a hydrogen-bonding interaction, making it a natural choice for a model system for intermolecular interactions. At certain concentrations, NMA exists in organic solution primarily as a free molecule and as a molecular dimer [139]. In the dimer, the N—H group on one molecule donates a hydrogen bond to the C═O group of the other molecule. This hydrogen-bonding interaction mimics what one would expect for interactions of a hydrogen-bonding solvent, such as water. Therefore, we can view this as a model system for solvation, where NMA is both the solvent and the solute.

This chapter is largely based off of a paper published in *The Journal of Chemical Physics* in 2014 [155]. Motivated by understanding solvent-solute interaction dynamics, we showed that it is possible to observe intermolecular cross peaks that directly report on the hydrogen-bonding interaction using broadband 2D IR. As it would later turn out, this method of observing intermolecular interactions only works well for particularly strong interactions, such as that in the NMA dimer which is also mediated by the change in electronic resonance structure upon dimerization. In addition to the published work, this chapter also contains data on NMA dynamics as well as 2D IR polarization anisotropy which gives a more direct understanding of the structures of the monomer and dimer.

4.1.2 The Molecular Structure of NMA

N-methylacetamide is a small organic molecule which consists of an amide group capped with methyl groups. The structures of the NMA monomer and NMA dimer are shown in Fig. 4.1A and 4.1B, respectively. Each NMA molecule can both accept a hydrogen bond at the carbonyl and donate a hydrogen bond via the N—H group. The molecule exists almost exclusively in the *trans*-configuration with less than 1% being in the *cis*-configuration [156].

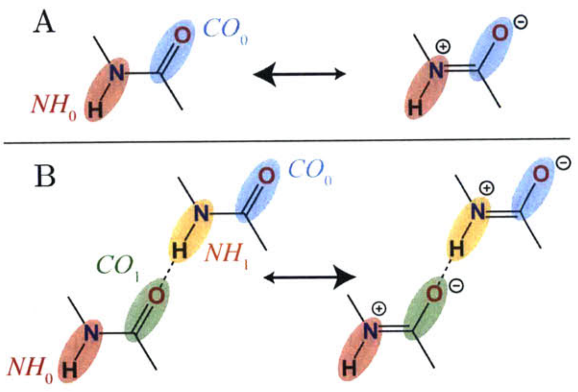

Figure 4.1: Resonance structures of the NMA monomer (A) and dimer (B).

In addition to the "normal" structure, amide groups posses a well-known resonance structure, shown schematically in Fig. 4.1, in which the the molecule is in a zwitterionic form. In this form, the oxygen and nitrogen atoms formally take on a negative and psoitive charge, respectively, and the bond between the carbon and the nitrogen is a double bond. The effect of this resonance structure is not subtle. In the zwitterionic form, the nitrogen atom is sp^2 hybridized; this renders the molecule essentially planar in solution. Furthermore, the double bond character of the C=N bond creates a large barrier to rotation, and the molecule is basically fixed in the *trans*-configuration.

One of the most interesting properties of NMA is the intricate interplay between the electronic structure and the hydrogen-bonding configuration. Upon forming a hydrogen bond, the zwitterionic structure is stabilized for both the hydrogen-bond-accepting and hydrogen-bond-donating molecules due to the increase in local polarity [157,158]. That is, the close proximity of the negatively charged oxygen atom in the carbonyl bond with the positively charged hydrogen atom in the N—H bond results in a stabilizing effect for the charged resonance structures. This results in a cooperative effect in which forming a second hydrogen bond is facilitated due to the extra stabilization provided by forming the first. As a result, at sufficient concentrations, NMA forms long chains[1] in solution held together by hydrogen-bond linkers [159,160].

4.1.3 Thermodynamics of Cooperative Aggregation

The goal of this work was to study the monomer and the dimer species and not the long aggregated chains formed in solution. In fact, if such chains were present in a significant fraction in the data presented in this chapter, this would call into question its interpretation. As such, an understanding of how these chains form as a function of concentration is important; this basically amounts to understanding the thermodynamics of a cooperative aggregating system and ensuring that for thermodynamic parameters appropriate to NMA, the number of oligomers of order higher than two is negligible.

To understand the thermodynamics of cooperative aggregation, we develop a simplified version of the standard theory [161,162]. We consider a system comprised of a molecule, A, which may form oligomers under suitable concentrations. If we denote the various oligomeric species by A_n, where n is the number of monomeric units in the aggregate, then the system of reactions we are concerned with is

---

[1] This is not true in liquids with a high dielectric constant or hydrogen-bonding liquids such as water. In this case, the solvent's interactions with NMA can stabilize the monomers such that chain formation is not entropically or enthalpically favorable.

$$\begin{aligned} A_1 + A_1 &\overset{k_2}{\rightleftharpoons} A_2 \\ A_1 + A_2 &\overset{k_3}{\rightleftharpoons} A_3 \\ &\vdots \\ A_1 + A_{n-1} &\overset{k_n}{\rightleftharpoons} A_n \\ &\vdots \quad , \end{aligned} \tag{4.1}$$

where k_n is the equilibrium constant for adding a monomer to a chain of length n. In Eq. 4.1, we approximate the number of possible reactions as infinite; this is justified if the equilibrium constants are such that the probability of having a chain consisting of more than the total number of molecules in the solution is essentially zero. We may neglect reactions between different oligomers since these may be represented by a reaction of an oligomer with several monomers [161, 162]. For each reaction in Eq. 4.1, we may write

$$k_n = \frac{[A_n]}{[A_1][A_{n-1}]}, \tag{4.2}$$

which provides a recursive relationship relating $[A_n]$ to $[A_{n-1}]$ as a function of k_n and $[A_1]$. We can therefore rearrange Eq. 4.2 and iterate $n-2$ times to give

$$[A_n] = [A_1]^n \prod_{j=2}^{n} k_j. \tag{4.3}$$

This expression provides the concentration of the n^{th} oligomer in terms of the concentration of the monomers and the equilibrium constants for oligomerization. However, only total concentration is controllable experimentally. We therefore must express the monomer concentration in terms of the total concentration, which is given by

$$[C] = \sum_{n=0}^{\infty} n[A_n] = \sum_{n=0}^{\infty} n[A_1]^n \prod_{j=2}^{n} k_j, \tag{4.4}$$

where in the second equality, Eq. 4.3 was used to eliminate $[\mathrm{A}_n]$. In principle, what remains is straightforward. Equation 4.4 must be inverted so as to write $[\mathrm{A}_1]$ as a function of [C]. With this result and Eq. 4.3, the n^{th} oligomer concentration is determined as a function of the total concentration and the equilibrium constants. In practice, however, this is made difficult by the nested product and sum. At this point, it is therefore necessary to make some approximation to continue.

The simplest approximation is to set all the equilibrium constants equal to some k. However, this does not capture the phenomenon of cooperativity. For a truly cooperative system, k_3 would be larger than k_2 and each subsequent equilibrium constant would be slightly larger than the previous one. In practice, the difference between subsequent equilibrium constants is negligible, and we may set $k_n = k$ with $n \neq 2$. Noting then that $\prod_{j=2}^{n} k_j = k_2 k^{n-2}$, we have

$$y = \sum_{n=0}^{\infty} n x^n, \tag{4.5}$$

where $y = k^2[\mathrm{C}]/k_2$ and $x = k[\mathrm{A}_1]$. The sum in Eq. 4.5 can be related to the geometric sum via a derivative with respect to x, and it will converge provided that $k[\mathrm{A}_1] < 1$. From Eq. 4.2, we see that this corresponds to $[\mathrm{A}_n] < [\mathrm{A}_{n-1}]$; that is, the concentration of every n-order oligomer is less than that of the $n-1$ order oligomer. Physically, this constraint arises because we let the sum in Eq. 4.4 run to infinity, when in reality it should terminate at a value of n corresponding to the total number of monomers in the system. In reality, this is a good approximation, and $k[\mathrm{A}_1]$ is almost always less than one.

The sum may be evaluated to give the total concentration as a function of the monomer concentration

$$y = \frac{x}{(1-x)^2}. \tag{4.6}$$

Equation 4.6 can easily be inverted to give the desired result. Choosing the negative root of the quadratic formula gives the physically meaningful result that $[\mathrm{A}_1] \to 0$ as $[\mathrm{C}] \to 0$.

The monomer concentration is therefore given by

$$x = 1 + \frac{1}{2y} - \frac{1}{2y}\sqrt{4y+1}. \tag{4.7}$$

Using Eq. 4.3, we can now compute the ratio of n-order oligomer to monomer, η_n. The result, for $n \geq 2$ is

$$\eta_n = \frac{[\mathrm{A}_n]}{[\mathrm{A}_1]} = \frac{k_2}{k}x^{n-1}. \tag{4.8}$$

In the work that follows in this chapter the distinction between inter- and intramolecular coupling between N—H and C═O oscillators is only possible in the limit that the concentration of oligomers of order three or higher is insignificant. It is therefore crucial to our analysis that the working concentration be kept sufficiently small such that mostly monomers and dimers are present. Studies in other solvents have shown that the dimerization constant of NMA is strongly dependent on the polarity of the solvent [163–166] and has been measured to lie within the range of $k_2 = 0.5$–$2.5\ \mathrm{M}^{-1}$ in various polar organic solvents [156, 164, 165]. Given that dichloromethane (the solvent primarily used in this study) has a higher dipole moment and larger dielectric constant than any of the solvents in the referenced studies, we can safely assume that the dimerization constant in dichloromethane is at the lower bound of that range.

Nonetheless, it is interesting to use Eq. 4.8 to compute upper bounds for concentrations of oligomers of order higher than 2. In Ref. [156], the authors report values of $k_2 = 0.6\ \mathrm{M}^{-1}$ and $k = 1.42\ \mathrm{M}^{-1}$ for NMA in $\mathrm{CDCl_3}$ which has a dielectric constant of 4.81. The dielectric constant of $\mathrm{CH_2Cl_2}$, used in these experiments, is 8.93 and so the equilibrium constants will be substantially smaller in our experiments. With a working concentration of $[\mathrm{C}] = 0.25$ M, this gives $y = 0.84$ and $x = 0.35$ and $\eta_2 = 15\%$, $\eta_3 = 5\%$, and $\eta_4 = 2\%$, which implies $> 75\%$ of molecules are in the monomer form. In our experiments, the number of longer chains will actually be reduced compared to these values. In addition, the authors of Ref. [166] measured that the average chain length of NMA in dicholoromethane at a concentraction of 0.25 M is only about 1.1 which is consistent with having mostly monomers and dimers in solution.

4.2 Vibrations of the NMA Monomer and Dimer

4.2.1 Linear Absorption Spectroscopy

Figure 4.2 shows the solvent-corrected linear IR spectrum of NMA in dichloromethane in the N—H stretch and amide stretch regions as a function of increasing concentration. At the lowest concentration of 30 mM, the molecules are almost exclusively monomers (Fig. 4.1A), and a single sharp peak in the high frequency region is observed at 3465 cm^{-1}. This corresponds to the stretching motion of the non-hydrogen-bonded N—H oscillator (Amide A) which is only weakly influenced by the solvent. Similarly, the C═O stretch (Amide I) shows up as a single sharp peak at 1675 cm^{-1} and the Amide II band, which consists primarily of N—H wag with some amount of C—N stretch, absorbs at 1530 cm^{-1} [140].

As the concentration is increased to 250 mM, dimers form, as shown schematically in Fig. 4.1B. This is evidenced by the peak that grows in at 3340 cm^{-1}, which corresponds to the stretch of the N—H groups which are donating hydrogen bonds to C═O groups on other NMA molecules. The 125 cm^{-1} redshift is accompanied by an increase in transition dipole strength due to the vibrational non-Condon effect [167,168]. The hydrogen-bonding interaction is also reflected in the absorption of the C═O stretch peak, which shows a shoulder that is approximately 10 cm^{-1} redshifted from the non-hydrogen-bonded carbonyl peak. Similarly, the Amide II band shows a shoulder which is blueshifted by roughly 25 cm^{-1} from the non-hydrogen-bonded peak. As discussed above, these correlated frequency shifts can be attributed to stabilization of the zwitterionic electronic resonance structure of NMA. Upon donating a hydrogen bond, the N—H bond weakens which is accompanied by a weakening of the C═O bond, a strengthening of the C—N bond, and a stiffening of the HNC bend potential. The same effects are indeed observed upon C=O accepting a hydrogen bond [169]. In addition to the shifting of the Amide A, I, and II band centers, we also observe the growth of new peaks with increasing concentration: one at 3100 cm^{-1}, typically referred to as Amide B, and another at 3220 cm^{-1}. The former is usually assigned to the overtone of the Amide II band, however, there is some uncertainty in this assignment [170–172]. The exact origin of the 3220 cm^{-1} peak is unknown, but likely arises from a combination band between Amide II and the C═O stretch (1665 cm^{-1} + 1555 cm^{-1}= 3220 cm^{-1}).

At a concentration of 1000 mM, the hydrogen-bonded N—H band redshifts 20 cm^{-1} compared to 250 mM. The Amide I and II bands continue to shift red and blue, respectively, as well. This reflects the formation of oligomeric chains at these concentrations caused by the cooperative interactions between the induced dipoles on hydrogen-bonded molecules [141]. As concentration is further increased (not shown) the peaks continue to shift following these trends, but stop shifting as some critical length after which the contribution of the monomers capping the chains is negligible.

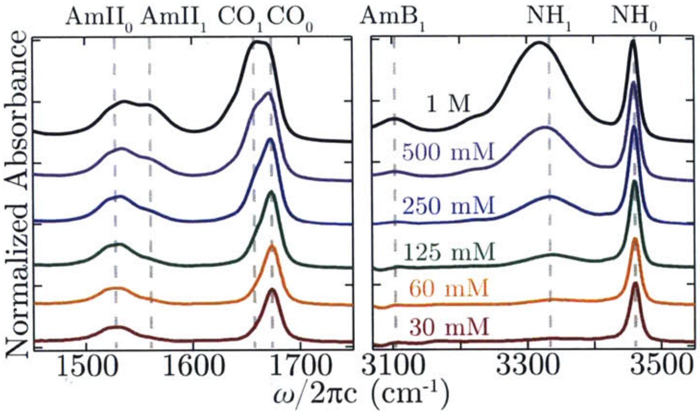

Figure 4.2: Linear spectrum of NMA in CH_2Cl_2 as a function of concentration illustrating the formation of oligomers as concentration increases.

Aggregated chains have been studied both in the context of small amides [159, 160] as well as in other hydrogen-bonding systems such as methanol [173]. While the study of these chains is interesting in its own right as it provides a realization of a one-dimensional excitonic model system, we aim to study the simpler monomer-dimer system, and to that end, we generally refer to the properties 250 mM solution in this chapter, unless otherwise stated.

Even from simple considerations of the linear spectrum, it stands to reason that the N—H and C═O stretching are going to be strongly coupled through the influence of the vibrations on the electronic structure. The electronic trends with hydrogen bonding are discussed above, but there is no reason to believe that the same trends will not hold with vibrational excitation. For example, excitation of the N—H stretch weakens the chemical bond. This weakening is accompanied by a shift in the equilibrium of the resonance structures towards the zwitterionic form, which in turn results in a weakening of the C═O bond. In that sense, the vibrations of the amide unite are unique, and one must proceed carefully when applying arguments, which are typically intuitive and based off of weakly anharmonic oscillators, when discussing them.

4.2.2 Simplified Notation

The designation of hydrogen-bonded versus non-hydrogen-bonded vibrations quickly becomes cumbersome (and at times confusing) when discussing the spectra of NMA. To that end, we introduce a simplified notation. We use the notation X_1 to signify that the X vibration is singly hydrogen bonded and X_0 to signify that it is not hydrogen bonded. For example, in the 250 mM spectrum the NH_0 vibration corresponds to the peak at 3465 cm^{-1} while the NH_1 vibration corresponds to the peak at 3340 cm^{-1}. We label the amide A, B, I, and II modes by NH_x, AmB_x, CO_x, and AmII_x, respectively. In addition, we will use a prime to signify a vibration arising from an NMA-d7 molecule (e.g., CO'_1). The stretching modes are color coded in Fig. 4.1 and peaks have been labeled in Fig. 4.2.

4.3 The Short-Time 2D IR Spectrum of NMA

4.3.1 Amide A and Amide I

The 2D IR spectrum for 250 mM NMA, taken at a waiting time of $\tau_2 = 100$ fs (in order to minimize non-resonant response), is shown in Fig. 4.3. In the 250 mM spectrum, the NH_0 and NH_1 bands are bleached upon excitation of the N—H stretching region, giving rise to the two ground state bleaches (GSBs) on the diagonal of the spectrum (Fig. 4.3, upper panel). Associated with these GSBs are excited state absorptions (ESAs) from the first excited state of the N—H stretch to the second, which are shifted to lower frequency in ω_3 due to vibrational anharmonicity. The NH_0 peak is centered on the diagonal at $(\omega_1, \omega_3) = (3465\ \text{cm}^{-1}, 3465\ \text{cm}^{-1})$ while its excited state transition is centered at $(3465\ \text{cm}^{-1}, 3325\ \text{cm}^{-1})$. The anharmonicity of the free N—H stretch,[2] which we define as the difference in transition frequencies $\omega_{10} - \omega_{21}$, is therefore 140 cm^{-1}, which is in agreement with the near-IR overtone transition of $\omega_{20} = 6805\ \text{cm}^{-1}$ in CCl_4 [163, 164]. The GSB of the NH_1 peak is centered at $(3340\ \text{cm}^{-1}, 3340\ \text{cm}^{-1})$ and its ESA is peaked at $(3340\ \text{cm}^{-1}, 3220\ \text{cm}^{-1})$, although we cannot read off the anharmonicity due to overlap between the two features.

In the lower panel of Fig. 4.3, we see cross peaks between various N—H and C═O vibrations that are qualitatively different depending on the hydrogen-bonding state of the donor or acceptor group. The NH_0 vibration shows a cross-peak to the CO_0 vibration centered at $(3465\ \text{cm}^{-1}, 1675\ \text{cm}^{-1})$. This peak represents the intramolecular coupling between the NH_0 and CO_0 within a single monomer unit. The splitting between the bleach of the NH_0–CO_0 cross peak and its associated induced absorption is 30 cm^{-1}, which is determined by the coupling between the two vibrations; this splitting is consistent with what has previously been measured for *cis*-amides [174].

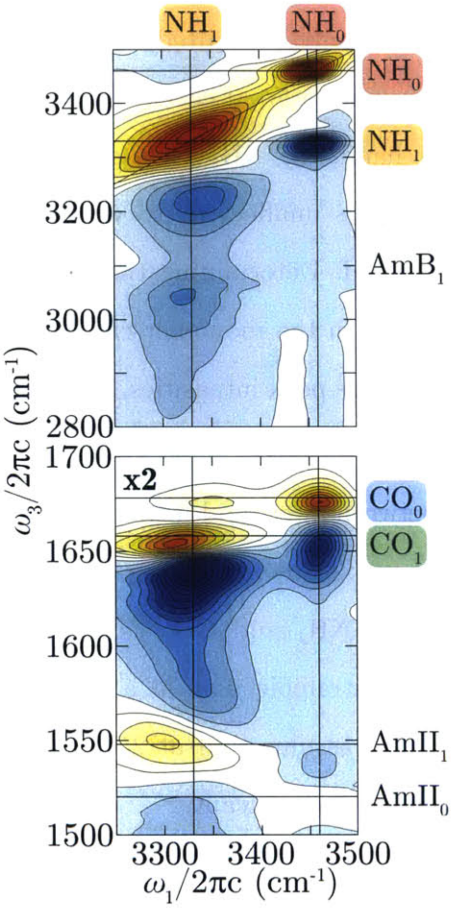

Figure 4.3: 2D IR spectrum of NMA taken at $\tau_2 = 100$ fs.

In contrast to NH_0,the NH_1 vibration shows two cross peaks to the CO band. Based on the linear IR spectrum, the cross-peak at $(3370\ \text{cm}^{-1}, 1675\ \text{cm}^{-1})$ corresponds to intramolecular coupling between the NH_1 and CO_0 on the hydrogen-bond-donor molecule, while the one at $(3326\ \text{cm}^{-1}, 1658\ \text{cm}^{-1})$ corresponds to the intermolecular vibrational coupling between NH_1 and CO_1. That is to say, when the N—H group is donating a hydrogen bond, it couples both to the dangling carbonyl (CO_0, Fig. 4.1B) and to the one to which it is donating a hydrogen bond (CO_1, Fig. 4.1B). That the center of the NH_1–CO_0 cross-peak is 30 cm^{-1} blueshifted in ω_1 from the center of the NH_1 frequency (i.e., 3370 cm^{-1} as opposed to 3340 cm^{-1}) suggests that the N—H oscillators with the weakest hydrogen bonds have the strongest intramolecular coupling.

---

[2] We note that the anharmonicity of a feature can only be determined accurately in the limit that its anharmonicity is a fair bit larger than its linewidth.

The NH_1–CO_1 cross peak is elongated parallel to the diagonal with a slope of +0.21, which is an indication that the more strongly hydrogen bonded the N—H is, the carbonyl mode to which it is donating a hydrogen bond is more strongly redshifted. While this correlation is intuitive based on the linear spectrum, it provides a good check that we are indeed observing intermolecular coupling. On the other hand, the NH_1–CO_0 cross peak has a slope of zero, which implies that the CO_0 frequency is unaffected, to within our resolution, by the donation of a hydrogen bond by the N—H. Determining the splitting between these bleaches and ESA is not as straightforward as in the monomer case due to overlapping features in this region, but based on the similar cross peak intensities, it appears the intermolecular coupling is of the same magnitude as intramolecular coupling.

At this point, it is worth noting that the distinction between inter- and intra- molecular coupling can only be made in the limit that the number of oligomers of order three and higher is negligible. This is because a cross peak between NH_1 and CO_1 can only be intermolecular if we are considering a dimer, but can be intramolecular in a trimer or longer oligomer. Given the discussion of §4.1.3 we can safely assume that at 250 mM, we are well within the limit where the concentration of trimers is insignificant.

In addition to the observed features, we expect an intramolecular cross peak between NH_0 and CO_1 since every hydrogen-bond-acceptor molecule of the NMA dimer should have a free N—H group and hydrogen-bonded C═O; however, no bleach is observed at the NH_0–CO_1 frequency. To explore this further, we performed isotopically dilute experiments in which either 50% or 80% of the NMA molecules were replaced with their fully deuterated isotopologue NMA-d7. In the former case, we expect a 1:1:1:1 ratio of the hh:hd:dh:dd

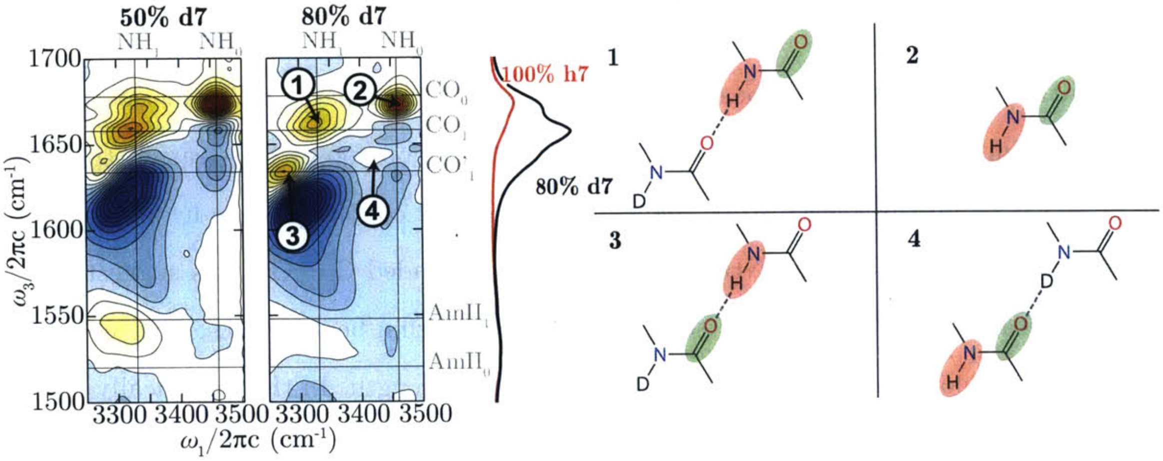

Figure 4.4: 2D IR spectra of NMA taken at $\tau_2 = 100$ fs with 50% NMA-d7 and 80% NMA-d7 (left). Schematic illustration of couplings in the dimer (right). Peak labels in the 80% d7 spectrum correspond to structures on the right where the excited bond is highlighted in red, and the probed bond is highlighted in green.

dimers, while in the latter case, we expect a 1:4:4:16 ratio, assuming that the association constant is not significantly influenced by deuteration. In NMA-d7, the carbonyl stretch is redshifted by roughly 20 cm^{-1} due to the heavier methyl groups and deuterated N—H bond [158]; this conveniently allows us to distinguish carbonyl stretches arising from the deuterated versus non-deuterated molecules.

The left part of Fig. 4.4 shows the C═O stretch region of the 2D IR spectrum for 250 mM concentration solutions for the two isotopic ratios taken at $\tau_2 = 100$ fs along with the linear spectrum for the isotopically pure and 80% d7 solutions. In the spectrum of the 50% d7 solution, we now see three cross-peaks in the NH_1–$\text{CO}_{0/1}$ region. In addition to the cross peaks observed in the isotopically pure spectrum, another cross-peak corresponding to the NH_1–CO'_1 coupling, where the C═O acceptor is on a deuterated molecule, is present. This confirms that we also observe intermolecular coupling between the deuterated and non-deuterated species.

In the 80% d7 spectrum, where the NH_1–CO_1 is not discernable due to the low hh dimer concentration, we can isolate the NH_1–CO'_1 cross-peak (peak 3, Fig. 4.4) centered at (3282 cm^{-1}, 1634 cm^{-1}). We also note that the NH_1–CO_0 cross peak (peak 1, Fig. 4.4) is now centered at (3332 cm^{-1}, 1662 cm^{-1}), in contrast to the isotopically pure case where this peak is blue-shifted in ω_1. We comment on this further in §4.3.5. That the ESA associated with the NH_0–CO_0 cross peak is reduced in intensity compared to in the isotopically pure spectrum, suggests that there is a bleach which sits on top of this feature (peak 4, Fig. 4.4).We assign this bleach to be due to intramolecular coupling in the hydrogen-bond acceptor between the dangling NH_0 and the hydrogen-bonded C═O. This suggests that this cross peak is not visible in the isotopically pure spectrum because NH_0–NH_1 coupling gives rise to a delocalized mode which has low oscillator strength. In the isotopically mixed dimer, the different frequencies of the N—H and N—D stretches reduces the effect of the coupling.

The various couplings we observe in the 80% d7 spectrum are summarized in the right part of Fig. 4.4. In this schematic, the numbered structures correspond to the peaks labeled in the 80% d7 spectrum. The red highlight shows which vibration is being excited initially and the green highlight shows which vibration is giving rise to that particular cross peak.

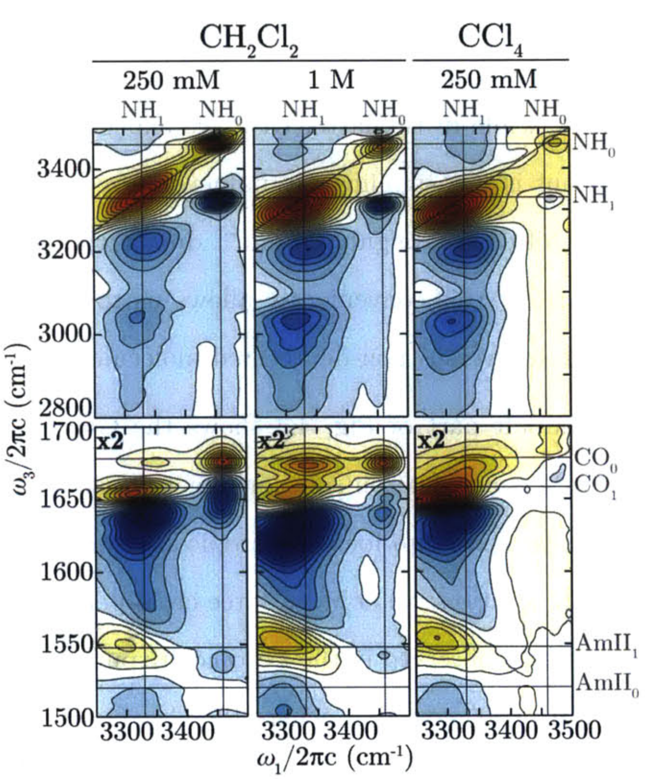

Figure 4.5: 2D IR spectra of 250 mM and 1 M NMA in CH_2Cl_2 and 250 mM NMA in CCl_4.

Solvent Dependence and Oligomer Length

In contrast to the NH_0 peak on the diagonal (Fig. 4.3, upper panel), the ESA of the NH_1 peak is several hundred wavenumbers broader in ω_3 than the fundamental GSB. This extreme broadening is consistent with that observed in hydrogen-bonded systems, which arises from both inhomogeneous broadening and strong anharmonicity due to hydrogen bonding [175], in addition to absorptions from the excited N—H stretch to combination bands of the amide vibrations.

While this is the most likely explanation for the broadening, it was of concern that the ESA for the NH_1 vibration overlaps with the two intense, sharp symmetric and asymmetric C—H stretches of dichloromethane. To that end we also measured the 2D IR spectrum of 250 mM NMA in carbon tetrachloride where there are no solvent absorption peaks in this region. The comparison between the two solvents is shown in Fig. 4.5A and 4.5C. While the oligomer to monomer ratio is significantly increased in carbon tetrachloride compared to dichloromethane due to the former having a lower dielectric constant and no dipole moment, we see that the NH_1 peaks and its cross peaks are qualitatively similar between the two solvents. This shows that the broadening we observe is in fact intrinsic to NMA dimers and not solvent interference.

At this point we comment briefly on the difference in the 2D IR spectra with increasing oligomer length. The 1000 mM NMA in dichloromethane (Fig. 4.5B) and 250 mM NMA in CCl_4 (Fig. 4.5C) show changes in the 2D IR spectrum from increasing oligomeric concentration. As the higher-order oligomer concentration increases, the relative intensity of the NH_1 to NH_0 band increases as the former redshifts to 3300 cm^{-1} in CCl_4. In the C═O stretching region, we see significant changes in the NH_1–$CO_{0/1}$ cross peaks with increasing concentration. At 1000 mM,we can clearly see an intense NH_1–CO_0 cross peak as well as an NH_1–CO_1 cross peak that is redshifted in ω_3. This redshifting is due to chains of NMA molecules forming, which results in excitonic coupling between the N—H's and between the C═O's. In CCl_4, the NH_1–CO_0 cross peak has all but disappeared since the chains are so long that there are few dangling carbonyls.

4.3.2 Amide II and Amide B

In addition to cross peaks between amide A and amide I, the 2D IR spectrum shows cross peaks bewteen amide A and amide II. The intensity of the feature at (3465 cm^{-1}, 1530 cm^{-1}), which is nominally due to the coupling between $AmII_0$ and NH_0, is more than an order of magnitude smaller than the NH_0–CO_0 cross peak, reflecting the comparatively weak coupling between $\mathrm{AmII_0}$ and $\mathrm{NH_0}$.

In addition to coupling between $\mathrm{NH_1}$ and $\mathrm{CO_1}$, we observe a cross peak between $\mathrm{NH_1}$ and $\mathrm{AmII_1}$ centered at (3290 $\mathrm{cm^{-1}}$, 1550 $\mathrm{cm^{-1}}$) which is roughly an order of magnitude larger than the $\mathrm{NH_0}$–$\mathrm{AmII_0}$ feature. Upon forming a hydrogen bond, there is a strong intramolecular cross peak between the N—H stretch and the amide II mode which is not observed in the non-hydrogen-bonded species. The center-line slope of the $\mathrm{NH_1}$–$\mathrm{AmII_1}$ cross-peak is -0.43; the negative value of the slope reflects the facts that strongly hydrogen-bonded N—H species have an amide II frequency which is blueshifted compared to the weakly hydrogen-bonded ones. This is consistent with the trends observed in the linear spectrum and further confirms that this is an intramolecular coupling.

The $\mathrm{NH_1}$–$\mathrm{AmII_1}$ coupling is strongest for the most redshifted N—H oscillators, which is reflected by the fact that the peak of the cross peak is redshifted from the center of the $\mathrm{NH_1}$ band in ω_1. The mechanism of this coupling is hinted at in the 3300 $\mathrm{cm^{-1}}$ region of the spectrum (Fig. 4.3, upper panel). At (3290 $\mathrm{cm^{-1}}$, 3100 $\mathrm{cm^{-1}}$), a bleach removes intensity from the red side of the ESA of the $\mathrm{NH_1}$ peak at the frequency of the amide B mode. Given the similar cross-peak shape, and the fact that the amide B frequency is roughly twice the amide II frequency, we can attribute the amide B peak to the overtone of amide II. The large intensity of the amide B feature, which is a harmonically forbidden transition, in the linear spectrum (Fig. 4.2) can be attributed to a Fermi resonance with the fundamental transition of the $\mathrm{NH_1}$. This also gives rise to the intense $\mathrm{NH_1}$–$\mathrm{AmII_1}$ cross peak. The most red-shifted, strongly hydrogen-bonded N—H oscillators have the most intense cross peak to the amide II fundamental and overtone since the resonance condition is optimal for these oscillators. The 2:1 ratio which is characteristic of the frequencies of X—H stretches and their corresponding bending modes have been characterized extensively; given the breadth of absorption features of hydrogen-bonded oscillators, hydrogen-bond-induced Fermi resonances are clearly a general feature and these resonances play an important role in relaxation [176–178].

The assignment of a Fermi resonance between the $\mathrm{NH_1}$ mode and the $\mathrm{AmII_1}$ mode is corroborated by the data on longer oligomers (Figs. 4.5B and 4.5C). As the $\mathrm{NH_1}$ band redshifts with increasing chain length, it comes into better resonance with the amide B mode. As a result, the $\mathrm{NH_1}$–$\mathrm{AmB_1}$ cross peak intensifies as does the $\mathrm{NH_1}$–$\mathrm{AmII_1}$ cross peak, an effect that is particularly evident in the CCl_4 spectrum. This supports the interpretation that the amide B peak is in fact the amide II overtone and that its intensity is due to a Fermi resonance.

4.3.3 Fermi Resonances

Since Fermi resonance plays an important and recurring role in the spectroscopy of hydrogen-bonding systems, the phenomenon merits a thorough discussion. First explained in 1931 in the context of the Raman spectrum of gaseous CO_2 [179], a Fermi resonance occurs when there is an accidental degeneracy (that is, one not enforced by a fundamental symmetry of the Hamiltonian) between the fundamental of one vibrational mode and the first overtone of another. If this is the case, the anharmonic part of the nuclear Hamiltonian will cause these modes to mix if the symmetry of the molecule allows it.[3]

The nuclear Hamiltonian of a molecule, expressed in mass-weighted normal mode coordinates, is given by

$$H = \frac{1}{2}\sum_i (P_i^2 + \omega_i^2 Q_i^2) + \sum_{ijk} K_{ijk} Q_i Q_j Q_k + \dots, \tag{4.9}$$

where we have only explicitly written out the third-order anharmonic term. The generalized coordinates can be expressed in terms of the creation and annihilation operators,

$$Q_i = \sqrt{\frac{\hbar}{2\omega_i}}(a_i + a_i^\dagger) \tag{4.10a}$$

$$P_i = \frac{1}{\mathrm{i}}\sqrt{\frac{\hbar\omega_i}{2}}(a_i - a_i^\dagger), \tag{4.10b}$$

which obey the usual Bose commutation relation $[a_i, a_j^\dagger] = \delta_{ij}$. In what follows, we will take a minimalist approach in highlighting the basic features of the problem, since the general solution is rather involved. We consider two vibrational modes with frequencies $\omega_1 \approx 2\omega_2$, and we truncate the expansion of Eq. 4.9 at third order and keep only the term relevant to the Fermi resonance, $K_{122}Q_1Q_2^2$. Expanding this interaction term in terms of raising and lowering operators gives

---

[3] It is worth noting that Fermi resonance is not purely a quantum effect, and the same considerations apply to classical anharmonic oscillators as well.

$$\begin{aligned} K_{122}Q_1Q_2^2 = V \Big(& a_1a_2^2 + 2a_1a_2^\dagger a_2 + a_1a_2^{\dagger 2} + a_1 \\ & a_1^\dagger a_2^2 + 2a_1^\dagger a_2^\dagger a_2 + a_1^\dagger a_2^{+2} + a_1^\dagger \Big) , \end{aligned} \tag{4.11}$$

where $V = \hbar^{3/2}K_{122}/\sqrt{8\omega_1\omega_2^2}$ and has units of energy. This term therefore connects states in adjacent excitation manifolds, and as such produces terms that couple the overtone of the 2 state to the fundamental of the 1 state. That is, $\langle 10|K_{122}Q_1Q_2^2|02\rangle = \sqrt{2}V$. The Hamiltonian in terms of the eigenbasis of the harmonic Hamiltonian is given by

$$H = \begin{array}{c|ccccccc} & |00\rangle & |01\rangle & |10\rangle & |02\rangle & |11\rangle & |20\rangle & \cdots \\ \hline |00\rangle & 0 & 0 & V & 0 & 0 & 0 & \\ |01\rangle & 0 & \omega_2 & 0 & 0 & 3V & 0 & \\ |10\rangle & V & 0 & \omega_1 & \sqrt{2}V & 0 & \sqrt{2}V & \\ |02\rangle & 0 & 0 & \sqrt{2}V & 2\omega_2 & 0 & 0 & \cdots \\ |11\rangle & 0 & 3V & 0 & 0 & \omega_1+\omega_2 & 0 & \\ |20\rangle & 0 & 0 & \sqrt{2}V & 0 & 0 & 2\omega_1 & \\ \vdots & & & & \vdots & & & \ddots \end{array} , \tag{4.12}$$

and in principle, it is necessary to diagonalize the entire Hamiltonian to determine the effect of the Fermi resonance.[4] It has been shown that the diagonalization of the entire Hamiltonian can be achieved though the approximate solution of an infinite set of coupled differential equations for the retarded Green's function [180]. This is fairly challenging, and it suffices for our purposes to diagonalize the block that corresponds the states of interest. That is, we diagonalize only the portion corresponding to the $|10\rangle$ and $|02\rangle$ states,

---

[4] This approach is not rigorously possible if the entire third order interaction is retained, due to terms such as Q_1^3. This cubic potential is necessarily not bound as $Q_1 \to -\infty$, and as such produces a continuum of states. To include such diagonal anharmonicity, it is necessary to expand the potential to an even order. However, for the form used here, this is not a problem.

$$\begin{vmatrix} \omega_1 - \omega & \sqrt{2}V \\ \sqrt{2}V & 2\omega_2 - \omega \end{vmatrix} = 0,$$

which yields the results

$$\omega_{\pm} = \frac{\omega_1 + 2\omega_2}{2} \pm \frac{1}{2}\sqrt{(\omega_1 - 2\omega_2)^2 + 8V^2}. \tag{4.13}$$

In neglecting the rest of the matrix upon diagonalization, we have essentially neglected the bosonic character of the vibrations [180]. In fact, Eq. 4.13 is actually exact on resonance, that is, when $\omega_1 = 2\omega_2$. However, for typical values of K_{122} and ω_1 in molecules, the frequencies do not deviate by more than ~1 cm^{-1} and so this approximation is valid for most cases [180]. It is perhaps surprising given the large number of eigenvalues we ignored, however these have very different numerical values, and as such do not impact the eigenvalues of these states much. The same is true of the eigenstates, which are given by [62]

$$|+\rangle = \cos\frac{\theta}{2}|10\rangle + \sin\frac{\theta}{2}|02\rangle, \tag{4.14a}$$

$$|-\rangle = -\sin\frac{\theta}{2}|10\rangle + \cos\frac{\theta}{2}|02\rangle, \tag{4.14b}$$

with

$$\tan\theta = \frac{\sqrt{8}V}{\omega_1 - 2\omega_2}. \tag{4.15}$$

We have effectively reduced the Fermi resonance problem to that of a two-level system and so the knowledge of such systems carries over directly. If the coupling is weak relative to the splitting, $8V^2 \ll (\omega_1 - 2\omega_2)^2$, then the + and − states basically have the frequencies of the original states. Furthermore, $\theta \approx 0$, and the eigenstates resemble the initial states. On the other hand, on resonance, the frequencies of the new states are $\omega_{\pm} = \omega_1 \pm \sqrt{2}V$, which can differ significantly from the original states. At resonance, $\theta \to \pi/2$, and the states become even mixtures of the original ones. This can greatly enhance the oscillator strength of what would be the "forbidden" transition (i.e., the $|00\rangle$ to $|02\rangle$ transition) since the resulting states are mixtures of a bright and dark state.

Determining the coupling of amide A and amide B in NMA is not so straightforward [181] since there are a wide range of frequencies that the oscillators can take on due to the hydrogen-bonding interaction, which effectively acts as a tuning coordinate for ω_1 and $2\omega_2$. The variation of the frequency splitting with such tuning is well known, and leads to familiar phenomena such as avoided crossing at the degeneracy point. The variation of eigenfrequency with tuning is shown graphically in Fig. 11 of §IV.C of Ref. [62].

While a good estimate of the eigenfrequencies can be obtained from the linear or 2D IR spectrum, it is not really possible to obtain the site energies. Nonetheless, we may make a reasonable estimate of the coupling by guessing the site frequencies. If we assume that the reddest NH_1 oscillators couple to the blues AmB_1 oscillators, we can take $\omega_- = 3100\ \text{cm}^{-1}$ and $\omega_+ = 3250\ \text{cm}^{-1}$ for the eigenenergies while taking $2\omega_2 = 3110\ \text{cm}^{-1}$ and $\omega_1 = 3225\ \text{cm}^{-1}$ for the site energies. Using Eq 4.13 gives a value of $V = 34\ \text{cm}^{-1}$, which is actually a fairly large coupling between such modes. This corresponds to a force constant (Eq. 4.11) of $K_{122} = 6.10 \times 10^{12}\ \text{erg}\cdot\text{cm}^{-2} \cdot \text{u}^{-3/2}$. The value of $V = 34\ \text{cm}^{-1}$ corresponds to a mixing angle of $\theta = 0.70$ rad or 40°, which implies a mixing of about 12%; therefore, the modes mostly resemble a true NH_1 or AmII_1, even at this level of coupling.

4.3.4 Intermolecular Cross Peaks in 2D IR

The structural information content of the intermolecular cross peaks of 2D IR experiments varies considerably depending on the strength of the vibrational coupling. In 2D IR experiments, dynamical information that reports on the interaction between the molecules is sacrificed if the coupling between vibrations of different molecules is weak. In this limit, the nature of the vibrations on either molecule is almost unchanged as a result of the intermolecular interaction, and intermolecular cross peaks grow in with waiting time at the vibrational energy transfer rate, which can sometimes be many tens of picoseconds [182–184].

Of course, the relaxation rate has its origins in the anharmonic terms in the intermolecular nuclear potential; however, when the intermolecular vibrational energy exchange occurs more slowly than the solute-solvent dynamics of interest, these dynamics are washed out, and not observed in the resulting cross peak. That is, any spectral diffusion or frequency shifts associated with the solvent-solute interaction will be complete by the time the cross peak grows in. Structural information can, in principle, be recovered from the relaxation rate, although this information is model dependent and requires a detailed knowledge of the relaxation mechanism, and more often than not, such a model is not available especially for such hydrogen-bonding systems.

The hydrogen-bonded NMA dimer is an example of strong intermolecular coupling, in which cross peaks originate from the fact that the vibrations on the two molecules are anharmonically mixed, or, in other words, excitonic. That is, the multidimensional nuclear potential energy surface of the two molecules is influenced so significantly by their interaction that the vibrations actually involve both molecules and, as in the case of Fermi resonances, the two vibrations have mixed character. 2D IR experiments of even stronger hydrogen bonding interactions have exploited this phenomenon in the past [185–187].

In this limit, intermolecular cross peaks in the 2D IR spectrum are present from zero waiting time so that coherent vibrational excitation of one molecule (that is, excitation of a local mode) drives coherent vibrational motion on its coupled partner. This is simply another way of stating that, the vibrational eigenstates of the dimer do not resemble the eigenstates of two monomers, but rather, the states have vibrational character of both molecules. Under these circumstances, the evolution of intermolecular cross peaks with waiting time is a direct consequence of the structure and dynamics imposed by the interaction. We take advantage of this in §4.5 in order to explore the hydrogen-bonding interaction dynamics directly.

4.3.5 Vibrational Couplings of NMA Molecules

The NMA Monomer

In the NMA monomer, both CO_0 and AmII_0 frequencies are highly off-resonant from the NH_0 transition (over 1800 cm^{-1} detuned), and neither vibration is particularly poised for a Fermi resonance interaction (although the overtone of CO_0 will be several hundred wavenumbers closer to NH_0 than the overtone of AmII_0). However, the intramolecular coupling within the monomer is such that the coupling between the NH_0 and CO_0 modes is much stronger than the coupling between the NH_0 and AmII_0 modes as evidenced by the cross-peak region of the 2D IR spectrum (Fig. 4.3). The coupling between the various modes reflects the complicated nuclear Hamiltonian of the NMA molecule which is not only dictated by the 12 backbone modes, but also by its electronic resonance structures. As described in §4.1.2, NMA's resonance structures are such that the N—H and C═O bond lengths are correlated while the N—H and C—N bond lengths are anticorrelated (Fig. 4.1B), and these correlations have been characterized by DFT calculations [169]. Since the Amide II mode involves both N—H wag as well as C—N stretch, it is not possible to *a priori* predict how the AmII_0 frequency will shift upon excitation of the N—H stretch. On the other hand, one would expect a lengthening of the C═O bond upon N—H stretch excitation resulting in the observed redshift of the induced absorption of the CO_0.

When modeling Amide I vibrations, it is customary to neglect the contribution of the Amide A mode on the grounds that the coupling between the two is weak and that the Amide A mode is localized [188]. We set out to characterize and quantify the observed coupling between the N—H and C═O stretches by modeling the two stretches as harmonic oscillators that are coupled via a bilinear coupling term, $\beta_{ij}Q_iQ_j$, or a cubic coupling term, $K_{ijk}Q_iQ_jQ_k$, or both. Such treatments proved unsatisfactory, since fits yielded unphysically large coupling constants (several hundreds of wavenumbers) in any of the three coupling schemes. The failure of simple coupling models to give reasonable coupling constants indicates that weakly anharmonic normal modes are a poor approximation of the true vibrational eigenstates of the N—H and C═O stretches. That is, they represent a basis which is rather unlike the true eigenstates of the system. This is perhaps unsurprising when one considers the correlation between the two bonds due to the electronic resonance structures of the molecule as well as the possibility of indirect coupling via other vibrational modes.

The NMA Dimer

Understanding vibrations within the dimer is complicated further still due to coupling between the same vibrations on the different molecules. The effect of these couplings surface when comparing the 2D IR spectra of the isotopically neat dimers (Fig. 4.3) with that of the isotopically mixed dimers (Fig. 4.4). As mentioned above, the absence of a cross peak at the NH_0–CO_1 frequency in the pure dimer and its presence in the isotopically mixed spectrum is indicative that the N—H stretches of the two molecules couple. We expect a small electrostatic frequency shift of the dangling N—H due to the presence of the donor NMA molecule as well as an additional shift due to vibrational coupling between the N—H's. However, the electrostatic shift would be fairly insensitive to deuteration of the donating NMA which shows that vibrational coupling is the primary reason for the shift. The data shows that the new modes formed are such that the oscillator strength of one of the transitions is low or that the two frequencies overlap so that we cannot resolve them. Upon detuning the two oscillators by deuteration, the N—H stretches localize and all the cross peaks one would expect for local stretches are evident in Fig. 4.4.

A somewhat more subtle effect, which is observed in the isotopically mixed dimer, is the shifting of the NH_1–CO_0 cross peak from being centered at 3370 cm^{-1} in ω_1 in the non-deuterated case to being centered at 3340 cm^{-1} in the deuterated one. This shift can be explained in terms of the coupling between the C═O oscillators on the different molecules in the fully hydrogenated dimer. As the hydrogen bond between the N—H and the C═O becomes stronger, so too does the coupling between the two carbonyl oscillators. Therefore, for strongly hydrogen bonded molecules, the C═O modes will have symmetric and antisymmetric character, while for weakly hydrogen bonded molecules, the C=O stretches will be comparatively local.[5] The anti-symmetric mode, which due to the roughly planar geometry of the transition dipoles is at higher frequency [189], will be comparatively dark since there is no change in dipole moment of the dimer during the oscillation. At the same time, the symmetric mode will be at lower frequency and have large oscillator strength for stronger hydrogen bonds (i.e., stronger carbonyl–carbonyl coupling) since the overall oscillator strength is conserved. On the other hand, in the dimer in which one molecule has been deuterated, the carbonyl stretches are off resonance by ~20 cm^{-1} which drastically reduces the effect of this coupling. As a result, the carbonyls in the mixed dimer are local stretches, as are the N—H stretches, and the NH_1–CO_0 cross peak in the mixed dimer is centered at the NH_1 frequency in ω_1. The NH_1–CO_1' cross peak is still centered on the red side of the NH_1 band, reflecting that the strongest hydrogen bonds result in the strongest intermolecular coupling. That the relative intensity of the NH_1–CO_1' cross peak is weaker than the NH_1–CO_1 cross peak reflects the fact that the excitonic mixing in the isotopically pure case gives rise to a larger transition dipole moment for the symmetric stretch.

It is therefore in the isotopically mixed dimer in which it is appropriate to discuss intermolecular coupling in terms of a local stretch on one molecule perturbing a local stretch on another. This is representative of what would be expected of a solvent–solute interaction, in which a hydrogen-bond-donating solvent is strongly coupled to a hydrogen-bond-accepting solute, with the other groups on the solvent and solute being comparatively uncoupled. In contrast, in the isotopically pure dimer it is necessary to consider modes delocalized over the entire dimer affecting other delocalized modes. By extension, this is the language which appropriately describes coupling in protein systems and other resonant systems. For example, we have observed that intermolecular coupling due to strong hydrogen bonding enables exciton formation in water [190]. While water is immensely complicated due to the sheer number of coupled vibrations, NMA provides us with a way to study this phenomenon in relative isolation. In proteins, a delocalized description of carbonyl stretches is the norm and has had success in describing the spectral patterns of protein secondary structure, however, the observed coupling between amide A and amide I in NMA may suggest that the common neglecting of the effect of N—H stretch vibrations when interpreting the amide I spectrum of proteins may be unfounded. It is clear that further work is necessary to test the validity of this approximation.

---

[5] This can be clearly in the consideration of Eq. 4.15. As the coupling between two states gets larger, $\phi \to \pi/2$, and the states become a perfect mixture of each other since the coefficients approach $1/\sqrt{2}$.

Given the failure of a weakly coupled normal mode picture to give a reasonable description of the intramolecular NH_0–CO_0 coupling within the monomer, it is evident that a similar picture will not accurately describe the intermolecular coupling within the dimer. We must not only consider the strong coupling between the donor N—H stretch and acceptor C═O stretch, which is a problem similar to the monomer, but we must also consider the delocalization of the modes over both molecules as well as the contribution from other modes. In particular, the amide II mode, which becomes strongly coupled to the N—H stretch upon forming strong hydrogen bonds, is expected to play an important role. At this level of complexity, the appropriate basis in which to discuss the vibrations of the amide is entirely unclear.

In the 3300 cm^{-1} region (Fig. 4.3, upper panel), the GSB of the NH_1 peak has a larger slope compared to the NH_0 transition, showing that inhomogeneous broadening contributes significantly to the linewidth of the NH_1 transition, while the NH_0 transition is homogeneously broadened. Inhomogeneous broadening is common in hydrogen-bonding systems due to the broad distribution of possible hydrogen-bonding configurations. Furthermore, we see that the linewidth of the excited state NH_0 transition is comparable to that of the fundamental transition, which is expected for a weakly anharmonic system; however, the NH_1 band starkly contrasts this. The NH_1 ESA spans an ω_3 range that is several hundred wavenumbers broader than the fundamental transition. This is attributed to the extreme anharmonicity of the hydrogen-bonded N—H stretch which becomes more severe at higher levels of excitation as well as to ESA to combination bands.

The mixing between the high and low frequency modes of the dimer is expected to become stronger at high levels of excitation so that combination bands and multi-quantum transitions are intense [191]. That is, from the first excited state of NH_1, there are combinations of the C═O stretch and amide II mode, and the anharmonic mixing between these combination modes and N—H stretching results in their large oscillator strength. This explains why no associated bleach is observed for these transitions since the fundamentals of these modes are forbidden (in the harmonic sense) and therefore weak. These combination bands, in addition to the intrinsically broad ESA for the NH_1 band, can explain the smear of ESAs ranging from 2800 to 3220 cm^{-1} in the 2D IR spectrum.

4.4 Transition Dipole Orientations in the NMA

4.4.1 A Practical Note about Polarization Anisotropy

Polarization anisotropy measurements are perhaps the most powerful tool in nonlinear IR spectroscopy because they provide the most direct measurement of molecular structure. From a polarization anisotropy measurement on cross peaks in a 2D IR spectrum, it is in principle possible to extract angles between the transition dipole moment vectors (see §2.5.5) which can then be directly compared to calculations of moleuclar structure [72, 192]. In practice, however, polarization anisotropy measurements are particularly difficult to carry out. As a double-difference spectroscopy, the measurement is highly susceptible to noise especially considering the small differences in signal being measured. Furthermore, in congested spectra, overlap between different feature makes it essentially impossible to extract an angle with high fidelity.

So what can practically be learned from a polarization anisotropy measurement if peaks are not well separated? Even if features overlap significantly, qualitative trends can be extracted. That is, it is straightforward to determine whether a peak becomes more or less intense relative to other peaks in comparing the ZZZZ spectrum to the ZZYY spectrum. This qualitative assessment, combined with "chemical intuition," can actually provide a reasonable estimate of the structure of the transition dipoles. Unfortunately, hydrogen-bonding systems are almost always entirely in this regime due to the broad resonances and the small distribution of frequencies of hydrogen-bond donors and acceptors. Fortunately, a qualitative assessment is often satisfactory.

4.4.2 Polarization Dependence of the NMA Cross Peaks

The $\tau_2 = 100$ fs 2D IR spectra of the cross-peak region of NMA for ZZZZ (left) and ZZYY (right) polarization schemes are shown in Fig. 4.6. We immediately note that the two spectra are rather different from each other as well as different from the magic angle spectrum of Fig. 4.3. Most obviously, the ZZYY spectrum is lower in intensity than the ZZZZ spectrum, as expected. However, the changes in relative intensity are far more subtle.

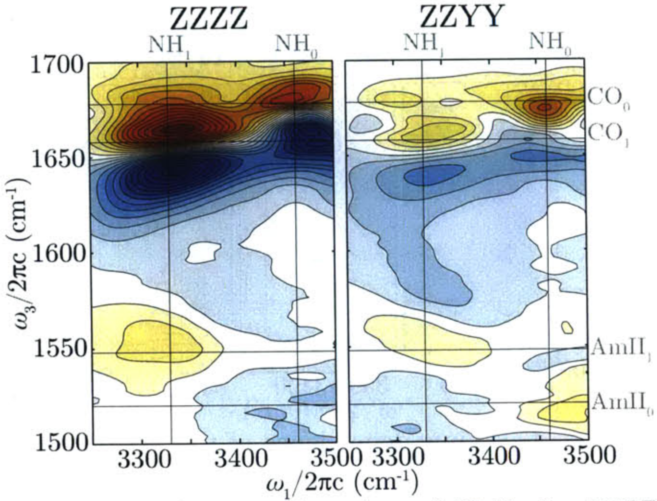

Figure 4.6: Cross-peak region of NMA for ZZZZ and ZZYY polarizations.

The intensity of the NH$_0$–AmII$_0$ cross peak relative to the NH$_0$–CO$_0$ cross peak is significantly enhanced in the ZZYY spectrum compared to the ZZZZ spectrum. This suggests that in the monomer, the AmII$_0$ transition dipole moment is almost perfectly perpendicular to that of the NH$_0$. Considering that the the AmII$_0$ mode is mostly in-plane N—H wagging with some amount of C—N stretch, this is not unexpected. The intensity of the NH$_0$–CO$_0$ peak in the ZZYY spectrum relative to the ZZZZ spectrum is reduced by a factor of ~0.5. For parallel dipoles, we expect a reduction of 1/3 and so, given the overlap of features in this region, we can conclude that a factor of 0.5 is consistent with mostly parallel transition dipoles between NH$_0$ and CO$_0$. Surprisingly, the ZZYY spectrum shows an extremely weak cross peak at the NH$_0$–AmII$_1$ frequency, which can only correspond to excitation of the NH$_0$ vibration on the dimer. In §4.3.1, it was concluded that this mode is either dark or shifted out of resonance due to coupling between the two N—H's in the dimer. This was predicated on the fact that 1) neither the

NH_0–CO_1 nor the NH_0–$AmII_1$ cross peaks are evident in the magic angle spectrum, and 2) these peaks become obvious if the hydrogen-bond-donating molecule is deuterated. Here, we see that the NH_0 is not shifted out of resonance, nor is it completely dark though it is extremely weak. Rather, this feature seems to sit under the NH_0 band of the monomer, but is almost entirely masked by it.

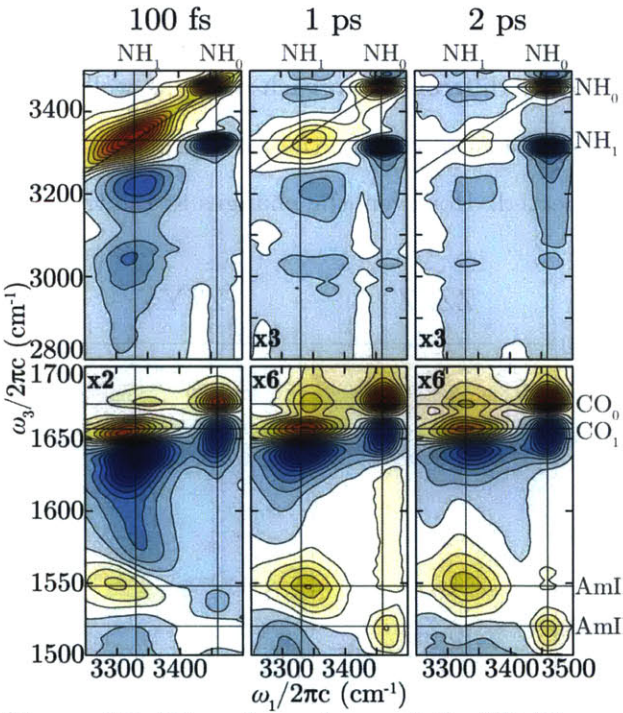

Figure 4.7: Time dependence of the 2D IR spectrum of 250 mM NMA.

Transition dipole angles in the dimer show significant differences compared to the monomer. In going from ZZZZ to ZZYY, the intensity of NH_1–$AmII_1$ cross peak relatively decreases as opposed to the NH_0–$AmII_0$ which increases significantly. This implies that the $AmII_1$ transition dipole is more parallel to the NH_1 transition dipole than their non-hydrogen-bonded counterparts. In some sense, this is intuitive: the force exerted by the hydrogen-bonding interaction ought to stiffen the potential of the N—H wagging motion and force less of the motion to be out of plane. This interpretation is consisted with the measured blueshift of the amide II mode upon hydrogen bonding. On the other hand, it appears as though the formation of a hydrogen bond has significantly changed the nature of the vibration such that the direction of charge flow, characterized by the transition dipole moment, is no longer the same direction. This effect is likely tied into the cooperative nature of the hydrogen-bonding interactions, which is in turn dictated by the electronic resonance structures of the amide group.

The C═O stretching region shows that the NH_1–CO_1 peak weakens, while the NH_1–CO_0 peak becomes comparatively more intense. This suggests that the CO_1 transition dipole is parallel to the NH_1 dipole while the CO_0 is perpendicular to it. If the two C═O bonds are not perfectly parallel in the dimer, that is, there is some small angle between them, then the symmetric stretch transition dipole will point along the major axis (due to the cancellation of off-axis components in the stretching motion) while the anti-symmetric stretching will be perpendicular to the major axis (due to the cancellation of the on-axis component of the motion). This effect is well-known in β–sheet secondary structures where the symmetric and anti-symmetric modes have transition dipoles perpendicular and parallel, respectively, with regard to the direction of the beta sheet [193–195]. Of course, in solution, the two molecules will not have a rigidly fixed orientation as two amide units in a β–sheet do, but there will be some average structure with a well-defined angle between the two C═O transition dipoles. The polarization anisotropy data shows that this average angle in solution is not zero (the dimer is not perfectly linear on average) and it further corroborates our interpretation of the magic angle spectrum (see §4.3.5).

4.5 Dynamics of the NMA Dimer

In order to obtain dynamical information, 2D IR spectra are measured as a function of τ_2. Figure 4.7 shows the spectrum of 250 mM NMA for τ_2 values of 100, 1000, and 2000 fs. A quick comparison shows that the monomer and dimer exhibit drastically different dynamics. Most notably, the NH_1 peak decays far more quickly than the NH_0 peak. This is expected, since the hydrogen-bonded N—H oscillators are coupled to a larger number of vibrational modes, both intra- and intermolecularly. Additionally, we see that the most strongly hydrogen-bonded oscillators (i.e., red-shifted in ω_1) relax most quickly –a feature which has been observed in many hydrogen-bonding systems [196–198]. This effect is likely due to the coupling to the amide II mode via the Fermi resonance interaction which gets stronger with increasing hydrogen-bond strength since the two come into better resonance. The NH_1–$AmII_1$ cross peak, which increases in intensity relative to the other features in time, suggests that the amide B to amide II path is efficient for relaxation. In addition to

NH_1 relaxing via amide II, the NH_0–$AmII_0$ cross peak intensifies with waiting time, showing that this is an efficient path for the non-hydrogen-bonded oscillators as well.

As waiting time increases, we see that all the peaks symmetrize and shift to the center of the band. By 2 ps, the NH_1–$CO_{0/1}$ and NH_1–$AmII_1$ peaks have shifted in ω_1 such that the peaks are centered at 3340 cm^{-1}. This spectral diffusion reflects the fact that frequency memory is lost on the ~1 ps timescale. That is, N—H oscillators which started either redshifted or blueshifted, have randomized their hydrogen-bond configuration such that there is no correlation between the initial frequency and the final one by 2 ps. We also note that we do not observe the growth of any new peaks which we may attribute to chemical exchange between free monomer and dimer as would be expected [37]. So although there is time for hydrogen bonds to fluctuate within a particular configuration, vibrational relaxation is rapid compared to hydrogen-bond formation or breaking.

In the remaining sections in this chapter, we take a more quantitative approach to characterizing the relaxation dynamics of the NMA monomer and dimer, and we contrast the difference between them with an emphasis on the effects of hydrogen bonding on the dynamics. This is done by integrating the various features in the 2D IR spectrum and fitting the resulting time traces to characterize how these features evolve in time.

4.5.1 Peak Dynamics in the 2D IR Spectrum

The relaxation of the N—H stretching modes are shown in Fig. 4.8A. Red points correspond to the integrated ESA of the NH_0 peak, while blue points correspond to the integrated ESA of the NH_1 band. The solid lines are the associated fits which are bi-exponential for the NH_0 feature and mono-exponential for the NH_1 feature. No significant difference in timescale was observe if the entire ESA of the NH_1 band was integrated or just the portion at frequencies higher than the AmB_1 feature.

The NH_0 ESA shows two timescales. The fast timescale, which is by far the fastest in the system, is 310 fs and contributes about 40% of the overall amplitude of the signal. The

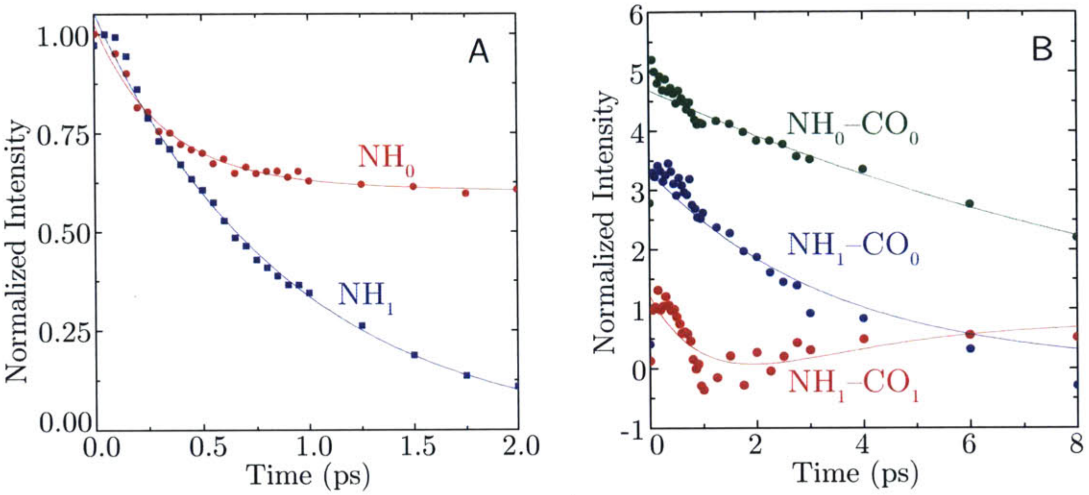

Figure 4.8: Relaxation traces for the amide A (A) and amide I (B) features in the NMA monomer and dimer.

remaining 60% is long-lived and does not decay appreciably on a 2 ps timescale,[6] which is the entirety of the x-axis of Fig. 4.8A. Therefore, fitting the long timescale is not reliable, but overall fits only converge to reasonable values if the long timescale is forced to have an upper bound of at least 10 ps. It is important to note that the data presented here is taken in the magic angle polarization scheme, and, as such, the fast component is not due to orientational effects.

The NH$_1$ feature is well described by a mono-exponential decay with a time constant of 890 fs. That this timescale is much faster than the long timescale of the free N—H is not surprising, as fast relaxation is a well-documented phenomenon in hydrogen-bonding systems [23, 199, 200]. In addition, the most redshifted oscillators efficiently mix with the amide B mode, resulting in a faster decay on the red side than the blue side. Integrating the ESA on the two sides separately (not shown) results in a 670 fs decay on the red side of the ESA and a 1.0 ps decay on the blue side. The faster decay on the red side is consistent both with the notion of stronger hydrogen bonds as well as a Fermi resonance interaction with the amide B mode.

The dynamics of the amide I region are more complex than the amide A region since population may both flow into and out of the various vibrational modes. In addition, multiple cascaded relaxation pathways, as well as strong coupling between different vibrations (e.g. coupling to amide II modes [158, 201]), mean that the relaxation will be all but a simple exponential. In principle, with consideration of all the "important" modes, one can construct a kinetic scheme that reproduces the data. However the identification of which modes are important is non-trivial since low-frequency modes are expected to contribute significantly and these are usually difficult to measure directly. Therefore we take a minimalist approach and only describe the largest differences between the amide I traces.

---

[6] Data was only collected to 2 ps in this region due to scattering of the sample.

The GSB of the NH_0–CO_0 cross peak (Fig. 4.8B, green data) shows rapid non-exponential dynamics at early times, but becomes fairly exponential after a few hundred femtoseconds. The exponential tail decays with a time constant of 12.4 ps. For strong coupling between modes, we expect that the cross peak and the diagonal peak to decay on the same time scale if population does not relax into the coupled mode. Since the cross-peak trace is exponential at long times and no increase in cross-peak intensity is observed, we expect that this is indeed the case and that the N—H stretch does not decay into the C=O bond. Furthermore, it stands to reason that the time constant of 12.4 ps is similar to the long-time tail of the NH_0 ESA which could not be accurately measured due to limited data in this region.

The GSB of the NH_1–CO_0 and NH_1–CO_1 cross peaks show qualitatively different behavior from each other (Fig. 4.8B, blue and red data, respectively). The NH_1–CO_0 and NH_0–CO_0 features show similar behavior in that the former shows exponential behavior after a few hundred femtoseconds and decays on a 3.4 ps timescale. That this is longer than the 890 fs decay of the NH_1 feature suggests that some amount of population from the NH_1 mode has leaked into the CO_0 mode, though this is hidden in the early-time dynamics. This population subsequently relaxes on a 3.4 ps timescale. It should be noted that this number may suffer somewhat from interference from the NH_1–CO_0 cross peak due to their proximity.

On the other hand the NH_1–CO_1 shows both a rapid decay of signal follow by a rise.

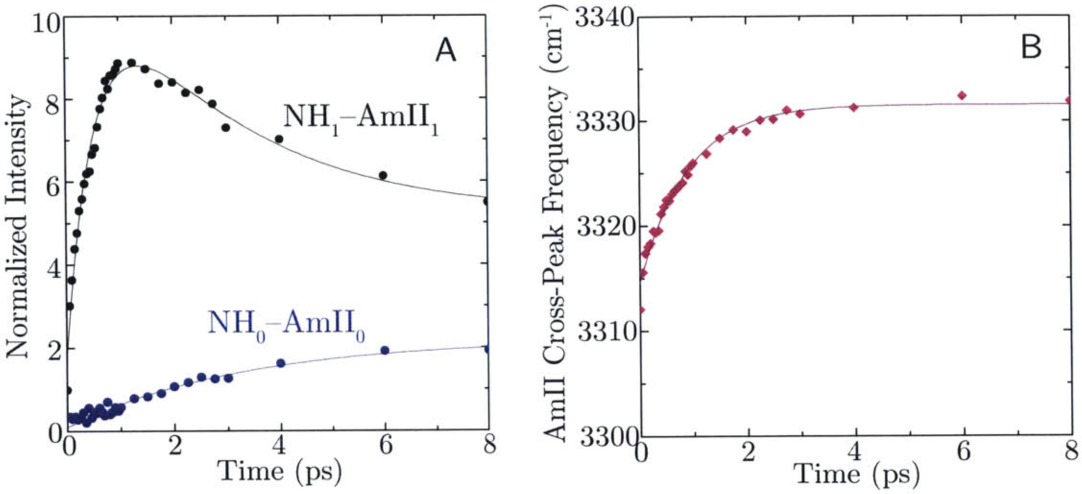

Figure 4.9: Relaxation traces for the amide II features (A) and ω_1 frequency shift of the NH$_1$–AmII$_1$ cross peak.

However, if the timescales associated with such a bi-exponential form are similar, it becomes difficult to fit accurately as many combinations of timescales can give a similar functional form as the position of the dip is mainly determined by the relative timescales. We therefore assume that the initial decay is associated with dynamics of the NH$_1$ mode and force the initial timescale to be that of the NH$_1$. This results in a rise of 3.4 ps which is identical to the decay of the NH$_1$–CO$_0$ feature.

Finally, we consider the amide II modes which, in a certain sense, show relatively clear-cut dynamics. The integral of the GSB for the NH$_0$–AmII$_0$ and NH$_1$–AmII$_1$ features are shown in Fig. 4.9A as blue and black points, respectively. The NH$_0$–AmII$_0$ cross peak starts at a value close to zero, and shows a mono-exponential rise on a 3.2 ps timescale suggesting that population is leaking into this mode. The fact that the growth timescale is not identical to the decay timescale of the NH$_0$ mode implies that there are multiple modes involved in the relaxation dynamics. These other modes can be intramolecular, such as C—H stretches and bends, or intermolecular energy transfer to the solvent. Within the 8 ps window over which data was collected, there is no evidence of a decay of the AmII$_0$ mode, suggesting that it is a relatively stable vibration and population relaxation from it occurs on a timescale longer than 10 ps.

The NH_1–$AmII_1$ mode shows markedly different behavior. Unlike the NH_1–$AmII_1$ feature (and as mentioned in previous sections), the NH_1–$AmII_1$ starts at a non-zero value implying that there is strong coupling between the hydrogen-bonded N—H stretch and its amide II mode. As a function of time, we then observe a rapid rise to roughly 4.5 times its initial value on a timescale of 540 fs followed by a slower decay of 2.7 ps. The fast rise implies that population is rapidly transferred to the amide II mode.

In addition to measuring the the change in magnitude of various features which report on relaxation, we may measure frequency shifts which report on fluctuations. In particular, frequency shifts in ω_1 of the hydrogen-bonding modes report on the fluctuations of the interaction and thus provide a fairly direct metric of the interaction dynamics. Congestion in the spectrum makes it impractical to do this for all features, but the $AmII_1$ peak, being relatively isolated is a good candidate. Fig. 4.9B shows the peak shift in ω_1 of the $AmII_1$ mode as calculated by tracking the first moment of the peak. The $AmII_1$ peak is initially at a value of 3315 cm^{-1} and shifts by 17 cm^{-1} to a final value of 3332 cm^{-1} on a 900 fs timescale. This implies that an oscillator initially in a strongly-hydrogen-bonded configuration explores more weakly-hydrogen-bonded configurations on a 900 fs timescale, and this gives a timescale for the fluctuations of the interaction. The fact that the peak shift timescale is longer than the NH_1–$AmII_1$ rise timescale suggests that this is not simply an effect of relaxation.

Table 4.1: Timescales associated with the NMA monomer and dimer.

Feature	First Timescale	Second Timescale
NH_0	310 fs	–
NH_0–CO_0	–	12.4 ps
NH_0–$AmII_0$	3.2 ps (rise)	NA
NH_1	890 fs	NA
NH_1–CO_0	–	3.4 ps
NH_1–CO_1	890 fs (decay, forced)	3.4 ps (rise)
NH_1–$AmII_1$	540 fs (rise)	2.7 ps (decay)
$AmII_1$ Peak Shift	900 fs (blue)	NA

The various timescales associated with the dynamics of the monomer and dimer are summarized in Table 4.1. An 'NA' in the table implies single exponential dynamics, while a dash implies that the timescale could not be measured in this study.

4.5.2 Relaxation of the NMA Monomer

At the outset, it is clear that extracting the vibrational dynamics from the 2D IR spectrum, even in a system as simple as the NMA monomer, is not straightforward. The various relaxation pathways and couplings (and even coherence transfers in certain system) make teasing the molecular vibrations out of the spectrum complicated. In addition, it is also necessary to take into account all the states that the experiment is dark to, either because they are outside the bandwidth of the pulse or have weak oscillator strength. Nonetheless, the timescales extracted are indeed related to molecular dynamics even if that relation is somewhat cryptic.

The most puzzling observation in the dynamics of the NMA monomer, is the fast 310 fs timescale associated with the NH_0 mode. This fast timescale seems to result in non-exponential dynamics of the low-frequency amide I features at early times. Given that the amide A mode is relatively isolated in frequency in the monomer, the fast dynamics were originally attributed to a vibrational Stokes shift in which reorganization of the solvent reduces the oscillator strength of the NH_0 vibration. In this mechanism, the excitation of the N—H bond, which results in a bond which is on average longer, displaces nearby solvent molecules to be on average further. This distancing of the solvent molecules is effectively seen as a reduction in local solvent polarity, which reduces the oscillator strength of the NH_0 vibration (due to the cooperative electronic effects, §4.1.2).

However, this interpretation is inconsistent with the relatively fast (3.2 ps) rise of the AmII_0 mode. If relaxation out of the N—H stretching mode truly occurred on a >10 ps timescale, it would not be possible to populate the AmII_0 mode on a timescale faster than this. Since the only timescale faster than 3.2 ps in the monomer is the fast relaxation of the NH_0, this is necessarily the source of the rise of the AmII_0 mode. In other words, the fast dynamics must be due to population that leaks out of the NH_0 mode and ends up in the $AmII_0$ mode. There are no bright states close to the NH_0 mode, but there are several dark states –namely, the overtones of the CO_0 and $AmII_0$ modes and their combination band. We attribute the fast timescale to a reversible leakage of population into the dark modes which is followed by irreversible decay to the $AmII_0$ mode that can be represented by

$$\mathrm{NH_0} \underset{k_2}{\overset{k_1}{\rightleftharpoons}} \mathrm{DS} \tag{4.16a}$$

$$\mathrm{DS} \overset{k_3}{\rightarrow} \mathrm{AmII_0}. \tag{4.16b}$$

In this scheme, DS can represent several dark states that can exchange population on relatively fast timescales. The solution of the kinetic equations for this system does indeed reproduce a fast initial decay followed by a slow decay of the NH_0 mode. The initial decay into the dark modes is fast since these are not initially populated and it is reversible since the energy gap between these is small (i.e. due to detailed balance [202]). The dark state manifold likely consists of at least three states, and their energy levels serve to fine tune the relaxation rates.

If the 2D IR spectrum reported only on populations, then Eqs. 4.16 would provide a good description of the dynamics. However, the coupling between various modes, which is as important as population transfer, means that the peaks in the 2D IR spectrum are not related to populations in a simple way. For example, it has been shown that amide I and II are strongly coupled [158], and as such, the population of one mode will affect the intensity and lineshape of the other. In principle, if all the couplings were known, then the kinetic equations could be used to reproduce the 2D IR spectrum.

4.5.3 Relaxation of the NMA Dimer

Oftentimes, if a system becomes complex enough, many of the fine details are washed over, and the 2D IR spectrum ironically seems more straightforward to interpret. This seems to be the case with the NMA dimer, which is in principle a far more complex system due to the hydrogen-bonding interaction. The NH_1 shows dispersive mono-exponential dynamics ranging from about 600 fs to 1 ps. The decay of the NH_1 stretch is accompanied by a rapid rise of the $AmII_1$ mode. We interpret the fast rise as being due to population relaxation from the NH_1 stretch to the $AmII_1$ mode. In fact, the $AmII_1$ mode rises on a similar timescale to the most redshifted N—H oscillators. This corroborates the interpretation that the Fermi resonance is essentially a relaxation funnel that drives population of the N—H stretch to the low-frequency amide II mode. Given that the rise timescale of the amide II mode is identical (within our errorbars) to the decay of the most redshifted NH_1 oscillators we conclude that almost 100% of strongly-hydrogen-bonded N—H oscillators decay via the $NH_1 \rightarrow AmB_1 \rightarrow AmII_1$ pathway.

The $AmII_1$ peak shift measurement shows that the hydrogen bond fluctuates on a 900 fs timescale. Therefore, it seems reasonable that the fluctuation of this interaction brings a weakly-hydrogen-bonded oscillator to a strongly-hydrogen-bonded one, resulting in a rapid decay via the Fermi resonance pathway. This explains why the peak shift and overall relaxation occur on such similar decays.

The amide I region is less straightforward to understand due to the congestion and overlap of the CO_0 and CO_1 features. We interpret the initial decay of the CO_1 features as the decay of a strong-coupling cross peak since it decays on the same timescale as NH_1 which decays to an intermediate state. Subsequently, some amount of population flows back into the CO_1 mode, resulting in a rise of the cross peak. This most likely originates from the CO_0 which appears to rise somewhat at early times, possibly due to a small amount of direct relaxation from the NH_1 mode.

Chapter 5

Resonances and Relaxation in Isotopically Dilute Water

5.1 Isotopically Dilute Water

5.1.1 Why Isotopically Dilute?

The study of liquid water is incredibly complex. In a minimalist picture, liquid H_2O is a network of strongly coupled resonant anharmonic oscillators whose characteristic motions occur on the 10 fs to 1 ps timescale. As such the challenges associated with studying liquid water are significant and originate almost entirely due to the hydrogen bond. Unfortunately, there is not much that can be done to liquid water to alter this complexity. The interactions between molecules cannot be modified significantly barring temperature changes, and even then, they can only be modified slightly.

Isotopically dilute water provides something of a solution to the challenge by removing a layer of complexity. By dissolving a small amount of HOD in either D_2O or H_2O, and probing the dilute oscillator, the resonant interaction between molecules is effectively removed. Since the dilute oscillator is far from resonance with the surrounding oscillators, the effect of the intermolecular and intramolecular coupling is significantly diminished, and the the vibration is essentially localized onto the bond. This offers a local probe of structure and dynamics, and in most cases, offers a greatly simplified picture of the molecular details.

The main question then is how accurately the structure and dynamics of isotopically dilute water resembles that of isotopically pure water. On the one hand, it is obvious that the dynamics of the isolated oscillator do not reflect the dynamics of the highly-coupled oscillators in the isotopically pure case. The dynamics of the latter are delocalized over multiple molecules and intimately tied to the local structure of the liquid, whereas the dynamics of the dilute HOD oscillator are only sensitive to a highly local interaction potential. This is not to say that studies of dilute HOD are not without merit, however. The local nature of the isotopically dilute oscillator provides a sensitive probe of the interactions between water molecules, which, barring nuclear effects, reflect the interaction between isotopically pure molecules. Furthermore, isotopically dilute water provides a unique opportunity to study isolated vibrations in a hydrogen-bonding liquid, which is an intrinsic utility in it of itself.

To make HOD, we appreciate that a mixture of H_2O and D_2O does not stay as such. Proton transfer rapidly scrambles the protons and deuterons of the molecules in an reaction of the form

$$\mathrm{H_2O} + \mathrm{D_2O} \rightleftharpoons 2\mathrm{HOD}, \tag{5.1}$$

which proceeds with an equilibrium constant of K. This reaction necessarily implies that HOD cannot exist in isolation, which poses a challenge to studying its properties in the liquid phase. If the reaction were entirely random, that is, if the reaction were solely entropically driven, the value of K would be exactly 4. This can be understood, for example, if we consider a 50:50 mixture of H_2O and D_2O which for a random reaction would give a 1:1:2 mixture of H_2O:D_2O:HOD. This is not the case, however, and the actual equilibrium constant is found to lie in the range of $K = 3.75$–3.86 [203–205]; that is, the unmixed species are more energetically stable than the mixed ones. This effect has been attributed to differences in the anharmonic shifts of the zero-point energy between the different isotopologues [206].

If x_0 is the initial mole fraction of H_2O, then the final concentrations are given by solving the equilibrium:

$$x_{H_2O} = x_0 - x \tag{5.2a}$$

$$x_{D_2O} = 1 - x_0 - x \tag{5.2b}$$

$$x_{HOD} = 2x, \tag{5.2c}$$

with

$$x = \frac{K}{2(4-K)}\left(\sqrt{1 + \frac{4(4-K)x_0(1-x_0)}{K}} - 1\right). \tag{5.3}$$

Since $K < 4$, x cannot reach 0.25 for any initial concentration, and as such, the concentration of HOD is always below 0.5. If x_0 is close to either zero or one, corresponding to mostly D_2O or H_2O respectively, then a binomial approximation of the square root in Eq. 5.3 shows that $x \approx x_0$ corresponding to a concentration of HOD of $2x_0$. In this dilute limit, each dilute water molecule breaks up into two HOD molecules, as is intuitively expected.

This chapter is almost entirely based off of a paper published in *The Journal of Physical Chemistry B* in 2013 [196]. The advent of broadband IR probing in 2D IR afforded us with the possibilty of monitoring relaxation dynamics of the O—H stretch of isotopically dilute HOD in D_2O while simultaneously monitoring the HOD bending mode. In doing this, we observed Fermi resonances between the streching and bending modes in both the ground and excited states that manifested themselves as cross peaks in the 2D IR spectrum. We also showed that relaxation proceeds via these Fermi resonances in a stretch-to-bend mechanism before ultimately relaxing to low-frequency modes.

5.1.2 What has been done?

Given its enormous utility as a proxy for pure water and as a model hydrogen-bonding liquid, it is no wonder that isotpoically dilute water has been studied extensively in the literature. In particular, the ability of IR spectroscopy do distinguish hydrogen-bonding configurations has made it an indispensable tool. It is a well-accepted fact that the O—H stretching frequency of isotopically dilute HOD in D_2O is highly sensitive to its local environment. In particular, the frequency of the O—H stretch is extremely well correlated with the electric field projected along the O—H bond which is, in turn, almost entirely determined by the hydroxyl's hydrogen-bond configuration [15, 25, 26, 207]. Hydroxl oscillators in strongly-hydrogen-bonded configurations tend to absorb at lower frequencies, while oscillators in weakly or non-hydrogen-bonded configurations absorb at higher frequencies. The HOD bending mode shows the opposite trend and blueshifts upon formation of strong hydrogen bonds [208]. These opposing frequency trends for forming hydrogen bonds results in the bend overtone coming into better resonance with the O—H stretching mode since the former blueshifts while the latter redshifts as the hydrogen-bond strength is increased. This is expected to have a profound impact on the vibrational dynamics of these modes.

Since the frequency of the O—H stretch is so highly correlated with its local structure, it has escaped no one that following these frequencies on the timescales associated with the reorganization of the liquid would provide a direct measurement of the molecular dynamics [31, 209]. The earliest time-resolved studies of dilute HOD were made as soon as the technology to produce picosecond pulses in the mid-IR was available. The first study was performed as a transient spectral hole burning measurement in which the O—H stretching band was excited at different frequencies, and the resulting changes in absorption were monitored [210]. The authors concluded that the population relaxation out of the O—H stretch occurred on a 8 ps timescale and that multiple sub-populations of HOD could be identified. These studies were unable to make accurate measurements of the dynamics due to the limited time resolution offered by the picosecond pulses. With the ability to generate sub-picosecond pulses, a burst of TA studies were published that refined the previous work and reported evidence for local substructures of HOD in D_2O and population relaxation timescales ranging from 0.7–1.0 ps [197, 211–214]. Vibrational relaxation of HOD in H_2O was found to occur on a longer 1.5 ps timescale [215].

Once these experiments could be performed with high fidelity, the relaxation mechanism of the O—H stretch was examined. The earliest study to probe the relaxation mechanism using TA spectroscopy concluded that the O—H stretch relaxed primarily to the intermolecular hydrogen-bonding modes [216,217] at a level sufficient to cause vibrational predissociation. Shortly thereafter, however, IR-Raman experiments were used to show that the O—H stretch relaxed primarily to the HOD bending mode, which subsequently relaxed to low-frequency hydrogen-bonding modes [218,219]. These measurements inferred the relaxation pathway and could not directly correlate the stretch and the bend. The stretch-to-bend relaxation mechanism was also supported by direct measurement of the HOD bending lifetime of ~400 fs [220].

As coherent techniques became available, the community saw a shift in the interpretation of the vibrational spectroscopy of HOD. These studies showed sub-100 fs dephasing of the O—H stretch vibration [221]. In addition, studies measured two distinct timescales of the decay of frequency correlations: a fast 130–340 fs timescale associated with the fluctuations and breaking of a single hydrogen bond and a slow 0.9–1.4 ps timescale associated with collective rearrangement of the hydrogen-bond network [15,222–224].

2D IR measurements of HOD in D_2O [33,34,225–228] and HOD in H_2O [32,229–231] were performed shortly thereafter. With the ability to accurately extract quantities such as the frequency-frequency correlation function and time-dependent lifetimes, these measurements confirmed previous ones. Most importantly, however, with these measurements the notion of substructure in liquid water fell out of favor when it was shown that the non-hydrogen-bonding configurations were but transition states that live for less than 200 fs [225]. Now, for the most part, people view liquid water as taking on a continuum of structures from hydrogen bonding to weakly hydrogen bonding that rapidly interchange on the femtosecond timescale.

In addition to the enormous effort to understand the structure of liquid water, there has been an equally tremendous effort to understand reorientation of the dilute oscillator of HOD in order to give insight into the hydrogen-bond switching mechanism. These measurements have largely been performed using TA polarization anisotropy [211,212,223,232–234] and, more recently, 2D IR polarization anisotropy [184,235,236]. The measurements show a fast 50–70 fs component associated with loss of orientational correlation due to interial librational motion and a slow 2.7–3 ps component associated with large-scale rearrangement of the hydrogen-bond network. Furthermore, by using 2D IR to correlate the orientation of the inital and final hydrogen-bonding state, it was shown that water molecules undergo large-angle reorientation when switching hydrogen-bonding partner [236], with jump angles of at least ~20°.

Finally, it is necessary to mention the incredible body of computational work that has accompanied the experimental developments. From the initial molecular dynamics (MD) simulation of 216 water molecules [237] is was clear that such simulations would be indispensable for understanding liquid water. Since then, the number of force fields developed to describe water has exploded [238], with the extended simple point charge (SPC/E) model finding particular use in IR spectroscopy [239]. Of course, classical dynamics simulations of water alone are not enough to compute the IR absorption spectrum and nonlinear spectrum of liquid water. To that end, it is necessary to adopt a formalism to calculate the relevant correlation functions. There are indeed at least as many methods as there are MD force fields and we refer to Ref. [240] and references therein for details.

5.1.3 Sample Preparation

Isotopic water solutions were prepared by mixing H_2O, purified by reverse osmosis (to a resistance of 18 MΩ), with D_2O (>99.96%d, *Cambridge Isotope Laboratories*) in a ratio of 1:99. This results in a ~2% mole fraction (1.67 M) solution of HOD in D_2O, with a negligible amount of H_2O present (~0.1%). Samples were held between two 1 mm thick CaF_2 windows separated by a 50 µmTeflon spacer. To avoid spectral distortions caused by the non-resonant electronic response of the CaF_2 windows, we studied spectral features only for waiting times equal to or longer than 100 fs.

5.2 The Linear Absorption Spectrum of HOD

The normalized linear IR absorption spectra for 2% HOD in D_2O (black curve) and pure D_2O (red curve) are shown in Fig. 5.1A. The D_2O spectrum shows three principle features: a broad peak at 2505 cm^{-1} corresponding to the O—D stretching vibrations, a narrower peak at 1210 cm^{-1} corresponding to the DOD bending mode, and a broad low-intensity feature at 1555 cm^{-1} that is attributed to a combination band of the bending and the ~400 cm^{-1} librational mode [178].

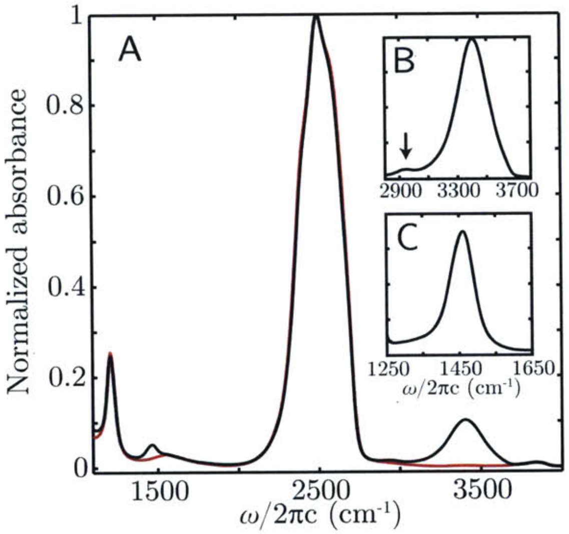

Figure 5.1: Linear absorption spectrum of 2% HOD in D_2O and neat D_2O.

The spectrum of HOD in D_2O shows additional features corresponding to the O—H stretch, centered at 3405 cm^{-1}, and the HOD bend at 1460 cm^{-1}. However, the O—D stretch of the HOD molecule is masked by the intense D_2O stretching absorption. In addition to these intense features, a weak peak is observed at 2950 cm^{-1}, which has been assigned to the overtone of the HOD bend [178, 210, 219]. Correction for the background absorption of the O—D stretch yields a center frequency of 2925 cm^{-1} for the overtone peak, and the background-corrected spectrum is shown in Fig. 5.1B; the arrow indicates the overtone peak. Given that overtone transitions of vibrations are weak compared with the fundamental transitions, it is surprising that the HOD bend overtone would be visible in the absorption spectrum at all. This suggests that the oscillator strength of the bend overtone is increased by mixing with other modes, namely, the O—H stretch, O—D stretch, or solvating D_2O molecules. On the basis of the common observation of Fermi resonance enhancements (see §4.3.3) in IR spectra for methyl and methylene [176, 241] and other hydride stretching vibrations [177] that have near 2:1

frequency ratios between stretch and bend, it is likely that this interaction exists for the HOD molecule as well.

Interestingly, while Fermi resonances can exist between the HOD bend and either O—H or O—D vibrations, the stretch oscillators that mix with the bend most strongly must have different hydrogen-bonding interactions to optimize the resonance condition. The general trends for shifts in the frequency of stretch, bend, and their overtones and combination bands as a function of hydrogen bonding interactions are summarized schematically in Fig. 5.2. As a hydroxyl oscillator engages in an increasingly strong hydrogen bond, the O—H stretch frequency redshifts and comes into better resonance with the HOD bend overtone at 2925 cm^{-1}. O—D stretch oscillators are in better resonance with the HOD bend overtone when they are weakly hydrogen-bonded or blueshifted. Because the bend frequency will, to a large extent, be determined by both of these hydrogen bonds, simple correlations between the hydroxyl hydrogen bond and HOD bend frequency are not expected. However, it can be said that HOD molecules with strong O—H hydrogen bond and weak O—D hydrogen bonds will have the most mixed vibrations. Based solely on its frequency shift from the stretching vibrations it is equally likely that both the O—H (3405 cm^{-1}) and O—D stretching vibrations (2505 cm^{-1}) couple to the HOD bend overtone. We note that this is very different from the HOD-bend Fermi resonance in the gas phase, where the bend overtone is in almost perfect resonance with the O—D stretch but ~1000 cm^{-1} off-resonance with the O—H stretch. Therefore, while the cubic force constant between the O—H stretch

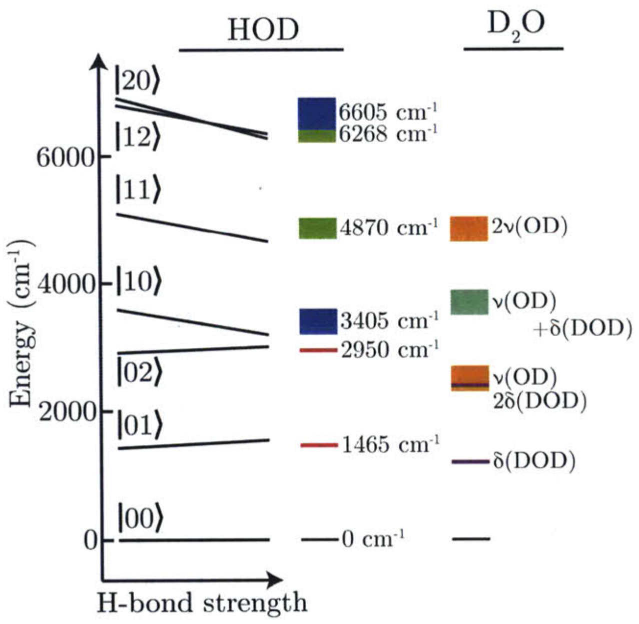

Figure 5.2: Energy levels of isotopically dilute HOD in D_2O as a function of hydrogen-bond strength.

and the HOD bend overtone in the gas phase has been calculated to be 171 cm^{-1}, the effect of this coupling is expected to be small due to the large splitting between the two states [242].

5.3 Nonlinear Spectroscopy of HOD in D_2O

5.3.1 Diagonal Features in the Early-Time Spectrum

Transient absorption (TA) and 2D IR spectra allow us to probe the spectrum of states that are typically not accessible in the linear spectra, including excited state absorptions (ESAs) and cross peaks that reflect coupling between various states. The TA spectrum upon excitation of the O—H stretch at 3400 cm^{-1} for $\tau_2 = 100$ fs and $\tau_2 = 6$ ps and the 2D IR spectrum for $\tau_2 = 100$ fs of HOD in D_2O are shown in Figs. 5.3 and 5.4, respectively. Even at the earliest waiting times, ground state bleaches (GSBs) and ESA features appear in all spectral regions in the TA and 2D IR spectra. These are located not only at transition frequencies observed in the linear spectrum, which are clearly due to stretching and bending modes, but also at frequencies whose assignments are not clear and may originate in the D_2O solvent.

At frequencies above 2750 cm^{-1}, in the O—H stretching region, the 100 fs TA spectrum shows a prominent bleach as well as two distinct ESA peaks. The GSB at 3400 cm^{-1} is due to the pump-induced depopulation of the O—H stretch ground state as well as stimulated emission induced by the probe from the first excited state of the O—H stretch. The ESA centered at 3120 cm^{-1} is the transition from the first to second excited state of the O—H stretch. This feature is redshifted from the bleach of the fundamental transition due to the anharmonicity of the nuclear potential of the O—H bond.

The GSB and ESA features overlap, so it is not possible to determine the anharmonicity and center frequencies directly. To do so, the three features are fitted to Gaussians, shown in Fig. 5.3A. The anharmonicity of the O—H stretch is taken to be the difference of the center frequency of the Gaussians. This procedure yields a GSB centered at $\langle\omega_{10}\rangle = 3375$ cm^{-1}

and an ESA centered at $\langle\omega_{21}\rangle = 3200\ \text{cm}^{-1}$, which leads to an anharmonic shift of 175 cm^{-1}. Because fitting data to the sum of overlapping Gaussians of opposite sign is typically not robust, we calculated constrained fits where the anharmonicity was held constant and the width of the fundamental bleach was forced to match the linear spectrum. Using the sum of the squares of the residuals to quantify the goodness of the fit, anharmonicities of $190 \pm 20\ \text{cm}^{-1}$ gave a reasonable fit. While this value is consistent with the near IR spectrum [243] and in reasonable agreement with cluster based DFT calculations [244], it is significantly lower than the 250 cm^{-1} value that was reported previously and used to argue that the O—H potential is predissociative with two quanta of excitation [216, 217, 245].

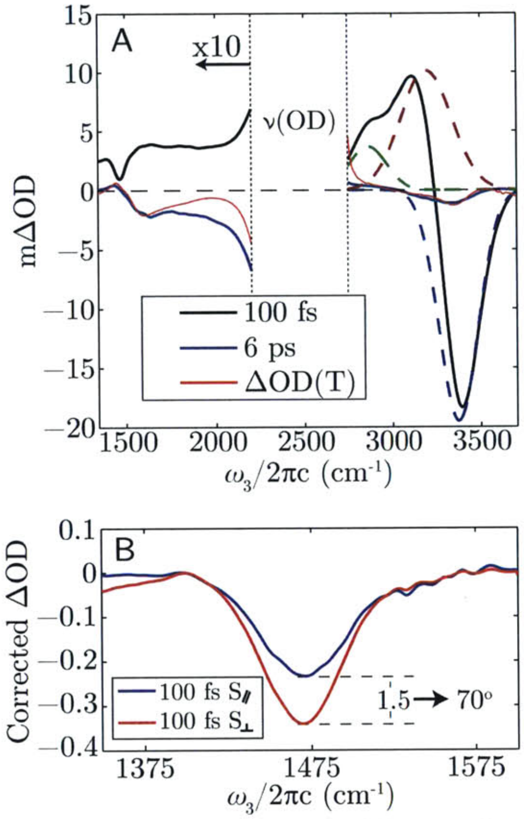

Figure 5.3: TA spectrum of HOD at early and late times (A) and bend cross peak for parallel and perpendicular polarizations (B).

A second ESA peak appears as a shoulder on the ESA of the hydroxyl stretch and is centered at 2860 cm^{-1}, as determined from the Gaussian fit. Given that this feature is not observed in the linear spectrum and is at the energy of the HOD bend overtone, we are led to conclude that it results from a $|\nu_\text{s}\nu_\text{b}\rangle = |10\rangle \rightarrow |12\rangle$ transition, which has significant intensity due to a stretch-bend Fermi resonance (see §4.3.3) in the excited state. Here and in what follows in this chapter, the states of the system are labeled $|\nu_\text{s}\nu_\text{b}\rangle$, where ν_s refers to the number of quanta in the O—H stretching mode and ν_b is the number of quanta in the HOD bending mode. From picosecond TA experiments it was concluded that this feature arises due to energy transfer from the O—H stretch to the HOD bend overtone [211]; however, the femtosecond time resolution in our experiment shows there is an immediate bleach indicating true anharmonic coupling. Unlike the lower energy $|10\rangle$ and $|02\rangle$ states, the large anharmonic shift of the stretch relative to the bend results in the stretch overtone $|20\rangle$ ($\sim$6575 cm^{-1}) being in near-resonance with the $|12\rangle$ state, and fluctuations in hydrogen-bond strength likely cause the two states to cross in energy. The intersection of these states is illustrated in Fig. 5.2.

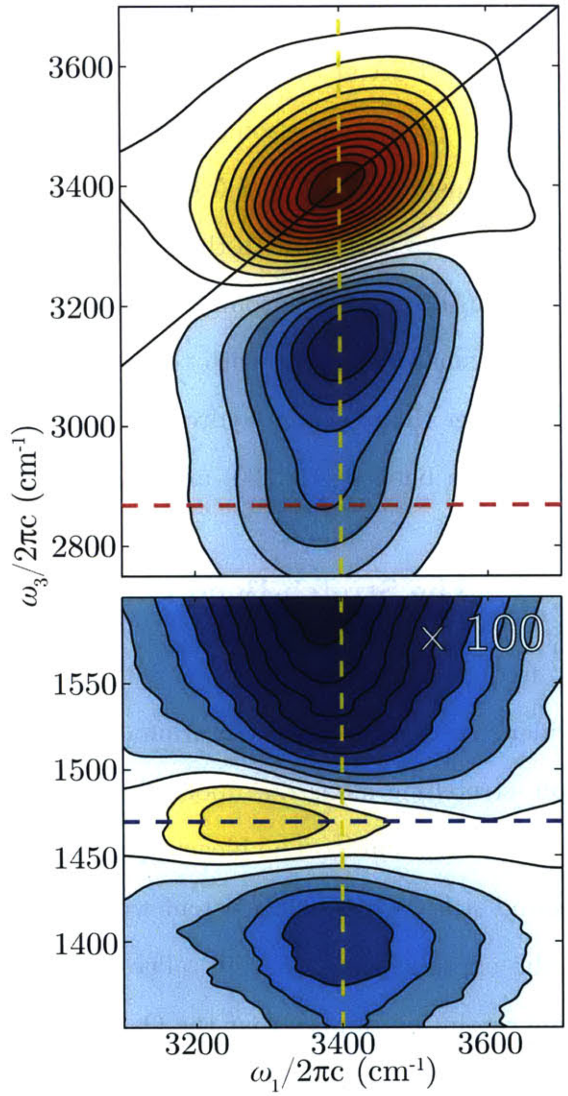

Figure 5.4: 2D IR spectrum of 2% HOD in D_2O.

Comparison of the $|10\rangle \rightarrow |12\rangle$ and $|00\rangle \rightarrow |02\rangle$ transition frequencies shows that O—H stretch excitation leads to a bend overtone redshift of $\sim$90 cm^{-1}. In the idealized case of harmonic oscillators coupled by an exact 2:1 Fermi resonance, the energy shift of an overtone that results from exciting one quantum of the coupled mode is twice the strength of coupling, $\Delta = -2X_{122}$, where the Fermi resonance coupling potential is $V_{\mathrm{FR}} = X_{122}(a_1 a_2^{+} a_2^{+} + a_1^{+} a_2 a_2)$. The resulting 45 cm^{-1} is an upper bound on X_{122} but neglects any other off-diagonal terms. In the gas phase, this shift is only 16 cm^{-1} despite X_{122} being 60 cm^{-1} [242]. This supports strong mixing between the $|20\rangle$ and $|12\rangle$ states in the liquid phase. This coupling is accompanied by a shifting of oscillator strength from the nominally bright transition ($|\nu_{\mathrm{s}}\nu_{\mathrm{b}}\rangle = |10\rangle \rightarrow |20\rangle$) to the dark transition ($|\nu_{\mathrm{s}}\nu_{\mathrm{b}}\rangle = |10\rangle \rightarrow |12\rangle$). This redistribution results in the $|10\rangle \rightarrow |20\rangle$ ESA being only $\sim$70% the intensity of the $|00\rangle \rightarrow |10\rangle$ GSB, with the other

$\sim$30% being in the $|10\rangle \rightarrow |12\rangle$ ESA.

The additional resolution of the pumping frequency in 2D IR provides greater insight into the Fermi resonance between the $|20\rangle$ and $|12\rangle$ states. In Figure 5.4, the bleach of the $|00\rangle \rightarrow |10\rangle$ fundamental transition is peaked at $(\omega_1, \omega_3) = (3400\ \text{cm}^{-1}, 3400\ \text{cm}^{-1})$ and appears elongated along the diagonal due to inhomogeneous broadening, while the ESA of the $|10\rangle \rightarrow |20\rangle$ transition is centered at (3400 cm^{-1}, 3140 cm^{-1}). The spectrum in this region is in good agreement with previous work [33, 226–228]. As in the TA spectrum, the $|10\rangle \rightarrow |12\rangle$ ESA at (3375 cm^{-1}, 2870 cm^{-1}) appears just below the $|10\rangle \rightarrow |20\rangle$ transition in ω_3 but peaked at a somewhat lower excitation frequency than the GSB. This is most clearly illustrated in Fig. 5.5 by the comparison of a slice of the 2D IR spectrum taken at $\omega_3 = 2870\ \text{cm}^{-1}$ (red) with the linear absorption spectrum (black) and the spectrum of the pump pulse (pink background). While the $\sim$30 cm^{-1} redshift of the $|10\rangle \rightarrow |12\rangle$ transition in ω_1 is small compared with the O—H line width, it does indicate that O—H oscillators in stronger than average hydrogen-bond configurations have an enhanced Fermi resonance interaction between the $|20\rangle$ and $|12\rangle$ states.

5.3.2 The Stretch-Bend Cross Peak and Off-Diagonal Features

At frequencies below 2200 cm^{-1}, the TA and 2D IR spectra for $\tau_2 = 100$ fs show clear evidence of stretch-bend vibrational coupling. Both spectra show a broad induced absorption, stretching along ω_3, upon which we see a narrow bleach of the HOD bend, centered at $\omega_3 = 1470\ \text{cm}^{-1}$. The bleach arises from pump-induced depopulation of the vibrational ground state, which is consistent with the observations from picosecond IR-pump/Raman-probe experiments [218, 219]. The immediate observation of the bleach with our <70 fs time resolution implies that the O—H stretch and HOD bend are strongly coupled. In the weak coupling limit, the cross peak would grow in with waiting time as population relaxes from the O—H stretching mode to the lower lying bending mode. Instead, a cross peak is observed immediately upon excitation, implying that the "O—H stretching" vibration is mixed with bend degrees of freedom as well.

This strong interaction is somewhat surprising given that stretch and bend fundamentals are split by $\sim$2000 cm^{-1} but is consistent with a Fermi resonance between the HOD stretch and bend states. The Fermi resonance between $|10\rangle$ and $|02\rangle$ shifts the $|10\rangle$ state to higher frequency, which results in the $|00\rangle \rightarrow |01\rangle$ and the $|10\rangle \rightarrow |11\rangle$ transitions having different frequencies. This effect should result in a cross peak in the transient spectra between the redshifted O—H oscillators and the bend. The blueshift of this bleach relative to the linear spectrum suggests that the strongly-hydrogen-bonded oscillators are most strongly coupled to the O—H stretch. The TA and 2D IR spectra clearly show the stretch-bend cross peak overlapped with a broad induced absorption that extends more than 1000 cm^{-1} from the low-frequency edge of the O—D stretch absorption to frequencies well below the bending vibration.

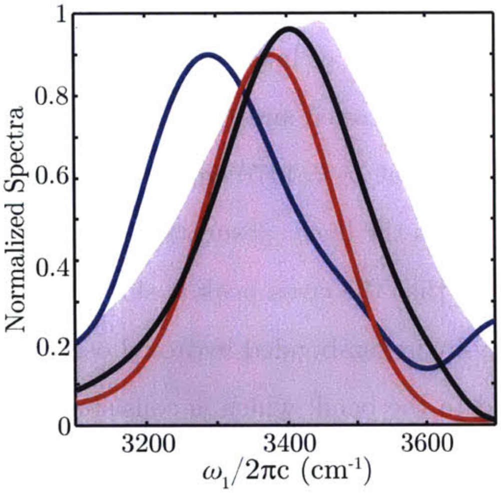

Figure 5.5: Slices through the 2D IR spectrum of HOD taken at constant $\omega_3 = 2870$ cm^{-1} (red line) and $\omega_3 = 1470$ cm^{-1} (blue line). The linear absorption spectrum is shown in black and the pump spectrum is the pink background.

Polarization-dependent TA measurements of the bend bleach at $\tau_2 = 100$ fs are shown in Fig. 5.3B. After using a linear correction for the background, we observe that the depth of the bleach increases by 150% going from ZZZZ to ZZYY polarization. This ratio of bleach intensities corresponds to a projection angle of $\sim$70° between the transition dipole moment of the O—H stretch and the HOD bend (see §2.5.5, Eq. 2.73, and Fig. 2.9). This angle is considerably larger than the half angle between the bonds, which is expected from the fact that the O—H transition dipole moment is observed to be offset from the hydroxyl bond by $\sim$20° in the gas phase [246] and from the small oscillation amplitude of the deuterium compared with hydrogen in the bending mode.

The 2D IR spectrum provides insight into the nature of the coupling between the stretch and the bend. The cross peak is asymmetric, with its peak at (3290 cm^{-1}, 1470 cm^{-1}) and a tail that extends to high frequency in ω_1. Overall, the peak is weakly anticorrelated with the O—H stretch, with the cross peak absorbing at $\omega_3 = 1455$ cm^{-1} for blue-stretch excitation but at $\omega_3 = 1475$ cm^{-1} for red-stretch excitation. This anticorrelation reflects the trend of the bending mode blueshifting upon the O—H forming stronger hydrogen bonds, as is evident from the temperature dependence of the linear spectrum [208]. The fact that the cross peak is not centered at the center frequency of the pump or linear spectrum suggests that there is a frequency-dependent coupling between the stretch and the bend. The blue line in Fig. 5.5 shows a slice of the 2D IR spectrum taken at $\omega_3 = 1470$ cm^{-1}, which shows that the cross peak is peaked 115 cm^{-1} to the red of both the linear absorption (black line) and the pump spectrum (pink background). The fact that the cross peak is shifted to the red side of the O—H stretch shows that the strongly-hydrogen-bonded hydroxyl oscillators (i.e., the redshifted ones) are more strongly coupled to the bend, which is consistent with O—H stretch-HOD bend coupling arising from a Fermi resonance.

Typically cross peaks in nonlinear vibrational spectra appear in doublets: a bleach corresponding to the depopulation of the vibrational ground state and an ESA corresponding to an excited-state transition. From the 100 fs TA spectrum in Fig. 5.3A and the 2D IR spectrum in Fig. 5.4, no ESA as narrow as the bleach of the bend transition is evident, making assignment of a $|\nu_s\nu_b\rangle = |10\rangle \rightarrow |11\rangle$ transition ambiguous. This would suggest that the $|\nu_s\nu_b\rangle = |10\rangle \rightarrow |11\rangle$ transition has little oscillator strength, has a frequency that is outside our detection range, or is extremely broad. Of these three possibilities, the last one is the most likely. Overall the TA spectrum between $\omega_3 = 1350$ and 2000 cm^{-1} appears as a bleach of the bend superimposed on a broad background that gently peaks in the bend region. Fitting can be used to estimate that its maximum is near 1660 cm^{-1}; however, significant overlap with the response of the O—D stretch makes it difficult to confidentially assign a frequency to this feature. A closer look at the 2D spectrum in the same region reveals that the peak excitation frequency (ω_1) for a given detection frequency (ω_3) is weakly anticorrelated, as would be expected for stretch-bend coupling. These observations suggest that the broad background possibly involves transitions to a broad distribution of stretch-bend combination bands that have distinct bend character.

Additionally, one cannot neglect the influence of the O—D stretching vibration of the HOD or the solvating D_2O molecules. The energy of the HOD $|11\rangle$ state is expected to be near or slightly lower than the sum of the stretch and bend fundamentals (4865 cm^{-1}). This is essentially in perfect resonance with the overtone of the O—D stretch [247]. Coupling between the $|11\rangle$ state and the solvent ought to be extremely efficient, which contributes to the extreme broadening of the $|\nu_s\nu_b\rangle = |10\rangle \rightarrow |11\rangle$.

With the TA and 2D IR spectrum at hand, we are in a position to assign frequencies to most of the energy levels for the bend and O—H stretch vibrations of HOD in Fig. 5.2, using bands to represent broadening as a result of hydrogen bonding or vibrational coupling within the liquid. The frequencies shown are obtained from the linear or nonlinear IR spectra, except for the $|11\rangle$ state, where we report the sum of the $|01\rangle$ and $|10\rangle$ states. The correlation of the bending states with hydrogen-bond strength is somewhat exaggerated in Fig. 5.2 because the effect of the hydrogen bonding of the HOD deuteroxyl oscillator is not taken into account. We see that the $|20\rangle$ and $|12\rangle$ states cross in energy for strong enough hydrogen bonds, while the $|10\rangle$ and $|02\rangle$ states never actually cross. Adding bands to reflect the vibrational modes of liquid D_2O emphasizes that HOD cannot be considered in isolation, as the former can strongly affect the latter. This is expected to be especially important for the D_2O stretching overtone, which is coincident with the HOD stretch-bend combination band and any intramolecular hydroxyl-deuteroxyl coupling.

5.4 Relaxation Dynamics of the O—H Stretch

The vibrational relaxation processes that occur over 6 ps after O—H stretch excitation, characterized through TA measurements, are presented in Fig. 5.6.

Figure 5.6A illustrates that vibrational relaxation processes are observed at all frequencies, and representative slices taken at individual frequencies are shown in Fig. 5.6B.

Qualitatively, the relaxation time scales for probe frequencies >2800 cm^{-1} appear complete within 2 to 3 ps, whereas those below 2200 cm^{-1} are noticeably longer. From the 100 fs TA spectrum, shown in Fig. 5.3, relaxation processes evolve toward a TA spectrum that resembles a thermal difference spectrum at long waiting time. Fig. 5.3 shows a comparison of the $\tau_2 = 6$ ps TA spectrum with the 23–20°C linear difference spectrum, showing that this close similarity, observed originally in the stretch region [33, 216] extends to all probe frequencies. The so-called hot ground-state (HGS) spectrum has been attributed to the local heating of the sample due to the relaxation of the excitation generated by the pump pulse [199,215,224], resulting in the overall weakening in the hydrogen-bond strength in the liquid and the observed blue shift of the O—H stretch [248]. Although this is a non-equilibrium system, the appearance of the HGS clearly implies that the O—H stretch vibrational excitation is transferred into kinetic energy of the intermolecular motions of the liquid, leading to the average weakening of hydrogen bonds. Similarly, a blue shift of the O—D stretch is evident from either side of the uncollected region in the TA spectrum: the 2750 cm^{-1} side appears as a rising edge and the 2200 cm^{-1} side shows a bleach corresponding to a blueshifted deuteroxyl stretch. In the bending region, the HGS response is dominated by the redshift of the D_2O bend-libration combination band, which is centered at 1555 cm^{-1} in the linear spectrum, rendering the expected redshift of the HOD bend unobservable at the working concentration.

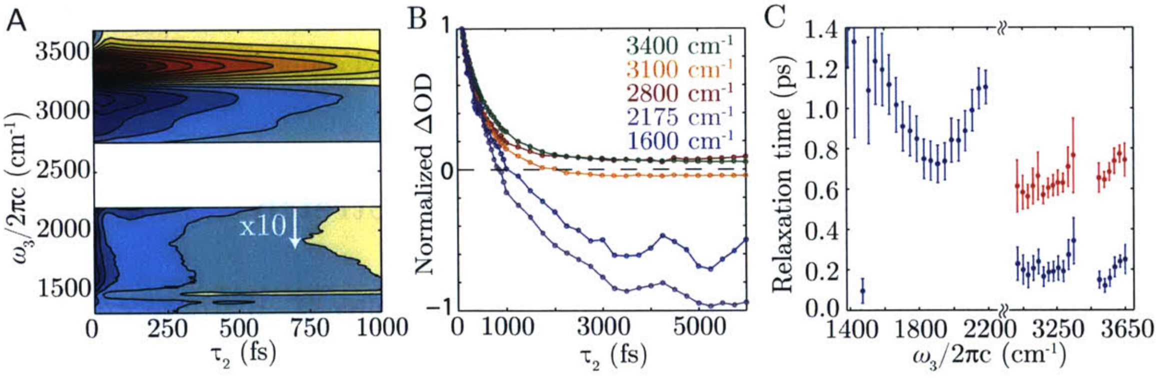

Figure 5.6: (A) TA spectrum of HOD and (B) normalized slices through the TA spectrum taken at constant ω_3 values. (C) Dispersive relaxation rates of the O—H stretch.

5.4.1 Dispersive Relaxation

To extract frequency-dependent relaxation rates, we fit slices of the TA spectrum for constant ω_3 using robust nonlinear least-squares regression using the trust region algorithm as implemented in MATLAB. All transients are only fit for τ_2 values larger than 100 fs to avoid distortions induced by the nonresonant electronic response of the CaF_2 windows that dominates the nonlinear response in the region of pulse overlap. The relaxation of the HOD features is well-fit by either a mono- or bi-exponential. Time scales from these fits are reported in Fig. 5.6C.

The decay of the O—H stretch bleach has a low amplitude fast component with an average time scale of 190 ± 10 fs but is dominated by a slow time scale of 700 ± 20 fs. In previous studies the latter was attributed to the population relaxation of the O—H stretch and the former to the fast intermolecular motions of the hydrogen-bonded HOD molecule [223]. As is evident from Fig. 5.6C, the slow relaxation time scale for the bleach of the O—H stretch is weakly frequency-dependent and changes linearly at a rate of $\sim$1.5 fs/ cm^{-1}, in agreement with previous studies [214]. The frequency dependence of the relaxation time is expected to arise from a number of effects. The 2D IR spectrum shows that strongly-hydrogen-bonded oscillators are more strongly coupled to the HOD bend than weakly bonded ones, which can in principle dissipate energy more efficiently via relaxation to the bend. The formation of strong hydrogen bonds also gives rise to low-frequency motions that may serve as an energy sink for the O—H excitation while at the same time providing stronger coupling to the solvent. The frequency dependence is somewhat weakened as a result of rapid spectral diffusion that randomizes the O—H stretch frequency on a time scale similar to the vibrational relaxation [224]. For example, in studies on polyalcohols in chloroform, where spectral diffusion is much slower, a stronger frequency dependence of the lifetime is observed [198].

The ESA in the 2800 to 3150 cm^{-1} region decays on average on 200 ± 10 and 610 ± 20 fs time scales, with a weaker frequency dependence ($\sim$0.15 fs/ cm^{-1}) than the fundamental. The fact the ESA due to the $|\nu_s \nu_b\rangle = |10\rangle \rightarrow |12\rangle$ transition decays on the same time scale as the $|\nu_s \nu_b\rangle = |10\rangle \rightarrow |20\rangle$ transition reflects the fact that both transitions originate from the $|10\rangle$ state and decay with the lifetime of the O—H stretch. The discrepancy between the 610 fs time scale for the induced absorption and the 700 fs time scale observed for the bleach can be explained by variations in long-time spectral shifts in this region.

At frequencies below 2200 cm^{-1}, the broad induced absorption that extends from the O—D stretch decays with time scales varying between 750 and 1400 fs with a non-monotonic frequency dependence. This observation is consistent with the idea that the ESA arises from more than one spectral feature and is not simply correlated with the relaxation of the stretch. We interpret the extended relaxation times, which are ~1 to 2 times longer than the lifetime of the O—H stretch, as indicative of complex coupling between the hydroxyl stretch and the solvating D_2O. This feature likely arises from a number of phenomena that include contributions from coupling to solvent and structural reorganization. What is clear is that the relaxation of the O—H stretch is not the rate-limiting step in thermalizing the vibrational excitation, consistent with the idea that vibrational relaxation passes through an intermediate state [216].

5.4.2 Relaxation Pathways

As mentioned above, the relaxation pathway of the O—H stretch and the role played by the HOD bend has been a point of contention. However, because of the decay of the broad induced absorption background in this region, it is not possible to extract the relaxation time scale of the bend directly from the data (Fig. 5.7A); however, we can isolate it using a linear correction for the background for each τ_2 value (Fig. 5.7B). The decay of the bend bleach obtained by this procedure is fairly insensitive to the details of how the correction is applied. A bi-exponential fit to this data (Fig. 5.7C) shows that the bend bleaches immediately upon pumping the stretch but then continues to grow with a 320 ± 40 fs time scale. In addition to the Fermi resonance that leads to the immediate bleach, there are additional channels for energy initially in O—H stretch or bend overtone vibrations to transfer to the bend fundamental on a 320 fs time scale.

The decay from the stretch to the bend can, in principle, occur with any hydroxyl stretch,

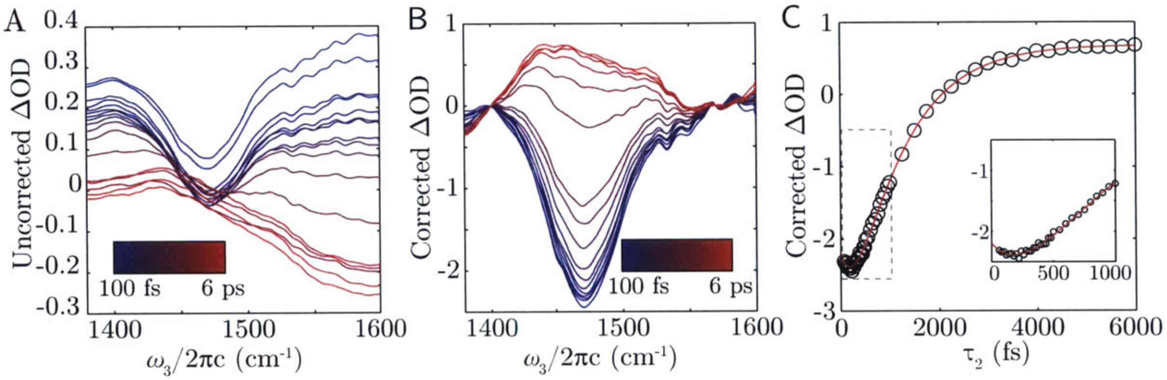

Figure 5.7: (A) TA spectrum of HOD bending mode without and (B) with background correction. (C) Associated dynamics of the HOD bend.

but it is expected that the redshifted oscillators will most easily transfer to the $|02\rangle$ state because these oscillators are most strongly mixed with the bend overtone. This relaxation pathway is identical to what was observed for the relaxation of the hydrogen-bonded N—H stretch in NMA (see §4.5). From $|02\rangle$, the energy can transfer to the solvent or into the $|01\rangle$ state. This shows that, for the strongly-hydrogen-bonded oscillators, relaxation through the HOD bend is an efficient process.

The immediate response of the D_2O solvent and the HOD bend coupled to the fact that the O—H stretch relaxation time is substantively longer than the 320 fs feeding of population into the bend suggest that relaxation of the O—H stretch proceeds through a variety of channels involving intra- and intermolecular D_2O and HOD vibrations. (We note that even in the case of intramolecular hydroxyl-deuteroxyl coupling, the O—D stretch of HOD is expected to be delocalized over the O—D stretches of the solvent so that the distinction between "O—D on HOD" and "O—D on D_2O" is not possible to make.) The bend bleach recovers with a 1010 ± 60 fs time scale, which is consistent with the growth of the long-time thermal difference spectrum [216] and the relaxation of the O—D stretch at ~2200 cm^{-1}, suggesting that the bend finally relaxes into D_2O intermolecular motions. The immediate response of the O—D stretch in the 2200 cm^{-1} region shows that O—D stretches of the solvent anharmonically couple to the O—H stretch. Its subsequent picosecond relaxation is indicative that thermalization requires structural relaxation of the liquid.

Chapter 6

Molecular Dynamics of Liquid Water

6.1 A Liquid Like No Other

Without a doubt, understanding the vibrational dynamics of of liquid water is among the most complex, yet most pressing, problems in the field. As such, it is not surprising that liquid water has received so much attention in the literature both with linear techniques, ranging from the terahertz to X-ray [6], as well as nonlinear techniques, which have mostly been in the infrared or visible part of the electromagnetic spectrum, with recent advances in time-resolved terahertz experiments [249]. Despite this tremendous effort, progress in understanding the molecular dynamics of liquid water has been slow, with new challenges and questions arising at every corner.

The difficulty associated with understanding water lies entirely in its ability to form hydrogen bonds. What is more, the geometry of the water molecule is such that the liquid can form an extended hydrogen-bond network in which each molecule can accept and donate two hydrogen bonds in a geometry that is tetrahedral on average [6]. Therefore, unlike other molecular liquids, water's intermolecular motions span an enormous range of frequencies, with a particularly dense spectrum of thermally-accessible states, principally due to hydrogen-bond stretching and bending [47]. That these states are thermally accessible is important –this results in the hydrogen-bond network fluctuating and rearranging on the femtosecond to picosecond timescale. In addition, the anisotropic hydrogen-bonding interaction results in strongly hindered rotations that give rise to a libration band spanning the region traditionally separating high and low-frequency vibrations. These intermolecular hydrogen-bonding modes, collectively termed "low-frequency modes" (though there is no clear separation between high and low in this case), are at the heart of what makes understanding water's dynamics so difficult.

In addition to the creation of a dense forest of low-frequency modes, hydrogen-bonding introduces strong mechanical coupling between hydrogen-bonded O—H oscillators. No water molecule is independent of its neighbor or its neighbor's neighbor. Indeed, no water molecule in a sample of liquid water is truly independent of any other (though this is somewhat of a hyperbole, to be sure). How do we interpret spectroscopic experiments where our chromophore comprises 100% of the sample? Gone is the luxury of separation of system and environment; for liquid water, the two are one and the same. The sample must be considered as a whole and interpreted in terms consistent with how one would understand experiments carried out on a solid, for example, though the language must be adapted for a highly disordered system that fluctuates on ultrafast timescales.

The strong hydrogen-bonding interactions in liquid water make the analysis of its nonlinear IR spectrum more complicated than typical systems. Since the complexity across the various features and timescales, arises from the same underlying cause, there is a need to take a holistic approach to interpreting and understanding the data, with a focus on how individual features fit together. Certainly almost all of the unique dynamics observed in water can be traced back to the effect that hydrogen bonding has on the nuclear potential energy surface. However, taking such a unified approach to the interpretation of the data is rather difficult. Instead, we must analyze the features separately, and attempt to unify them once all of the pieces are at hand.

The work in this chapter is based partly off of a paper published in *Nature Chemistry* in 2013 [190] and a follow-up paper that is currently in preparation. Here we discuss the linear and nonlinear spectra of liquid H_2O, while exploring and trying to understand water's dynamics. The data is interpreted in terms of delocalized vibrational excitons, and this is used to explain observations in the time, temperature, and polarization dependence of the spectrum. The chapter is concluded with a summary of our current understanding, and a perspective on the direction of future experiments.

6.1.1 A Field Divided

The majority of experiments carried out in the literature have been on isotopically dilute water, HOD, in either H_2O or D_2O (see §5.1.2 for a brief review of these experiments). This is due to the challenges associated with studying the isotopically pure species which arise due to the resonant coupling between O—H oscillators [250].

The earliest work on H_2O employed transient absorption (TA) spectroscopy, and by comparing polarization anisotropy measurement to a series of isotope dilutions, it was concluded that resonant energy transfer was a dominant effect in the dynamics [213, 251]. The results were interpreted in terms of Förster resonance energy transfer between O—H oscillators and, as such, neglected the strong intermolecular coupling between oscillators. Followup studies probed the temperature dependence of the lifetime of the O—H stretch, and found it to increase with temperature from 260 fs at 298 K to 320 fs at 358 K [252]. This was attributed to reduced overlap between the bend overtone and stretch fundamental, since it was found using IR-Raman spectroscopy that excitation of the stretch resulted in a significant response from the bending mode [218]. Furthermore, in these early studies, spectral diffusion was found to occur on a 0.5–0.7 ps timescale [199, 252, 253].

With the first 2D IR measurements [254, 255] and additional TA measurements [256, 257], it became increasingly clear that delocalization effects were particularly important in the vibrational spectroscopy of water, ruling out the Förster mechanism of incoherent vibrational energy transfer. Furthermore, these conclusions were supported by theoretical considerations that showed that delocalization is indeed important [44, 258] and that the

Förster model is not valid in this limit [259]. These contradictory results split the water community into two distinct camps, with people ascribing to one doctrine or another.

Our experiments on H_2O [190] were the first to employ pulses short enough and with enough bandwidth to cover the entire spectral range of the O—H stretching band in water. While our results certainly necessitate a picture of delocalized excitons, the broader bandwidth illustrated two points that are at odds with the previous literature. With a time resolution of ~70 fs, we showed that the timescale for spectral diffusion is 175 fs, which is inconsistent with the value of 50 fs obtained with a longer time resolution [254]. Furthermore, our data shows direct and ultrafast relaxation to low-frequency modes as opposed to the stretch-to-bend mechanism proposed based on transient absorption data [256]. The complexity of the data clearly shows the necessity of broadband probing, as narrowband probes can give the appearance of changing spectral features, with the source of these changes not being understood.

6.1.2 Notation

In this chapter, we will most often be discussing the two high-frequency vibrations: the O—H stretch and the HOH bend. As such, it is useful to establish notation early. The normal-mode state notation $|\nu_s \nu_b\rangle$, typical of harmonic modes of vibration, will be used to label the quanta of excitation in the stretch and bend. However, this notation is both limited and incomplete. The complex nature of the vibrations in H_2O, particularly the strong coupling between various high and low-frequency modes, necessarily means that a separation between these two states is unjustified. That is, there will be no pure bending or stretch mode in the liquid –the true eigenstates will be mixtures of these and low-frequency modes. We use this notation purely as a convenient tool to label the peaks nonetheless, as it still represents the dominant type of motion in the vibration as well as keeps track of the total vibrational energy in the system.

Furthermore, there are enough transitions in water (especially considering that harmonic selection rules are not applicable to transitions in H_2O) that it is convenient to develop a convention with regard to transitions in the nonlinear spectrum. To that end, we will use a right-pointing arrow to indicate that a transition corresponds to a positive feature in the spectrum such as an excited state absorption, while we will use a left-pointing arrow to indicate a negative-going feature such as a bleach. For example, $|10\rangle \rightarrow |20\rangle$ corresponds to an excited state absorption of the O—H stretch, while $|02\rangle \leftarrow |01\rangle$ corresponds to a stimulated emission of the second excited state of the bend to the first.

6.2 Linear Infrared Spectroscopy of H_2O

The linear infrared absorption spectrum of H_2O has been studied at length in the literature over an enormous range of wavelengths [46, 260], and we cannot hope to give a complete survey of all of these studies. Rather, we focus on outlining the features important for understanding the the nonlinear IR spectroscopy that follows in the rest of this chapter.

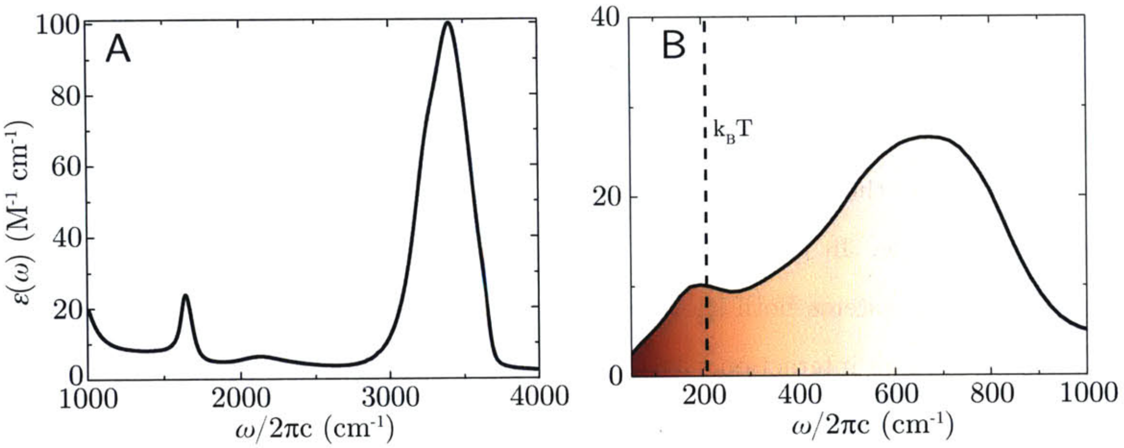

Figure 6.1: (A) Molar extinction coefficient of liquid H_2O in the mid-IR region of the spectrum. (B) Low frequency spectrum of liquid H_2O. Dashed line indicates k_BT and shading below curve indicates thermal population of modes. Adapted from Ref. [46].

The room-temperature spectrum of liquid H_2O taken over a range of 1000–4000 cm^{-1} is shown in Fig. 6.1A. This spectrum was collected by sandwiching ~1 μL of pure (18.2 MΩ resisitivity) water between two 1 mm thick CaF_2 plates. Given a final optical density of 0.6–1.0 at 3400 cm^{-1}, we estimate that the thickness of the layer of water is 1.1–1.8 μm based on a molar extinction coefficient of 100.6 $M^{-1} \cdot cm^{-1}$ at 3400 cm^{-1} [260, 261].

The mid-IR spectrum of liquid H_2O shows two distinct features: a broad, intense feature at 3400 cm^{-1} corresponding to the O—H stretching mode and a (relatively) narrow, weak feature at 1650 cm^{-1} corresponding to the HOH bending motion. In addition, a broad, weak feature is evident in between these two, at a frequency of 2150 cm^{-1}, that is typically attributed to a combination band between the HOH bending mode and the librational modes in the 500–800 cm^{-1} region of the spectrum [178]. Outside of these features, the intensity of the absorption spectrum never truly reaches zero, showing that the strongly coupled water network contains a continuum of structures that absorb throughout the 1000-4000 cm^{-1} region.

A brief look at the O—H stretching mode shows that it is not a typical infrared absorption profile. Rather, the band shows substructure which immediately indicates that there is more than a simple O—H stretch to consider. In fact, the structure in the O—H stretching band is even more evident in the Raman spectrum of H_2O [262]. The origin of this substructure is not agreed upon across the board (this has been an ongoing debate in the IR spectroscopy community –see Chapter 7 for a somewhat more elaborate discussion of this debate) though most people agree that it arises, in part, due to the overtone of the bending mode. In the previous chapters (4 and 5) we have seen that two distinct hydrogen-bonding systems both show bend–stretch Fermi resonances that are enabled by the hydrogen-bonding interaction. We expect that H_2O, being even more anharmonic and coupled than the previous systems, is no different. In fact, the frequency ratio of the bend and the stretch in H_2O is almost perfectly 2:1, so we expect that it is an even more prevalent effect. This is important in the consideration of the nonlinear spectra, where excitation of the O—H stretch is necessarily accompanied by direct $|00\rangle$ to $|02\rangle$ excitation of the bend.

In isotopically dilute solutions of HOD in D_2O, there is a natural way of interpreting and understanding the linear absorption spectrum. There, it has been shown that the stretching frequency of the dilute O—H oscillator is highly sensitive to its local environment; in particular, its frequency is almost entirely determined by its hydrogen-bonding configuration [15, 25, 26, 207]. A strong hydrogen bond, corresponding to a large, negative electric field along the O—H bond, results in a redshift of the O—H stretching frequency, while a weak hydrogen bond results in a blueshifted stretching frequency. The question then is whether there is such a trend in isotopically pure H_2O. Based on the discussion above, and the results that follow in this chapter, the answer is a definitive "no." At the simplest level, the frequency of a single oscillator is going to be determined by the hydrogen-bond configuration of both O—H bonds due to intramolecular coupling. In reality, strong intermolecular coupling is going to significantly alter the character of the modes, giving rise to no simple correlation between frequency and structure. In addition, the overtone of the bend complicates this matter further. Nonetheless, we may still keep this trend in mind as long as we understand that the frequency is only related to an average hydrogen-bond strength, but that there is a large deviation in the number of possible hydrogen-bonding configurations.

We now turn to the consideration of the low-frequency spectrum, discussed qualitatively in the introduction of this chapter. Figure 6.1B shows the spectrum of liquid H_2O in the 50–1000 cm^{-1} region of the spectrum, adapted from Ref. [46]. The spectrum shows two main features: a broad band in the 500–800 cm^{-1} range, peaked at 700 cm^{-1}, corresponding to the librational motions and a narrower band corresponding to hydrogen-bond stretching at $\sim$200 cm^{-1} [45–47]. At lower frequencies still, are resonances corresponding to hydrogen-bond bending modes and large-scale collective motions (e.g. dielectric relaxation) [263]. These low-frequency modes give liquid water its immense complexity.

Finally, we comment on the effect of temperature in the linear infrared spectroscopy of H_2O. The value of the thermal energy at room temperature, $k_BT = 208.5\ \text{cm}^{-1}$ at $T = 300$ K, is indicated in Fig. 6.1B by a vertical line. This implies that modes within the shaded region are statistically likely to be populated at room temperature. Increasing the temperature, results in a greater likelihood of populating these modes to a higher occupation number as well as populating higher-energy modes. This manifests itself in longer hydrogen bonds, since more highly excited hydrogen-bond-stretching states will have a root-mean-squared displacement which is larger on average. This results in the O—H stretching band blueshifting somewhat and the HOH bending mode redshifting and narrowing (a thermal difference spectrum is shown as a black line in Fig. 6.5A).

6.3 The 2D IR Spectrum of Liquid Water

6.3.1 The Early-Time Spectra

The 2D IR spectrum of H_2O, taken at waiting times of $\tau_2 = 100$ fs with magic angle polarization, is shown in Fig. 6.2. This waiting time represents the smallest waiting time such that pulse-overlap effects can be neglected (i.e. non-resonant response [224]), but it is worth noting at the outset that significant dynamical evolution has already occurred by this time. In the early-time 2D IR spectrum, the O—H stretching mode shows a prominent ground state bleach (GSB) along the diagonal corresponding to the depopulation of the ground state due to the pump pulse as well as stimulated emission from the excited state due to the probe pulse. As a function of ω_3, the width of the spectrum reflects that of the linear spectrum; however, the width in ω_1 is limited by the excitation pulse bandwidth ($\sim$350 cm^{-1}). The bleach is somewhat elongated along the diagonal, with a slope of 0.6–0.8, which reflects that after 100 fs the excitation has not had sufficient time to completely randomize its frequency.

Shifted to lower frequencies in ω_3 lies the excited state absorption (ESA), which corresponds to the transition from the excited O—H stretch to higher lying excited states. Unlike the bleach, it is significantly broader in ω_3 than either the fundamental transition in the linear absorption spectrum at 3405 cm^{-1} or the $|00\rangle$ to $|20\rangle$ transition in the near-IR spectrum at 6800 cm^{-1}. In fact, the red tail of the ESA even continues past our lowest possible detection frequency at $\sim$1350 cm^{-1}. In a typical 2D IR spectrum, ESA peaks correspond to peaks in the linear overtone spectrum; however, despite the near-IR spectrum being clear at $\sim$6000 cm^{-1} for H_2O [46,264], the ESA spans transitions covering this region. Simulations of the 2D IR spectrum of water somewhat capture the width of the GSB, but cannot reproduce the breadth of the ESA [258, 265].

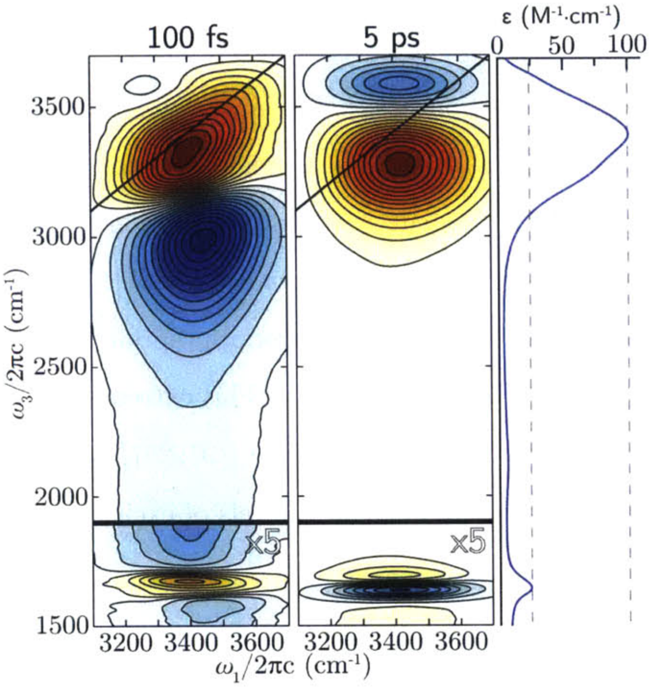

Figure 6.2: 2D IR spectra of H_2O taken at waiting times of $\tau_2 = 100$ fs and 5 ps with magic angle polarization. Molar extinction coefficient shown on right-hand side.

If the main cause for signal decay in a 2D IR experiment is pure dephasing, the width of the ESA is expected to be the same as the width of the GSB. For a system which fluctuates as rapidly as water, this is certainly expected to be the case. If pure dephasing is not the main cause of relaxation, the ESA will be a factor of $\sqrt{2}$ broader than the GSB in the limit of weak coupling between system and bath [266]. For H_2O, the ESA is far broader still. This shows that a single interaction reaches a different set of possible states than two sequential interactions. This is represented diagrammatically in Fig. 6.3, wherein the near-IR states accessible in linear and nonlinear spectroscopy are schematically shown in blue and green, respectively, in addition to the linear absorption spectrum. The states shown in green (corresponding to the broad ESA observed in the experiments) are dark for transitions originating the in ground state. This is obvious from the linear absorption spectrum, where little to no absorption is observed between the $|11\rangle$ and $|20\rangle$ states. However, these states are bright when the transitions originate in the first excited state of the O—H stretch, as is evident from the 2D IR spectrum.

To understand why this is so, it is necessary to consider the nuclear potential energy surface (NPES) and its relation to linear and nonlinear spectroscopy. In linear spectroscopy, transitions originate from the ground state of the high frequency mode, while in 2D IR experiments, the final transition originates from the first excited state. The ground state, being close to the bottom of the NPES, is more harmonic since the displacements from the minimum are, on average, small. On the other hand, the first excited state is significantly higher in energy such that displacements from the minimum are much larger. At this level of excitation, the potential deviates fairly drastically from harmonicity. A transition originating in a more anharmonic state implies stronger coupling between all vibrational modes (or equivalently, weakened selection rules) such that there are more transitions with nonzero oscillator strength available [267]. It stands to reason that the modes are mixed enough such that it is no longer appropriate to identify these features as arising solely from O—H stretching-type motion. This extreme mode mixing has been observed and discussed previously in the context of ice [191, 267], where the character of the modes was changed significantly even at modest levels of excitation.

This extreme anharmonicity has its origins in the hydrogen-bonding interaction, which significantly modifies the NPES. A good example of this was seen in the spectrum of NMA dimers in dichloromethane discussed at length in Chapter 4 (in particular, see Fig. 4.3). The 2D IR spectrum of the NMA monomer shows that the N—H stretching mode has an ESA which is roughly the same width as the GSB. As discussed above, this suggests that the decay of the 2D IR signal for this mode is dominated by pure dephasing. On the other hand, the ESA of the hydrogen-bonded mode is at least three times broader than the GSB. This shows that the formation of

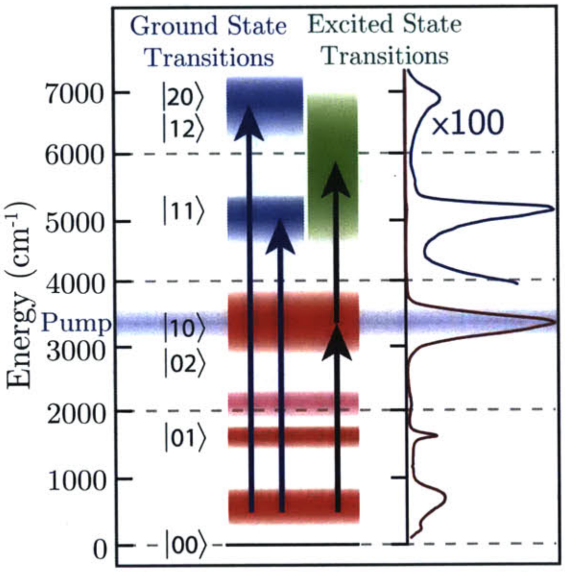

Figure 6.3: Schematic of energy levels accessible in linear (blue) and nonlinear spectroscopy (green). Linear absorption spectrum, adapted from Ref. [46], of H_2O shown on right-hand side. Blue background indicated pumping frequency in nonlinear spectroscopy.

a hydrogen-bond results in a deformation of the NPES that is significant enough to alter even the first excited state of the hydrogen-bonded oscillator. If this effect is evident even for a single hydrogen bond, certainly it can explain the extreme broadening in H_2O, which has an extended hydrogen-bond network. We must therefore interpret the unusual shape of the 2D IR spectrum as a result of the anharmonicity of the NPES induced by the strong hydrogen-bonding interactions. This is paramount since it implies that even the language of weakly anharmonic oscillators is merely a convenience, and, from a physical perspective, is wholly inappropriate when discussing the vibrations in liquid H_2O. Nonetheless, as it is the usual language in which molecular vibrations are discussed, we use it through, though we keep in mind that this is mostly notational.

In addition to the GSB and ESA in the O—H stretching region of the spectrum, a bleach of the HOH bending mode at $(\omega_1, \omega_3) = (3400\ \text{cm}^{-1}, 1675\ \text{cm}^{-1})$ is evident, consistent with previous two-color TA measurements [256,257]. The presence of a cross peak between the stretching mode and the bending mode indicates that the two vibrations are coupled, and the excitation of the stretching mode has changed the frequency and/or oscillator strength of the bending transition. Physically, this implies that the stretching mode has a certain amount of bend character to it; if a local stretching mode were excited, this would result in the coherent exchange of energy between it and the local bending mode. The bend cross peak shows only a weak slope, which means that there is little frequency correlation with the stretching mode. This is somewhat expected: even though the bend blueshifts as the stretch redshifts with hydrogen bonding (a correlation of this type should result in a cross-peak bleach with a negative slope), the frequency of the bend is determined by the hydrogen-bonding configuration of both O—H oscillators (as well as intermolecular degrees of freedom) and so the correlation would be quite weak.

At first glance, the presence of a cross peak is surprising, since it implies a strong mixing of states despite a detuning of over 1700 cm^{-1} between the modes. For such off-resonant modes, the frequency shift due to coupling is expected to be small [62], and as such a cross peak should not be evident. However, these considerations neglect that the $|02\rangle$ state is resonant with the $|10\rangle$ state. These states will couple strongly in a Fermi-resonance-type interaction, resulting in the shifting of the stretching and bending modes (see §4.3.3). The shifting is different from the "classic" Fermi resonance since the $|02\rangle$ state lies entirely in the breadth of the $|10\rangle$ band, and so the shifting most likely appears as broadening. With a Fermi resonance interaction, even in the limit where the direct coupling between the stretching and the bend was zero (i.e. the matrix element $\langle 01|V_{\mathrm{a}}|10\rangle$ is zero, where V_{a} is the anharmonic part of the nuclear potential energy surface), a cross peak would be present because of the interaction of the $|02\rangle$ state with the $|10\rangle$ state. The GSB of the bend in the 2D IR spectrum is blueshifted by 35 cm^{-1} from its peak value in the linear absorption spectrum, which suggests that the bend–stretch coupling is stronger for water molecules with higher bending frequencies, on average. Higher bending frequencies correspond to water molecules with hydrogen bonds that are stronger than the average, reflecting that this subset of water molecules have the strongest stretch–bend coupling.

Unlike usual cross peaks [79], there is no clear ESA peak associated with the bleach that would normally correspond to the $|10\rangle \rightarrow |11\rangle$ transition. The reason for this absence is unclear. We note that the $|11\rangle$ state in the linear spectrum peaks at a frequency of $\sim$5200 cm^{-1} [264], which suggests that the $|10\rangle \rightarrow |11\rangle$ transition ought to happen at a frequency of $5200 - 3400 = 1800$ cm^{-1}. This is atypical in that the combination band $|11\rangle$ is normally shifted to lower frequencies than the sum of the fundamentals and this represents an unusual example of a "negative anharmonicity". This suggests that the ESA peak of the bend is mixed in with the long ESA tail of the O—H stretch.

Furthermore, it is necessary to consider the $\omega_{\mathrm{s}} \approx 2\omega_{\mathrm{b}}$ level structure of H_2O. Excitation of the O—H stretch necessarily results in either the direct or indirect excitation of the bend overtone at approximately 3300 cm^{-1}. Therefore, in addition to the expected $|00\rangle \leftarrow |01\rangle$ GSB and $|10\rangle \rightarrow |11\rangle$ ESA, there ought to be a bleach arising from the stimulated emission of the $|02\rangle \leftarrow |01\rangle$ transition as well as an ESA from the $|02\rangle \rightarrow |03\rangle$ transition. In addition, the strong anharmonicity of the potential means that two-quantum transitions are not forbidden, and so we also expect a bleach at the difference frequency between the bend and the stretch, $|01\rangle \leftarrow |10\rangle$. All of these features are expected to be at roughly the same frequency and highly overlapping. Therefore, it is unsurprising that there is no clear ESA associated with the $|10\rangle \rightarrow |11\rangle$ transition, but rather a broad smear of ESA associated with all of these different transitions. In fact, upon close inspection, the bleach of the bend cross peak deviates from the lineshape of the linear spectrum [190]. The lineshape strongly implies the presence of at least two bleaches, which are likely to be the fundamental $|00\rangle \leftarrow |01\rangle$ bleach and the $|01\rangle \leftarrow |02\rangle$ bleach.

6.3.2 The Late-Time Spectrum

In addition to the early-time spectrum, Fig. 6.2 shows the 2D IR spectrum of H_2O taken at $\tau_2 = 5$ ps. After $\tau_2 = 1$ ps, the 2D IR spectrum is essentially unchanged as waiting time increases further. At this point in time, ω_1 and ω_3 are completely uncorrelated, and each vertical slice through the 2D IR spectrum has the same shape. In previous literature [199,215,224], this static long-time spectrum has been attributed to the heating of the liquid upon relaxation of the initial excitation and, as such, has been referred to as the "hot ground state" (HGS). In the HGS spectrum, we observe reduced absorption at the red side of the O—H stretch and an increased absorption on the blue side. This corresponds to an overall blueshift of the stretching mode, implying that hydrogen bonds are weaker compared to the equilibrium spectrum. Similarly, the bending mode is redshifted and narrowed, which is consistent with weaker hydrogen bonds. These features are in agreement with what is observed in a heated linear difference spectrum [264] and so has led to the natural interpretation that the sample is at a higher temperature after relaxation than before excitation.

While it is discussed in greater detail in §6.5, we wish to emphasize that the HGS in fact has nothing to do with heating of the liquid, and it is actually a state which is still far from equilibrium for which temperature is not even defined. Nonetheless, the projection of the 2D IR spectrum onto the ω_3 axis qualitatively matches a linear thermal difference spectrum of $\Delta T = 15$ K (see Fig. 6.5A, black line), and for consistency with previous literature, we will use the name "HGS" throughout.

6.4 Vibrational Dynamics in H_2O

6.4.1 Transient Absorption

While 2D IR provides a more complete measurement of the third-order response function, transient absorption (TA) spectroscopy provides a simpler and more straightforward method for characterizing dynamics than 2D IR since the ω_1 axis is not measured in these experiments. Additionally, TA spectroscopy has the benefit of directly measuring the change in absorption, which can be related back to a physical bleaching of the sample by comparison to the linear spectrum. This provides a useful metric for contrasting long-time TA spectra and linear thermal difference spectra.

The TA surface for H_2O is shown in Fig. 6.4, both at early times and at late times. The TA surface shows features that resemble those observed in the 2D IR spectrum. At early times, a clear bleach of the O—H stretch and associated ESA is visible. The GSB appears to rapidly redshift, continuously evolving towards the HGS spectrum. However, a singular value decomposition of the TA spectrum [190] shows that two spectral components suffice to reproduce the entire TA surface. This implies that the GSB does not actually shift, but rather appears to do so due to the ingrowth of the HGS signal. The apparent shifting is accompanied by the growth of a blueshifted induced absorption, corresponding to the weakening and breaking of hydrogen bonds with increasing temperature.

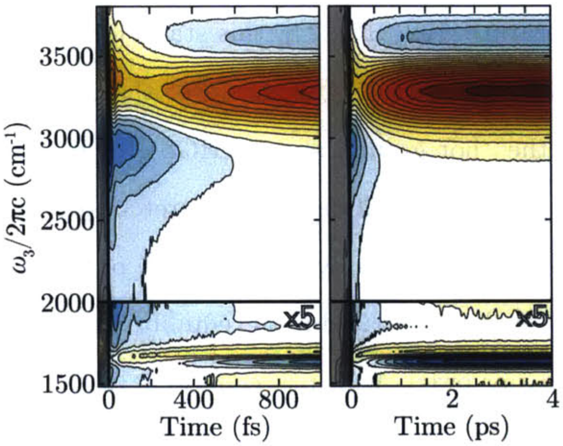

Figure 6.4: Magic angle TA spectrum of H_2O. The left panel shows early times, while the right panel shows data past when the evolution of vibrational dynamics is complete.

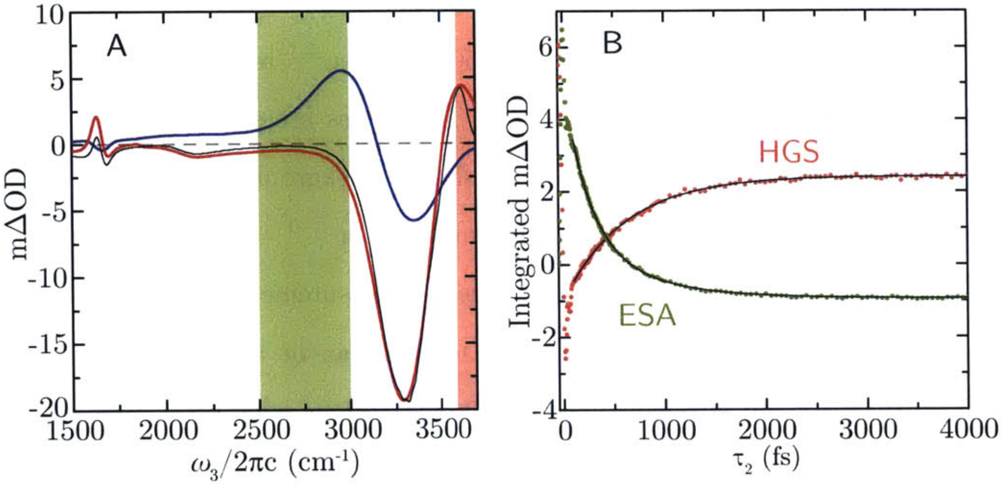

Figure 6.5: (A) Slices through the magic angle TA spectrum taken at waiting times of $\tau_2 = 100$ fs (blue) and 5 ps (red) as well as a comparison to the linear thermal difference spectrum for $\Delta T = 15$ K. (B) Time traces for integrated regions of the TA spectrum. Regions correspond to colored panels in A.

A slice through the early-time TA spectrum of H_2O, taken at $\tau_2 = 100$ fs, is shown in Fig. 6.5A. It shows a GSB of the fundamental O—H stretch and associated ESA which is broadened as it is in the 2D IR spectrum. Sitting atop the ESA at 1680 cm^{-1} is the cross peak to the bending mode as expected based on the 2D IR spectrum. The observation of this cross peak in the TA experiment is consistent with previous reports of two-color TA experiments [256, 257]. A slice through the late-time spectrum, $\tau_2 = 5$ ps, is also shown in Fig. 6.5A, in addition to a comparison to a $\Delta T = 15$ K linear thermal difference spectrum. The comparison of the two shows good agreement, with features in the HGS spectrum and thermal difference spectrum lining up perfectly in frequency. However, the agreement is qualitative, particularly in the bending region, in that the features do not match in amplitude or breadth. These discrepancies likely arise from artifacts associated with the collection and processing of the nonlinear spectrum.

The dynamical evolution of the TA spectrum is characterized by the lifetime of the first excited state of the O—H stretch, γ^{-1}, and the growth of the HGS spectrum, Γ^{-1}. The simplest method of extracting these parameters from the data is to integrate the TA spectrum in frequency over certain regions and fit the resulting signal. To that end, we integrate the ESA of the O—H stretch in the 2500–3000 cm^{-1} region to extract γ^{-1}, and in the 3600–3800 cm^{-1} region to extract Γ^{-1}. The traces are shown in Fig. 6.5B, with the corresponding areas of integration shown as shaded backgrounds in Fig. 6.5A. The two features evolve exponentially, characterized by timescales of $\gamma^{-1} = 250$ fs and $\Gamma^{-1} = 610$ fs. These values are in good agreement with previous TA measurements of H_2O [199,254,256].

In principle, extracting timescales with this method can be inaccurate due to overlap between the early-time and late-time spectra, though regions have been integrated where interference between the two is minimal. To separate these effects entirely, SVD decomposition of the TA spectrum can be used to obtain the evolution of the early-time and late-time spectra independently [190]. This method results in timescales of $\gamma^{-1} = 275$ fs and $\Gamma^{-1} = 720$ fs. While the values for the decay of the excited O—H stretch are roughly the same in both methods, the values for the growth of the HGS differ by over 100 fs. This reflects the fact that there is a significant contribution of the early-time spectrum to the 3600–3800 cm^{-1} region of the TA spectrum.

6.4.2 Dynamics of the 2D IR Spectrum

Figure 6.6 shows the 2D IR spectrum of H_2O, taken at magic angle polarization, for several waiting times. (Other polarizations are shown in Appendix 6.B.) As a function of increasing τ_2, there are several obvious changes to the 2D IR spectrum associated with the relaxation of the O—H stretching mode. Most notably, the broad ESA decays with increasing waiting time, corresponding to the relaxation of the system out of the initially excited $|10\rangle$ state. Overall, the O—H stretch ESA peak decays on a $\gamma^{-1} = 260$ fs timescale, as characterized by fitting the integral of the ESA peak to a monoexponential timescale. This value is consistent with that obtained from TA measurements, either by direct integration or by the SVD method.

It is evident from the 2D IR waiting-time series that the red side (in ω_1) of the ESA decays more quickly than the blue side. For example, in the $\tau_2 = 500$ fs surface, the intensity of the ESA on the blue side is large relative to that on the red side. By separating the spectrum into $\omega_1 > 3400$ cm^{-1} and $\omega_1 < 3400$ cm^{-1}, it is possible to characterize the dynamics on the blue side and red side, respectively. The decays of the ESA follow exponential dynamics with time constants $\gamma_r^{-1} = 220$ fs on the red side and $\gamma_b^{-1} = 310$ fs on the blue side. This shows that the effective averaging over the ω_1–axis carried out in the TA experiment masks the frequency dependence of the lifetime of the O—H stretch.

The difference between the two relaxation rates is expected to come from several sources. As observed in other hydrogen-bonding systems [196–199], oscillators in strongly hydrogen-bonded configurations relax more quickly than those in weak or non-hydrogen-bonded configurations due to the increased density of low-frequency modes (LFMs). In H_2O, the correlation between frequency and hydrogen-bonding configuration is not as strong as in dilute HOD in D_2O, for example, but it is expected that the red side of the O—H stretching band is going to correspond to more strongly hydrogen-bonded configurations on average. In addition to the hydrogen-bonding relaxation mechanism, the overtone of the bend, which is expected to peak at ~3300 cm^{-1}, provides, in principle, another efficient path for relaxation. That the integrated value, $\gamma^{-1} = 260$ fs, is somewhat closer to γ_r^{-1} than γ_b^{-1} can be understood in terms of the vibrational non-Condon effect [167, 168]. The transition dipoles for red oscillators are on average larger, meaning that these oscillators contribute more significantly to the integrated signal than do the blue oscillators. Given all this, however, it is worth noting that the rapid spectral diffusion scrambles the initial frequency of the excited oscillator so that a clean separation between the red and blue side cannot be made after the system has evolved beyond a certain point in time.

In evolving from the early-time spectrum to the HGS spectrum, the GSB broadens somewhat and shifts to lower frequency in ω_3 as the blueshifted induced absorption grows in at $\omega_3 \approx 3600$ cm^{-1}. The blueshifted absorption does not grow in uniformly, but rather grows in first on the red side of ω_1, which reflects the fact that the red oscillators decay most quickly. However, it is important to note that the elongation of the GSB at early times likely contributes the the appearance of the HGS growing in at low ω_1 values faster. Integrating the region of the spectrum corresponding to the blueshifted induced absorption (3600–3800 cm^{-1}) absorption, provides a timescale for the growth of the HGS of $\Gamma^{-1} = 700$ fs, which agrees well with the value obtained via SVD of the TA spectrum [190] and is in reasonable agreement with previous TA measurements [256]. It is in principle possible to characterize the growth of the HGS on the red and blue sides separately, in a similar manner to the ESA; however, given the strong ω_1-dependent overlap with the GSB, the timescales do not provide much reliable information.

The fact that the HGS grows in more than twice as slowly as the O—H stretch relaxes ($\Gamma^{-1} > 2\gamma^{-1}$), suggests an intermediate state through which the system passes while relaxing. The bend is the most natural candidate for such an intermediate state. In this case, relaxation would proceed via a stretch-to-bend-to-LFM mechanism characterized by rates γ^{-1} and Γ^{-1}. This ought to result in population building up in the bend state (evidenced by the bending-mode bleach becoming more intense) before relaxing to LFMs, because of the discrepancy between γ^{-1} and Γ^{-1}. Indeed, previous TA measurements, using narrower bandwidth pulses, concluded that this is the mechanism of relaxation [256, 257]. However, we do not observe this in the 2D IR spectrum. Rather, the bend cross-peak GSB appears to disappear uniformly on a timescale similar to γ^{-1} as the HGS grows in, though due to the strong overlap of the early and late-time spectra in this region, it is difficult to extract a precise timescale of the decay of the bend cross-peak bleach. This is in direct contrast to previous interpretations of the TA spectrum of liquid H_2O in which a stretch-to-bend mechanism was claimed to be the primary relaxation pathway. This suggests that the intermediate state is some other state that is outside the window of detection. This interpretation is corroborated by the fact that population relaxation out of the bending mode occurs on a 170 fs timescale [268, 269], though previous measurements determined a lifetime of 400 fs [270]. In either case, these timescales are significantly faster than Γ^{-1} and so this state would not provide the observed delay between the relaxation of the O—H stretch and growth of the HGS. As in the O—H band, the HGS grows in on the red side (in ω_1) of the bending mode as the relaxation of the stretching mode proceeds fastest for low frequencies.

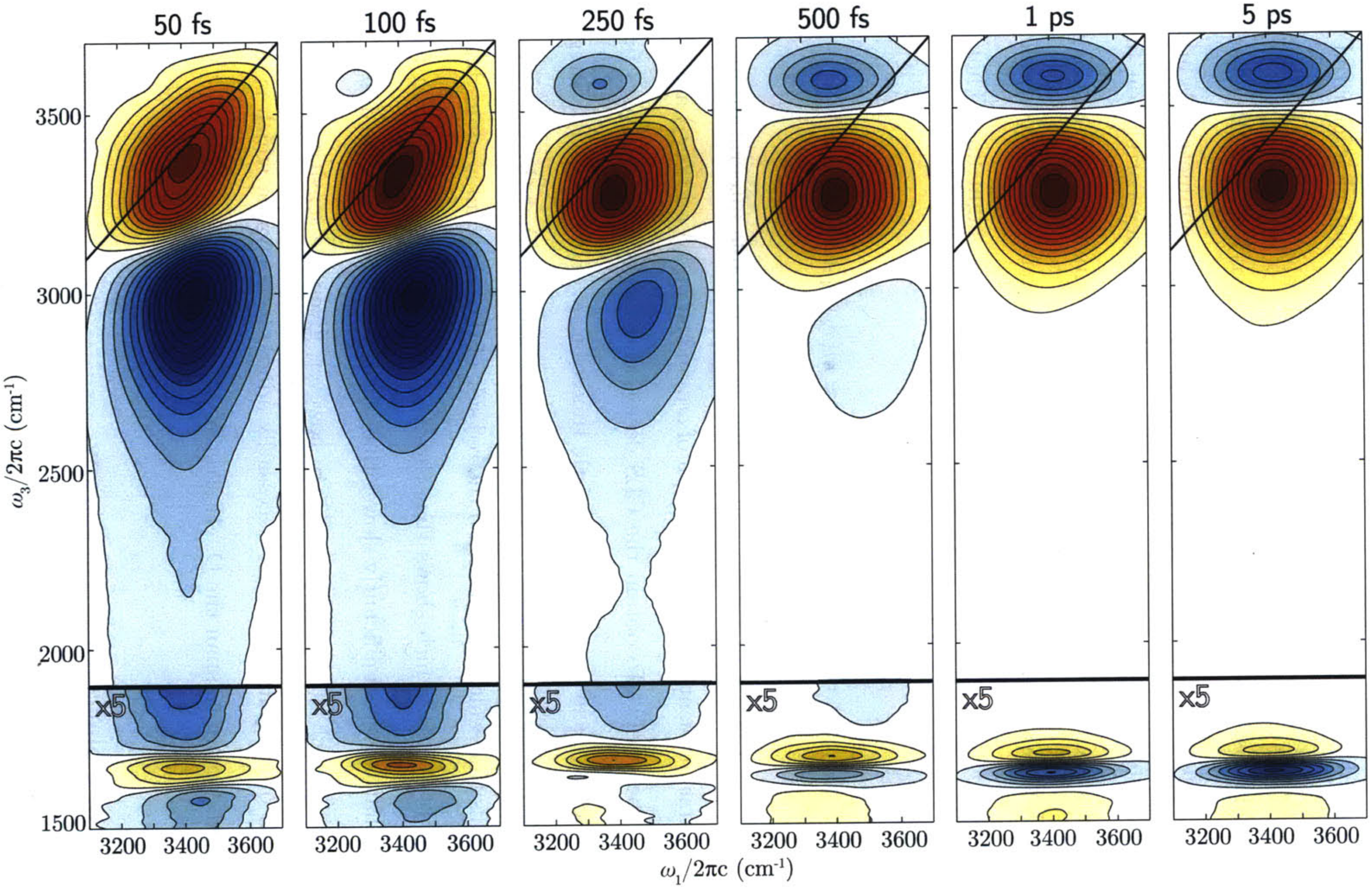

Figure 6.6: Magic angle 2D IR spectra of H_2O taken at waiting times of τ_2 = 50, 100, 250, 500, 1000, and 5000 fs.

In addition to evolving from the early time spectrum to the late time one with increasing τ_2, the elongation of the GSB of the O—H stretch along the diagonal, characterized by the center line slope (CLS) decay [88,89], changes from its initial value of ~0.8 to a final value of 0. As red and blue oscillators interchange, frequency memory is lost, and the bleach goes from being elongated along the diagonal of the spectrum to being symmetric. While there are many ways of quantifying the decay of the frequency–frequency correlation function (FFCF), for H_2O, the CLS is best since it is not susceptible to interference from the growth of the HGS which grows in without a slope. The CLS for a given value of τ_2 is calculated by fitting the first moment of the GSB as a function of ω_1 to a straight line. That is, the center line, $c(\omega_1, \tau_2)$ is calculated by

$$c(\omega_1, \tau_2) = \frac{\int_{\omega_\mathrm{i}}^{\omega_\mathrm{f}} \mathrm{d}\omega_3 S(\omega_1, \tau_2, \omega_3)\omega_3}{\int_{\omega_\mathrm{i}}^{\omega_\mathrm{f}} \mathrm{d}\omega_3 S(\omega_1, \tau_2, \omega_3)} \approx m(\tau_2)\omega_3 + b(\tau_2), \tag{6.1}$$

where $S(\omega_1, \tau_2, \omega_3)$ is the 2D IR signal, and ω_i and ω_f are suitable integration limits. In most cases, the first moment is a linear function of ω_3, and so $m(\tau_2)$ and $b(\tau_2)$ are the CLS and intercept, respectively. To obtain the CLS decay, the CLS is measured as a function of τ_2, which typically decays on a characteristic timescale, κ. For H_2O with integration limits between 3200–3600 cm^{-1}, a value of $\kappa = 165$ fs, suggesting that the environment is randomized on this timescale. The decay on the red side of the spectrum is somewhat faster than that of the blue side, which shows that the center line is not truly a linear function of ω_3. We note that this is significantly slower than the value of 50 fs obtained in previous measurements with much narrower pulses [254]; however, given the sensitivity of the CLS to the bandwidth of the pulse, we must necessarily adhere to our value which is obtained with pulses broad enough to span the O—H stretch.

6.4.3 Decay of Polarization Anisotropy

From polarization-dependent TA measurements, it is possible to determine the polarization anisotropy and its decay, as discussed in §2.5.5. The polarization anisotropy for the GSB of

H_2O is shown in Fig. 6.7, as measured by integrating the TA signal over the 3300–3500 cm^{-1} window. The curve is well fit to an exponential decay which has a $\tau_2 = 0$ amplitude of 0.39 and a decay timescale of $\tau_r = 70$ fs . That the initial value is slightly less than 0.4 suggests that the system evolves somewhat within the temporal pulse envelope. The timescale of 70 fs, which is consistent with other measurements in the literature [254], is limited by the response function of the instrument, and it should be taken as an upper bound for the true decay timescale. Nonetheless, a timescale of 70 fs corresponds to a frequency of $\sim$500 cm^{-1} which is consistent with slow librational motion in H_2O (see Fig. 6.1B). The measurement is therefore suggestive that within one period of librational motion, orientational correlation is completely lost.

In §2.4, the loss of polarization anisotropy was discussed in the context of reorientation of the excited transition dipole of the molecule. That is, for a spherical rotor, the measured timescale is related to the orientational diffusion constant by a numerical factor of 6. Clearly, the loss of orientational memory is H_2O is not due to the diffusion of a spherical rotor; rather, it has its roots in the strong coupling between water molecules. It is expected that in such a strongly-coupled network, excitation of the O—H stretch can travel more or less freely, resulting in random reorientation of excited transition dipoles on a timescale similar to vibrational energy transfer.

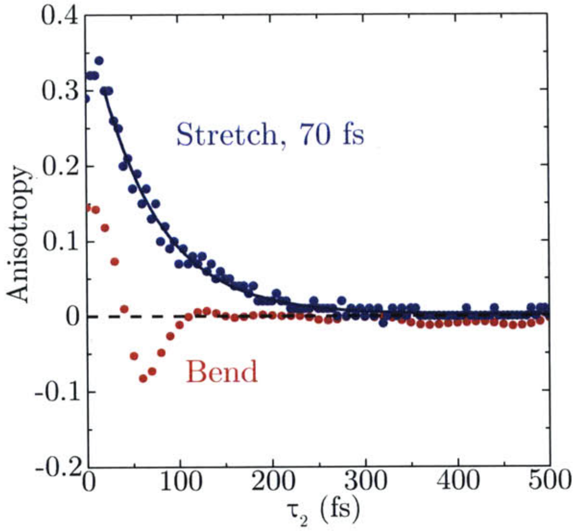

Figure 6.7: Polarization anisotropy decays for the diagonal O—H stretch and cross peak to the HOH bend.

The cross-anisotropy between the stretch and the bend is more telling still. The cross-anisotropy measurement between the stretch and the bend, after correction for the background arising from the ESA of the O—H stretch, is shown in Fig. 6.7. Unlike the diagonal anisotropy measurement, the stretch–bend anisotropy is effectively zero at all times, barring a strongly damped oscillation at early times associated with experimental artifacts. This observation can be explained in two ways: either, the angle between the stretch and the bend transition dipoles is rigidly fixed at $\Theta_{\mathrm{sb}} = 54.7^\circ$ which corresponds to $r(\tau_2) = 0$ in the broadband TA experiment, or there are no correlations between the stretch and bend transition dipoles. For gas-phase normal modes, the angle between the dipoles of the stretching and bending modes is $\sim 0^\circ$ and $\sim 90^\circ$ for the symmetric and antisymmetric stretching modes, respectively. While the liquid-phase modes of vibration are certainly going to be different from the gas-phase ones, it is highly unlikely that the angle between the stretching and bending modes is rigidly fixed at the 54.7°. We are therefore led to conclude that there is no correlation between the orientation of the stretching mode and that of the bending mode.

6.4.4 Vibrational Excitons in H_2O

At this point, we take a step back to try and understand the origin of the incredibly fast dynamics observed in H_2O. Table 6.1 shows a comparison of the dynamics observed in H_2O to those in other hydrogen-bonding liquids (Appendix 6.A shows example 2D IR spectra of other hydrogen-bonding liquids). It is clear that the vibrational dynamics in water are significantly faster. The relaxation of the O—H stretch FFCF in water is at least a factor of five smaller than other hydrogen-bonding liquids, including isotopically dilute water. The case of isotopically dilute water is perhaps not so surprising, since the isolated oscillator is not resonantly interacting with its surroundings. Therefore, comparison to methanol, for example, is more appropriate; the question then, is how water and methanol differ on a fundamental level.

In water, hydrogen bonds are formed in a geometry which is, on average, tetrahedral, and this allows for the formations of extended networks. On the other hand, in methanol, which forms hydrogen-bonded chains of O—H oscillators, the ability to form an extended network is limited by the crowding due to the methyl groups. We must therefore conclude

	Properties				
	γ^{-1} (fs)	Γ^{-1} (ps)	κ (ps)	τ_r (fs)	η^* (cP)
H_2O	275	0.720	0.18	70	0.890
HOD in D_2O	700	1.00	1.4[a]	2700/70[b]	0.890
HOD in H_2O	1400[c]	-	1.8[c]	2900[c]	1.103
MeOH	390	0.720	1.08	860[d]	0.54
EtOH	570	1.75	1.63	-	1.074
PrOH	590	1.15	1.79	-	1.945
iPrOH	850	3.89	2.55	-	2.038
tBuOH	1130	2.15	5.2	-	4.312

Table 6.1: Dynamic timescales and viscosities for water, isotopically dilute water, and various alcohols. See Appendix 6.A for a more detailed discussion of alcohols and viscosity. [a]Ref. [224] [b]Ref. [236] [c]Ref. [231] [d]Ref. [271] (26% MeOD in CCl_4) *Ref [272].

that the rapid relaxation dynamics observed in water stem from its ability to form extended hydrogen-bond networks between resonant oscillators. We are naturally led to a picture in which vibrations are delocalized over multiple molecules and form vibrational excitons. The rapid relaxation observed is due to the evolution of these excitons and not necessarily the fluctuations of the molecules. In some sense, this is not surprising since one expects coupled resonant oscillators to form such delocalized normal modes. On the other hand, the fact that the dynamics are largely dominated by these excitonic effects is a testament to the strong intermolecular coupling resulting from the hydrogen-bonding interaction.

The discussion of vibrations in water then turns out to be rather nuanced, and three separate but related properties of the system must be understood. We must understand 1) the eigenstates of the vibrations, 2) what is actually excited in an experiment, and 3) how this excitation evolves in time. The nature of the eigenstates is determined by the coupling between different O—H stretching oscillators. If the intramolecular coupling was much larger than the intermolecular coupling, then vibrations would be mostly localized to a single molecule and strongly resemble the symmetric and antisymmetric vibrations of the gas phase. In light of the discussion of the previous paragraph, however, we must consider that the eigenstates of the system are excitonic. In other words, the intermolecular coupling, effected by the hydrogen-bonding interaction, is comparable to (or possibly even stronger than) the intramolecular coupling, directly resulting in the eigenstates being delocalized over multiple molecules. These eigenstates are of course rather complex, and span an enormous range of frequencies due to the wide range of structures the molecules in the liquid can take on. The strength of the couplings are determined of course by the nuclear potential energy surface (NPES), and as a general rule, the more anharmonic the NPES is, the stronger the mixing between various modes [267]. As discussed above, the specific form of the NPES for water is dictated almost entirely by the hydrogen-bonding interaction. Therefore, on a fundamental level, the phenomenon responsible for making the early-time spectrum unique is responsible for the extremely fast dynamics observed.

The nature of the initial excitation is somewhat more difficult to understand. If the experiment was being performed with a narrow-band laser, this would result in a superposition between the initial (ground) state and a single delocalized eigenstate. However, with short laser pulses, the situation is rather different. The laser pulse generates a coherent superposition of the ground state and many O—H stretching eigenstates, each with an amplitude and phase reflecting the driving laser field [273]. In this case, the excited vibration can really be anything —even entirely localized to a single bond; the exact nature of the excitation is going to depend intimately on the properties of the excitation field. With increasing time, the initial excitation evolves as a coherent superposition of eigenstates and results in rapid delocalization of the excitation. Given the density of eigenstates, the odds of a recurrence occurring, where the system comes back to its initial state, are exceedingly small. We therefore imagine that the initial excitation can be anything –even relatively localized– depending on the laser pulse used to excite it, but almost immediately delocalizes over multiple molecules.

This picture of the molecular vibrations in water raises the difficult question of how to interpret delocalized excitations that evolve over stochastically fluctuating molecules. If the fluctuations of the water molecules are slow enough, that is, much slower than the timescale defined by the energy of the exciton, then the evolution ought to be adiabatic and the excitonic vibration evolves continuously as the molecules move [274]. On the other hand, if the fluctuations were much faster than the frequency of the excitation, this would tend to localize the vibrations [275] onto a single molecule, resulting in incoherent dynamics. In fact, this has been one of the central debates in the vibrational spectroscopy of water (discussed in §6.1.1), albeit the question is usually framed somewhat differently. Researchers in the field tend to adhere to one of two pictures: excitations in water are delocalized and evolve coherently as water molecules move [190, 256, 258] or excitations are localized and hop from one molecule to the next incoherently via a Förster-type mechanism [251]. Here, we emphasize that these two interpretations are actually two sides of the same coin and one transfers smoothly into the other. In the first interpretation, it is assumed that the vibrations localize on timescales that are long compared to the experiment, while in the second interpretation, it is assumed that the vibrations localize on timescales that are short compared to the instrument response function of the experiment.

Therefore, the question is not whether the dynamics are coherent or not, but rather on what timescale the initially formed exciton localizes and is probed. Considering the timescales associated with low frequency motions in water, (e.g. ~30 fs for high-frequency librations to ~300 fs for hydrogen-bonding modes) the conclusion that is almost inescapable is that experiments are in an intermediate regime which is neither completely coherent nor incoherent. Rather an initial excitation evolves coherently while it simultaneously localizes until eventually evolving incoherently. This picture provides an intuitive explanation for why the dynamics in water are so rapid and why a non-adiabatic description of the relaxation is necessary (see §6.5.3).

This picture of coherent excitonic vibrations in liquid water provides a satisfying interpretation of the experimental data. In particular, such an interpretation is inescapable in trying to understand the cross-anisotropy between the stretching and bending modes. Since the initial excitation, regardless of what it may be, rapidly becomes delocalized, there is no correlation between the orientation of the excitonic O—H stretching mode and the bending mode of the randomly-oriented water molecules over which the exciton is delocalized. Furthermore, the notion of excitonic vibrations provides a natural way of rationalizing the relative timescales of vibrational dynamics in hydrogen-bonding liquids.

6.4.5 2D Depolarization

From 2D depolarization measurements, it is possible to obtain spectrally resolved orientational correlations [184, 236]. Figure 6.8 shows the 2D depolarization surface H_2O taken at a waiting time of $\tau_2 = 100$ fs. The black and grey contours show parallel and perpendicular signals, respectively. Given that the timescale for the decay of polarization anisotropy is 70 fs in H_2O, it is expected that most orientational correlations will have decayed significantly by this waiting time. Indeed, that is what is observed in the data since the entire peak shows an average depolarization of ~0.8. (We recall that the depolarization nominally starts at 1/3 and evolves to a final value of 1 at long times.)

However, at low and high values of ω_1, the depolarization is significantly lower. In particular, for $\omega_1 = 3150$ cm^{-1} the depolarization is still close to its initial value of 1/3. This shows that for the most redshifted oscillators, which are basically the most strongly-hydrogen-bonded oscillators as well as bend overtone, there has been no significant reorientation of the transition dipole of the excitation. Within the framework of vibrational excitons, this implies that the most redshifted oscillators are in fact more localized than oscillators in the center of the band. This is consistent with previous theoretical predictions [44] in which the most strongly-hydrogen-bonded oscillators were found to be the most localized. In this study, vibrations at the center of the band (3400 cm^{-1}) were delocalized over up to 6 molecules, while vibrations at 3150 cm^{-1} were localized to a single molecule.

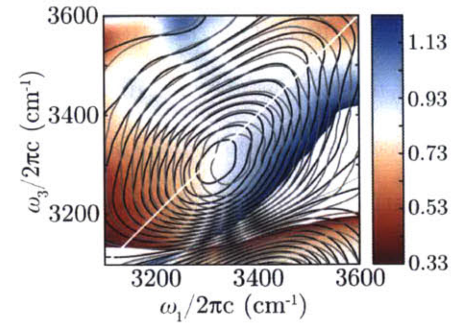

Figure 6.8: 2D depolarization ratio surface for water taken at a waiting time of $\tau_2 = 100$ fs.

Similarly, the most blueshifted oscillators show a depolarization value of about 0.6, which also suggests that these oscillators are more localized than those in the center of the band. This is again consistent with theoretical predictions [44], and can be understood by the fact that these oscillators correspond to the most weakly-hydrogen-bonded ones. Being such, these O—H oscillators do not couple strongly to their neighbors and so are mostly localized to a single bond or molecule.

6.4.6 Temperature Effects on Water's Dynamics

Changing the temperature of the sample allows us, in principle, to tune the interactions between water molecules by weakening hydrogen bonds. Measuring the dynamic properties of the system as a function of temperature is a direct reporter on how the intermolecular interactions affect the dynamics of the system. For temperatures between 265 and 325 K, lifetime traces were extracted by integration of the $|10\rangle \rightarrow |20\rangle$ transition in the 2D IR spectrum to obtain the lifetime, γ^{-1}, of the O—H stretch (the 2600–3000 cm^{-1} region) and the HGS region (the 3600–3800 cm^{-1} region) to obtain the growth of the HGS, Γ^{-1}. Representative spectra from this set of over 1700 2D IR surfaces are shown in Appendix 6.C. In addition, CLS decay timescales were measured as a function of temperature, along with polarization anisotropy measurement from TA spectra in the manner described above. Figure 6.9 shows the dynamic observables, γ^{-1}, Γ^{-1}, κ, and τ_r, as a function of temperature. Strikingly, no significant dependence of the lifetime of the O—H stretch, γ^{-1}, is seen with temperature over the entire range studied (Fig. 6.9, red circles). Over this range, almost all of the points lie within a 14 fs standard deviation centered about a mean value of 260 fs. While a weak temperature dependence of the lifetime was found in previous work, from 260 to 320 fs over a range of 298 to 360 K, the variation in their data is not statistically significant over the temperature range we have studied [252].

The temperature dependence of the growth of the HGS, Γ^{-1}, shows more significant differences upon increasing temperature (Fig. 6.9, blue diamonds). Qualitatively, a weak temperature dependence is apparent, with the HGS growing in more slowly at low temperatures and more quickly at high temperatures with a mean of ~700 fs across the entire range. For temperatures above ~280 K, however, the timescale plateaus at around 650 fs, though the data shows a variation on the order of 100 fs.

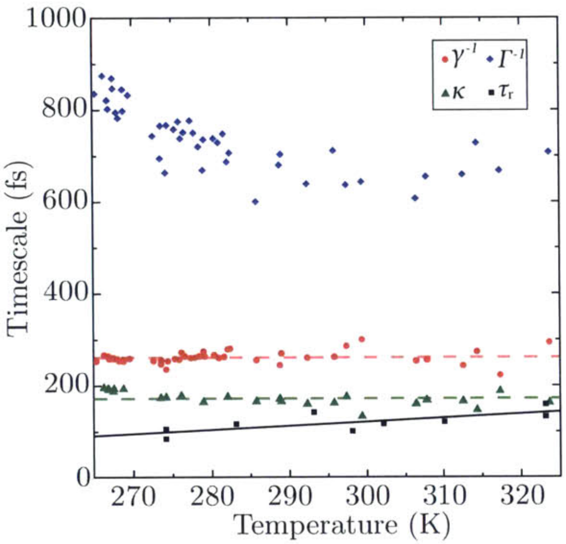

Figure 6.9: Dynamic timscales extracted from the 2D IR spectrum of H_2O as a function of temperature.

Like the lifetime of the O—H stretch, the decay of the CLS (Fig. 6.9, green triangles), characterized by κ, shows no significant temperature dependence. The CLS decay has an average value of $\kappa = 173$ fs across all temperatures and lie within a standard deviation of 16 fs. This is in contrast with previous studies carried out with narrow bandwidth pulses, which found that spectral diffusion occurs more slowly at 274 K compared to 304 K [255]. The polarization anisotropy decay, characterized by τ_r, shows similarly surprising behavior. The polarization anisotropy decay actually shows a modest increase in τ_r as a function of temperature (Fig. 6.9, blacks squares), increasing from ~80 fs at our lowest temperature to ~160 fs at our highest with a slope of ~0.85 fs/K. While the anisotropy measurement is inherently quite noisy, this increase is outside the range of statistical error. This trend is at odds with intuition in which we would expect to lose orientational correlations more rapidly at higher temperature.

The fact that the O—H stretch lifetime and CLS decay timescale do not depend on temperature in any significant way is also surprising. Intuitively, we expect that increasing the temperature ought to increase molecular fluctuations and drive the decay of the various correlation functions that determine these timescales to decay faster. In particular, we expect frequency fluctuations to be affected most strongly, and we therefore expect a large variation of κ with temperature. A brief comparison of the O—D stretch of dilute HOD in H_2O (Fig. 6.10) shows that the CLS decay changes by at least a factor of 2 over a similar temperature range while water remains constant [231]. This lack of temperature dependence is therefore clearly an excitonic effect, and to understand how spectral features change with temperature, we must not only consider that the fluctuations will be faster, but also that the intermolecular coupling will be weaker due to the weakened hydrogen bonds.

Increasing the temperature not only increases fluctuations, which would cause the FFCF to decay more quickly, but also localizes the excitations which causes the FFCF to decay more slowly. The odds of these effects balancing out almost perfectly are small, however. The more likely situation is one in which the sample is effectively in a high-temperature limit; in other words, the vibrational dynamics are simply too fast to be affected significantly by the fluctuations of the environment. If we consider that at room temperature, $k_BT = 210$ cm^{-1}, only hydrogen-bonding modes and ones of lower frequency will be excited (see Fig. 6.1B). These correspond to fluctuations on a 160 fs timescale and longer. Given that the CLS decays on a $\kappa = 170$ fs timescale, it stands to reason that the decay will not be significantly affected by the fluctuations of the environment, which occur on a similar timescale. Similar arguments hold for the O—H stretch lifetime.

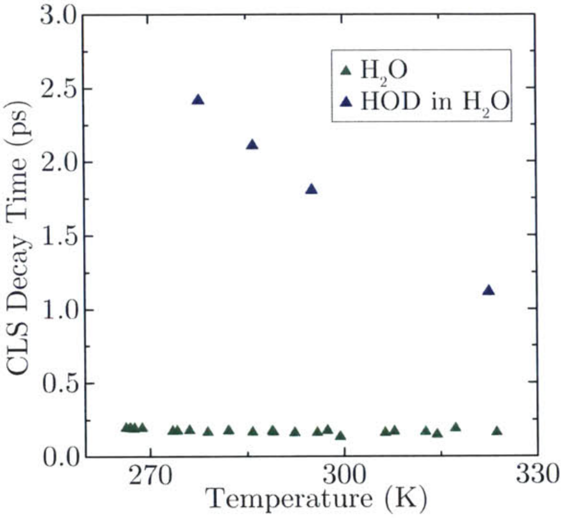

Figure 6.10: Comparison of the CLS decay of HOD in H_2O and pure H_2O as a function of temperature. HOD data adapted from Ref. [231].

This interpretation is consistent with the trend observed in the anisotropy decay. In typical systems (for example, isotopically dilute water [231]), as temperature is increased, the anisotropy decays more quickly due to increased molecular fluctuations; however, in H_2O we see the opposite. As temperature is increased, it takes longer for orientational memory to be lost. To understand this, we must again consider that excitons localize to some extent upon increasing temperature in addition to larger environmental fluctuations. If excitons are more localized, orientational correlations ought to persist for longer since the vibrations are delocalized over fewer molecules that independently fluctuate, resulting in an increase in the anisotropy decay time. It is worth noting that even at our highest temperature, the anisotropy decay is still exponential, which implies that vibrations are not completely localized in the way that an HOD oscillator is; that is, we do not observe large scale reorientation of the hydrogen-bonding network (resulting in biexponential dynamics, for example), implying that the transition dipole orientation is still completely randomized on a timescale much faster than the liquid can reorganize.

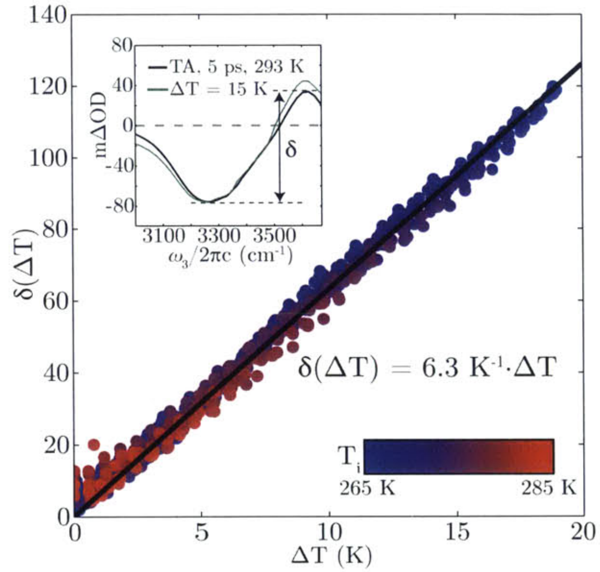

Figure 6.11: (Main) Quantity δ, described in Eq. 6.2, as a function of the change in temperature. Color of the data point is the inital temperature. (Inset) Long-time TA spectrum compared to a 15 K linear thermal difference spectrum. The quantity δ is illustrated.

In fact, the only timescale that varies appreciably with temperature is the growth rate of the HGS, which grows in 100–200 fs slower at low temperatures compared to high temperatures. This is perhaps the only trend that is consistent with intuition. As temperature is increased, the fluctuation of low-frequency modes becomes larger, and as such are more readily populated. Clearly then, the dissipation of energy in water is limited by the ability to relax to low-frequency modes, and not by the relaxation of the O—H stretch.

6.5 The Hot Ground State

6.5.1 Temperature Changes in the Linear Spectrum

As mentioned above, after the initial relaxation of the O—H stretch is complete, the spectrum resembles that of a heated equilibrium liquid. The long-time TA spectrum shown in

Fig. 6.5A is compared to a linear thermal difference spectrum of $\Delta T = 15$ K (black line). While the correspondence between the thermal difference spectrum and the HGS spectrum has been consistently made in the literature for the O—H stretching region, we note here that the correspondence holds across the entire mid-IR spectrum.

To determine the magnitude of temperature changes in nonlinear spectroscopy, a series of linear temperature difference spectra were measured for temperatures varying between 265 and 285 K. To ensure that the results were directly comparable to the nonlinear experiments, the linear difference spectra were measured on the same instrument as the nonlinear spectra. For each temperature, the transmission of the broadband probe pulse (with pump pulses blocked) was measured. The magnitude of each difference spectrum increases with an increasing temperature difference; however, the shape of each difference spectrum is roughly the same, showing a broad intense bleach centered at ~3400 cm^{-1}, and a weaker narrow induced absorption centered at ~3600 cm^{-1}, corresponding to weaker hydrogen bonds in the liquid [264]. The overall loss in intensity on the red side of the band is larger than the increase on the blue side due to the vibrational non-Condon effect [167, 168], which results in larger transition dipoles for more strongly hydrogen-bonded oscillators.

Describing these features quantitatively is somewhat challenging due to the fact that there are many possible metrics to choose from that may characterize the temperature change. We have empirically found that the quantity

$$\delta(T_\mathrm{i}, T_\mathrm{f}) = \max[A(T_\mathrm{f}) - A(T_\mathrm{i})] - \min[A(T_\mathrm{f}) - A(T_\mathrm{i})] \tag{6.2}$$

scales linearly with T_f, where $A(T)$ is the absorption of the sample at temperature T. The quantity δ is representatively illustrated in the inset of Fig. 6.11. Furthermore, δ shows no dependence of the scaling on the initial temperature, T_i, and that $\delta(T_\mathrm{i}, T_\mathrm{f}) = \delta(T_\mathrm{f} - T_\mathrm{i}) = \delta(\Delta T)$. The quantity $\delta(\Delta T)$ is plotted as a function of ΔT for various T_i in Fig. 6.11. A linear fit to the data results in a temperature difference which scales as $\Delta T = \delta/6.3$ K. It is important to note that δ is not a fundamental quantity; the slope of the fit is found to depend on the sample preparation, and varies depending on the overall absorbance of the sample.

Ideally, we would carry out a careful study of the change in molar extinction coefficient with temperature, which provides a universal metric for the change in temperature of the sample. However, without a precise and independent way to measure the pathlength of the sample, we must stick to our empirical metric to accurately calculate temperature changes. The data in Fig. 6.11 was collected on a sample with an optical density of ~0.6 in the O—H stretching region at room temperature. From this, we may estimate a pathlength of 1.1 μm. Therefore, we may rewrite an *approximate* expression for the temperature change that takes pathlength into account, $\Delta T = \delta/5.7\ell$ K μm, where ℓ is the pathlength in micrometers. We emphasize that this is an estimate since we do not accurately know the pathlength of our sample. We note, however, that if the constant in this expression could be determined accurately, then controlled changes in temperature can be used to determine the pathlength.

6.5.2 Temperature Changes in Nonlinear Spectroscopy

Under the assumption that the energy has thermalized at long waiting times, the linear calibration of the previous section provides a means for quantifying the temperature increase in a nonlinear IR experiment. In typical experiments, we find a value of δ ranging between 45–100, depending on the pump characteristics (energy, center wavelength, bandwidth, etc...), corresponding to temperature increases ranging from 7–16 K. For example, for the thermal difference spectrum shown in the inset of Fig. 6.11, we can estimate a temperature rise of ~15.5 K after excitation. These values are significantly larger than the values of ~2 K which are typically reported in the nonlinear spectroscopy of dilute HOD [215]; however, this can be rationalized by the fact that the excitation density is significantly higher in H_2O than in HOD due to the higher number of chromophores per volume.

In addition to calibration of the nonlinear HGS spectrum against the linear spectrum, we may predict the temperature jump from simple energy conservation arguments. We may use the absorption spectrum of the sample, power spectrum of the pulse, and the thermodynamic properties of water to estimate that the temperature jump will be

$$\Delta T = \int_{-\infty}^{\infty} \mathrm{d}\omega \frac{E_{\mathrm{p}}(\omega) \cdot \left(1 - 10^{-A(\omega)}\right)}{V \rho_w c_p}, \tag{6.3}$$

where, V is the excitation volume, ρ_{w} the density of water, and c_p is its specific heat at constant pressure. This simple analysis ignores losses of the pump due to scatter and reflections off the windows, for example, and assumes that any nonlinear processes will be negligible compared to linear absorption. Furthermore, we have ignored the dependence of the thermodynamic parameters on the initial temperature; this is justified since these vary slowly over the temperature ranges we are considering. For a typical pump spectrum, we calculate a temperature jump of 15.0 K, in good agreement with the linear calibration.

6.5.3 Formation of the Hot Ground State

The HGS is a characteristic of the nonlinear spectroscopy of all strongly hydrogen-bonding systems, which is normally attributed to heating of the system due to the initial excitation by the intense pump pulses. The conventional wisdom is that the energy, which is initially in high-frequency modes, relaxes to low-frequency modes that thermalize on the picosecond timescale, resulting in a system that is locally equilibrated at a higher temperature. This interpretation is corroborated by the fact that the HGS spectrum qualitatively resembles a linear thermal difference spectrum with a ΔT of ~15 K. Subsequently, thermal diffusion brings the excitation volume back to the initial temperature. In these experiments, the excitation volume is approximately a cylinder with a diameter which is ~50 times larger than its height, and so most of the thermal diffusion actually occurs longitudinally through the CaF_2 windows and not radially, especially given the high thermal conductivity of CaF_2 compared to H_2O (the latter has a thermal conductivity of 0.61 $\mathrm{Wm^{-1}K^{-1}}$ while the former's is 10 $\mathrm{Wm^{-1}K^{-1}}$ [272]). Based on the heat equation, we estimate that the sample returns to its initial temperature on a timescale on the order of 20 ns.

The fact that the HGS spectrum strongly resembles a temperature increase suggests that the assumption that the energy has thermalized at waiting times of about 1 ps seems to hold. However, accepting such a notion, at face value, is nonsensical. As mentioned earlier, the HGS spectrum grows in with a timescale of $\Gamma^{-1} = 700$ fs, and signatures of the HGS are evident earlier than 200 fs. This means that if the system were really thermalized, it would have had to heat up at a rate of on the order of 2×10^{13} K/s. This rate of heating, being reminiscent of temperature changes in the early universe, is clearly unphysical and far too large to produce a thermalized equilibrium state on the timescales we can access. Furthermore, it is in no way possibly for hydrodynamic modes to equilibrate on these timescales. For example, after excitation of the O—H stretch, there will be a local increase in pressure which must be dissipated through acoustic waves, resulting in a smaller density. Given the speed of sound in water (1497 m/s), or CaF_2 for that matter (5000–6000 m/s in common glasses) [272], there is no way for the 100 m spot to come to a local equilibrium. With these speeds, acoustic waves can travel at most 4.5 nm in 1 ps, a lengthscale over which continuum hydrodynamics does not even hold. We must necessarily adhere to the notion that in the 1 to ~100 ps after the pump pulse passes through the sample, it is in a highly non-equilibrium state and, as such, requires careful consideration. We emphasize that this state is not even locally thermalized, and the fact that the HGS spectrum resembles a heated linear difference spectrum has absolutely nothing to do with the notion of temperature.

This implies that the HGS arises entirely due to populating low-frequency modes. The fact that the linear thermal difference spectrum is almost identical to the HGS, suggest that the differences observed in the linear spectra are also due to populating low-frequency modes. That is, spectroscopically, we are insensitive to the other processes which accompany the march to equilibrium (e.g.: changes in density). Indeed, no change in the thermal difference spectrum is observed as the temperature is scanned through the density maximum at 277 K [47, 178]; whereas, if the spectroscopy was sensitive to density, we would expect a change in the trend of our thermal difference signal and see a redshift as temperature is increased for temperatures below 277 K. We must therefore conclude that only the population of the low-frequency modes affects the spectrum of O—H stretch and the fact that we observe "heating" when the system is out of equilibrium is a result of the same low-frequency modes being populated, regardless of whether the energy is delivered thermally or via laser pulse.

This behavior is consistent with the recently developed notion of prethermalization [276, 277], which is a universal feature of non-equilibrium systems. In prethermalization, the equation of state and kinetic temperature reach constant values on timescales much shorter than the equilibration timescale in an approximate equipartition of kinetic and potential energy. Nonetheless, several important quantities (e.g. occupation number for low-frequency modes) may resemble their equilibrium values despite being in a highly non-equilibrium state that can persist for long times. It is therefore perhaps more reasonable to associate the 15 K temperature increase observed with a sort of kinetic temperature and not a thermal one.

The question that remains then, is how the system reaches this HGS so quickly and efficiently. Given that within less than 200 fs, the fastest timescale on which the liquid can move at room temperature, signatures of the HGS are evident, we must conclude that the excitation of the O—H stretching mode results in a change in the low-frequency modes. In other words, driving the O—H stretch results in a simultaneous driving of low-frequency modes including high-frequency librations. If the language of a Born-Oppenheimer separation between O—H stretch and LFMs were to be used, this would correspond to a non-Condon transition (i.e. non-vertical transitions between adiabatic potential energy curves) [274]. Since the HGS implies a weakening of hydrogen bonds, we expect that this transition results in an increase of the hydrogen-bond length, $R_{\mathrm{O}\cdots\mathrm{O}}$. This is a fairly dramatic deviation from how spectra are normally interpreted, where the fact that the slow-moving environment does not change upon excitation is usually an implicit assumption. Keeping the language of a Born-Oppenheimer separation between high and low-frequency modes, after the initial excitation is generated, the excited vibrational wavepacket propagates along the excited state O—H potential energy surface. However, within 1–2 periods of hydrogen-bond stretching motion, the vibrational wavepacket ends up on the ground-state potential energy curve, and populates a different set of low-frequency modes than the initial distribution, giving rise to the HGS. This relaxation is illustrated schematically in Fig. 6.12.

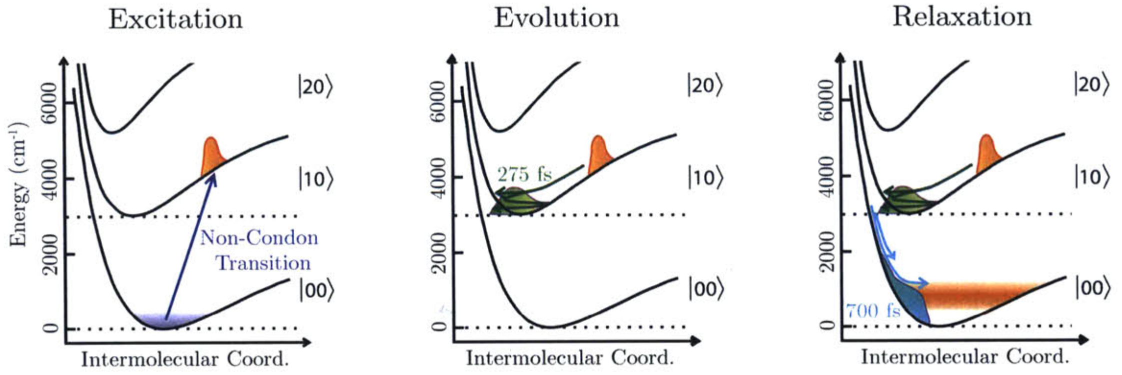

Excitation Evolution Relaxation

Figure 6.12: Schematic illustration of the relaxation of the the O—H stretch. Curves are meant to represent adiabatic potential energy surfaces of the O—H stretch as a function of some low-frequency coordinate. The excitation of an initial wavepacket, its subsequent evolution, and relaxation/prethermalization are shown.

The funneling of energy from the excited state to the ground state within a few cycles of the low-frequency tuning coordinates is indicative of vibrational conical intersections [278], where a true crossing of adiabatic potential energy curves results in ultrafast relaxation. Indeed, it has been shown that relaxation rates as fast as 60 fs are possible at a conical intersection in a H_2O–HCO_2^- dimer including only three high-frequency modes and three low-frequency modes [279]. Furthermore, such vibrational conical intersections have been shown to play an important role in the relaxation of the water dimer [280]. Given the enormous number of modes in pure liquid water, there is no reason not to believe that such vibrational conical intersections play a significant role in the relaxation dynamics of liquid water.

We emphasize that this mechanism of relaxation is notably different from that which has been well accepted in the literature. Previously, studies concluded that relaxation occurred through a cascade of weakly-coupled normal modes [219,256,257,281]; however, the evidence for non-adiabatic relaxation presented here is in direct contradiction to these interpretations.

Recent computational works, however, are also finding that a simple cascaded mechanism does not hold [282]. The ability to look beyond a narrow spectral window shows that the dynamics are far more complex than a simple theory would suggest, and necessarily forces us to step out of our comfort zones when trying to understand how water evolves in time.

6.6 Summary & Outlook

Before concluding this chapter with a perspective on future experiments and open questions, we review our observations and how they tie into each other.

6.6.1 Water in a Nutshell

The vibrational dynamics of liquid water are almost entirely determined by the strong hydrogen-bonding interaction, which results in a NPES that differs dramatically from a harmonic one. This highly anharmonic NPES results in intermolecular couplings comparable to intramolecular couplings, and it enables strong mixing between high and low-frequency modes. This strong coupling results in eigenstates at 3400 cm^{-1} that are excitonic in nature and are delocalized over multiple water molecules; while they are predominantly O—H stretch in character, they contain a significant amount of bending, librational, and hydrogen-bond stretching motion. This strong mode mixing results in an extremely broadened excited state absorption in the 2D IR spectrum.

In an experiment, a coherent superposition of excitonic eigenstates are excited, and the nature of the excited state depends intimately on the spectrum and phase of the excitation pulse. This superposition evolves coherently for some time during which the initial excitation is distributed over many eigenstates. As the molecules constituting the delocalized exciton fluctuate, the vibration is localized after which it evolves incoherently. This combination of coherent and incoherent dynamics results in ultrafast relaxation of the various correlation functions that IR spectroscopy is sensitive to, on timescales of 100–250 fs —the fastest motions in the liquid. Since the relaxation rates are comparable to the rates of thermal fluctuations, they are almost entirely insensitive to the temperature and the system is effectively in a high-temperature limit. This insensitivity is accompanied by a competition between larger thermal fluctuations and less delocalized excitons due to the weaker intermolecular coupling with increasing temperatures. The latter effect is further evidenced by the increase in the polarization anisotropy decay timescale; orientational correlations persist longer at high temperatures due to the fact that the excitonic vibrations are less delocalized.

After the initial relaxation on a 250 fs timescale, there is a growth of a HGS signal on a 700 fs timescale. The spectrum after ~1 ps is static and qualitatively resembles a linear thermal difference spectrum with $\Delta T = 15$ K. Interpreting this as a heated equilibrium state necessitates an unphysical heating rate, as well as hydrodynamic relaxation on impossibly short timescales. Instead, we understand that this is a prethermalized non-equilibrium state which has nothing to do with an actual equilibrium temperature. Rather, we interpret the 15 K temperature rise as an effective kinetic temperature increase which is a result of populating low-frequency modes. While the HGS looks like a heated equilibrium state as far as the spectroscopy is concerned, we emphasize that they are two very different states. This population of low-frequency modes proceeds via fast non-adiabatic dynamics effected by vibrational conical intersections which are expected to occur for a large number of hydrogen-bond configurations.

6.6.2 Outlook on Water

The results presented in this chapter raise more questions than they answer, and it is worth outlining what some of these questions are in somewhat more detail.

The first of such questions undoubtedly concerns the understanding of the NPES. Clearly, the highly anharmonic NPES results in a strong mixing between high and low-frequency modes, even at moderate levels of excitation. To understand the vibrational dynamics of water in any kind of detail, it is necessary to take measures to better understand the NPES. One possible route is taken in the following chapter, wherein the vibrational spectroscopy of D_2O is compared to that of H_2O; however, this is only done at the qualitative level. Furthermore, an experimental understanding of the NPES is necessary to guide the future of computational simulations of the IR spectrum of H_2O, constraining which modes must be included for an accurate model of the IR spectroscopy of liquid water.

The next issue regards the nature of energy dissipation in H_2O in ultrafast IR experiments. While this is not necessarily related solely to water, it certainly seems to be most perplexing in it. Spectroscopic signatures of heating, resulting from relaxation of the O—H stretch to low-frequency modes, are present almost instantly upon excitation of the O—H stretch and dominate after a single cycle of hydrogen-bond stretching motion. Clearly, the system is not in an equilibrium state such a short time after excitation, and characterizing this nonequilibrium state is necessary to understanding the vibrational dynamics of H_2O. While the phenomenon of prethermalization [276,277] appears to be a promising candidate to explain the observation, a detailed understanding of the physical mechanism is entirely lacking. To experimentally address this question, it will be useful to collect careful TA data over timescales much longer than the relaxation of the O—H stretch (in the ps to ns range) and precisely track and model the evolution of the HGS spectrum. Hopefully, a cross-over to the hydrodynamic regime can be identified in such experiments, revealing insight into the HGS.

A related, but equally difficult to address, question is the role of vibrational conical intersections in the dynamics of liquid water. Clearly, relaxation on timescales faster than most motions in the system necessitate a relaxation mechanism that goes beyond the canonical picture of weakly coupled anharmonic modes. The recent work of vibrational conical intersections [278] is highly promising, but must be further refined in the consideration of the liquid with an enormous number of intermolecular degrees of freedom. Of course, computational modeling of these intersections requires a detailed knowledge of the NPES, which brings us to the initial question. Furthermore, it is important to note that any model that includes vibrational conical intersections and explains relaxation in H_2O must be consistent with observations made in D_2O and isotopically dilute HOD as well.

We must also consider the delocalized vibrations that are excited in the experiments. These excitonic effects dominate the dynamics, and they manifest themselves as decays in correlation functions that are much faster than other hydrogen-bonding liquids and effectively independent of temperature. From an experimental perspective, measuring the delocalization length as a function of time is paramount. We have already seen an example in which 2D IR depolarization measurements give hints of the relative delocalization of oscillators at different frequencies. A more thorough study is necessary to understand the details of this measurement. Furthermore, a careful mapping of timescales to deuterium concentration can in principle provide insight into how much deuterium is necessary to disrupt these excitons in a nontrivial way.

Finally, and most interesting in my opinion, is the nature of the dynamical evolution of these delocalized vibrations. How do these excitons evolve under the stochastic motion of the water molecules they are delocalized over? Answering this question requires a far deeper understanding not only of water itself, but of the fundamental many-body physics governing the evolution of this excitation. Unlike many-body localization [283], which tracks the evolution of interacting excitations on a static and disordered potential energy landscape (and is the many-body version of the better known Anderson localization [275]), in water it is necessary to understand the evolution on a fluctuating disordered potential. This pushes the limit of what is currently understood theoretically, and water is a physical realization of this phenomenon just waiting to be explored.

6.A Vibrational Dynamics of Alcohols

In order to compare the vibrational dynamics observed in water to other hydrogen-bonding liquids, a 2D IR series of isotopically neat alcohols was collected. The series of alcohols, listed in Table 6.1, included methanol (CH_3OH), ethanol (CH_3CH_2OH), propanol ($CH_3CH_2CH_2OH$), isopropanol ($(CH_3)_2CHOH$), and tert-butanol ($(CH_3)_3COH$). A series of 2D IR spectra are shown in Fig. 6.13.

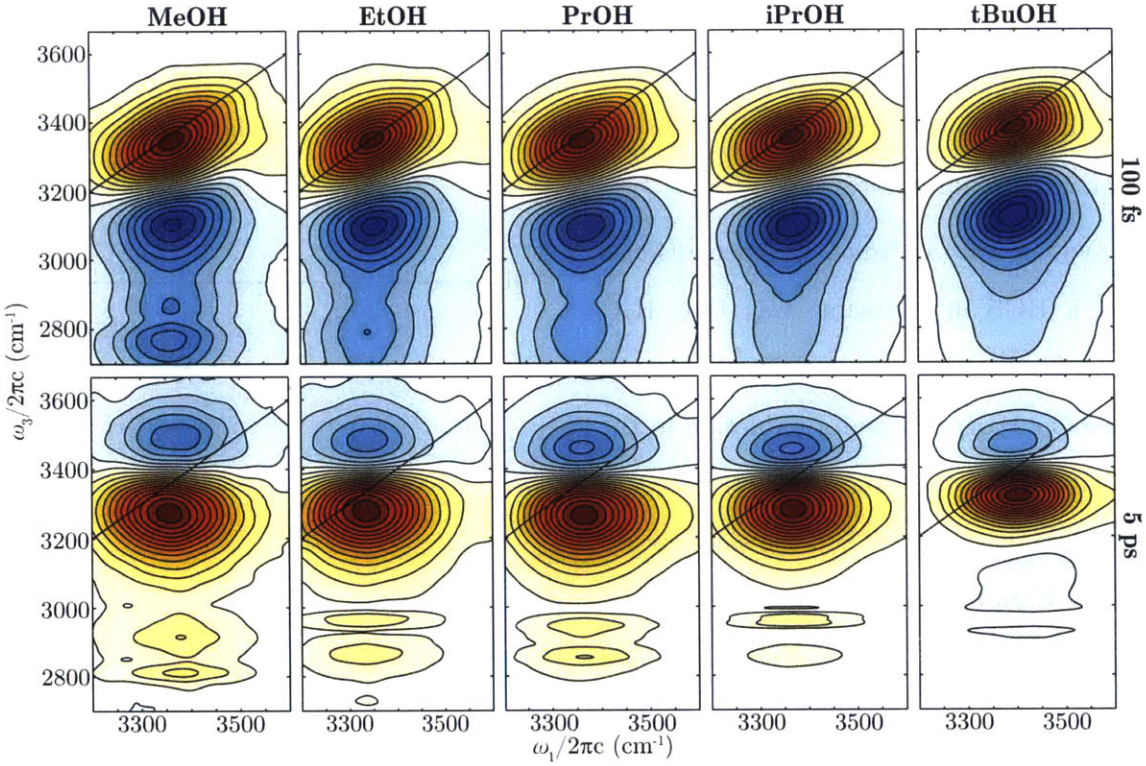

Figure 6.13: 2D IR spectra of various alcohols taken in the magic angle polarization scheme for τ_2 = 100 fs and 5 ps.

Qualitatively, alcohols show similar features to H_2O. In particular, at early times alcohols' O—H stretching modes show a GSB elongated along the diagonal and an ESA that is several times broader than the GSB. Unlike H_2O, the ESA shows significant structure associated with cross peaks to the C—H stretching modes. This structure becomes less pronounced as the length of the alcohol chain is increased and the O—H group becomes further from C—H groups. For example, the C—H cross peaks are less evident in isopropanol compared to propanol since the O—H is attached to a CH group in the former and a CH_2 group in the latter. Furthermore, no cross peaks are evident whatsoever in tert-butanol, consistent with the fact that there are no hydrogen atoms bonded to the oxygen-bonded carbon.

Interestingly, as the chain length is increased, the breadth of the ESA becomes more comparable to the GSB. This is consistent with our interpretation of the H_2O data in which the extremely broad ESA was attributed to the massive anharmonicity in the NPES that arises due to hydrogen-bonding. That is, with increasing carbon-chain length, the ability to form long chains of hydrogen-bonded O—H groups decreases and the O—H oscillators become more harmonic.

At long waiting times, the alcohols also show a HGS in the same way that H_2O does. This is characterized by a blueshift of the O—H stretch and a reduction in the oscillator strength of the C—H stretches. A careful study of the HGS of the alcohols has not yet been carried out, but based on the ratio of the O—H stretch relaxation and HGS growth given in Table 6.1, the alcohols' HGS presumably shares many of the same characteristics as that of H_2O.

Finally, we comment on the variation of the CLS decay timescale of the various alcohols. Figure 6.14 shows the CLS decay timescale as a function of viscosity for the alcohol series (black dots). The points fall on a line with a slope of 1.10 ps/cP with an intercept of 0.27 ps, shown as a black line. If the CLS decay timescales for isotopically dilute water are plotted on this graph (red dots), they

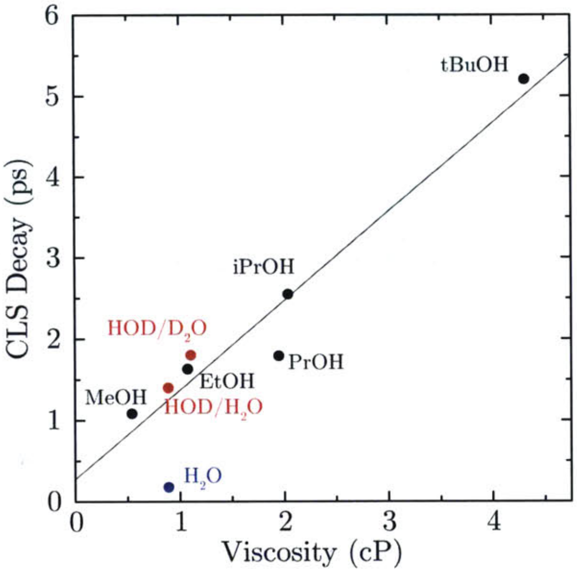

Figure 6.14: CLS decay timescale as a function of viscosity for neat water, isotopically dilute water, and alcohols. Black line is a linear fit to the alcohol data.

surprisingly follow the same trend as the alcohols do. On the other hand, plotting neat H_2O on this figure (blue dot) shows a large deviation from the trend.

This illustrates the importance of an extended network of hydrogen bonds in observing the unique dynamics exhibited in H_2O. That is, alcohols and isotopically dilute water behave the same –while the dynamics for both systems are dictated by hydrogen bonding, the alcohols do not seem to care whether their hydrogen-bonding partner is resonant or not. The fluctuations of the environment, determined empirically from the macroscopic viscosity, dictate the decay of the CLS; this behavior has previously been observed in systems that only weakly interact with their environments [284]. This suggests that alcohols' O—H stretching modes do not participate in excitonic vibrations and are relatively localized.

6.B Waiting Time Series of H_2O

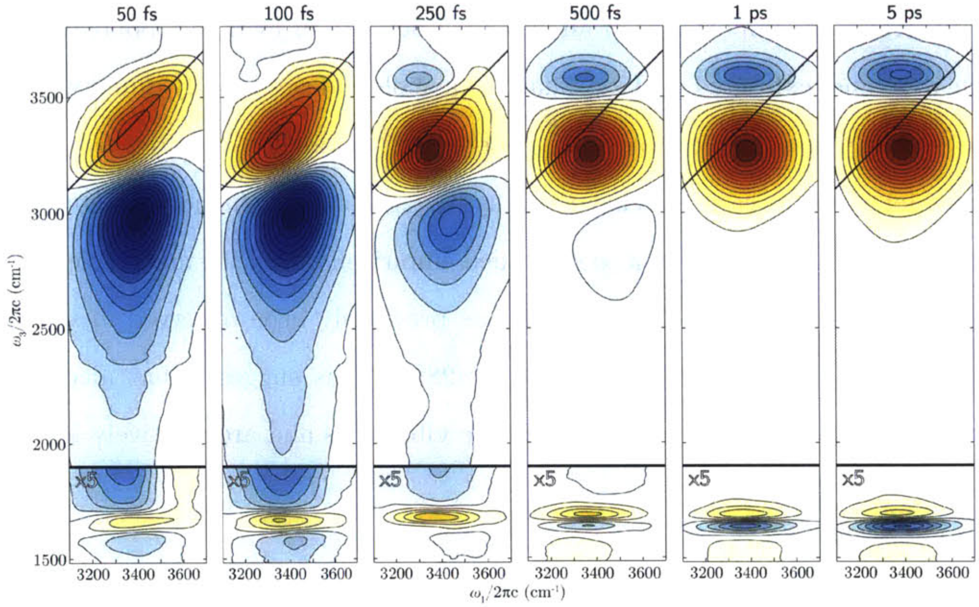

Figure 6.15: Parallel (ZZZZ) 2D IR spectra of H_2O taken at waiting times of $\tau_2 = 50$, 100, 250, 500, 1000, and 5000 fs.

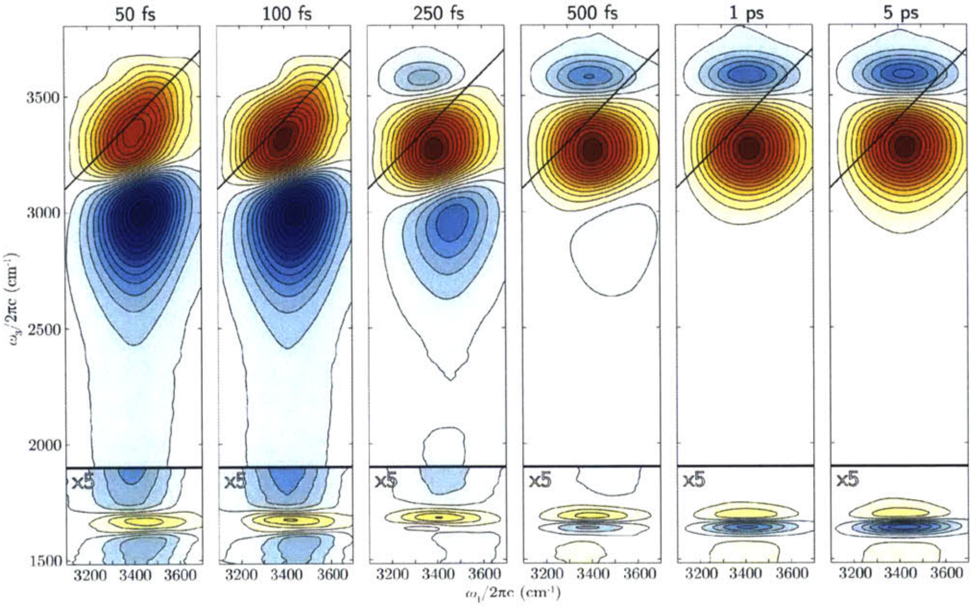

Figure 6.16: Perpendicular (ZZYY) 2D IR spectra of H_2O taken at waiting times of $\tau_2 = 50$, 100, 250, 500, 1000, and 5000 fs.

6.C Temperature Dependent 2D IR Spectra

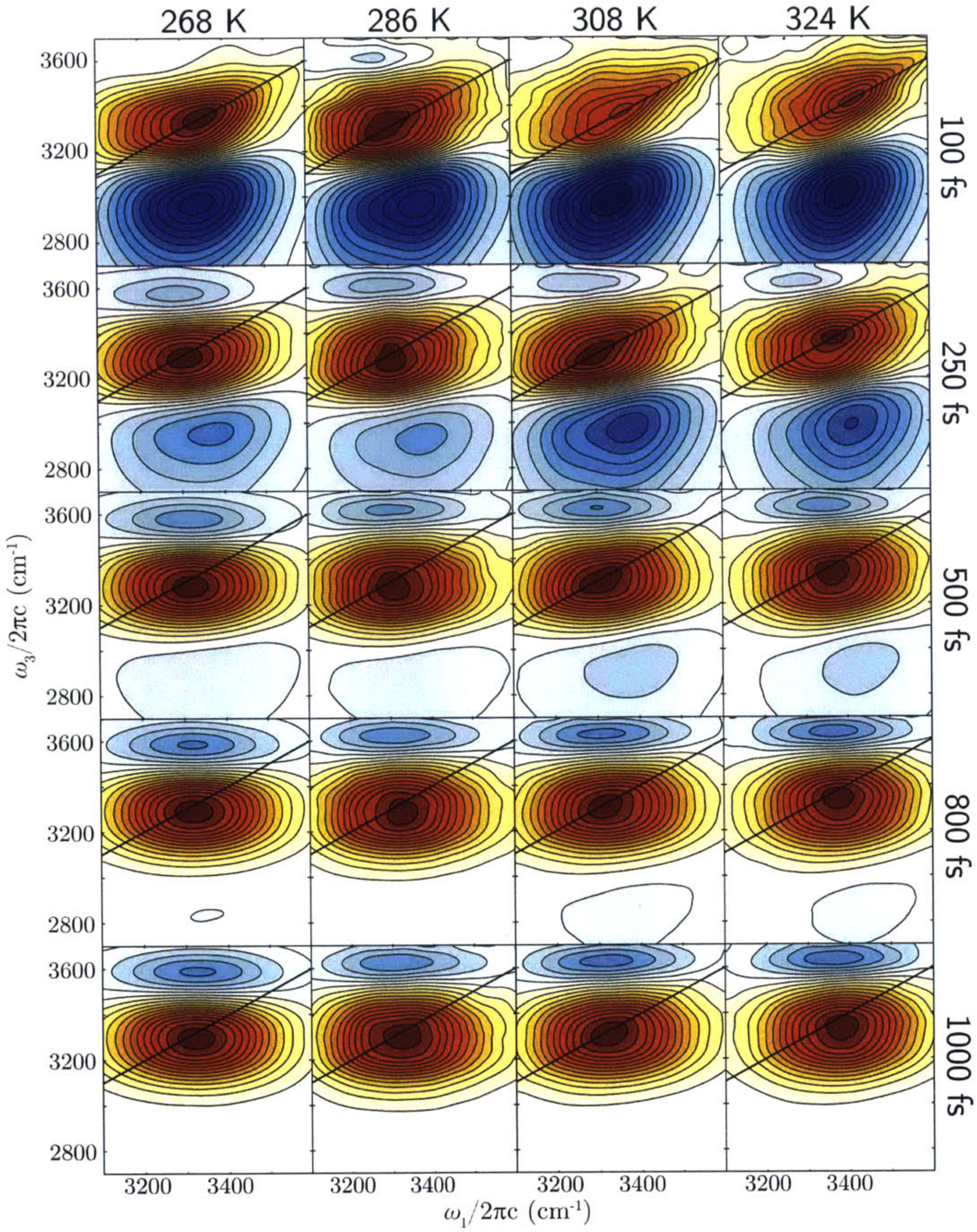

Figure 6.17: Representative 2D IR spectra of H_2O for various temperatures and waiting times taken at magic angle polarization. These spectra are taken out of a data set of 43 temperatures, each taken for 41 different waiting times between 50 and 3000 fs.

Chapter 7

Molecular Dynamics of Heavy Water

7.1 A Predictable Experiment?

Given the rich vibrational dynamics observed in H_2O, it seemed natural that a similar study should be carried out on its heavier brother, D_2O. For all intents and purposes this ought to have been a boring experiment since in principle, the effect of isotope substitution on vibrational dynamics is well understood [83]. In the limit in which only hydrogen atoms are moving in a particular vibration, it is expected that substitution with deuterium reduces the frequency of vibration by a factor of $1/\sqrt{2}$, the change in reduced mass. Experimentally, small deviations from this simple scaling relation are observed due to deviations of the nuclear potential energy surface from harmonicity.

Surprisingly, or perhaps not given liquid water's complexity, it was clear from the first experiments we carried out that D_2O differs from H_2O in nontrivial ways. That is, heavy water's vibrations are qualitatively different than light water's and are not related to those of H_2O by a simple scaling of frequency and timescales. Rather, the O—D stretch appears more localized than the O—H stretch, and unlike H_2O, the symmetric and antisymmetric forms of the O—D stretching vibrations are retained in the liquid phase, although with a significantly different character than in the gas phase. This difference in molecular dynamics reflects the shift in the balance between intra- and inter-molecular couplings upon deuteration —an effect which can be understood in terms of (and gives direct insight to) the anharmonic nuclear potential energy surface. While this effect must be explored further, it is clear that these differences could result in significant variations in the outcome of dynamical processes and chemical reactions in heavy versus light water.

Unlike H_2O, heavy water has not received as much attention in the ultrafast IR spectroscopy community. Rather, D_2O has served as a background solvent for studies of isotopically dilute HOD. Literature studies have measured the vibrational lifetime of the O—D stretch to be 350 fs [285] and 400 fs [286]. The latter study also reported a polarization anisotropy decay of $\sim$200 fs, which was interpreted in terms of Förster resonance energy transfer between O—D oscillators. This is despite the necessity to make some dubious assumptions that do not likely hold in liquid water [259]. This appears to be the extent of direct studies of the O—D stretching mode in D_2O with nonlinear IR spectroscopy. Indirect studies, probing the isotpoically dilute O—H stretch of HOD in D_2O have reported hydrogen-bond-breaking times in the range of 0.9–1.4 ps [15, 222, 223], which provides a timescale for molecular fluctuations in D_2O. These values are consistent with the values ranging from 0.75–1.4 ps measured for the fluctuations of the D_2O network (see §5.4).

The work in this chapter is an expansion of a letter submitted to *The Journal of Physical Chemistry Letters* in 2016 [287]. Here we discuss the linear and time-dependent nonlinear spectroscopy of heavy water, while comparing the results to those for H_2O. Particular emphasis is place on the polarization dependence of the 2D IR spectrum data which opens a window into understanding D_2O's vibrations and provides strong experimental evidence for the presence of symmetric and antisymmetric vibrations in heavy water. These observations are supported by Local Monomer simulations of the transition dipole moment angle that were carried out in a brief but fruitful collaboration with Hank Liu and Joel Bowman at Emory University.

7.2 Linear Spectroscopy of D_2O

In principle, upon deuteration of the entire molecule, we expect the frequencies of water's vibrations to redshift by a factor of $1/\sqrt{2}$ under the approximation that only hydrogen atoms move significantly within a particular mode. A comparison of the gas-phase antisymmetric stretching frequencies shows that this is almost, but not quite, the case. The ratio of gas-phase antisymmetric stretching is $\omega_a'/\omega_a = 2788\ \text{cm}^{-1}/3756\ \text{cm}^{-1} = 0.742$ (a prime is used to denote D_2O frequencies). The ratio is about 5% larger than the expected value, which alludes to the fact that there are effects that are not accounted for in a simple scaling factor. The ratio of the symmetric stretching frequencies is even larger, $\omega_s'/\omega_s = 2672\ \text{cm}^{-1}/3657\ \text{cm}^{-1} = 0.755$.

The linear IR spectrum of liquid D_2O is shown in Fig. 7.1A as a black curve. The spectrum shows a broad O—D stretching band centered at 2505 cm^{-1}, a narrower DOD bending mode at 1210 cm^{-1}, and a bend–libration combination band at 1555 cm^{-1}. Along with the spectrum of D_2O is plotted the spectrum of liquid H_2O on a frequency axis scaled by the ratio of gas-phase antisymmetric stretching frequencies, 0.742. Such a scaling results in the bending mode and the bend–libration combination band lining up almost perfectly in frequency, amplitude, and breadth. The stretch lines up almost perfectly in frequency, however the lineshape shows significant differences. The fact that the gas-phase frequency scaling is the same as the liquid phase one is surprising in and of itself. Of course, the gas-phase scaling has nothing built into it that reflects intermolecular interactions, and given that the hydrogen bonds in D_2O are on average somewhat stronger [288,289], it would seem that the liquid and gas phases ought to require different scaling factors to put them on a common axis.

The difference in lineshape between the O—D and O—H stretching resonances is rather striking. Figure 7.1B shows the two stretching bands on a zoomed axis. A quick comparison of the H_2O and D_2O stretching features shows that the two have considerable substructure whose origins are complex and not universally agreed upon. Contradicting proposals suggest

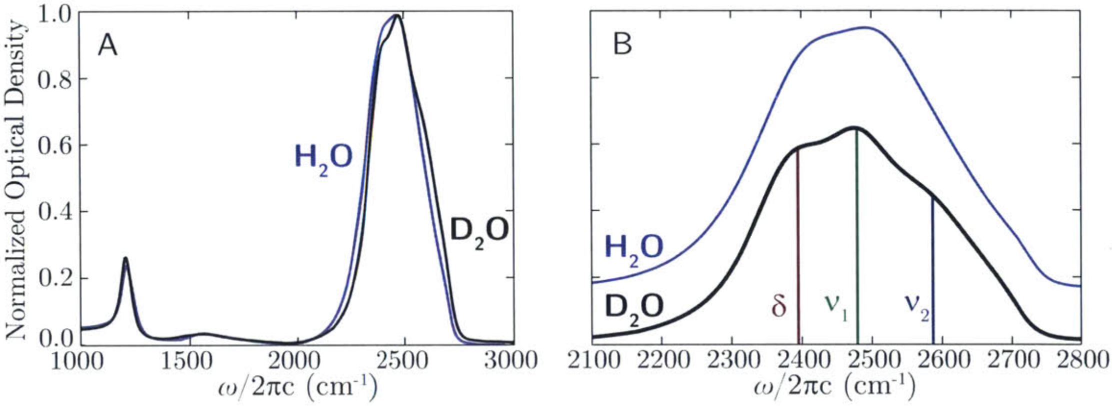

Figure 7.1: (A) Linear IR spectrum of D_2O (black line) and H_2O (blue line) plotted on a frequency axis scaled by the ratio of the gas-phase antisymmetric stretches, 0.742. (B) Expansion of the stretching region of A. Colored lines indicate the positions of the peaks making up the O—D stretch.

that the vibrations are either excitonic or that the substructure comes different hydrogen-bonding environments [44, 219, 290]. The low-frequency shoulder has in some cases been assigned to an overtone of the bending mode, enhanced by a Fermi resonance [219, 291], or alternatively, to strongly hydrogen-bonded molecules in structured geometries [47, 211, 292]. The differences in these spectra indicate that there are non-trivial isotopic effects present. In fact, D_2O shows three distinct peaks at 2395, 2479 and 2587 cm^{-1} within the O—D band, which we will refer to as peaks δ, ν_1, and ν_2, respectively. These are marked by colored lines in Fig. 7.1B. Although the O—H stretch in H_2O appears to have similar structure, the peaks are far less discernible and the high frequency peak has essentially disappeared (though it is discernable in the Raman spectrum [262]).

7.3 Nonlinear Spectroscopy of D_2O

7.3.1 Early and Late Time Spectra

To delve further into the differences between H_2O and D_2O, 2D IR spectroscopy of the O—D stretching mode was performed. This is a natural path for disentangling the substructure in the O—D stretching band for two reasons: 1) the quartic scaling of the dipole moment in third-order spectroscopy sharpens the features relative to the linear spectrum, in principle rendering them more distinguishable and 2) the possibility of observing cross peaks between the features making up the substructure gives enormous insight into their origin. 2D IR spectra of the O—D and O—H stretches were collected at a waiting time of 100 fs for parallel ($I_{\parallel}$, ZZZZ) and perpendicular ($I_{\perp}$, ZZYY) polarizations between the excitation and probe fields. The results are shown in Fig. 7.2, where the frequency axes of the H_2O spectra are scaled by 0.742.

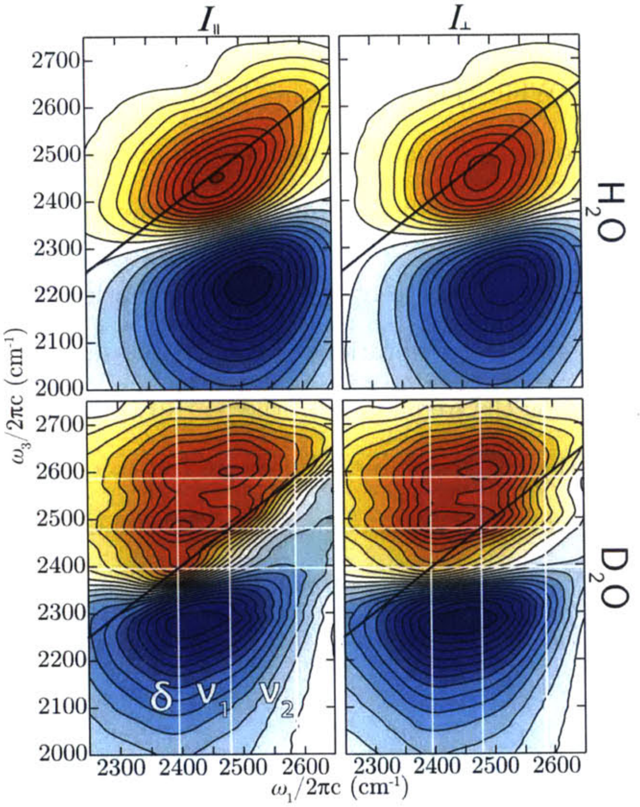

Figure 7.2: Comparison of the 2D IR spectra of H_2O (upper half) and D_2O (lower half) for $I_{\parallel}$ (left half) and $I_{\perp}$ (right half) polarizations. H_2O axes have been scaled by the ratio of gas-phase antisymmetric stretches. Lines in the D_2O spectra indicate the position of the δ, ν_1, and ν_2 resonances.

Both H_2O and D_2O show a broad ground state bleach (GSB) of the fundamental transition near the diagonal, $\omega_1 = \omega_3$. In addition, the spectra show an excited state absorption (ESA) that peaks several hundred wavenumbers red-shifted in ω_3 due to anharmonicity of the O—^{x}H bond. Whereas the GSB of H_2O is a single peak on the diagonal, the GSB of D_2O lies mainly above the diagonal, and shows cross peaks between the three resonances corresponding to the δ, ν_1, and ν_2 frequencies. We expect cross peaks to be present below the diagonal as well; however, they are not resolved due to overlap with the ESA. The spectrum of D_2O is highly anisotropic, showing significant differences in the parallel and perpendicular spectra. This is particularly evident just below the diagonal, where $I_{\perp}$ has significantly more intensity in the GSB than $I_{\parallel}$. This is discussed further in the following section.

That the D_2O resonances show cross peaks between them, immediately shows that there are three distinct modes of vibration with strong vibrational coupling between the atoms comprising them [78]. The three peaks must therefore come from the same molecule or group of molecules, precluding the possibility that the substructure in the O—D stretching band arises due to disconnected water environments. While this substructure is not as evident in the 2D IR spectrum of H_2O, it is reasonable to assume that the weak O—H substructure observed in the absorption and Raman spectra has its origins in similar phenomena.

The clear evidence of cross peaks in the 2D IR spectrum of D_2O naturally harks back to the notion of symmetric and antisymmetric stretching vibrations of the gas phase and a Fermi resonance with the bend overtone. Based on the frequencies of the features, the only reasonable assignment is that δ corresponds to the bend overtone while ν_1 and ν_2 to the two stretching modes. This interpretation is consistent with previous models of the anharmonic potential energy surface of liquid water [293]. Whether ν_1 or ν_2 corresponds to symmetric or antisymmetric is discussed in the following section. Given the strong intermolecular coupling in liquid water, we cannot expect that these vibrations are simply related to the symmetric and antisymmetric vibrations of individual molecules. Rather, we expect that vibrations will be delocalized over some number of molecules while retaining a particular symmetry overall. Indeed, theoretical studies [290] have predicted that the collective vibrations of H_2O water molecules should retain some of their symmetric/antisymmetric character though this is not universally accepted [294,295]. Furthermore, collective symmetric/antisymmetric

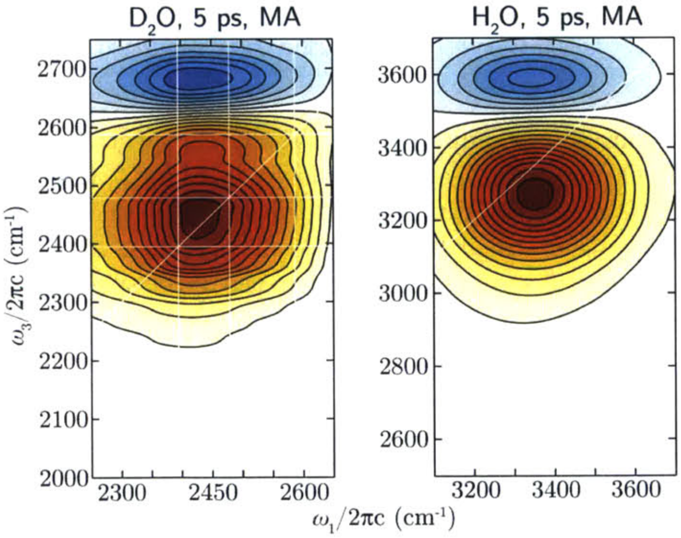

Figure 7.3: Hot ground state spectra of D_2O (left) and H_2O (right) taken at magic angle polarization and $\tau_2 = 5$ ps.

vibrations have been invoked to understand the spectrum of the solid phase [293]. In any case, it is clear that the vibrations of D_2O are fundamentally different from those of H_2O, even just by looking at the 2D IR spectra. H_2O appears to have highly delocalized excitonic modes in which most of the oscillator strength is in one dominant mode [190], while D_2O seems to show distinct vibrations.

Like H_2O, at long times the nonlinear spectrum of D_2O shows a hot ground state (HGS). Figure 7.3 shows a comparison of the HGS for D_2O and H_2O taken at $\tau_2 = 5$ ps. Of course, at these waiting times, the spectrum is isotropic, since the polarization anisotropy decays on a 200 fs timescale in D_2O [286] and a 70 fs timescale in H_2O [190, 254]. Like H_2O, the HGS of D_2O shows a blueshift corresponding to the weakening of hydrogen bonds. Furthermore, the magnitude of the HGS signal relative to the overall optical density is similar to that of H_2O, suggesting that the kinetic temperature rise is similar to the 10–20 K observed in H_2O (see §6.5). Unlike H_2O, however, D_2O retains traces of the structure observed in the linear and nonlinear spectra as evidenced by the feature at $\omega_3 \approx 2550$ cm^{-1}.

7.3.2 Polarization Anisotropy

Given the large difference between the $I_{\parallel}$ and $I_{\perp}$ signals in the 2D IR spectra, we stand to learn a great deal from a careful analysis of the polarization dependence. In particular, we may turn to the depolarization ratio, $D(\Theta_{ij}) = I_{\perp}^{ij}/I_{\parallel}^{ij}$, defined in Eq. 2.72 of §2.5.5, to characterize the angle between the transition dipole moments of vibrations i and j, $\hat{\boldsymbol{\mu}}_i \cdot \hat{\boldsymbol{\mu}}_j = \cos \Theta_{ij}$.

Slices of the $I_{\parallel}$ and $I_{\perp}$ 2D IR spectrum taken at constant ω_1 values corresponding to the frequencies of the δ, ν_1, and ν_2 transitions are shown in Fig. 7.4. Solid lines correspond to $I_{\parallel}$ and dashed lines correspond to $I_{\perp}$. Furthermore, the zero value for each slice is shown as a dashed grey line. For each slice, $I_{\parallel}$ has not been scaled relative to $I_{\perp}$, though the slices are scaled relative to each other. Slices through the δ and ν_1 resonances show similar features that vary slightly in intensity. These variations are subtle, and they are difficult to interpret due to significant overlap between the different features. A cursory glance shows that for these slices, the depolarization ratio is close to one. However, for excitation of ν_2, the enhancement of the (ν_2, ν_1) cross peak in $I_\perp$ relative to $I_\parallel$ is striking (this enhancement is indicated by a blue arrow in Fig. 7.4). Indeed, this difference between the two signals is evident in the 2D IR surface itself. Whereas the GSB in the parallel spectrum lies mainly above the diagonal, there is significant intensity below the diagonal in the perpendicular spectrum, corresponding to an intensification of the (ν_2, ν_1) cross peak.

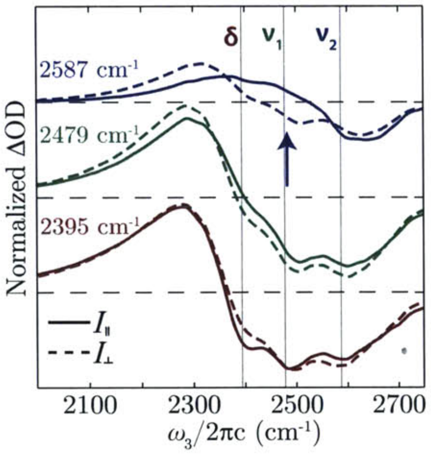

Figure 7.4: Slices through the $I_\parallel$ (solid line) and $I_\perp$ (dashed line) 2D IR spectra of D_2O taken at a waiting time of $\tau_2 = 100$ fs. Arrow indicates the position of the (ν_2, ν_1) cross peak.

Whereas parallel transition dipole moments should result in a cross peak with $D(\Theta_{ij} = 0) = 1/3$, we observe that the bleach of the (ν_1, ν_2) cross peak is actually more intense in the $I_\perp$ spectrum than the $I_\parallel$ spectrum with a depolarization ratio of $D(\Theta_{12}) = 1.08$. This indicates that there is an angle close to 90° between the transition dipole moments of the two modes, as one would expect for gas-phase symmetric and antisymmetric vibrations. Furthermore, this $\tau_2 = 100$ fs measurement indicates that the angular correlations exist for delays > 100 fs, which is consistent with the previously measured value of $\sim$200 fs for the polarization anisotropy decay [286] and in contrast to H_2O, in which angular correlations are lost on a timescale of 70 fs [190, 254].

In the latter studies, the ultrafast relaxation of the polarization anisotropy in H_2O was interpreted in terms of delocalized excitonic vibrations.The excitation of a delocalized vibrational O—H stretching mode rapidly results in the scrambling of the initially excited transition dipole due to diffusion of the exciton to other nearby vibrational modes. The persistence of such a large difference between polarizations in D_2O therefore suggests that its vibrations are somewhat more localized compared to H_2O. This of course does not preclude the possibility that D_2O's vibrations are still delocalized, just that they are not as delocalized as those of H_2O. The converse is that excitation of O—D stretching mode does not result in energy diffusion as rapid as in H_2O since the initial excitation is less extended.

It is tempting to extract an angle based on the measured depolarization; however, this cannot be determined directly from the spectrum, since overlapping features, in particular those of opposite sign, skew the intensities in significant and unpredictable ways. Nonetheless, if we consider that the depolarization ratio of the (ν_1, ν_2) cross peak is $D(\Theta_{12}) = 1.08$, an angle of 79° or 101° between the transition dipoles of these modes is implied [72, 192]; the latter is consistent with the angle of 96° which was fitted between the symmetric and antisymmetric modes for monomeric H_2O in acetonitrile [296].

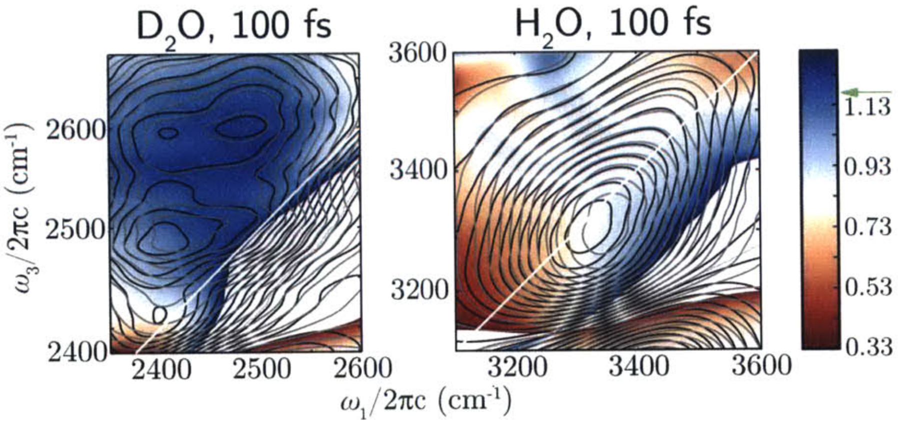

Figure 7.5: 2D depolarization surfaces for D_2O and H_2O taken at a waiting time of τ_2=100 fs. The black and grey contours show the parallel and perpendicular spectra, respectively. The green arrow on the color bar indicates the theoretical depolarization limit.

From the 2D IR spectra, it is possible to calculate a depolarization surface in which the depolarization is plotted as a function of the two frequency variables. The 2D depolarization surfaces, taken at a waiting time of $\tau_2 = 100$ fs, for D_2O and H_2O are shown in Fig. 7.5. Figure 7.5 also shows the contours corresponding to the original data, with black contours being $I_{\parallel}$ and grey contours $I_{\perp}$. The depolarization surface for the GSB of D_2O appears to be mostly blue, corresponding to depolarization ratios $D(\Theta) > 1$. In fact, certain parts of the depolarization surface, in particular near the (ν_1, ν_2) cross peak, are actually larger than

7/6, which is the theoretical limit for perpendicular dipoles (this limit is indicated by a green arrow in the color bar of Fig. 7.5). Of course the actual numerical value is an artifact of the overlap with nearby features, but its magnitude is consistent with the interpretation that these features have large angles between them. At low or high frequencies, corresponding to the diagonal δ and ν_2 features, the depolarization shows a pronounced drop because these features do not suffer from as much interference from the cross peaks.

The 2D depolarization surface for H_2O is quite different compared to that of D_2O. Unlike heavy water, H_2O shows a surface which is mostly white, corresponding to a depolarization ratio of $D(\Theta) \approx 0.80$. Based on earlier measurements [190, 254], it is known that water's polarization anisotropy begins at a value between 0.3 and 0.4 and decays to zero on a timescale of 70 fs [190, 254]. Therefore, the measured depolarization ratio corresponds to the decay of the initial anisotropy as the depolarization progresses to its ultimate value of 1. Interestingly, at low frequencies (equivalently, strong hydrogen bonds), the depolarization ratio is ~ 0.33, implying that these dipoles are still roughly parallel to their intial value. This shows that strongly-hydrogen-bonded oscillators tend to retain their initial configuration for longer times than average. This is consistent with what has been measured previously for isotopically dilute water [236]. This difference between H_2O and D_2O is clear evidence for entirely different types of vibrations between the two liquids. Whereas H_2O appears to behave like a single vibration whose depolarization decays quickly, D_2O shows multiple vibrations with a defined angle close to 90° between them.

In principle, the polarization data cannot be explained by a unique angle between the transition dipole moments of the bending and stretching modes in the molecular frame. That is, since the vibrations are delocalized over multiple molecules, and each set of multiple molecules will have a different configuration, each vibrational excitation will have a different set of angles between its modes. Additionally, these configurations will fluctuate, so that the angle between the stretch and the bend, for example, will change with time due to the low-frequency motion of the water molecules. Therefore, the angle between the excitation and detection transition dipoles is necessarily statistical. In this case, the expressions for

$I_{\|}$ and $I_{\perp}$ must be averaged over a probability distribution reflecting the wide range of transition dipole angles that various configurations can take on. That is, the measured depolarization ratio is given by

$$D[\mathcal{P}_{ij}(\cos\Theta)] = \frac{\langle I_{\perp}^{ij}\rangle}{\langle I_{\|}^{ij}\rangle} = \frac{\int \mathrm{d}(\cos\Theta)\mathcal{P}_{ij}(\cos\Theta)I_{\perp}^{ij}(\cos\Theta)}{\int \mathrm{d}(\cos\Theta)\mathcal{P}_{ij}(\cos\Theta)I_{\|}^{ij}(\cos\Theta)}, \tag{7.1}$$

where $\mathcal{P}_{ij}(\cos\Theta)\mathrm{d}\cos(\Theta)$ is the probability of finding the cosine of the angle between the transition dipoles i and j, $\hat{\boldsymbol{\mu}}_i \cdot \hat{\boldsymbol{\mu}}_j$, between $\cos\Theta$ and $\cos\Theta + \mathrm{d}(\cos\Theta)$. Now, the depolarization ratio is a functional of this probability distribution, and a fixed angle between two transition dipoles corresponds to $\mathcal{P}_{ij}(\cos\Theta) = \delta(\cos\Theta - \cos\Theta_{ij})$. Furthermore, we note that $\mathcal{P}_{ij}(\cos\Theta)\mathrm{d}(\cos\Theta) = \mathcal{P}'_{ij}(\Theta)\sin\Theta\mathrm{d}\Theta$.

It is worth noting that this average is different than the rotational average carried out on the third-order response function in §2.4. The averaging in Eq. 7.1 is over an ensemble of molecules that possess different transition-dipole angles in the molecular frame. On the other hand, the averaging of the third-order response function is carried out to account for the ensemble of molecules that possess different orientations in the laboratory frame. Since the orientation of a molecule in the laboratory frame is independent of the transition dipoles in the molecular frame, the averages can be carried out separately.

To explore the distribution of transition-dipole angles and the effect of this distribution on the 2D IR spectrum, molecular dynamics simulations were performed and transition dipoles calculated using the Local Monomer method [297] in which the Schrödinger equation for coupled local normal modes is solved. Ten snapshots from a 300 ps MD simulation of 500 water molecules of liquid D_2O at 300 K were used in quantum Local Monomer calculations of the vibrational eigenstates of each monomer. In these calculations, only the three intramolecular modes are explicitly coupled. The more computationally intensive calculations that include intermolecular modes, reported in Ref. [298], show only very minor differences with the 3–mode calculations for this band and so they were not done here. The coupled 3–mode calculations are used to obtain the IR spectrum and dipole moment of each monomer using the WHBB potential [299]. The final spectrum is a Gaussian smoothed IR spectrum of a total of 1000 Local Monomer calculations. The full details of the simulation along with a near-quantitative calculation of the IR spectrum of D_2O is presented in Ref. [298]. Of course, this local monomer method is incapable of capturing the range of transition-dipole angles taken on in delocalized vibrations, but it provides a suitable starting point for their consideration.

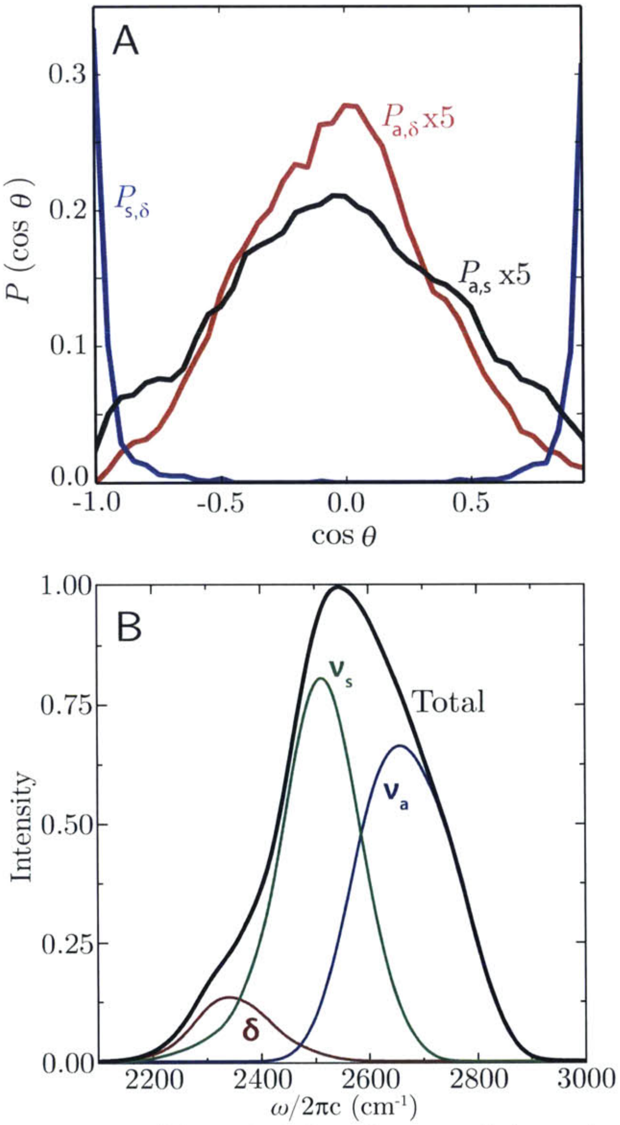

Figure 7.6: (A) Probability density of the cosine of the angle between the δ, ν_s, and ν_a resonances based on Local Monomer calculations. (B) Corresponding IR spectra of the three different modes making up the O—D stretching band.

The probability density for the cosine of transition-dipole angles within one molecule is shown in Fig 7.6A. The distribution of angles between the symmetric stretch and bend overtone is sharply peaked at $\cos\Theta = \pm 1$, which shows that these transition dipoles are aligned, as expected based on the gas-phase spectrum and the symmetry of the molecule. However, the transition-dipole angle between the symmetric and antisymmetric stretches (and by extension between the antisymmetric stretch and bend overtone), shows a broad distribution. While it is peaked at $\cos\Theta = 0$, corresponding to perpendicular dipoles, they can take on a broad range of angles, and even show non-zero probability to be parallel. Therefore, even at the local monomer level, the transition dipole moment angle between the symmetric and antisymmetric stretching modes is statistical.

Averaging the signal with the probability distributions shown in Fig. 7.6 as per Eq. 7.1, results in reduced depolarization ratios of $D[\mathcal{P}_{\mathrm{s},\delta}(\cos\Theta)] = 0.38$, $D[\mathcal{P}_{\mathrm{a},\delta}(\cos\Theta)] = 0.90$, and $D[\mathcal{P}_{\mathrm{s,a}}(\cos\Theta)] = 0.81$. These can be compared to the theoretical values of 0.33 and 1.16 for perfectly parallel and perpendicular dipoles. The fact that the experimentally measured value of the depolarization for the (ν_1, ν_2) cross peak is 1.08 is surprising, since it suggests that the experimental distribution of angles is actually narrower than that computed for the monomer. However, this is most likely an artifact of the fact that the intensities are skewed by overlapping features.

While this calculation is done at the Local Monomer level, it is safe to assume that any delocalized mode with symmetric or antisymmetric character will result in transition dipole distributions that are broader than those shown in Fig. 7.6A since there are a larger number of possible configurations. However, for a completely random distribution of angles, that is $\mathcal{P}(\cos\Theta) = 2^{-1}$, a depolarization ratio of 0.66 is expected (as per Eq. 7.1). This is significantly smaller than the observed depolarization in the experiment, and so we are led to conclude that there is necessarily residual symmetric and antisymmetric character in D_2O's vibrations even if the modes are delocalized.

The assignment of the ν_1 and ν_2 modes to symmetric and antisymmetric stretches from experimental data alone is not straightforward since the condensed-phase modes cannot possibly reflect the gas-phase ones. To investigate how intermolecular interactions in D_2O influence the nature of collective O—D stretch vibrations, we turned to the calculation of the IR spectrum based on the simulation described above. Vibrations making up the O—D stretching band were separated into symmetric stretch, antisymmetric stretch, and bend overtone; the three components are shown in Fig. 7.6B. This is done based on an analysis of the virtual-state-configuration interaction coefficients obtained in the diagonalization of the Local Monomer Hamiltonian matrix. The zero-order state with the largest coefficient is the one used to assign the molecular eigenstate to a given sub-band. This is a reasonable (but somewhat blunt) criterion to make these assignments. The results show that the

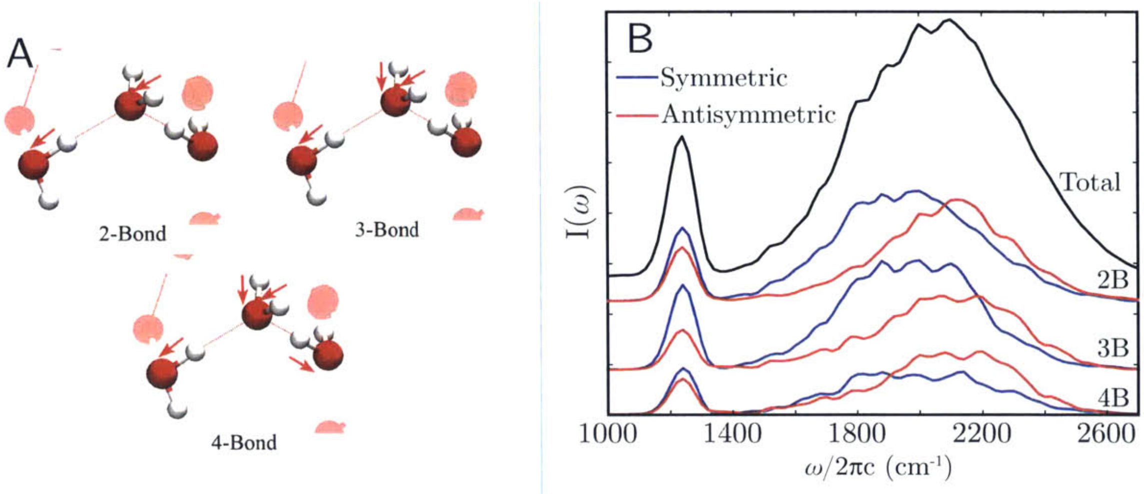

Figure 7.7: (A) Definition of displacements used for calculating bond correlations. Arrows indicate local mode displacement vectors within the normal mode. (B) Density of states for 2- to 4-bond correlations. Symmetric stretching and antisymmetric stretching shown in blue and red, respectively.

antisymmetric stretching mode is at higher frequency than the symmetric mode, as it is in the gas phase, though there is a significant amount of overlap between the two bands. The δ, ν_s, and ν_a features in the calculation respectively peak at 2431, 2598, and 2782 cm^{-1}, which is comparable to the frequencies measured in the linear spectrum of 2395, 2479 and 2587 cm^{-1}. In particular, the bend overtone frequencies are in good agreement. However, the stretching bands are intense and strongly overlapped so that a direct comparison between the calculations and experiment is not so easy. The anharmonicity that gives rise to the Fermi resonance of the bend overtone is going to result in a mixing of the character of the vibrations; in particular, we expect that the mixing is strongest with the symmetric stretch based on gas-phase symmetry considerations and resonance. However, we cannot rule out mixing with the antisymmetric stretch since, by virtue of the distribution of angles between it and the symmetric stretch, it only statistically retains the same symmetry character as the gas-phase modes.

While many of the effects that are suspected of giving rise to D_2O's 2D IR spectrum are present at the Local Monomer level, we attempted to go one step further and characterize delocalized modes. To investigate how intermolecular interactions in D_2O influence the nature of collective O—D stretch vibrations, we turned to density functional theory (DFT) based normal-mode calculations of D_2O water clusters drawn from molecular dynamics simulations. From an SPC-Fw molecular dynamics simulation of H_2O [300], clusters centered on a central H atom with a 5 Å cutoff were chosen every 50 fs. Normal modes and harmonic frequencies were calculated using the Gaussian DFT package [301] at the B3LYP level using the 6-311++G** basis set. Modes were binned based on vibrational correlations, in which the relative vibrational phase over two, three, and four bonds were analyzed and classified as symmetric or antisymmetric. That is, the sign on the local mode displacement vectors along a normal mode were compared; vibrations with the same sign on the displacement were deemed symmetric and vibrations with dissimilar signs were deemed antisymmetric. An example of 2-, 3-, and 4-bond displacements is shown in Fig. 7.7A.

In essence, the results show no strong correlation between frequency and symmetry. Over all bond correlations, symmetric vibrations occurred at frequencies somewhat lower than antisymmetric, but with significant overlap between the two distributions. Two-bond correlations show the most separation between symmetric and antisymmetric; however, frequency trends become less pronounced for three and four bond correlations though antisymmetric stretching still tends to occur at higher frequencies. Spectra for individual bond correlations are shown in Fig. 7.7B. It is worth noting that these calculations do not capture the anharmonicity that gives rise to the Fermi resonance with the bending mode. In the gas phase, we expect mixing with the bend overtone to occur predominantly with the symmetric modes, thus pushing the latter to higher frequencies and it is likely that this occurs in the liquid phase as well, rendering the modes even less spectrally distinct.

Given that symmetric and antisymmetric stretching modes are evident in the experimental data, and based on these calculations as well as the Local Monomer calculations, we are led to conclude that the O—D stretching modes are relatively local. If the DFT calculations are to be trusted, this would suggest that we should not be able to observe distinct symmetric and antisymmetric stretching modes in D_2O, much like in H_2O. Furthermore, the simulations consistently show that the ν_1 mode corresponds to the symmetric stretch, while the ν_2 mode corresponds to the antisymmetric stretching mode, though it is likely that these modes have some character of the bend overtone.

7.4 Relaxation Dynamics of Heavy Water

7.4.1 Transient Absorption of D_2O

The fact that there are multiple overlapping bands within the O—D stretching resonance makes an accurate characterization of the relaxation dynamics difficult. 2D IR is indispensable, since resolution in the excitation frequency, ω_1, is necessary to separate the different features. To that end, we draw dynamical conclusions from the 2D IR spectra, however, we begin by analyzing the transient absorption (TA) spectrum to compare our measurements to the previous literature.

Previous TA studies of neat D_2O have been minimal compared to H_2O. However, Refs. [285,286] have reported lifetimes of the O—D stretch of 350 and 400 fs, and it was found that the HGS spectrum grew in on a 630 fs timescale. In addition, a polarization anisotropy decay timescale of ~200 fs was measured [286] (this value is estimated from a figure within the reference since the actual timescale is not reported). The rapid decay of anisotropy was attributed to Förster resonance energy transfer between O—D oscillators, though, as mentioned, the strong coupling between oscillators and the clear delocalization of vibrations, renders this interpretation questionable.

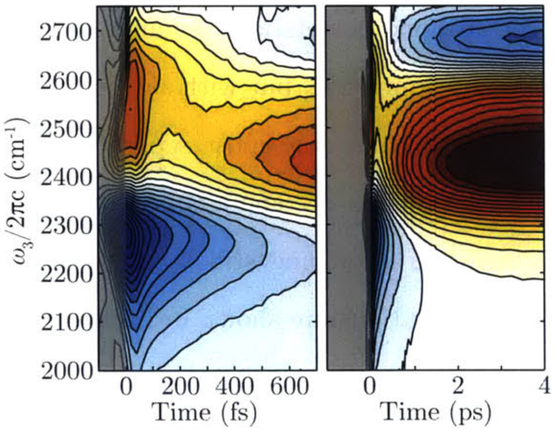

Figure 7.8: Magic angle TA spectrum of D_2O. The left panel shows early times while the right panel shows data well past when the growth of the HGS is complete.

Figure 7.8 shows the magic angle TA spectrum for short times as well as long times.

Qualitatively, the TA spectrum shows similar features to that of H_2O. At early times, a clear bleach of the O—D stretch and associated ESA is visible. The GSB appears to rapidly redshift, but like H_2O, is actually due to the ingrowth of the HGS spectrum. This is accompanied by the growth of a blueshifted induced absorption, corresponding to the broken or weak hydrogen bonds due to the increase in temperature. By ~2 ps, the ESA of the O—D stretch has completely decayed away and the spectrum no longer evolves in time on the timescale of our experiment.

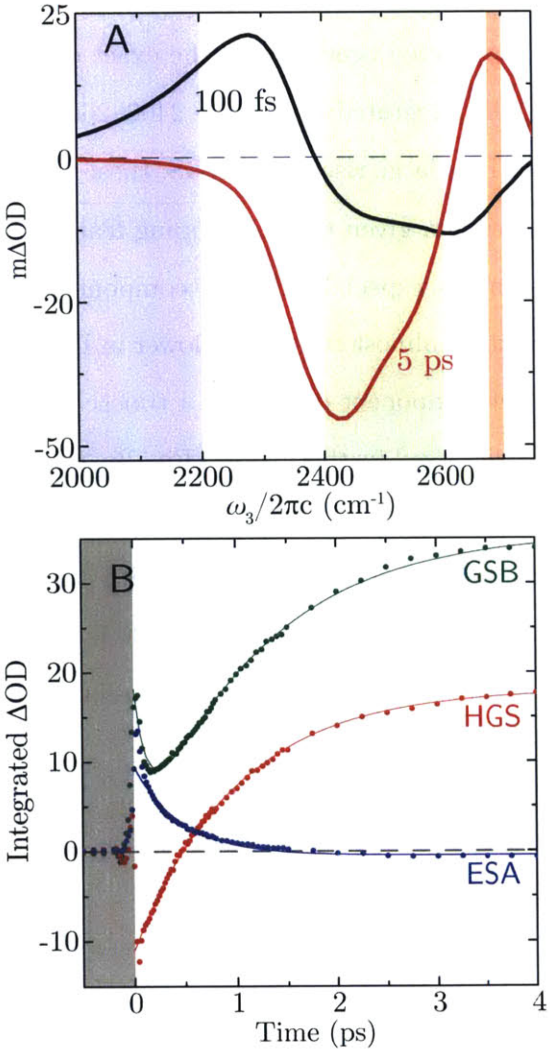

Figure 7.9: (A) Slices of the D_2O TA spectrum at $\tau_2 = 100$ fs and 5 ps. (B) Time traces corresponding to the decay of the ESA (blue), GSB (green), and HGS (red). Solid lines are fits to the data. ESA curve has been multiplied by -1.

Slices through the TA spectrum are shown in Fig. 7.9A for $\tau_2 = 100$ and 5000 fs and time traces are shown in Fig. 7.9B for the ESA, GSB, and HGS. Unlike H_2O, the TA spectrum of D_2O shows considerable structure in the GSB, reflecting the features observed in the 2D IR spectrum. Since the TA spectrum is equivalent to a projection of the 2D IR spectrum onto the ω_3 axis, the δ, ν_1, and ν_2 are not as clear as in the latter, and structure with less pronounced features is observed. As in the 2D IR spectrum, there is no evident structure in the ESA. Similarly, the HGS spectrum shows structure that reflects the long-time 2D IR spectrum (Fig. 7.3) and somewhat resembles the linear spectrum.

Figure 7.9B shows that the ESA, integrated from $\omega_3 = 2000$–$2200\ \mathrm{cm}^{-1}$, decays exponentially with a timescale of 465 fs. This timescale of course depends on the integration window, and values of up to 800 fs can be found if the higher frequency portion of the ESA is integrated and fit. This value is somewhat longer than those reported previously in the literature, but given the sensitivity of the extracted timescale on the exact details of the data treatment, it agrees fairly well. The GSB, integrated from $\omega_3 = 2400$–$2600\ \mathrm{cm}^{-1}$, shows a rapid decay of the initial bleach followed by a large rise of the HGS; these occur on timescales of 138 fs and 1.21 ps, respectively. However, given the overlapping features evident in the GSB of the 2D IR spectrum, these numbers, especially the fast component, must be interpreted with caution. While the HGS growth is almost two times slower in D_2O than it is in H_2O, it is interesting to note that the fast component decays on a timescale faster than the relaxation of the O—H stretch. This is discussed further below. Finally, the HGS, which is given by the induced absorption on the blue side of the spectrum ($\omega_3 = 2675$–$2700\ \mathrm{cm}^{-1}$), grows on a 1.0 ps timescale, which is roughly in agreement with the value extracted from the GSB. This value is significantly longer than the value of 630 fs reported in the literature [286]; however, it is consistent with our measurements of the relaxation of the solvent in solutions of dilute HOD in D_2O (see Chapter 5).

7.4.2 Changes in the Integrated 2D IR Spectrum

In order to obtain vibration-specific dynamics, it is necessary to integrate the separate features in the 2D IR spectrum. Figure 7.10A shows the magic angle 2D IR spectrum taken at $\tau_2 = 100$ fs, and Fig. 7.10B shows the time traces corresponding to the integrated boxes in the 2D IR spectrum. In Fig. 7.10A, the blue box corresponds to the (ν_1, ν_2) cross peak ($\omega_1 = 2400 - 2550\ \mathrm{cm}^{-1}$, $\omega_3 = 2550 - 2650\ \mathrm{cm}^{-1}$), the green box corresponds to the (δ, ν_1) cross peak ($\omega_1 = 2350 - 2500\ \mathrm{cm}^{-1}$, $\omega_3 = 2450 - 2550\ \mathrm{cm}^{-1}$), and the red box corresponds to the δ diagonal peak ($\omega_1 = 2350 - 2450\ \mathrm{cm}^{-1}$, $\omega_3 = 2370 - 2430\ \mathrm{cm}^{-1}$). In addition to the bleach features, the black box corresponds to the area of the ESA feature ($\omega_1 = 2250 - 2650\ \mathrm{cm}^{-1}$, $\omega_3 = 2000 - 2200\ \mathrm{cm}^{-1}$).

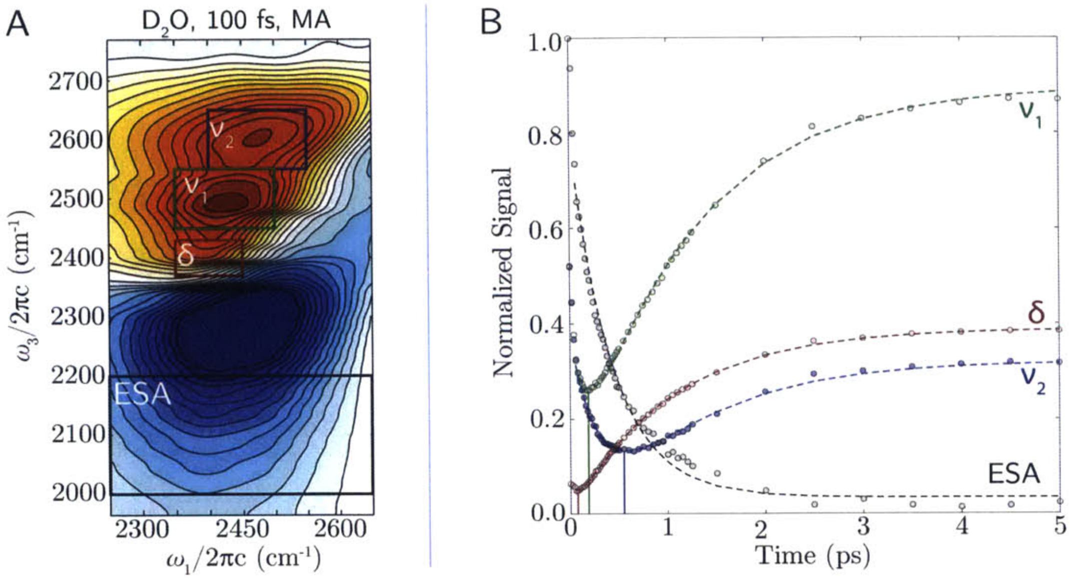

Figure 7.10: (A) Magic angle 2D IR spectrum of D_2O showing regions of integration to extract timescales. (B) Signal intensity as a function of time corresponding to integration boxes in A. ESA signal has been multiplied by -1.

The time traces corresponding to these features show a variety of different timescales reflective of the multitude of dynamics occurring in heavy water. The ESA shows an exponential decay with a timescale of 430 fs, which is more consistent with previous TA measurements [285,286], as well as the TA measurements of the previous section. It is worth noting that this timescale is ~1.5 times slower than the excited-state lifetime measured for water and that this is not far off from the factor of $\sqrt{2}$ that would be expected for a weakly anharmonic system.

Characterization of the diagonal peaks, on the other hand, is more complex due to strong overlap of the δ, ν_1, and ν_2 with the ESA as well as the ingrowth of the HGS signal with time. The peaks in the diagonal region show an inital rapid decay followed by a much longer growth of the HGS signal. For all three diagonal features, the growth of the HGS signal occurs on a timescale ranging from 1–1.2 ps, which is consistent with our TA measurements. Interestingly, the ratio of the lifetime of the O—D stretch to the timescale for growth of the HGS is rather similar to that of H_2O. However, this may be a simple coincidence given that the vibrations of D_2O are rather different than those of H_2O. The

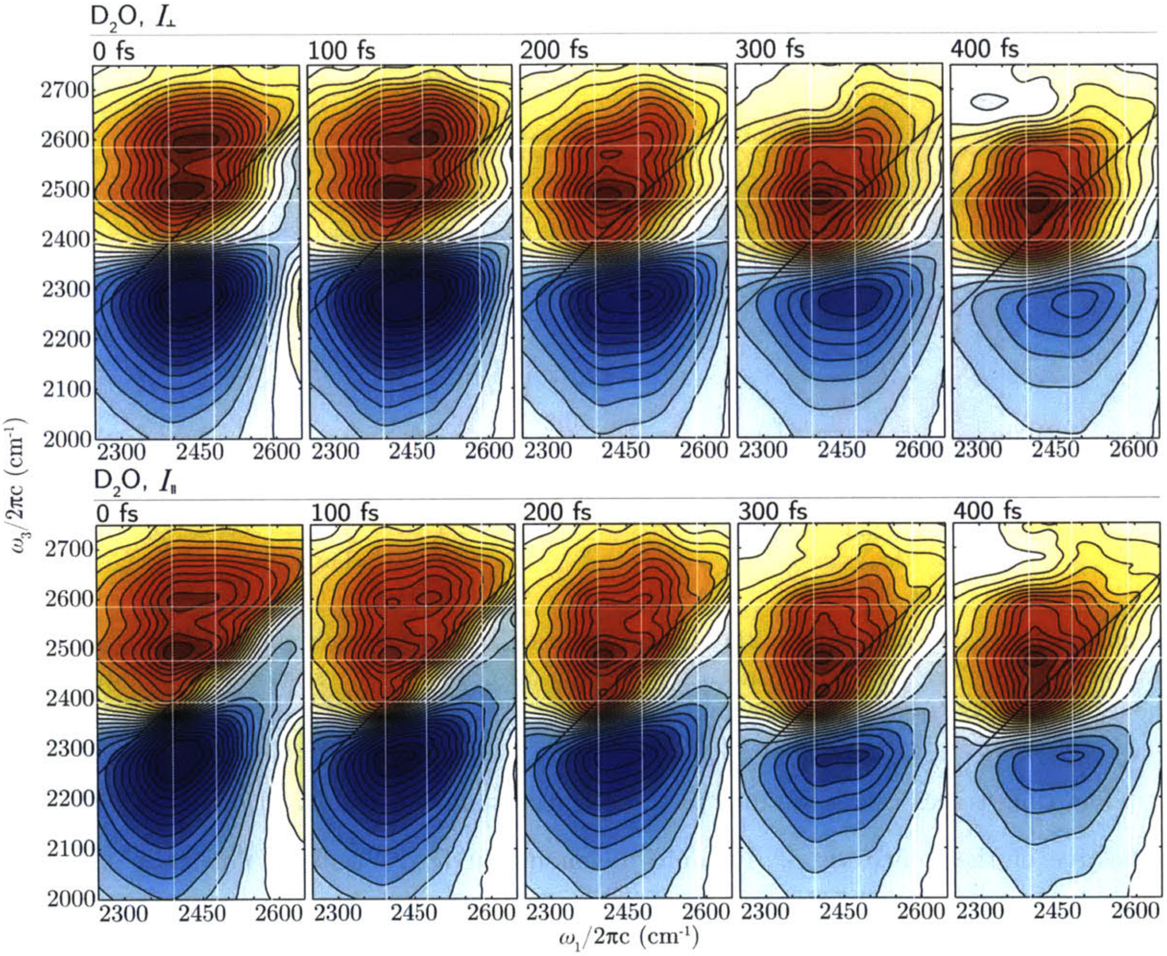

Figure 7.11: 2D IR spectra of D_2O for several different waiting times from 0 to 400 fs in the parallel and perpendicular polarization schemes.

fast time scales for the (ν_1, ν_2) cross peak, (δ, ν_1) cross peak, and δ diagonal peak are 300, 165, and 80 fs, respectively. The average of these decays, 180 fs, is only somewhat longer than the decay obtained from TA. The ordering of the decays can be clearly seen in seen in Fig. 7.10B, where each curve shows a minimum at a time related to the decay of the fast timescale. These minima are indicated by solid vertical lines in the figure.

That the reddest peak decays fastest is consistent with assignment of a Fermi resonance of the bending mode with the stretch, such that the $\delta = 2 \rightarrow 1$ relaxation pathway of the bend is efficient. That is, it appears that two quanta of bending motion can easily and rapidly produce two molecules each with one quantum of bending motion. Since the ν_1

mode is closer in energy to the bend overtone than the ν_2 mode, and since it nominally has the same symmetry as the bend overtone, it can transfer energy to the δ mode more efficiently. This gives rise to a decay of the ν_1 mode that is fast compared to the decay of the ν_2 mode.

In fact, the ordering of the timescales involved in the relaxation mechanism exhibited by D_2O can almost be seen directly from the 2D IR spectra. Figure 7.11 shows the $I_{\parallel}$ and $I_{\perp}$ 2D IR spectra for a series of waiting times. As a function of time, intensity is gained at the δ diagonal corresponding to the rapid growth of the HGS compared to decay of the diagonal feature in this region. The upper right part of the spectrum appears to evolve more slowly due to the long timescale associated with the ν_2 mode, and the relatively little intensity of the HGS in this region. Like H_2O, the HGS growth begins on the red side of the spectrum showing that the bend overtone and most strongly hydrogen-bonded O—D oscillators relax most quickly. Unlike H_2O, however, it appears that the disparity in growth of the HGS is not as dramatic. That is, the HGS in H_2O appears almost instantly and is fairly evident for $\tau_2 \geq 100$ fs, while for D_2O, signatures of the HGS are present only after $\tau_2 \sim 300$ fs.

These observations point to a cascaded energy-relaxation mechanism in which the antisymmetric mode transfers to the symmetric one, which in turn transfers to the Fermi resonance before relaxing to lower-frequency modes. This behavior is similar to that seen in other hydrogen-bonding systems, of which the NMA dimer is a good example (§4.5). However, this cascaded mechanism was not observed in our recent work on H_2O. Rather, light water showed a relaxation mechanism in which energy from the O—H stretching mode seemed to be directly transferred to low-frequency modes. In D_2O this does not seem to be the case since signatures of the HGS are only present significantly after several relaxation times of the δ and ν_1 modes. From this, we conclude that the cascading relaxation observed in D_2O is consistent with the expected dynamics of a weakly anharmonic system, and thus supports the interpretation that D_2O dynamics are more harmonic than H_2O.

7.5 The Difference between Light and Heavy Water

In our studies of H_2O (Chapter 6), signatures of symmetric and antisymmetric stretching modes were not observed in the 2D IR spectrum. Furthermore, although there appears to be a mode corresponding to δ, the bend overtone, in the linear spectrum, distinct resonances for the bend overtone and O—H stretch were not observed in the 2D IR spectrum (Fig. 7.2). This is consistent with our interpretation that the vibrations in H_2O are highly excitonic such that distinguishing vibrations based on symmetry is not possible; rather, all or most of the oscillator strength is in a single excitonic mode. In contrast, it appears that D_2O shows behavior that is somewhat more characteristic of a weakly anharmonic oscillator. As mentioned previously, that is not to say that the vibrations are completely local, but that they are not as extended as those of H_2O.

While the differences between the linear spectra of H_2O and D_2O are evident, the contrast between the nonlinear time-dependent spectra is even more striking. Other than the obvious differences in the structure of the GSB of the 2D IR spectra, it was observed that the ESA in H_2O was extremely broad compared to the fundamental GSB; however, in D_2O, the ESA has roughly the same width as the GSB as one would expect for a weakly anharmonic system. The extreme broadening of the ESA of H_2O reflects the extreme anharmonicity in the O—H stretch, which directly results in stronger mixing between various modes and thus a more excitonic character to its vibrations. This is consistent with the O—D bond being more harmonic than the O—H bond.

Furthermore, D_2O also shows a drastically different relaxation pathway compared to our previous study on H_2O. In H_2O, signatures of the HGS in the 2D IR spectrum as early as 100 fs suggested that the high and low-frequency modes were intrinsically mixed, and direct O—H to low-frequency-mode relaxation was observed, prompting a discussion of non-adiabatic relaxation dynamics. On the other hand, D_2O appears to show cascaded relaxation in which the antisymmetric mode, ν_2, funnels energy into the symmetric mode and penultimately the bend overtone before finally relaxing via a Fermi-resonance mechanism (such as was observed in the NMA dimer). This behavior is characteristic of weak coupling between normal modes, and is not observed in H_2O.

These differences can be understood in terms of the energies at which IR spectroscopy probes the nuclear potential energy surface (NPES) of the two isotopologues. Although the Hamiltonian differs only in nuclear mass, H_2O's IR vibrational transitions initiate and terminate at higher energy than D_2O's. At higher energies, the NPES appears significantly less harmonic than at its minimum. This is obvious, for example, for a simple Morse potential, but will most likely deviate even more dramatically from a parabolic potential for water's complex hydrogen-bonding network. Thus H_2O IR spectroscopy samples, on average, a significantly more anharmonic part of the NPES compared to D_2O. The greater anharmonicity, in general, implies stronger coupling between modes, weakened selection rules, and faster relaxation rates [267]. The enhancement of these anharmonic effects in H_2O over D_2O, manifests itself through more delocalized vibrations, an extremely broadened ESA, and faster vibrational energy relaxation. Similar effects that are attributed to the same physics, have been observed in the gas phase, where the linewidth of a hydrogen-bonded oscillator sharpens significantly upon deuteration. [302]. In addition, this is also the explanation for the suppressed quantum beating observed in ice $\mathrm{I_h}$, wherein the isotopically dilute O—D oscillator reaches a less anharmonic part of the NPES than the isotopically dilute O—H oscillator [267].

7.5.1 A Toy Model

We conclude this section by considering how such behavior can arise in a simplistic model. To that end, we analyze the Lippincott–Schroeder (LS) model, which was originally developed to describe the hydrogen-bonding interaction in hydrogen-bonding crystals [20, 21]. The model explicitly treats two coordinates: the length of the covalent bond, r, and the oxygen–oxygen distance (or equivalently, the length of the hydrogen bond), R. The interaction potential contains three interactions terms that are given by

$$V_{Ia}(r) = D_{Ia}\left(1 - \mathrm{e}^{-n_{Ia}\frac{(r-r_{\mathrm{OH}})^2}{2r}}\right), \tag{7.2a}$$

$$V_{Ib}(R,r) = D_{Ib}\left(1 - \mathrm{e}^{-n_{Ib}\frac{(R-r-r_{\mathrm{OH}})^2}{2(R-r)}}\right), \tag{7.2b}$$

$$V_{II}(R) = D_{II}\left(1 - \mathrm{e}^{-n_{II}(R-R_{\mathrm{OO}})}\right)^2. \tag{7.2c}$$

The first term, $V_{Ia}(r)$, describes the covalent bonding of the proton to the oxygen atom. This is characterized by a binding energy, D_{Ia}, an equilibrium bond length, r_{OH}, and a characteristic lengthscale, n_{Ia}. The second term, $V_{Ib}(R,r)$, accounts for the interaction with the hydrogen-bond acceptor, and it accounts for the possibility of proton transfer; that is, it provides a metastable state at some value of $r \neq r_{\mathrm{OH}}$, which depends on the hydrogen-bond length. It too is characterized by a binding energy and characteristic lengthscale as well as a equilibrium oxygen–oxygen distance, R_{OO}. The final term, $V_{II}(R)$, is a Morse potential in the coordinate of the oxygen–oxygen distance, describing the potential of the hydrogen-bond itself.

The LS model successfully captures some of the salient features of a hydrogen-bonding interaction. In particular, it reproduces the strong frequency dependence of the O—H stretch on the hydrogen-bond length. Of course, the model is not realistic for liquid water in that it reduces the high-dimensional NPES of the actual liquid to that of a dimer, in addition to neglecting other vibrational modes that necessarily play an important role in the liquid. Nonetheless, this model has been used to explain certain features in TA spectroscopy of isotopically dilute water [217, 245]. Furthermore, it successfully explains the spectroscopy of isotopically diluted ice $\mathrm{I_h}$ if the non-adiabatic couplings between the two degrees of freedom are included [191,267].

Here, we do not use the LS model to explain any particular feature observed in the 2D IR spectrum, since it is obvious that the simplicity of the model cannot capture the complex features of the liquid. Rather, we use it to show how a simple change of mass can dramatically change the nature of vibrations on a sufficiently anharmonic potential.

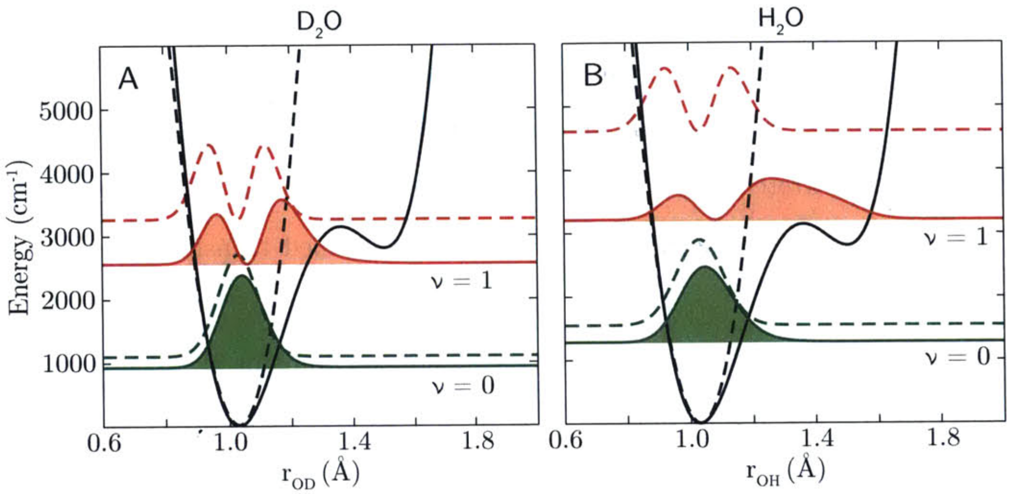

Figure 7.12: (A) Probability densities of the O—D bond in a harmonic potential (dashed lines) and the LS potential (solid lines). (B) Same as A except for an O—H bond.

To that end, we consider the LS potential with the oxygen–oxygen distance fixed at 2.6 Å, which corresponds to a particularly strong (almost unphysically so) hydrogen bond [15,303]. However, this length is chosen so as to more clearly show the effects we seek to observe. To that end, we modify the parameters reported in Refs. [217,245,267] slightly so that the hydrogen-bonding interaction is some 10% stronger than the previously used values. The values we use are $D_{Ia} = 38750$ cm^{-1}, $D_{Ib} = 27500$ cm^{-1}, $n_{Ia} = 10$ Å^{-1}, $n_{Ib} = 16.5$ Å^{-1}, $r_{\mathrm{OH}} = 0.97$ Å, and $R = 2.6$ Å. Since we are only considering the displacement of the O—H bond, $V_{II}(R)$ and the parameters therein do not come into the analysis. We solve for the eigenstates and eigenvalues by expressing the Hamiltonian, $H = p^2/2m + V_{Ia}(r) + V_{Ib}(R, r)$, in the harmonic oscillator basis with $m = m_{\mathrm{p}}$, the mass of the proton, and $\omega = 2\pi c \cdot$ 3400 cm^{-1}. Diagonalization of the resulting Hamiltonian using harmonic-oscillator basis functions up to $\nu = 70$ gave converged eigenvalues and wavefunctions.

The results of the calculation are shown in Fig. 7.12A and B, where the results for the O—D stretch and O—H stretch are shown, respectively. In both cases, the solid line shows the LS potential, while the dashed line shows a harmonic approximation to the minimum. The LS potential, in addition to a global minimum, shows a local minimum at $r \approx 1.5$ Å corresponding to the proton or deuteron being associated with the hydrogen-bond acceptor.

The calculated harmonic probabilities (wavefunction squared) are shown in colored dashed lines and the probabilities for the LS model as shown as solid filled curves. The harmonic approximations give rise to transition energies that are consistent with the frequencies of the O—D and O—H stretches. However, by virtue of changing the parameters of the LS potential to unphysically strong hydrogen bonds, the obtained transition frequencies for this potential are too low.

In both cases, the ground state probabilities are not too different between the harmonic potential and the LS potential, though the latter are skewed to slightly longer bond distances. Similarly, the first excited state of the O—D stretch does not deviate too strongly from the harmonic case, however, there is certainly a propensity for longer O—D bonds. In addition, the state is broader overall, and tunneling to large extensions is more likely than the harmonic oscillator case. On the other hand, it is clear that the probability distribution for the O—H bond length is largest at long extensions, showing a complete deviation from the harmonic-oscillator behavior as well as from the O—D bond. This complete deviation is achieved simply by changing the mass of the oscillator from $2m_p$ to m_p. Clearly, then, the O—H bond will show very different spectroscopy from the weakly anharmonic O—D bond. Even if the standard LS parameters are used, the same behavior is seen though the difference is not as evident. Clearly, the use of a more realistic potential, which is presumably more anharmonic since it necessarily includes a larger number of modes, will amplify this effect.

Finally, we note that this analysis has been done in a quantum mechanical framework and the question naturally arises as to whether this is necessary. While it has become fashionable to attribute such observations to quantum mechanical phenomena, it is important to note that a purely classical system of anharmonic oscillators would show the same behavior. In addition to a lower resonance frequency, thermal fluctuations classically excite the classical O—D bond to lower amplitudes and it would remain on average in a lower energy, and therefore more harmonic, part of the NPES than would the O—H bond.

Chapter 8

Water at the Protein Interface

8.1 Looking at Water–Protein Interactions

Without a doubt, water is one of the most important molecules in biology. Almost every biological process takes place in an aqueous environment, and what is more, liquid water is necessary to carry out most biological functions [41]. The presence of water molecules in and around biological macromolecules is, in part, responsible for a variety of phenomena such as protein folding [11,304,305], micelle and membrane formation (through the hydrophobic effect) [306–309], enzyme function [310–312], and the gating of ion channels [313–315] (to name a few). Yet despite recognizing water's importance in biology for many decades, and studying it thoroughly for just as long, there exists no general picture of water's microscopic dynamics at the molecular level in biological systems [316,317].

Partly, the reason for this lack of understanding stems from the complexity of the constituent components: proteins are highly complicated and bulk water, as well as small-molecule solvation, are not yet understood. On the other hand, "biological water" is a formidable beast in and of its own right [318]. There are an enormous number of effects and factors at work in the consideration of the dynamics of water in a cell, for example; this alone makes a strong case for making an attempt to try and take the problem apart piece by piece. Interestingly, as pointed out in Ref. [317], the increasing sophistication of experimental methods has resulted in the field of research breaking into method-oriented specialties that tend to isolate themselves. Certainly, this is damaging to the field as a whole. However, I thoroughly believe that it is only through the coming together of seemingly disparate methodologies, tackling the problem from many different angles, that any progress be made in this impressively difficult system.

One of the main difficulties with the study of the molecular dynamics of liquid water around biomolecules is that it *absolutely necessitates* exceptional time resolution *and* structural resolution. Having just one or the other is not sufficient to truly develop a molecular picture of biomolecular solvation. Current experiments largely posses either exceptional structural resolution or exceptional time resolution, but not yet both. For example, nuclear magnetic resonance and X-ray diffraction are both exquisitely sensitive to structure in their ability to capture atomistic distances and detail. However neither of these techniques possess the time resolution necessary to capture the rapid fluctuations of water molecules on the femtosecond to picosecond timescale (it should be mentioned that enormous strides are being made in time-resolved X-ray crystallography, but even then, the technique is more or less insensitive to the position of protons). On the other hand, there exists a number of ultrafast electronic spectroscopies that boast phenomenal time resolution, but lack the structural sensitivity necessary to understand the molecular details. 2D IR spectroscopy is a middle ground, offering sufficient temporal and structural resolution.

The other difficulty associated with observing and studying water dynamics at a biological interface is the overwhelming response from bulk water that typically swamps any experimental signal. One possibility is to employ a technique that is only sensitive to molecules hydrating the biomolecule. This is what is done, for example, in certain NMR experiments where a pulse sequence to isolate the solvating water molecules is used. We attempted to do the same by looking at *inter*molecular cross peaks in 2D IR, which should in principle only arise from the interaction of water molecules with the biomolecule. Indeed, this was the primary motivator for studying NMA dimers (Chapter 4). However, we have found (for example, in mixtures of water and amides, esters, or ketones) that this method only works if the vibrational coupling between the water and the solute is stronger than the water–water interactions. If this is not the case, then signal is overwhelmingly swamped by the bulk water.

In the end, we took an alternative approach in which we eliminated the bulk altogether. By casting a protein into a thin film, it was possible to take both linear and nonlinear IR spectra of dry proteins. This film could be hydrated to various levels, such as to control the water content in the film. This in principle provides us with an incredibly versatile system in which the level of hydration of the film could be controlled, in addition to other external variables (e.g. temperature). Furthermore, a great deal of literature on the study of protein films exists and provides us with a foothold to carry out these experiments.

In practice, however, there are a number of challenges associated with performing nonlinear IR spectroscopy on protein films. Most notably, it is difficult to produced films of high enough optical quality so that scatter is not a major issue. Even with polarization discrimination, it is not possible to perform TA measurements on the films, let alone polarization anisotropy measurements. However, the added robustness of 2D IR against scatter (see §3.5.4) allows us to obtain relatively clean 2D IR spectra in the ZZYY polarization scheme. In addition, there is a certain amount of irreproducibility in the making of the films. That is, the films that are produced depend on a number of variables that are currently out of our control, such as the drying rate and how reproducibly the protein solution is deposited on the substrate. Another less serious challenge is that our current apparatus does not allow us to control or measure relative humidity with much accuracy. This is merely a technical challenge and can be overcome with some engineering.

Despite these challenges, the study of protein films has the potential to be incredibly informative. It is clear that even at the level of linear spectroscopy (which does not require films of pristine optical quality), there is plenty of low-hanging spectroscopic fruit.[1] Careful and accurate absorption spectra of protein films as a function of hydration, which requires a well-constructed humidity-controlled cell, can certainly provide us with the ability to learn about the average structure of water in and around proteins. This is in no small part due to the ability to measure highly accurate difference spectra. Furthermore, the ability to measure water dynamics with nonlinear IR spectroscopy provides an unprecedented opportunity to observe water–protein interactions in isolation. I believe that these studies will be indispensable in moving the field of protein hydration forward.

---

[1] I believe credit goes to Prof. Field for coining this phrase.

Of course, protein films are not exactly what one commonly finds is relevant in the context of biology. Furthermore, we expect that the water's dynamics and equivalently, its interactions with the protein, are going to be dramatically different in the presence of bulk water. These are valid criticisms, and, as such, we must be careful to not be too eager to apply the interpretation of our results directly to true biological systems. On the other hand, there exists biological contexts in which proteins are highly crowded (or the protein density is high) and the level of hydration is low. This is the case, for example, in hydrophobic pockets possessed by certain proteins. Furthermore, there are examples showing that certain enzymes still posses catalytic function in film form provided a certain amount of hydrating water is present. Clearly, our studies can report on these types of proteins directly. Whatever the case may be, the study of protein films is important in and of its own right and we take full advantage of this opportunity to study water–protein interactions directly.

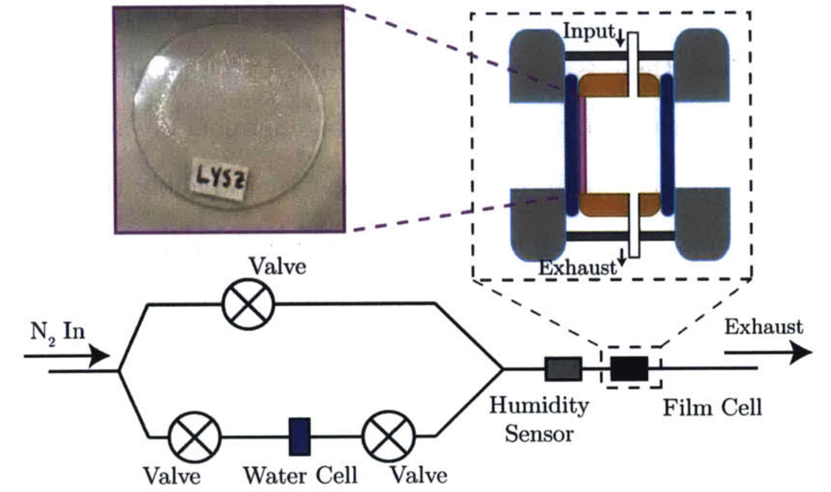

Figure 8.1: Schematic of humidity controlled sample cell used in protein film experiments. Image shows a typical film of hen egg-white lysozyme.

The experiments discussed in this chapter are but a scratch on the surface of what promises to be a lucrative research project. The experiments I have performed are certainly the most preliminary ones that can be done, and yet, it seems as though every single one has been fruitful and yielded an interesting tidbit of information. While experiments were done on a number of different proteins, in this chapter we focus on those that report in some way on the dynamics of water at the biological interface. The experiments presented here show clear evidence for two types of water dynamics at the protein interface in which protein–water or water–water interactions dominate.

8.1.1 Sample Preparation

Proper sample preparation is crucial to be able to collect 2D IR spectra of protein films. Unlike liquid samples, which are usually held between CaF_2 windows, the optical quality of a protein film basically determines whether or not a nonlinear spectrum can be collected. However, even for films of high optical quality, scatter is problematic and care must be taken when setting up a measurement. While one would expect that polarization discrimination ought to do a lot to mitigate the issue, certain films seem to be birefringent and rotate the polarization of the excitation pulses somewhat. This precludes the possibility of collecting transient absorption data, since scatter is a more significant problem for this experiment (see §3.5.4).

Protein films were prepared by allowing protein solutions to dry slowly on CaF_2 windows. Lysozyme from Chicken Egg White (*Sigma-Aldrich*) and Poly-L-Proline (*Sigma-Aldrich*, 32,000 MW) were purchased and used without further purification. The GVG(VPGVG)$_{251}$ elastomer was synthesized by Dan Urry (*Bioelastics Research Ltd.*) and also used without further purification. A number of different drying conditions were tested in which the concentration of the solution and drying rate were varied. The effect of adding salt was not investigated, and no salt was added to the protein solutions other than that which may be present from the synthesis and purification process. It was found that spotting ~200 μL of a 5 mg/mL solution on a CaF_2 window and allowing it to dry in a semi-dry atmosphere (~10% relative humidity) over the course of 6–8 hours produced films of the highest optical quality. A typical film of hen egg-white lysozyme is shown in Fig. 8.1. The films were stored under a dry atmosphere once fully dry.

At this point, controlling the optical quality of the film is more of an art than a science, and sometimes a few iterations are necessary to produce a workable film. Furthermore, the optical quality of the film seems, in part, to be determined by the nature of the protein, with certain proteins invariably resulting in films that were foggy or highly crazed.

During data collection, films were held in a variable humidity cell, whose construction is shown schematically in Fig. 8.1. The humidity cell consists of a brass ring onto which CaF_2 windows are sandwiched by a standard aluminum IR sample cell. The windows are held in place only with the pressure exerted by the sample cell, and a seal between the windows and the brass ring is made using Viton O-rings. The inner and outer diameters of the brass ring are 0.63 and 1.00 in, respectively, and its height is 0.465 in. The ring has two holes drilled into the side of diameter 0.165 in, separated by ~120° along the circumference, for input and exhaust air tubes.

Dry N_2 is split into a "dry" and a "wet" line, which are separately equipped with valves and pressure regulators. The nitrogen in the wet line is bubbled through either H_2O or D_2O, resulting in a mixture of nitrogen and water at 100% relative humidity (RH). The mixture is combined with the nitrogen in the dry line. The total RH is set by adjusting the relative flow rates on the wet line and the dry line. The overall flow was not measured, but it was usually adjusted to be as large as possible without over-pressurizing the setup. The RH is measured in a separate cell equipped with a humidity/temperature meter (*VWR International*). The humidity/temperature meter operates within a range of 10–95% RH and purports an accuracy of ±3% RH. Realistically, the meter seems to operate well within a narrower range and it cannot read an RH of greater than 80%. Therefore, the data in this chapter labeled with 80% RH likely corresponds to something much higher (i.e. close to 100%). Even at the highest levels of RH, no condensation was observed on the CaF_2 windows, the brass walls, or the protein film itself. The film is held in the main chamber, in which the film's substrate forms one of the chamber walls. Finally, the air is exhausted to atmosphere.

Substantial improvements can be made to the humidity cell in order to enable precise measurements and, in particular, data collected as a function of humidity. First and foremost, the humidity sensor ought to be replaced by a high accuracy one, and the humidity should be monitored continuously and logged. In addition, lines with both pressure and flow regulators are necessary to accurately set the humidity. This is important to be able to collect data reproducably. Finally, N_2 is bubbled through water held in a corked Erlenmeyer flask, which is prone to blowing the stopper off if the pressure is too high. It is therefore worth introducing a blowoff valve into the line to prevent this, or constructing a water cell capable of withstanding moderate pressures.

8.2 Linear IR Spectra of Protein Films

Vibrational spectroscopy has a long history in protein science, with a great deal of molecular information being contained in the mid-IR spectrum [188, 319, 320]. However, the vast majority of studies have been carried out in the aqueous phase with only a small percentage being carried out in dried or hydrated films [321–326].

To test the reproducibility of the protein film making process, several films were repeatedly made of different representative proteins. Other than changes in overall optical density, and possibly a sloping background due to scattering of the film, the spectra of proteins were highly reproducible[2] and showed similar amide I and amide A spectra even over different drying conditions. Furthermore, the protein films were highly stable, and storing a film for up to a year in a dry atmosphere showed no appreciable changes in its IR spectrum. Because the films are so stable, all of the linear and 2D IR data in this chapter was collected only on the best film made for each protein.

Figure 8.2 shows the IR spectrum of a hen egg-white lysozyme (HEWL) film under various conditions. We note that the IR absorption spectrum, in particular in the amide I region, is not too different from that obtained in the aqueous phase. While the spectra of particular films are described in the context of each protein in subsequent sections, we give an overview of the IR spectrum here, and use HEWL simply as a representative example.

---

[2] This is true for all the proteins we looked at except for poly-L-lysine. Poly-L-lysine showed large changes in protein structure, depending very sensitively on the drying conditions. Furthermore, it became evident that the structure sometimes changes irreversibly depending on the level of hydration of the film. These properties of poly-L-lysine are poorly understood, and it promises to be a fascinating avenue of research in the future.

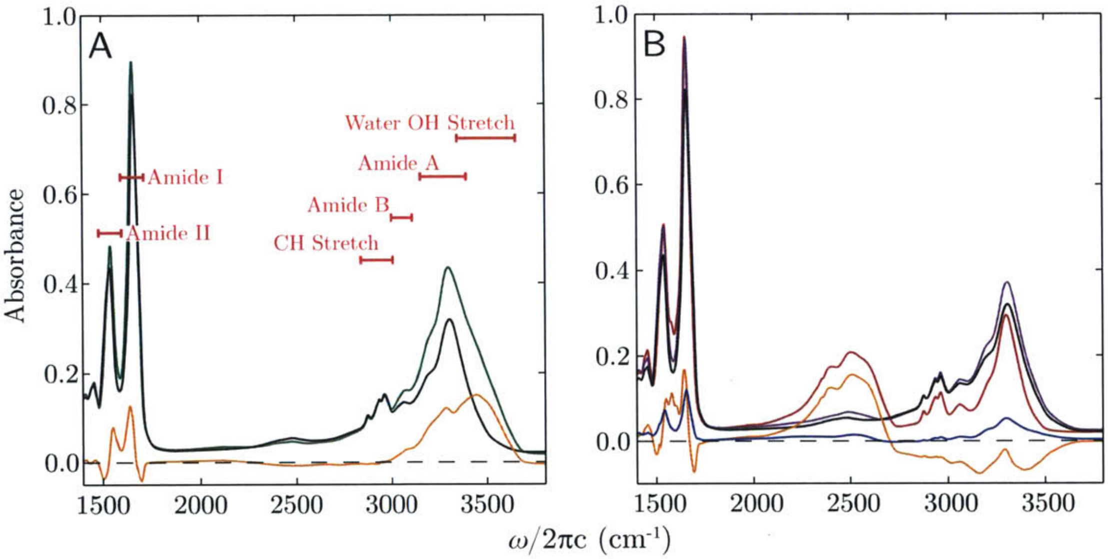

Figure 8.2: (A) IR spectra of HEWL at 0% RH (black curve), 80% RH (green curve), and their difference (orange curve). (B) IR spectra of HEWL at 0% RH (black curve), 80% RH hydrated with D_2O (red curve), 0% RH after hydration with D_2O (purple curve). The orange and blue curves correspond to the difference between the 80% RH and 0% RH, and the partially exchanged 0% RH and the 0% RH, respectively.

We begin with the consideration of the dry film (Fig. 8.2A, black curve), which shows several prominent features. In the amide A region (3100–3500 cm^{-1}), a structured peak is observed corresponding to the N—H stretching mode of the protein. In this case, the structure comes from coupled N—H stretching modes that delocalize over different secondary structure motifs, as well as various overtones and combination bands in this region [171]. The amide A mode appears along with the amide B mode in the 3000–3100 cm^{-1} region, which we have previously assigned to the overtone of the amide II mode (§4.3.2). At somewhat lower frequencies, are various C—H stretching modes of the amino acid side chains.

In the studies that follow in this chapter, we focus on the amide A mode; however, it is good practice to keep track of the lower frequency vibrations since the majority of IR experiments have been carried out on these. The amide I mode, which consists primarily of C=O stretching motion, lies in the 1600–1700 cm^{-1} region. This mode is delocalized over the protein backbone and is highly sensitive to the protein's secondary structure [327]. Furthermore, the fact that the amide I band of the protein films resembles the solution phase amide I band is a good indicator that the protein structure has not been compromised in the drying process. In particular, no sharp peak corresponding to protein aggregation is observed [195]. Indeed, circular dichroism studies have confirmed that there are no significant changes in the structure of globular proteins, nor orienting of proteins, when deposited as a film [321, 325, 328]. At slightly lower freqeuncies is the amide II mode (1500–1600 cm^{-1}), which corresponds to an in plane N—H wagging motion with some amount of C—N stretch involved, though this mode significantly changes its character upon deuteration.

Upon hydration to 80% RH (Fig. 8.2A, green curve) the amide A peak appears to broaden and increase in intensity. This is due to the absorption of water's O—H groups that hydrogen bond to the protein from the humid atmosphere. However, the changes in the IR spectrum upon hydration are not limited to the O—H stretching region, but rather are present across the entire mid-IR. No changes in the IR spectrum we observed after ~10 s upon exposing the film to humid air. Even after 18 hours of sitting in 80% RH air, the protein film showed the same spectrum as after a few seconds. We therefore assume that the film is as hydrated as it can be by being exposed to humid air. (Similar observations were made upon hydrating the film with D_2O where, in addition to hydration, H/D exchange occurs.) Similar timescales were observed for drying the film as well. In typical experiments, the film was left to sit at a new humidity for several minutes before data was collected. It is worth noting that hydrating the films changes their optical quality somewhat, and hydrated films tend to scatter somewhat less the dry films. We therefore must use caution when analyzing subtle features in the baseline of the spectra.

The changes between the wet and dry film are more evident in the difference spectrum (Fig. 8.2A, orange curve). The difference spectrum shows a broad peak at ~3450 cm^{-1}

corresponding to the O—H stretching of the hydrogen-bonding water as well as shoulders on the red side of this feature that can be attributed to changes in the amide A band upon hydration. This principally consists of redshifting of the N—H stretching mode. At lower frequencies, the amide I and II modes show an "M" pattern in the difference spectrum. This is characteristic of modes that shift in opposite directions upon hydrogen bonding. In particular, the amide I mode shifts red and the amide II mode shifts blue upon hydrogen bonding, consistent with previous observations (see §4.1.2 for a more detailed discussion). This is a clear indication that the water is directly interacting through hydrogen bonds with the backbone of the protein structure and simply adsorbing to the surface of the film or CaF_2 window. We note that the HOH bending mode is not evident in the difference spectrum due to strong overlap with the amide I band and much smaller oscillator strength than the O—H stretch.

In addition to hydrating the sample with H_2O, we may hydrate the protein film with D_2O. The spectrum of HEWL, hydrated to 80% RH with D_2O, is shown in Fig. 8.2B (red curve). Here, we do not see an increase in the O—H stretching region of the spectrum, but rather in the O—D stretching region between 2100 and 2700 cm^{-1}. This is particularly evident in the difference spectrum (Fig. 8.2B, orange curve) which shows an increase in the O—D stretching region, and decrease in the amide A region, and a similar, but distorted, pattern in the amide I and II region. The distortion in this region arises due to H–D exchange of the protein's labile and atmosphere-exposed protons, which alters the lineshape of the amide I and, in particular, the amide II modes.

Drying the sample after it has been hydrated with D_2O does not return the film to its original state. Rather, the protons that have exchanged for deuterons remain exchanged Fig. 8.2B (purple curve). This is most clearly seen in the difference spectrum between the partially-exchanged, dry film and the unexchanged, dry film (Fig. 8.2B, blue curve), in that there is some increased intensity in the $\sim$2500 cm^{-1} region. Curiously, it appears as though other features increase somewhat in intensity after hydration with D_2O. While the cause of this is unknown, it is possible that bringing the labile protons out of resonance with the structured N—H bonds results in an increase in oscillator strength of the remaining N—H groups since there is less coupling to disordered vibrations. By hydrating with D_2O then, we may effectively decouple the protein exterior, which readily exchanges, from the robust core, which does not.

8.3 Water Dynamics on Poly-L-Proline

Poly-L-Proline (PLP) films provide us with a unique opportunity to study water at the protein interface. Being mostly free of N—H groups, the spectral region from 3000–3800 cm^{-1} is almost entirely free of any absorption. As such, it is possible to study the O—H stretching band of adsorbed H_2O without interference from the peptide vibrations.

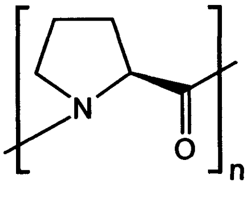

Figure 8.3: The sequence of PLP.

The sequence of PLP, shown in Fig. 8.3, consists of a chain of L-proline amino acids linked via peptide bonds. L-proline posses a pyrrolidine side chain that forms a closed ring with the α–amino group. This makes L-proline unique in that it is the only naturally occurring amino acid with a secondary amine group. Due to the formation of the ring, the proline unit has fewer degrees of freedom than other peptide units and, as a result, PLP forms a rigid polyproline II helix in solution, characterized by relatively restricted (ϕ, ψ) angles of $(-75°, 145°)$ [329–331]. Having no amide hydrogen atoms (and thus no internal hydrogen bonds), the (ϕ, ψ) angles are fixed by the rigidity imposed by the ring. In a polyproline II helix, both the carbonyl groups and the nitrogen are oriented outwards, and both are good hydrogen-bond acceptors. This structure therefore provides ample opportunity for water–protein hydrogen bonds to form.

As mentioned previously, circular dichroism studies have shown that there is no discernible change in structure nor orienting of proteins when deposited in a film [321,325,328], though these studies did not look at PLP specifically. Given the relatively rigid structure of the polyproline II helix in solution (recent studies have shown a persistence length of

~4.5 nm, which corresponds to about 15 repeats [332]), it is probable that the structure is retained when deposited randomly as a film. It is worth noting, however, that a molecular weight of 32,000 corresponds to about 280 proline repeats and so there will be significant deviations from rod structure on that scale. On a local level, the rigidity ensures that there is plenty of interstitial space for water molecules to penetrate into the film and form hydrogen bonds, provided there is no significant ordering of PLP chains on the substrate. This is a somewhat more difficult issue to address; though no ordering was observed for globular proteins it is possible that ordering will occur for the rigid PLP segments. Indeed, enhanced ordering of PLP on polystyrene/phosphate buffer interface relative to L-proline has been observed, though the degree of ordering was found to depend intimately on the chemical nature of the peptide and substrate [333].

The question then that needs to be addressed is whether the dynamics of water molecules at the protein interface are the same in the presence of N—H groups as in the absence of them. Certainly, we expect strong resonance coupling through the hydrogen-bonding interaction, which means that the dynamics of the O—H stretching mode are not going to be the same. Since the O—H stretch is coupled to other high and low-frequency modes, it is likely that these will be affected as well. Presumably, however, the interaction between the water molecule and the protein will dominate the intramolecular coupling within the water molecule, and to a first approximation the dynamics of water molecules around PLP reflect those around other proteins.

8.3.1 Water Structure at the Protein Interface

We begin by considering the linear spectroscopy of water on PLP in the O—H stretching region. Figure 8.4 shows the linear absorption spectrum of the dry film (black curve), the 20% relative humidity (RH) film (red curve), the 80% RH film (green curve), and bulk water (blue background). In this figure, the amplitudes of the PLP-film spectra are not normalized, but the bulk-water O—H stretch is. The dry film shows no prominent features in this region except for the C—H stretching feature at 2967 cm^{-1} and a weak bump at

3284 cm^{-1}. The former is assigned to anti-symmetric stretching of the CH_2 groups on the pyrrolidine side chain [334], while the latter was unassigned in previous studies. Given that the freqeuncy of the intense amide I mode is 1644 cm^{-1} (see Fig. 8.5), it stands to reason that this is the overtone of the C=O stretching mode. In fact, close inspection shows some intensity in a broad feature in the 3400–3600 cm^{-1} region. This likely arises due to either the capping NH groups of the polymer chains, or the most strongly bound water molecules which simply cannot be dried out. The dashed black line in Fig. 8.4 shows the spectrum of the dry film blown up by a factor of 80. While the C=O overtone is most prominent, there is considerable structure in the 3300–3600 cm^{-1} region corresponding to the capping N—H stretches and O—H stretches of tightly bound waters.

As the hydration level of the film is increased, the O—H stretching band of the hydrating water is observed. With increasing hydration, the peak of the band redshifts from 3468 cm^{-1} at 20% RH to 3422 cm^{-1} at 80% RH. In addition, the tail to red frequencies becomes more prominent in going from 20% to 80% RH, with the latter extending beyond the C—H stretching mode. Neither of the spectra reach the peak frequency or breadth of the bulk water band. In addition to shifting, the 80% peak is more structured than the 20% RH peak, showing what appears to be two distinct peaks (at ~3425 cm^{-1} and ~3499 cm^{-1}) whereas only one is observed in the 20% spectrum (at 3474 cm^{-1}). The thin grey lines in the background of Fig. 8.4 guide the eye to these features. It is likely that the higher frequency peak corresponds to protein-associated waters while the lower frequency one corresponds to water molecules interacting with other

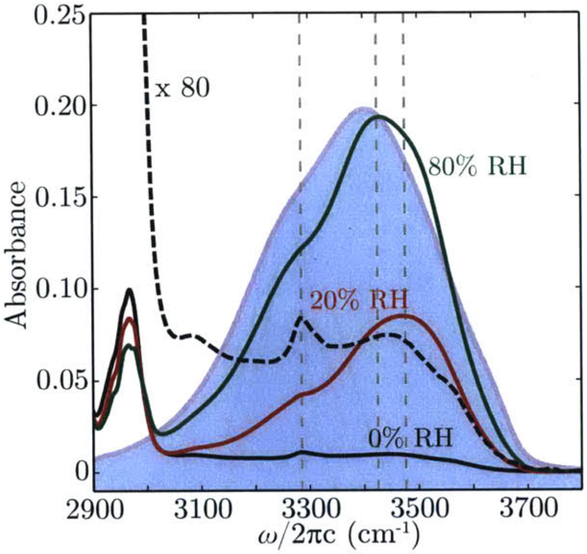

Figure 8.4: Linear absorption spectrum of the O—H stretch region of a hydrated PLP film at 0% RH (black), 20% RH (red), 80% RH (green). Bulk O—H stretch spectrum shown in blue.

water molecules since water–water interactions are stronger than the average water–protein interaction. While it is possible that the substructure has some contribution from symmetric and antisymmetric stretching, for example, it is not easy to justify why the spectrum would shift the way it does with increasing hydration.

The peak assigned to the C═O stretch overtone sits atop the red tail of the O—H stretching mode. As hydration is increased from 20% to 80% RH, the feature appears to become more intense, though it is difficult to determine whether this is simply an artifact of sitting atop of the tail of the O—H stretching mode. If the C═O overtone really is increasing in intensity, it is likely due to resonant mixing between the overtone of the amide I mode and the fundamental of the O—H stretching band. This would be an example of an intermolecular Fermi resonance, with the vibrational coupling provided by the hydrogen-bonding interaction.

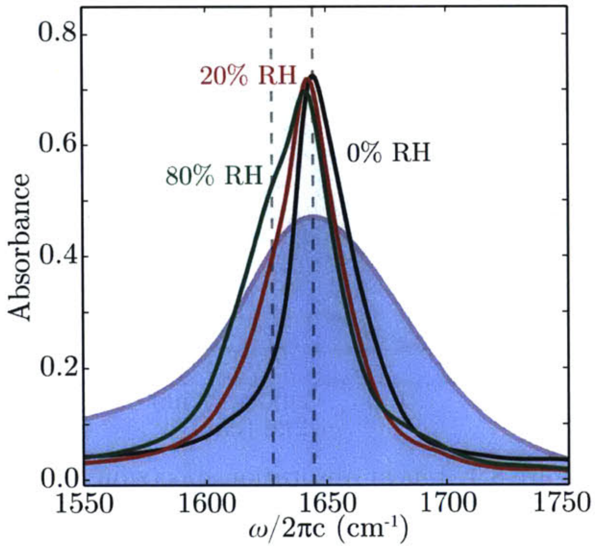

Figure 8.5: Linear absorption spectrum of the amide I region of a hydrated PLP film at 0% RH (black), 20% RH (red), 80% RH (green). Bulk HOH bend shown in blue.

The linear absorption spectrum of the amide I region is shown in Fig. 8.5. This region shows trends consistent with what is observed in the O—H stretching region. The dry film shows a single sharp peak centered at 1645 cm^{-1} and 27 cm^{-1} linewidth, which shifts to 1641 cm^{-1} with increasing hydration. In addition, a shoulder grows in on the red side of the peak centered at ~1628 cm^{-1}. This is consistent with the ~16 cm^{-1} shift of amide I associated with forming a hydrogen bond to a water molecule [142]. The 4 cm^{-1} shift of the non-hydrogen-bonded peak arises due to a combination of a change in vibrational coupling to other C═O oscillators as well as due to a change in dielectric constant surrounding the carbonyls.

Ideally, a measure of the water to PLP ratio would accompany the interpretation of the experimental results. However, an accurate measurement with IR spectroscopy requires a knowledge of many of the film properties which are difficult to know, even in principle (such as the film density, for example). Rather, we settle for a rough estimate. The extinction coefficient of the amide I mode is $\sim$6 $M^{-1}cm^{-1}$ [335], while that for *bulk* water is $\sim$100 $M^{-1}cm^{-1}$ [260]. Given that the absorption of the amide I mode in the 20% RH spectrum is 0.72, while for the O—H stretch it is 0.090, we obtain a concentration ratio of about 130 C═O oscillators to O—H oscillators. While a number of unjustified assumptions have been made here (namely assuming that the extinction coefficient for bulk water is the same as that for water in the film and assuming that the water uniformly disperses through the film) this gives an idea that the number of water molecules per C═O oscillator is rather low. Indeed, the persistence of the high-frequency C═O peak at 80% RH suggests that there are many non-hydrogen-bonded carbonyl oscillators. This is probably a good indication that the water vapor does not penetrate the film entirely. Given the discussion of the previous section, this may be a result of ordering of the PLP polymers on the substrate.

The 2D IR spectrum of PLP taken at τ_2 = 100 fs in the ZZYY configuration for the 20% and 80% RH films are shown in Fig. 8.6. The sharp ridge along the diagonal of the spectrum is due to scattering of the pump pulses by the film. Ideally the analyzing polarizer should filter any scattered pump light, but the films scramble the polarization of the laser pulses somewhat. The scatter present in these spectra has consequences for the center-line slope (CLS) measurement in that the values of the CLS are modified by the presence of scatter; however, since the scatter has a constant slope as a function of τ_2 (that is, it is due to scatter between $\boldsymbol{k}_1$ and $\boldsymbol{k}_2$), it should not affect the CLS decay timescale dramatically.

Qualitatively, the spectra show similar features to bulk water, except the hydrated PLP films show considerably more structure. Particularly evident in the 80% RH film, though discernible in the 20% RH film as well, is the fact that the ground-state bleach (GSB) is actually composed of two features. These features correspond the the two prominent peaks in the linear spectrum of the 80% RH film (Fig. 8.4) that were assigned to protein-

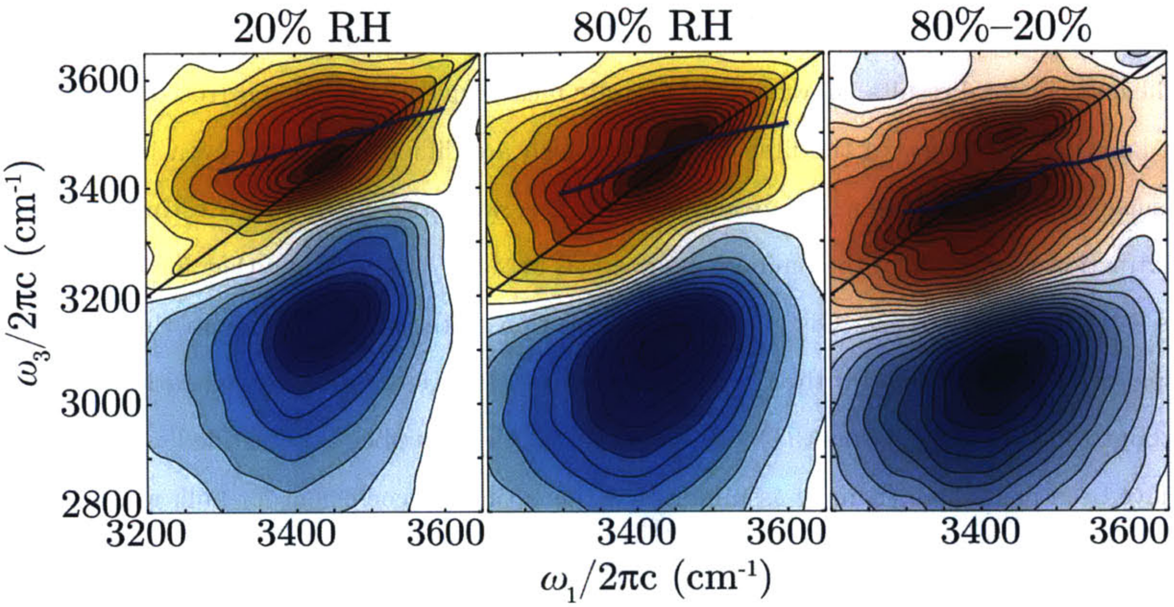

Figure 8.6: 2D IR spectrum of PLP at 20% and 80% RH taken at a waiting time of $\tau_2 = 100$ fs in the ZZYY polarization scheme. The rightmost panel shows their difference and highlights the structure within the O—H stretch.

associated and water-associated water molecules. In the 2D IR spectrum, these peaks appear to be separated by ~60 cm^{-1}, consistent with the observations made in the linear spectrum. Interestingly, the water–water peak is more intense in the 2D IR spectrum of the 20% RH film, despite it being barely discernible in the linear absorption spectrum. This change in intensity ratio is consistent with the notion that the transition dipoles of the water-bound molecules and the protein-bound molecules are different such that the quartic scaling of the transition dipoles changes the relative intensities in the nonlinear spectrum [336]. This is especially expected to be the case considering the non-Condon effect for the O—H stretch [167,168]. On the other hand, the peak assigned to the overtone of the C═O stretching mode at ~3280 cm^{-1} is not evident in the 2D IR spectrum. This is consistent with the idea that it is a peak with small oscillator strength, and as such, is washed out in the nonlinear spectrum.

Change in structure of the two peaks is particularly evident in the difference spectrum between the 80% and 20% RH spectra (Fig. 8.6). The difference spectrum clearly shows two peaks at ~3400 and ~3500 cm^{-1}, which again agree reasonably well with the peaks identified in the linear spectrum. There even appears to be a cross peak between the features, suggesting the possibility of coupling between the protein-associated and water-associated water molecules. However, it is difficult to determine whether or not this is a true cross peak from the difference spectrum alone.

Overlaid on the 2D IR spectra, Fig. 8.6 shows the CLS for the 100 fs surfaces. As mentioned, the scatter in the spectrum makes the interpretation of the absolute numbers unreliable, but the two may be qualitatively compared. Furthermore, it is difficult to interpret the meaning of the CLS when there are multiple overlapping peaks forming the feature under study; it is therefore necessary to proceed with caution when analyzing it. The 20% RH spectrum shows a CLS that is more or less linear with a value close to 0.4. On the other hand, the 80% spectrum shows the the CLS exhibits a distinct kink at $\omega_1 \approx 3500$ cm^{-1}, providing further evidence for distinct spectral components. We note that the CLS changes to a lower value at high frequencies despite scatter having the opposite effect on its value. This lowering of the CLS arises due to greater intensity below the diagonal in the 80% RH spectrum which is also evident in the difference spectrum. This can again be attributed to a cross peak between the protein-associated and water-associated water molecules.

The linear and nonlinear spectra lead us to conclude that there is an intricate balance between the protein–water interactions and the water–water interactions. Furthermore, the level of heterogeneity increases with increasing hydration as the propensity for water–water interactions increases. In the following section, we explore the dynamics of the various features and show how these dynamics are consistent with our interpretation.

8.3.2 Water Dynamics at the Protein Interface

As the waiting time increases, the 2D IR spectrum of both levels of hydration evolves from the early-time spectra shown in Fig. 8.6 to one that resembles a hot ground state (HGS) spectrum, shown in Fig. 8.7. This is suggestive that the same "heating process" observed in bulk water is present in hydrated protein films as well. We note that the HGS spectrum in Fig. 8.6 shows some artifacts due to scatter, which give the appearance of the spectrum not being quite uncorrelated. As discussed below, the timescale for the growth of the HGS is not slow enough to give rise to a true thermal state, and so the state is interpreted as it is for bulk water (see §6.5). We imagine that the interplay between the protein and the water greatly complicates the formation of the HGS. In addition to a blueshift of the O—H stretching band, the HGS shows an increase in the intensity of the C—H stretching modes. This is consistent with the observation that the intensity of the C—H stretching modes decreases with increasing hydration level (Fig. 8.4) since the HGS is presumably accompanied by a lower density of water around the proteins, and effectively less hydrated.

Figure 8.8A shows the intensity of the excited-state absorption as obtained from the 2D IR spectrum as a function of time. To obtain the signal, the 2D IR spectrum was integrated over ω_1, and integrated in ω_3 between 3000 and 3200 cm^{-1}. This lifetime measurement is not possible in a TA experiment since scatter entirely swamps the signal. The signal obtained in this manner is not free from interference, however. Figure 8.7 shows that there is significant contribution of the HGS in the 3000–3200 cm^{-1} region from both the O—H and C—H stretching modes. We must therefore use caution when interpreting the integrated data.

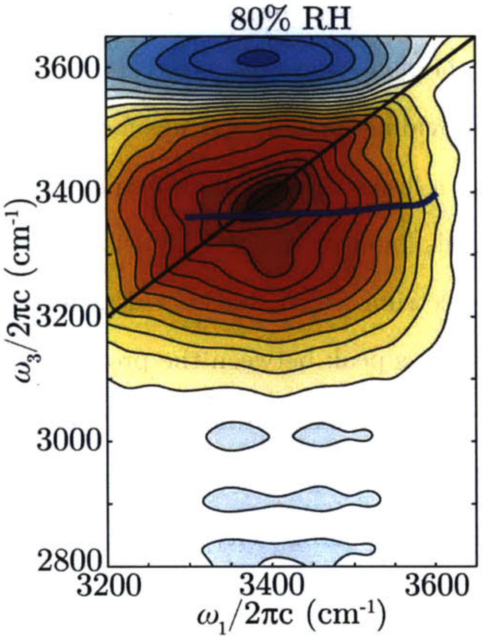

Figure 8.7: 2D IR HGS spectrum of PLP at 80% RH taken at a waiting time of $\tau_2 = 5$ ps.

Figure 8.8A shows that the signal intensity for the 20% and 80% RH films as well as their difference have bi-exponential dynamics. Each curve shows a rapid decay followed by a slow rise. We associate the rises with the growth of the HGS features, in particular the induced absorption arising from the C—H stretching modes, which occurs on a 1–1.2 ps timescale and is independent of the hydration level. On the other hand, the fast decay shows a strong dependence on the hydration level, with the 20% RH film decaying on a 1.1 ps timescale while the 80% RH film decays on a 660 fs timescale. Both of these values are several times slower than the relaxation timescales of bulk water, as expected. However, the fact that the O—H stretch in the 20% RH film decays almost twice as slow as the 80% film is telling. The difference in timescales reflects the larger number of water–water interactions (more bulk-like water) as the RH is increased.

The difference signal decays on a 530 fs timescale, which is even faster than the 80% RH signal. Assuming the effect of increasing hydration is additive, this suggests that adding water molecules at a certain RH only results in more water–water interactions, resulting in fast relaxation dynamics. This leads to a picture in which up to a certain RH, water hydrates the protein. However, beyond some RH the protein is saturated and, we develop a layer of bulk-like water around the protein.

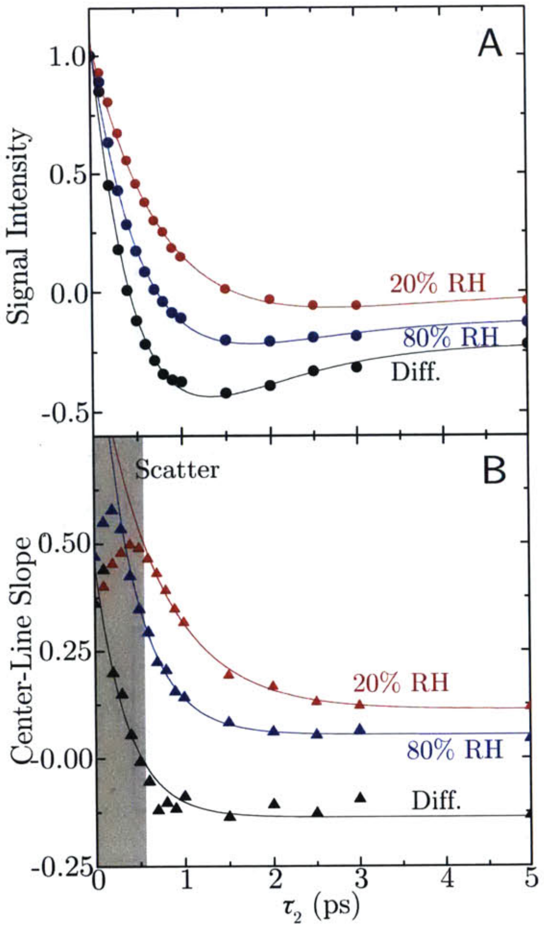

Figure 8.8: (A) Signal intensity and (B) CLS as a function of waiting time for the 20% RH film (red) 80% RH film (blue) and their difference (black). Solid lines are fits to the data.

The CLS measurement agrees with this interpretation, though the reliability of the data is called into question due to the scattering of the excitation pulses by the film. Figure 8.8B shows the CLS as a function of waiting time. At early times, the CLS appears to rise from its initial value. This is an artifact arising from the decay of the bleach while the scatter feature remains constant. As the HGS grows in, this causes the CLS to decay once more. Therefore, the CLS-decay timescales extracted are actually going to depend on the relaxation dynamics of the features themselves. Nonetheless, a comparison of the CLS in going from 20% to 80% RH is consistent with our interpretation. In particular, the 20% RH CLS decays on a 680 fs timescale while the 80% RH CLS decays on a 390 fs timescale. Furthermore, the difference spectrum also shows a CLS decay on a 350 fs timescale, consistent with the notion that above a certain RH, all of the hydrating water effectively behaves the same. We therefore conclude that the water in the vicinity of the protein, especially at low hydration, fluctuates significantly slower than in the bulk, which is consistent with the longer lifetime of the low-hydration water.

That the numbers at high RH still differ from the bulk shows that the water is not truly bulk-like and that the influence of the protein penetrates into the layer of water. This is consistent with observations in reverse micelles, in which the effect of the perturbed water near the surface was found to extend ~4 Å into the bulk [337]. While the surface chemistry of PLP is rather different from reverse micelles and isotropic confinement manifests itself differently than planar confinement, it stands to reason that the layer of water we generate on the surface of the protein cannot be much thicker than 1 nm if it is so perturbed by the PLP film.

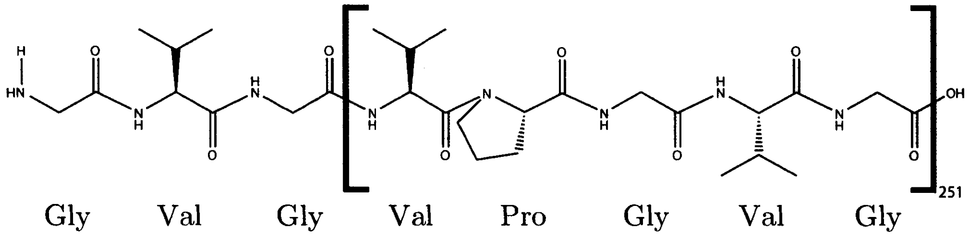

Figure 8.9: The sequence of the elastin-like polymer GVG(VPGVG)$_{251}$.

The question, then, is how the numbers measured at low RH, where presumably the dominant interaction is protein–water, relates to the dynamics of interfacial water at high RH or in bulk solution. This is of course a difficult question to address whose answer depends on the balance between the protein–water and water–water interactions. High-frequency vibrational dynamics will certainly be different since phenomena such as resonance energy transfer will come into play when bulk water (or N—H groups, for that matter) are present. However, given the slow decay of the CLS observed in PLP, it seems as though low-frequency dynamics will be at least several times slower.

8.4 Water Dynamics on a Hydrophobic Protein

We now look at a similar set of experiments as the previous section, except carried out on a hydrophobic GVG(VPGVG)$_{251}$ (abbreviated GVG) polymer. GVG is a disordered, hydrophobic polymer whose sequence, shown in Fig. 8.9, mimics that of various types of elastin found in nature [338, 339]. It is well known that the hydrophobic restoring force is a particularly important contributor to the polymer's elastic properties [340], and so understanding the interactions between the polymer and the water has garnered much interest.

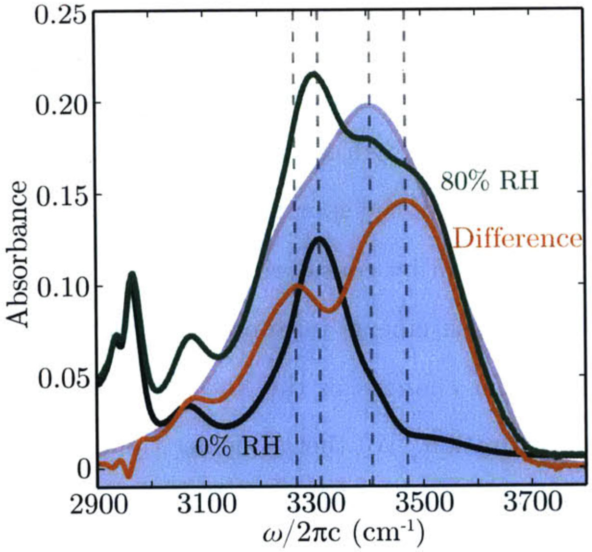

Figure 8.10: Linear absorption spectrum of the amide A region of a hydrated GVG film at 0% RH (black) and 80% RH (green) and their difference (orange). Bulk O—H stretch shown in blue.

For our purposes, a GVG film provides a unique opportunity to study water dynamics at a hydrophobic interface. Since the reduction in free energy for phase separation is large [341], the study of water dynamics in the vicinity of a hydrophobic solute in the solution phase is difficult. Any system in which a truly hydrophobic solute is dissolved in water is, by definition, a non-equilibrium system. Indeed, previous IR studies have relied on amphiphilic molecules [228, 233, 342] to study hydrophobicity, with questionable interpretation of the results. GVG allows us to study water adsorbed to a hydrophobic interface and compare these dynamics to those observed on PLP, for example.

Unlike PLP, GVG possesses N—H groups on its non-proline residues. This is a nuisance in that it complicates the spectroscopy. The N—H band and O—H band overlap in frequency, and so it is necessary to deal with spectral congestion. In addition, resonant coupling between the O—H stretch and N—H stretch results in added complexity in the lineshape and dynamics. On the other hand, we may use the presence of N—H groups to our advantage since we may treat them as a direct reporter on the structure and dynamics of the protein. Unlike the case of PLP, we may obtain an N—H stretching spectrum of GVG at 0% RH. Furthermore, because GVG is so hydrophobic, the O—H stretching peak is blueshifted compared to other films and therefore somewhat easier to isolate. Therefore, at all levels of hydration, we may consider the protein and water separately by observing the red side of the spectrum (protein) or blue side of the spectrum (water).

We begin by considering the linear and nonlinear spectra and discuss the implications these measurements have on the structure of water near a hydrophobic protein. We show that clear changes in the lineshape are evident in the nonlinear spectrum upon increasing hydration. We then consider the dynamics which show drastically different timescales depending on the level of hydration.

8.4.1 Water Structure at a Hydrophobic Interface

We turn to the consideration of the linear spectrum of the GVG film, shown in Fig. 8.10 at 0% (black) and 80% RH (green). In addition to the raw spectra, Fig. 8.10 also shows their difference (orange). The 0% RH spectrum shows a prominent amide A peak at 3309 cm^{-1} corresponding to the N—H stretching mode of the non-proline residues and a less prominent amide B feature at 3068 cm^{-1}. The N—H stretch shows a weak shoulder on the blue side corresponding to weakly or non-hydrogen bonded oscillators as well as a broad feature in the 3450–3600 cm^{-1} range that may correspond to water trapped in the dried film.

Upon hydration to 80% RH, the film spectrum changes significantly. Most notably, two intense peaks centered at ∼3405 cm^{-1} and ∼3500 cm^{-1} grow in, which are indicated by the grey background lines in Fig. 8.10. These peaks are also clearly visible in the difference spectrum. The lower-frequency peak comes at the same wavelength as bulk water (see blue background in Fig. 8.10), and so it is likely that this is due to water molecules interacting with other water molecules. The higher frequency feature is thus assigned to water interacting with the protein. The fact that it is blushifted compared to the water band in the PLP film is consistent with GVG being a more hydrophobic film. We also note that the amide A mode is redshifted upon hydration, consistent with the expected trend for hydrogen bonding. The amide B band is blueshifted, which is consistent with the notion that it is in fact the overtone of the amide II mode. In addition to shifting, it appears that these features increase in intensity upon hydration, which is explained by the vibrational non-condon effect [167, 168].

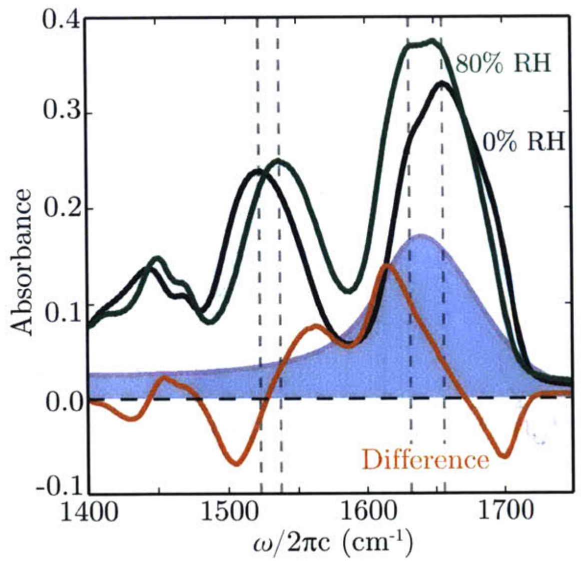

Figure 8.11: Linear absorption spectra of the amide I and II region of a hydrated GVG film at 0% RH (black) and 80% RH (green) and their difference (orange). Bulk HOH bend shown in blue.

The amide I and II region (shown in Fig. 8.11) also show trends consistent with hydrogen bonding. Unlike PLP, the amide I mode in the 0% RH film, which is peaked at 1655 cm^{-1}, is more structured due to the different environments taken on in the disordered GVG polymer. Upon hydration, intensity is lost on the blue side of the peak and gained on the red side at ∼1635 cm^{-1} corresponding to the formation of hydrogen bonds with water. Similarly, the amide II mode, which peaks at 1522 cm^{-1} in the dry film, is blueshifted by 16 cm^{-1} at 80% RH. Interestingly, there is also a relatively large (10–20 cm^{-1} redshift) response from the CH_2 bending modes on the proline and valine side chains despite there only being a shift

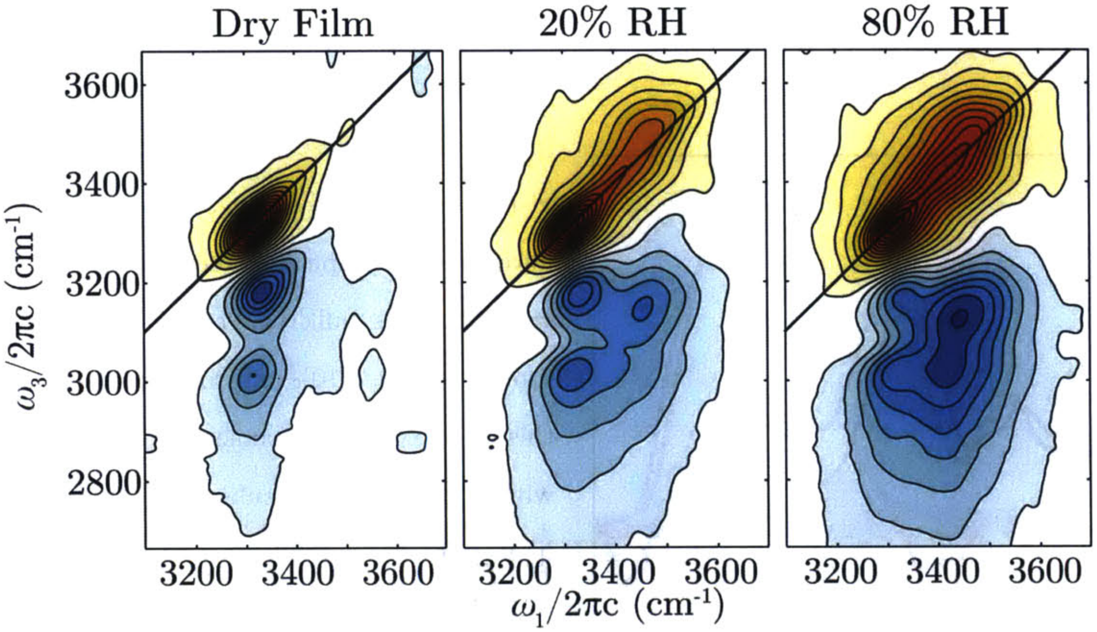

Figure 8.12: 2D IR spectra of GVG at 0%, 20%, and 80% RH taken at a waiting time of $\tau_2 = 100$ fs in the ZZYY polarization scheme.

of 3 cm^{-1} in the C—H stretching modes. As in the PLP film, there is no clear evidence of the HOH bending mode (shown as a blue background in Fig. 8.11), probably due to its low oscillator strength.

The 2D IR spectrum of 0%, 20%, and 80% RH GVG taken at a waiting time of $\tau_2 = 100$ fs is shown in Fig. 8.12. The 0% RH film shows a bleach of the N—H stretching mode elongated along the diagonal with a relatively high slope. This reflects the inhomogeneous broadening of the N—H groups on the protein backbone due to the lack of fluctuations on these timescales in the film. The spectrum also shows a broad ESA ranging from 3200–2800 cm^{-1} with a portion removed due to the bleaching of the amide B mode at ~3070 cm^{-1}. That is, the ESA is in fact a single broad feature, but the GSB of a cross peak to the amide B mode gives rise to a notch in the middle of the ESA and the appearance of two distinct peaks. The overall structure of the ESA peak is quite similar to that of the hydrogen-bonded NMA mode, and we assume that the spectrum can be assigned and interpreted in the same manner. (See §4.3.1 for a thorough discussion of the hydrogen-bonded amide A

2D IR spectrum.)

As the level of hydration is increased to 20% RH, a broad shoulder develops on the blue side of the GSB and ESA of the N—H stretching mode corresponding to the O—H stretch as in the linear spectrum. Unlike anything we have observed in bulk water, the peak that grows in is extremely inhomogeneous as evidenced by the high degree of diagonal elongation. In addition, the ESA of the O—H stretching peak is not massively broadened. Instead, it is a peak centered about 350 cm^{-1} redshifted in ω_3 relative to the GSB, with a width of ~100 cm^{-1}. This splitting, which would reflect an enormous anharmonicity, is unphysically large (we note that the splitting observed here is more than twice as large as that for the non-hydrogen-bonded N—H stretch in NMA [155].) Indeed this lineshape cannot be explained unless there is a cross peak between the O—H stretch of the water and the N—H stretch of the protein, which gives the appearance of a large splitting between GSB and ESA.

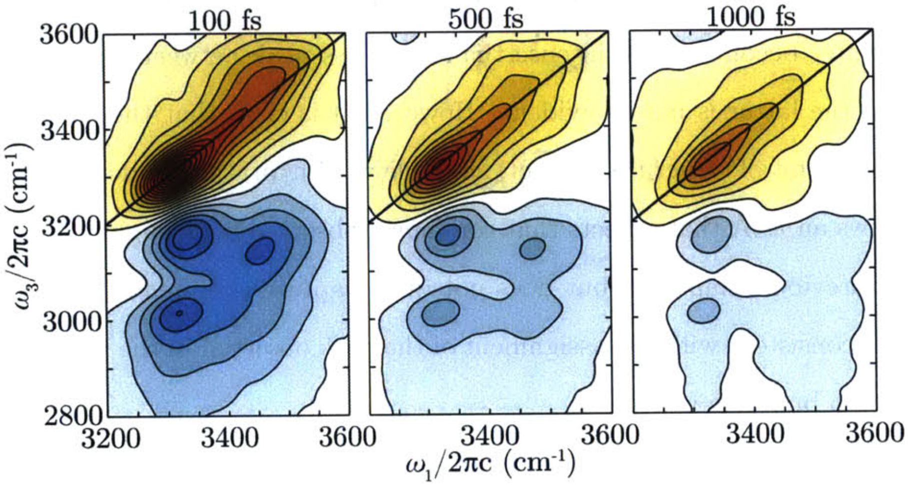

Figure 8.13: 2D IR waiting time dependence of the 20% hydrated GVG film, taken at waiting times of $\tau_2 = 100$, 500, and 1000 fs in the ZYYY polarization scheme. Spectra are normalized to the 100 fs surface.

Evidence for a cross peak between the O—H and N—H stretches can be seen in the waiting time dependence of the 2D IR spectrum, shown in Fig. 8.13. While dynamics in the GVG film are discussed at length in the following section, we note that there are nontrivial changes in the ESA of the water feature with increasing waiting time. In particular, it is evident that by 500 fs, the spectrum has evolved to a clear double-peak structure in the ESA of the water, which is a strong indicator for a cross peak between the water and the protein. We therefore understand that the splitting in the 100 fs spectrum is actually due to a cross peak at about (3450 cm^{-1}, 3300 cm^{-1}), which removes intensity from the ESA. Unfortunately, the overlap between the cross-peak feature and the ESA is strong, and it is not possible to isolate the dynamics of the two. In principle, this could be achieved with a careful fitting of the 2D IR spectrum; however, there are a number of assumptions that would go into such a fit whose validity would need to be thoroughly scrutinized.

As the level of hydration is increased further still to 80% RH, the shoulder corresponding to the O—H stretch intensifies, as expected, and the peak remains massively inhomogeneous. In addition, the ESA broadens to a width that is comparable to, or even larger than, the width of the ESA of the N—H stretching mode. This observation is consistent with the inferences made based on the 20% RH spectrum. As the level of hydration is increased, the ESA of the water becomes more intense than the cross peak between the protein and the water, and so the latter is not as evident. However, it is clear that the ESA of the water retains some amount of structure. In fact, as the level of hydration is increased to 80%, the spectrum shows an ESA that reflects that commonly observed in strongly hydrogen-bonded systems (see previous chapters), but does not quite capture the breadth observed in bulk water. This is consistent with the assignment of the peak observed in the linear IR spectrum at 3405 cm^{-1} to bulk-like water.

While these observations appear to give the notion of distinctly protein-associated water and water-associated water in the protein film, we now turn to the analysis of the dynamics within the film to corroborate this interpretation.

8.4.2 Dynamics at the Hydrophobic Interface

Since there is a certain degree of spectral separation between the O—H stretching mode of the water and the N—H stretching mode of the protein, we separate the measured dynamics into "protein dynamics" and "water dynamics." That is, we associate changes in the spectrum of features at $\omega_1 > 3400$ cm^{-1} with those of water and at $\omega_1 < 3400$ cm^{-1} with those of the protein. Of course, this is an approximation since there is still a fair amount of overlap between the two features. However, this approximation can be justified *post hoc* since the two sides of the spectrum show rather different dynamics.

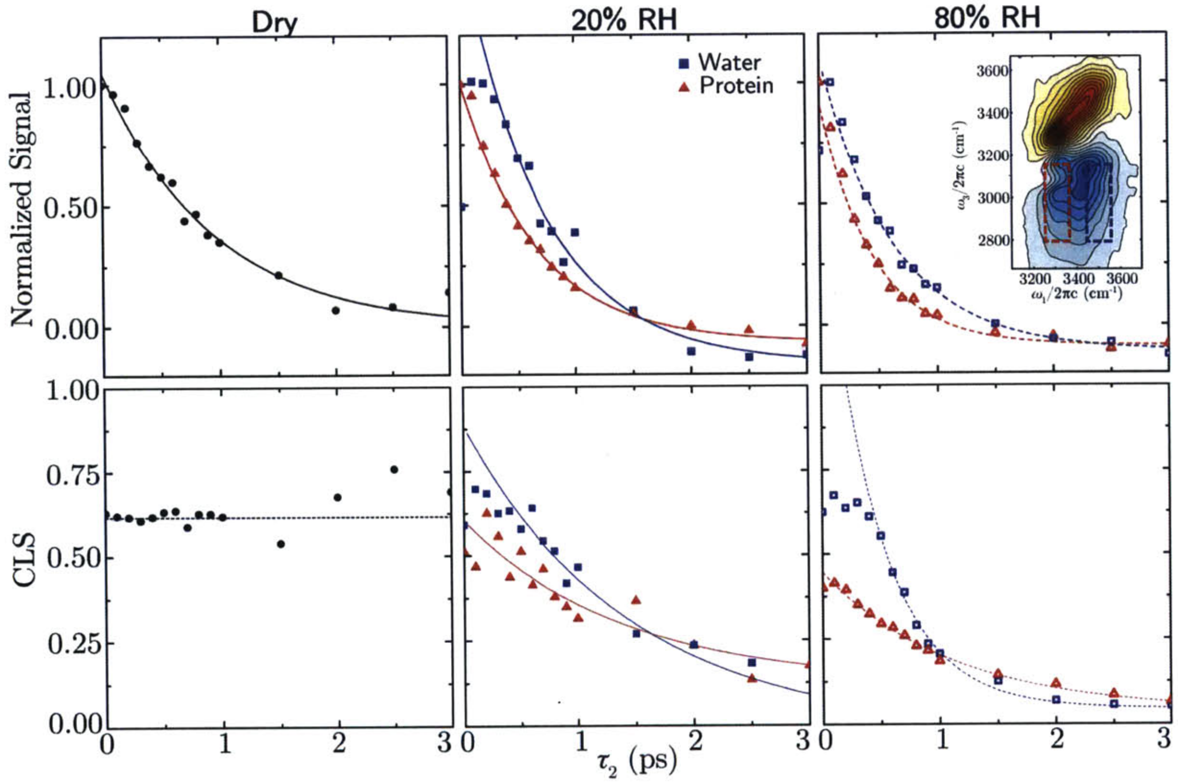

Figure 8.14: Dynamics associated with the GVG film at varying levels of hydration. The upper panels show the integrated ESA over the regions shown in the inset of the upper right panel. Black circles and red triangles correspond to the protein ESA and blue squares correspond to the water ESA. The lower panels use the same symbols to show the CLS evolution of the protein and water.

The upper panels of Fig. 8.14 show the integrated ESA signal as a function of waiting time. Black circles correspond to the ESA of the dry protein. Red triangles correspond to the ESA of the hydrated protein, integrated from 3240–3375 cm^{-1} in ω_1 and 2800–3150 cm^{-1} in ω_3. Blue squares correspond to the ESA of the hydrating water integrated from 3450–3550 cm^{-1} in ω_1 and the same range in ω_3. Full symbols correspond to 20% RH and empty symbols correspond to 80% RH. Exponential fits to the data are plotted as solid curves for the full symbols and as dashed curves for the empty symbols. The lower panels of Fig. 8.14 show the CLS as a function of waiting time, τ_2. Symbols correspond to the same features as in the upper panels. In analyzing this data, the CLS of the protein was measured in the 3250–3370 cm^{-1} range in ω_1 and the CLS of the water was measured in the 3400–3500 cm^{-1} range. The results of the analysis are summarized in Table 8.1.

Unsurprisingly, the 0% RH film shows the slowest dynamics, with an N—H stretch lifetime of 920 fs. This value is significantly slower than the lifetime of the free N—H stretch of NMA, but consistent with the 890 fs timescale measured for the lifetime of the N—H stretch in the hydrogen-bonded dimer, NH_1 (Table 4.1 summarizes the various timescales associated with NMA). While this number may be purely coincidental, it is also possible that the similarity in timescales reflects that the relaxation follows similar pathways. This result would not be unreasonable given that relaxation in the NMA dimer was found to proceed via an intramolecular mechanism within the amide unit through the amide B mode (see §4.5). Unlike the NMA dimer, however, the CLS of the N—H stretch does not decay on the timescale of the experiment. Rather, it begins at an initial value of 0.62 and stays constant (though becomes increasingly noisy as the signal decays away).[3] This shows that the molecular structure of the film is rigid, and N—H oscillators do not experience different environments within the lifetime of vibration.

The 80% film shows different dynamics for the protein and the water. At this level of hydration, the protein signal decays on a 480 fs timescale while the water ESA decays on a 630 fs timescale. It is difficult to determine whether or not the the protein signal truly decays faster than the water or whether the fast timescale is due to interference from the tail of the water band. In either case, the addition of water has clearly resulted in a significantly faster decay of the amide A vibration of the protein. The timescale for water, 630 fs, is more than two times slower than the relaxation time in the bulk. Again, however, it is difficult to know whether this is due solely to water dynamics or whether there is interference from the protein band. The difference in CLS decay timescales is more evident with the protein CLS decaying on a 1.13 ps timescale and the water CLS decaying on a 500 fs timescale. The water dynamics are about three times slower than in the bulk, suggesting that the dynamics of water are indeed slower at a hydrophobic interface.

---

[3] The integration method described in §6.4.2 does not work for particularly sharp peaks such as the N—H stretch of the dry film due to background interference. Therefore, to calculate the CLS, the maximum of the peak was taken instead of the first moment. This method only works for sharp peaks.

Table 8.1: Summary of timescales associated with hydrated GVG films.

	0% RH	20% RH		80% RH	
	Protein	Water	Protein	Water	Protein
Lifetime (fs)	920	710	730	630	480
CLS (ps)	–	1.44	1.39	0.50	1.13

The addition of hydrating water also results in a decay of the CLS of the protein, whereas the dry protein CLS did not decay. This decay can arise from a number of physical mechanisms: (1) Fluctuations of the water in the vicinity of N—H oscillators (e.g. fluctuations in hydrogen-bond strength) would result in the decay of the CLS of the N—H stretches. This should result in the protein CLS and water CLS decaying on the same timescale. (2) Protein and water fluctuations are dominated by water–water interactions. This results in a different decay timescale for the protein and the water since the latter dephases mainly through water–water interactions while the former through water–protein interactions. (3) The introduction of water actually causes the protein structure to fluctuate resulting in a loss of frequency memory in the protein. In §8.5.1 we show that (3) is not the case for Lysozyme and the timescales that we probe and therefore have no reason to expect that it is the case for the GVG film. Since the CLS decay timescales are not the same, we attribute the loss in frequency memory to case (2), where water–water interactions dominate. We expand on these concepts in the following section.

The 20% RH film provides us with qualitatively different results still, and the lifetimes show timescales intermediate between the 0% and 80% RH cases. The water and protein signals decay on 710 and 730 fs timescales, respectively, which for all intents and purposes can be considered identical. In addition, the CLS of the water and protein decay on 1.44 and 1.39 ps timescales, respectively, which are also almost identical. (Given the uncertainty in the CLS determination, the 50 fs difference is insignificant.) We therefore conclude that that at this level of hydration, the water and protein dynamics are locked and the two show a dynamical evolution this is highly dependent on each other. This behavior is consistent with case (1) described in the previous paragraph.

To corroborate our conclusions, we turn to the analysis of RH difference spectra. Of course the difference spectra are rather noisy, but we use the extracted numbers to determine whether the interpretation is plausible or not. The difference between 20% and 0% RH reports on the initial hydration interaction at low hydration levels, while the difference between 80% RH and 20% RH reports on the water molecules added after a substantial amount of hydration. We again calculate the decay of the ESA and the CLS, and the results are summarized and compared to bulk water in Table 8.2.

Table 8.2: Summary of difference timescales associated with hydrated GVG films.

	RH Difference		
	20%–0%	80%–20%	Bulk
Lifetime (fs)	690	280	280
CLS (ps)	3.7	0.44	170

The lifetimes associated with the 20%–0% and the 80%–20% are 690 and 280 fs, respectively. The former is consistent with the value of 710 fs measured directly from the 20% RH spectrum. This shows that at this level of hydration, the approximation of separating the water and the protein works relatively well. The lifetime associated with the 80%–20% spectrum, 280 fs, is identical with the lifetime of bulk water. This validates our conclusion that water begins to appear bulk-like at a certain level of hydration. That is, at some point between 20% and 80% RH, any added water added is effectively bulk-like and, in some sense, entirely independent of the protein. A similar trend is observed for the decay of the

CLS which occurs on a 3.7 ps timescale for the 20%–0% spectrum and 440 fs for the 80%–20% spectrum. The value of the latter is about 2.5 times slower than bulk water, but is consistent with the measurement made directly from the 80% RH spectrum. This suggests that at 80% RH, there are enough waters to act as an efficient sink for an excitation, but the fluctuations are not yet bulk-like and the presence of the protein is still an important factor. The extremely long value of 3.7 ps for the 20%–0% is considerably longer than the value of 1.4 ps in the directly measured spectrum, but this is to be taken with a grain of salt. The CLS is rather noisy, especially at long times, so we do not particularly trust this number. However, we do conclude that the water dynamics are significantly slower at the protein interface.

We therefore develop a picture of hydration of a hydrophobic protein that varies as a function of the level of hydration. At low hydration values, the protein and the water evolve together on timescales that are intimately dictated by the nature of the interaction between the protein and the water. Indeed, we may associate the frequency loss on the 1.4 ps timescale with fluctuations of the hydrogen-bonding interaction between the water and protein. Though we do not have any particular structural resolution in this measurement (due to the overlap of the broad features), the closeness of the timescales suggests that the measurement reports directly on hydrogen bonds between the NH of the protein and OH groups of the water. As the level of hydration is increased to 80%, it appears as though the dynamics of the protein and the water decouple due to water–water interactions, and the two evolve on different timescales. Effectively, some portion of the water behaves almost entirely bulk-like while only a small amount of water is affected by interactions with the protein. In this limit, the rapid fluctuations of the water cause the protein oscillators to lose frequency memory in a way that is incommensurate with the dynamics of the water.

The actual reason for this difference is difficult to determine from experiment alone. If bulk-water signals are dominating the observed spectral response, it may be that the water–protein interaction is unchanged (or possible even enhanced) when we add bulk-like water, and our signal is simply swamped by the bulk response. On the other hand, it may be possible that adding waters beyond the first solvation shell does affect the interactions between the water and protein due to a competition between water–water and water–protein interactions. Certainly, it will be necessary to carry out experiments in which the level of hydration is systematically varied in order to carefully probe the crossover between these two regimes.

Relating this picture of hydrophobic hydration to the bulk is not so straightforward. Naively, one would assume that the 80% RH film is most representative of the dynamics of the protein–water interactions in the bulk. However, this assumes that the surface of the protein is homogeneous and that every point along the protein–water interface truly appears as a bulk interface. Of course, real proteins are more complex than this and show structural motifs that differ significantly from a bulk interface. For example, a hydrophobic pocket in an enzyme may resemble water on the 20% RH film more strongly than water on the 80% RH on. In reality, we do not know how much water in the film is directly hydrogen bonded to the protein backbone and how much is solvating hydrophobic side-chain groups. We must naturally conclude that the dynamics of water around a protein in solution is going to depend strongly on the structure of the protein. That is, the water dynamics will vary smoothly from being locked to those of the protein in regions of low hydration to being dominated by water–water interactions in regions of high hydration.

8.5 The Effect of Water on Protein Structure

In the previous section, it was stated that there are three possibilities for the decay of the CLS in experiments on the hydration of protein films. In somewhat more detail, these were:

(1) Frequency fluctuations of the protein oscillators (i.e. N—H oscillators) are driven by direct, isolated interactions with water molecules. This is expected to be the case when there are few water molecules per protein residue and protein–water interactions dominate. Fluctuations in the interaction directly result in the loss of frequency correlation. In this case, frequency correlation in the water and the protein is lost at

the same rate, and the dynamics of the two are locked.

(2) Frequency fluctuations of the protein oscillators are again driven by direct interaction with water molecules, though it is not an isolated interaction. That is, the water molecule, in what is effectively the first hydration shell, is allowed to interact with other water molecules in the same or different hydration shell. Water–water interactions dominate the spectral response, though it is difficult to know whether there is a significant change in the water–protein interaction relative to case (1). In this case, frequency correlations in the protein and the water are lost at different rates.

(3) Frequency fluctuations of the protein are driven by fluctuations in the structure of the protein. Given that no CLS decay is observed in the dry film, this would suggest that structural fluctuations of the protein are driven by the hydration. In this case, it is expected that frequency correlations of the protein and water decay on different timescales. Given the slow timescales associated with structural fluctuations, we expect that the protein dynamics evolve far more slowly than the water.

In these scenarios, the effect of resonant energy transfer as well as vibrational relaxation has not been considered. We discuss this in somewhat more detail below, but for now, we note that this does not change the interpretation of the cases significantly. In case (1), resonant energy transfer results in exchange between N—H oscillators, but, by assumption, all of these oscillators lose frequency correlation at the same rate. Therefore, resonant energy transfer should not result in any observable difference. Nonresonant energy transfer, on the other hand, will result in a loss of frequency correlation. In this case the timescale does not directly report on the fluctuation of the interactions, but a combination of this and non-resonant energy transfer rates. Intuitively, however, we do not expect the non-resonant energy transfer rate to be large.

We expect that vibrational relaxation will have an effect intermediate between resonant and non-resonant energy transfer. Relaxation does not inherently change the frequency of an oscillator (which would give rise to a decay of the CLS); however, in a relaxation process, low-frequency modes are excited, and this typically does affect the frequency of an oscillator. Therefore, the decay of the CLS has some contribution from non-resonant energy transfer as well as loss in correlation due to vibrational relaxation. Therefore, we must be mindful that the timescale extracted has some contribution from these effects and is not solely due to the fluctuation of the interaction; though we expect the latter to be the dominant driver of the CLS decay.

The inclusion of energy transfer and vibrational relaxation modifies cases (2) and (3) in a similar manner.

In §8.4.2, it was stated that case (3) was indeed not the situation and therefore, examples of cases (1) and (2) was seen in the 20% and 80% RH GVG films, respectively. In this section, we provide experimental evidence that case (3) does not occur. Doing so, requires decoupling the structure of the protein from the oscillators interacting with the water molecules. This can be achieved by hydrating the protein film with D_2O. As mentioned in §8.2, hydrating a film with D_2O results in a rapid H–D exchange of labile protons. Effectively, the "exterior" of the protein (that is, the humid-air-exposed part of the protein) has its labile hydrogen atoms replaced with deuterium atoms. For our purposes, this will consist of N—H bonds being replaced by N—D bonds. On the other hand, the "interior" of the protein will be unaffected and it will retain its core N—H bonds. As such, the interior of the protein is spectroscopically accessible without interference from the exterior. If there are structural fluctuations of the protein on the timescale of the experiment, these should be reflected in the interior N—H bonds.

To demonstrate the robustness of the protein structure upon hydration, we use hen egg-white lysozyme (HEWL) as a model protein. HEWL is a ubiquitous enzyme that damages bacterial cell walls via the catalytic hydrolysis of glycosidic bonds. HEWL is of particular historic significance [343]; for example, it was the first enzyme (and second protein) whose crystal structure was determined [344]. Our reason for using HEWL for this study is primarily this, and there is no reason to believe that the results of this study do not hold for other globular proteins.[4]

The structure of HEWL [345] is such that 40-50% of the structure is in an α-helical conformation while 9–10% of the structure is in a β-sheet conformation. Presumably, the labile protons within these secondary structure motifs do not exchange on the timescale of the experiment. Indeed, HEWL does not exchange entirely in solution above a certain pH and even then only does so on a timescale of hundreds of minutes [346]. We therefore assume that the interior core of the protein is entirely hydrogenated with most of the exterior being deuterated.

8.5.1 Robust Protein Structure under Hydration

The linear absorption spectra of a HEWL film under different hydration conditions are shown in Fig. 8.15. The dry film and 80% RH H_2O–hydrated film are shown in black and green, respectively, while the 80% RH D_2O–hydrated film and 0% RH partially-exchanged film are shown in red and purple, respectively. The blue background shows the absorption spectrum of the bulk O—H stretching band.

Qualitatively, the 0% RH HEWL absorption spectrum shows the same features as the previously explored films, including the N—H stretch at 3305 cm^{-1}. In addition to this, features corresponding to the amide B mode as well as the C═O stretch overtone are evident. Upon hydration to 80% RH with H_2O, (green curve) the overall optical density increases as the HEWL uptakes water. A pronounced shoulder on the red side of the N—H stretch develops, and the N—H stretching mode is redshifted somewhat.

The spectrum looks different still upon hydration to 80% RH with D_2O (red). The N—H stretching band does not redshift in this case, but narrows and decreases in intensity, as discussed in §8.2. The narrowing is a result of H–D exchange. The protons that contribute to the breadth of the lineshape are primarily due to those in unstructured or disordered environments, and these are the protons that exchange most easily. In effect, most of the protons that are not exchanged are those in secondary structure environments, and so the N—H lineshape appears less broad upon hydration with D_2O. This interpretation is corroborated by the fact that the N—H stretch does not shift significantly upon hydration –a good indication that the N—H oscillators that do not exchange are not directly exposed to the hydrating water. The decrease in intensity is somewhat more difficult to understand. It may arise from the higher effective dielectric constant due to the hydration water. Though it may also be a result of reduced coupling to the disordered N—H environments, since these have exchanged off.

---

[4] The experiments performed on HEWL in this section were also performed on β–lactoglobulin with the same results. This data is not reproduced here.

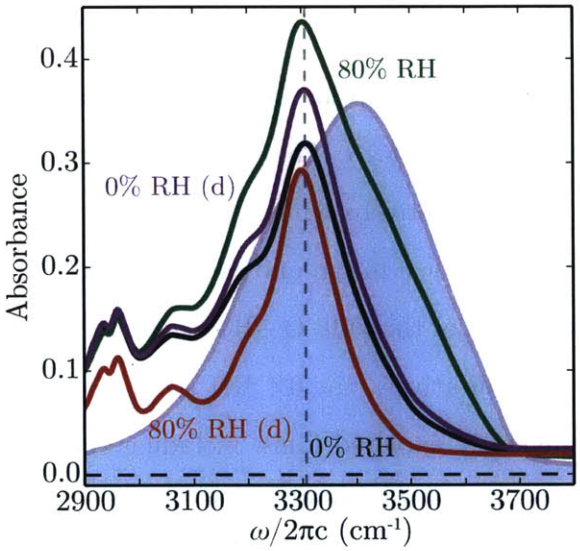

Figure 8.15: Linear absorption spectrum of the amide A region of a HEWL film at 0% RH (black) and hydrated at 80% RH (green) with H_2O and with D_2O (red). The spectrum after hydration with D_2O is shown (purple). Bulk O—H stretch shown in blue.

We are primarily concerned with the difference in the dynamics of the structure of the protein as to rule out case (3) in the discussion of the previous section. While these are expected to occur on long timescales, it is necessary to confirm our expectations experimentally. The CLS of the 0% RH HEWL film is shown in Fig. 8.16 (black circles) as a function of τ_2. Over the experimental range measured (5 ps) there is no appreciable decay of the CLS. In fact, the CLS even appears to rise somewhat; however, this is merely an artifact due to scatter. The fact that the CLS has an average value of 0.993 ± 0.013 shows that in the dry state, the structure of the protein is extremely rigid and stable on the timescale of the experiment. We cannot comment on whether there are large-scale structural changes on timescales longer than 5 ps, but given the robust structure of the globular protein, it is unlikely that such changes would occur on sub-microsecond timescales, though we do expect low-frequency fluctuations due to thermal agitation [347].

Upon hydration with H_2O to 80% RH, the CLS shows a rapid exponential decay (Fig. 8.16, green squares). Now, the CLS begins at an initial value of 0.67 and decays on a 900 fs timescale to a final value of zero. The fact the the CLS now decays shows that the addition of H_2O results in the loss of frequency memory. What is more, the fact that the CLS decays to a final value of zero is telling. Suppose there were two subsets of N—H oscillators, ones that fluctuated and lost frequency memory and ones that were rigid and did not lose frequency memory. If these were independent, the 2D IR spectrum would be a simple superposition of the two, and the CLS would decay to a final non-zero value that reflects the frequency memory of the rigid subset of N—H oscillators. Clearly, this is not the case in the current experiment. *All* of the N—H oscillators in the HEWL film lose frequency memory since the CLS decays to zero.

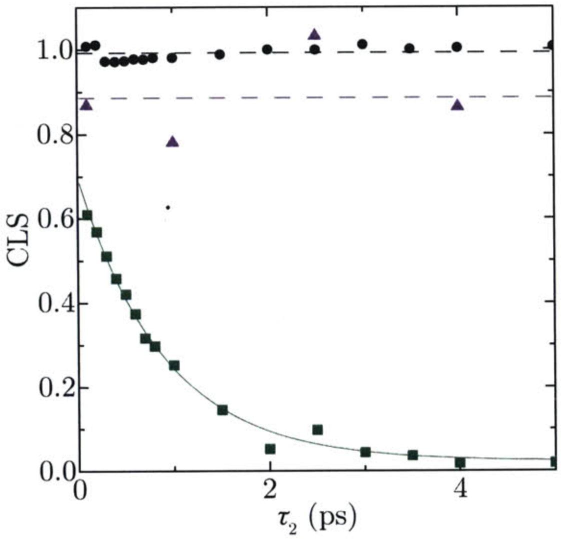

Figure 8.16: CLS decay of HEWL films hydrated at 0% RH (black circles), 80% RH with H_2O (green squares), and 80% RH with D_2O (purple triangles). Solid green line is an exponential fit to the data.

Naively, we might assume that all N—H oscillators undergo the same fluctuations, regardless of whether they are exposed to hydrating water or embedded in the secondary structure forming the protein core. This would necessarily imply that the protein secondary structure (that is, the α–helicies and β–sheets) undergo fluctuations due to the hydrating water. The key to the previous discussion, however, is that the rigid oscillators and exterior oscillators are independent. If there is cross talk between the two, in the form of dipole-dipole coupling, for example, then the oscillators in the secondary structure may lose frequency memory despite there being no direct contact with the hydrating water. However, with the H_2O data alone, it is not possible to distinguish between the two cases.

As mentioned, hydration with D_2O provides us with the ability to distinguish between the two cases. Fig. 8.16 shows the CLS of the HEWL film upon hydration to 80% RH with D_2O (purple triangles). There are few points and the data is noisy, but the CLS clearly does not decay. This implies that the CLS decay when hydrating with H_2O is not a result of structural fluctuations induced by the water, since these ought to be present upon hydration with D_2O as well. We must therefore conclude that the decay of the CLS of the secondary-structure oscillators is due to coupling between these oscillators and those that directly interact with the hydrating water and not due to structural fluctuations on the timescale of the experiment. Since the two types of oscillators are not resonant when hydrating with D_2O this effect is not observed. The CLS upon hydration with 80% RH D_2O shows an average value of 0.89 ± 0.11; while it is difficult to interpret this value due to the large standard deviation, it is clearly within range of the values observed in the dry film.

Much of the discussion in this and previous sections has been in the language of a local-mode picture. That is, we have implicitly considered an isolated hydrogen bond between an O—H and N—H or C═O. As is clear from Chapters 4, 6, and 7, reality is far more complex, and we expect the vibrations to delocalize due to the hydrogen-bonding interaction. In this case, it is difficult to interpret the dynamic variables we extract since, presumably, the spectral features we measure are due to vibrations that have some N—H as well as some O—H stretching character. In some sense, the CLS decay still reflects the dynamics of the interaction, though these are immensely complex since the very nature of the eigenstates will change with time. That is, it is no longer sufficient to consider only fluctuations in hydrogen-bond length and angle, but we must also consider the possibility that an initially delocalized excited vibration may localize as waiting time increases, adding yet another layer of complexity to the problem.

This latter point highlights the richness of the information contained in the 2D IR spectra of hydrated protein films. As mentioned in the introduction, the experiments and analyses presented in this chapter have barely made a dent in the understanding of these complex systems. Moving forward, it is necessary to develop a thorough understanding of a representative model protein. This is certainly no easy task, and I believe that this will necessitate studies where the RH is systemically varied in a well-controlled way, combined with detailed analysis of carefully measured difference spectra. In the future, these systems will provide an excellent platform on which to study proteins that exhibit specific or unusual water–protein interactions in unprecedented detail.

Bibliography

[1] W. M. Latimer and W. H. Rodebush. Polarity and Ionization from the Standpoint of the Lewis Thoery of Valence. *J. Am. Chem. Soc.*, **42**, 1419 (1920).

[2] G. Jeffrey. *An Introduction to Hydrogen Bonding.* Oxford University Press, Oxford (1997).

[3] L. Pauling. The Nature of Chemical Bond. Application of Results Obtained from a Theory of Parmagnetic Susceptibility to the Structure of Molecules. *J. Am. Chem. Soc.*, **53**, 1367 (1931).

[4] Y. Marèchal. *The Hydrogen Bond and the Water Molecule.* Elsevier, Amsterdam (2007).

[5] T. R. Dyke, K. M. Mack, and J. S. Muenter. The Structure of Water Dimer from Molecular Beam Electric Resonance Spectroscopy. *J. Chem. Phys.*, **66**, 498 (1977).

[6] D. Eisenberg and W. Kauzmann. *The Structure and Properties of Water.* Oxford University Press, Oxford (2005).

[7] E. D. Głowacki, M. Irimia-Vladu, S. Bauer, and N. S. Sariciftci. Hydrogen-Bonds in Molecular Solids from Biological Systems to Organic Electronics. *J. Mater. Chem. B*, **1**, 3742 (2013).

[8] A. E. Mirsky and L. Pauling. On the Structure of Native, Denatured, and Coagulated Proteins. *Proc. Natl. Acad. Sci. U. S. A.*, **22**, 439 (1936).

[9] L. Pauling, R. B. Corey, and H. R. Branson. The Structure of Proteins; Two Hydrogen-Bonded Helical Configurations of the Polypeptide Chain. *Proc. Natl. Acad. Sci. U. S. A.*, **37**, 205 (1951).

[10] J. D. Watson and F. H. C. Crick. Molecular Structure of Nucleic Acids. *Nature*, **171**, 737 (1953).

[11] P. Ball. Water as an Active Constituent in Cell Biology. *Chem. Rev.*, **108**, 74 (2008).

[12] E. Arunan, G. R. Desiraju, R. a. Klein, J. Sadlej, S. Scheiner, I. Alkorta, D. C. Clary, R. H. Crabtree, J. J. Dannenberg, P. Hobza, H. G. Kjaergaard, A. C. Legon, B. Mennucci, and D. J. Nesbitt. Definition of the Hydrogen Bond (IUPAC Recommendations 2011). *Pure Appl. Chem.*, **83**, 1637 (2011).

[13] E. W. Castner, Y. J. Chang, Y. C. Chu, and G. E. Walrafen. The Intermolecular Dynamics of Liquid Water. *J. Chem. Phys.*, **102**, 653 (1995).

[14] I. Ohmine. Liquid Water Dynamics - Collective Motions, Fluctuation, and Relaxation. *J. Phys. Chem.*, **99**, 6767 (1995).

[15] C. J. Fecko, J. D. Eaves, J. J. Loparo, A. Tokmakoff, and P. L. Geissler. Ultrafast Hydrogen-Bond Dynamics in the Infrared Spectroscopy of Water. *Science*, **301**, 1698 (2003).

[16] D. M. Carey. Measurement of the Raman spectrum of liquid water. *J. Chem. Phys.*, **108**, 2669 (1998).

[17] W. B. Monosmith and G. E. Walrafen. Temperature Dependence of the Raman OH Stretching Overtone from Liquid Water. *J. Chem. Phys.*, **81**, 669 (1984).

[18] M. L. Huggins. Hydrogen Bridges in Ice and Liquid Water. *J. Phys. Chem.*, **40**, 723 (1936).

[19] A. Luzar and D. Chandler. Effect of Environment on Hydrogen Bond Dynamics in Liquid Water. *Phys. Rev. Lett.*, **76**, 928 (1996).

[20] E. R. Lippincott and R. Schroeder. One-Dimensional Model of the Hydrogen Bond. *J Chem Phys*, **23**, 1099 (1955).

[21] R. Schroeder and E. Lippincott. Potential Function Model of Hydrogen Bonds. II. *J. Phys. Chem.*, **2** (1957).

[22] G. Zundel. Hydrogen Bonds with Large Proton Polarizability and Proton Transfer Processes in Electrochemistry and Biology. In *Adv. Chem. Phys.*, 1–217. John Wiley & Sons, Hoboken (1999).

[23] K. Giese, M. Petković, H. Naundorf, and O. Kühn. Multidimensional Quantum Dynamics and Infrared Spectroscopy of Hydrogen Bonds. *Phys. Rep.*, **430**, 211 (2006).

[24] C. P. Lawrence and J. L. Skinner. Vibrational Spectroscopy of HOD in Liquid D_2O. III. Spectral Diffusion, and Hydrogen-Bonding and Rotational Dynamics. *J. Chem. Phys.*, **118**, 264 (2003).

[25] K. B. Møller, R. Rey, and J. T. Hynes. Hydrogen Bond Dynamics in Water and Ultrafast Infrared Spectroscopy: A Theoretical Study. *J. Phys. Chem. A*, **108**, 1275 (2004).

[26] J. D. Eaves, A. Tokmakoff, and P. L. Geissler. Electric Field Fluctuations Drive Vibrational Dephasing in Water. *J. Phys. Chem. A*, **109**, 9424 (2005).

[27] L. Pauling. The Structure and Entropy of Ice and of Other Crystals with Some Randomness of Atomic Arrangement. *J. Am. Chem. Soc.*, **57**, 2680 (1935).

[28] P. A. Kollman, J. F. Liebman, and L. C. Allen. The Lithium Bond. *J. Am. Chem. Soc.*, **92**, 1142 (1970).

[29] E. D. Isaacs, A. Shukla, P. M. Platzman, D. R. Hamann, B. Barbiellini, and C. A. Tulk. Compton Scattering Evidence for Covalency of the Hydrogen Bond in Ice. *J. Phys. Chem. Solids*, **61**, 403 (2000).

[30] H. Graener, T. Q. Ye, and A. Laubereau. Ultrafast Dynamics of Hydrogen Bonds Directly Observed by Time-Resolved Infrared Spectroscopy. *J. Chem. Phys.*, **90**, 3413 (1989).

[31] E. T. J. Nibbering and T. Elsaesser. Ultrafast Vibrational Dynamics of Hydrogen Bonds in the Condensed Phase. *Chem. Rev.*, **104**, 1887 (2004).

[32] J. B. Asbury, T. Steinel, C. Stromberg, S. A. Corcelli, C. P. Lawrence, J. L. Skinner, and M. D. Fayer. Water Dynamics : Vibrational Echo Correlation Spectroscopy and Comparison to Molecular Dynamics Simulations. *J. Phys. Chem. A*, **108**, 1107 (2004).

[33] J. J. Loparo, S. T. Roberts, and A. Tokmakoff. Multidimensional Infrared Spectroscopy of Water. I. Vibrational Dynamics in Two-Dimensional IR Line Shapes. *J. Chem. Phys.*, **125**, 194521 (2006).

[34] J. J. Loparo, S. T. Roberts, and A. Tokmakoff. Multidimensional Infrared Spectroscopy of Water. II. Hydrogen Bond Switching Dynamics. *J. Chem. Phys.*, **125**, 194522 (2006).

[35] Y. S. Kim and R. M. Hochstrasser. Chemical Exchange 2D IR of Hydrogen-Bond Making and Breaking. *Proc. Natl. Acad. Sci. U. S. A.*, **102**, 11185 (2005).

[36] J. Zheng, K. Kwak, J. Asbury, X. Chen, I. R. Piletic, and M. D. Fayer. Utrafast Dynamics of Solute-Solvent Complexation Observed at Thermal Equilibirum in Real Time. *Science*, **309**, 1338 (2005).

[37] K. Kwak, J. Zheng, H. Cang, and M. D. Fayer. Ultrafast Two-Dimensional Infrared Vibrational Echo Chemical Exchange Experiments and Theory. *J. Phys. Chem. B*, **110**, 19998 (2006).

[38] R. G. Bryant. The NMR Time Scale. *J. Chem. Educ.*, **60**, 933 (1983).

[39] M. Harmand, R. Coffee, M. R. Bionta, M. Chollet, D. French, D. Zhu, D. M. Fritz, H. T. Lemke, N. Medvedev, B. Ziaja, S. Toleikis, and M. Cammarata. Achieving

Few-Femtosecond Time-Sorting at Hard X-Ray Free-Electron Lasers. *Nat. Photonics*, **7**, 215 (2013).

[40] P. Ball. Water — An Enduring Mystery. *Nature*, **452**, 291 (2008).

[41] F. Franks. *A Comprehensive Treatise of Water - The Physics and Physical Chemistry of Water.* Plenum Press, New York (1972).

[42] P. S. Ray. Broadband Complex Refractive Indices of Ice and Water. *Appl. Opt.*, **11**, 1836 (1972).

[43] I. Ohmine and S. Saito. Water Dynamics: Fluctuation Relaxation, and Chemical Reactions in Hydrogen Bond Network Rearrangement. *Acc. Chem. Res.*, **32**, 741 (1999).

[44] B. M. Auer and J. L. Skinner. IR and Raman Spectra of Liquid Water: Theory and Interpretation. *J. Chem. Phys.*, **128**, 224511 (2008).

[45] D. A. Draegert, N. Stone, B. Curnutte, and D. Williams. Far-Infrared Spectrum of Liquid Water. *J. Opt. Soc. Am. A*, **56**, 64 (1966).

[46] G. M. Hale and M. R. Querry. Optical Constants of Water in the 200-nm to 200-μm Wavelength Region. *Appl. Opt.*, **12**, 555 (1973).

[47] J. B. Brubach, A. Mermet, A. Filabozzi, A. Gerschel, and P. Roy. Signatures of the Hydrogen Bonding in the Infrared Bands of Water. *J. Chem. Phys.*, **122**, 184509 (2005).

[48] J. Messer, F. C. De Lucia, and P. Helminger. The Pure Rotational Spectrum of Water Vapor–A Millimeter, Submillimeter, and Far Infrared Analysis. *Int. J. Infrared Millimeter Waves*, **4**, 505 (1983).

[49] J. D. Jackson. *Classical Electrodynamics.* John Wiley & Sons, New York, 2nd edition (1975).

[50] H. Goldstein. *Classical Mechanics.* Addison-Wesley, New York, 2nd edition (1980).

[51] C. Cohen-Tannoudji, J. Dupont-Roc, and G. Grynberg. *Photons and Atoms: Introduction to Quantum Electrodynamics.* John Wiley & Sons, New York (1989).

[52] S. Mukamel. *Principles of Nonlinear Optical Spectroscopy.* Oxford University Press, New York (1995).

[53] D. M. Jonas. Two-Dimensional Femtosecond Spectroscopy. *Annu. Rev. Phys. Chem.*, **54**, 425 (2003).

[54] M. Cho. Coherent Two-Dimensional Optical Spectroscopy. *Chem. Rev.*, **108**, 1331 (2008).

[55] Y. Shen. *The Principles of Nonlinear Optics.* John Wiley & Sons, Hoboken (2003).

[56] P. Butcher and D. Cotter. *The Elements of Nonlinear Optics.* Cambridge UP, Cambridge (1990).

[57] M. Born and E. Wolf. *Principles of Optics.* Pergamon Press, Oxford, 4th edition (1970).

[58] T. Brabec and F. Krausz. Nonlinear Optical Pulse Propagation in the Single-Cycle Regime. *Phys. Rev. Lett.*, **78**, 3282 (1997).

[59] S. M. G. Faeder and D. M. Jonas. Phase-Resolved Time-Domain Nonlinear Optical Signals. *Phys. Rev. A*, **62**, 33820 (2000).

[60] R. Kubo. Statistical-Mechanical Theory of Irreversible Processes. I. General Theory and Simple Applications to Magnetic and Conduction Problems. *J. Phys. Soc. Japan*, **12**, 570 (1957).

[61] R. Kubo, M. Yokota, and S. Nakajima. Statistical-Mechanical Theory of Irreversible Processes. II. Response to Thermal Disturbance. *J. Phys. Soc. Japan*, **12**, 1203 (1957).

[62] C. Cohen-Tannoudji, B. Diu, and F. Laloë. *Quantum Mechanics.* Wiley-VCH, 2nd edition (1977).

[63] J. Sung and R. J. Silbey. Four Wave Mixing Spectroscopy for a Multilevel System. *J. Chem. Phys.*, **115**, 9266 (2001).

[64] J. M. Blatt and V. F. Weisskopf. *Theoretical Nuclear Physics.* Springer-Verlag, New York (1979).

[65] T. Joo, Y. Jia, J.-Y. Yu, M. J. Lang, and G. R. Fleming. Third-Order Nonlinear Time Domain Probes of Solvation Dynamics. *J. Chem. Phys.*, **104**, 6089 (1996).

[66] R. Agarwal, B. S. Prall, A. H. Rizvi, M. Yang, and G. R. Fleming. Two-Color Three Pulse Photon Echo Peak Shift Spectroscopy. *J. Chem. Phys.*, **116**, 6243 (2002).

[67] Y. Nagasawa, K. Seike, T. Muromoto, and T. Okada. Two-Dimensional Analysis of Integrated Three-Pulse Photon Echo Signals of Nile Blue Doped in PMMA. *J. Phys. Chem. A*, **107**, 2431 (2003).

[68] S. M. G. Faeder and D. M. Jonas. Two-Dimensional Electronic Correlation and Relaxation Spectra: Theory and Model Calculations. *J. Phys. Chem. A*, **103**, 10489 (1999).

[69] L. P. DeFlores, R. A. Nicodemus, and A. Tokmakoff. Two-Dimensional Fourier Transform Spectroscopy in the Pump-Probe Geometry. *Opt. Lett.*, **32**, 2966 (2007).

[70] W. Tung. *Group Theory in Physics.* World Scientific Publishing Co., Philadelphia (1985).

[71] K. Gottfried and T.-M. Yan. *Quantum Mechanics: Fundamentals.* Springer-Verlag, New York (2003).

[72] O. Golonzka and A. Tokmakoff. Polarization-Selective Third-Order Spectroscopy of Coupled Vibronic States. *J. Chem. Phys.*, **115**, 297 (2001).

[73] L. D. Favro. Theory of the Rotational Brownian Motion of a Free Rigid Body. *Phys. Rev.*, **119**, 53 (1960).

[74] A. Szabo. Theory of Fluorescence Depolarization in Macromolecules and Membranes. *J. Chem. Phys.*, **81**, 150 (1984).

[75] A. Tokmakoff. Orientational Correlation Functions and Polarization Selectivity for Nonlinear Spectroscopy of Isotropic Media. I. Third Order. *J. Chem. Phys.*, **105**, 1 (1996).

[76] B. J. Berne and R. Pecora. *Dynamic Light Scattering.* Dover Publications, Mineola (2000).

[77] P. Hamm, M. Lim, and R. M. Hochstrasser. Structure of the Amide I Band of Peptides Measured by Femtosecond Nonlinear-Infrared Spectroscopy. *J. Phys. Chem. B*, **102**, 6123 (1998).

[78] M. Khalil, N. Demirdöven, and A. Tokmakoff. Coherent 2D IR Spectroscopy: Molecular Structure and Dynamics in Solution. *J. Phys. Chem. A*, **107**, 5258 (2003).

[79] P. Hamm and M. T. Zanni. *Concepts and Methods of 2D Infrared Spectroscopy.* Cambridge UP, Cambridge (2011).

[80] A. W. Albrecht, J. D. Hybl, S. M. G. Faeder, and D. M. Jonas. Experimental Distinction Between Phase Shifts and Time Delays: Implications for Femtosecond Spectroscopy and Coherent Control of Chemical Reactions. *J. Chem. Phys.*, **111**, 10934 (1999).

[81] S. Yan and H. S. Tan. Phase Cycling Schemes for Two-Dimensional Optical Spectroscopy with a Pump-Probe Beam Geometry. *Chem. Phys.*, **360**, 110 (2009).

[82] S. K. Karthick Kumar, A. Tamimi, and M. D. Fayer. Comparisons of 2D IR Measured Spectral Diffusion in Rotating Frames using Pulse Shaping and in the Stationary Frame using the Standard Method. *J. Chem. Phys.*, **137** (2012).

[83] E. B. Wilson Jr., J. Decius, and P. C. Cross. *Molecular Vibrations.* Dover Publications, New York (1980).

[84] M. Khalil and A. Tokmakoff. Signatures of Vibrational Interactions in Coherent Two-Dimensional Infrared Spectroscopy. *Chem. Phys.*, **266**, 213 (2001).

[85] S. Woutersen and P. Hamm. Nonlinear Two-Dimensional Vibrational Spectroscopy of Peptides. *J. Phys. Condens. Matter*, **14**, R1035 (2002).

[86] R. Kubo. Note on the Stochastic Theory of Resonance Absorption. *J. Phys. Soc. Japan*, **9**, 935 (1954).

[87] K. Kwak, S. Park, I. J. Finkelstein, and M. D. Fayer. Frequency-Frequency Correlation Functions and Apodization in Two-Dimensional Infrared Vibrational Echo Spectroscopy: A New Approach. *J. Chem. Phys.*, **127** (2007).

[88] E. E. Fenn and M. D. Fayer. Extracting 2D IR Frequency-Frequency Correlation Functions from Two Component Systems. *J. Chem. Phys.*, **135**, 1 (2011).

[89] S. T. Roberts, J. J. Loparo, and A. Tokmakoff. Characterization of Spectral Diffusion from Two-Dimensional Line Shapes. *J. Chem. Phys.*, **125**, 084502 (2006).

[90] S. Backus, C. G. Durfee, M. M. Murnane, and H. C. Kapteyn. High Power Ultrafast Lasers. *Rev. Sci. Instrum.*, **69**, 1207 (1998).

[91] U. Morgner, F. X. Kärtner, S. H. Cho, Y. Chen, H. a. Haus, J. G. Fujimoto, E. P. Ippen, V. Scheuer, G. Angelow, and T. Tschudi. Sub-Two-Cycle Pulses from a Kerr-Lens Mode-Locked Ti:Sapphire Laser. *Opt. Lett.*, **24**, 411 (1999).

[92] J. Diels and W. Rudolph. *Ultrashort Laser Pulse Phenomena.* Academic Press, San Diego (1996).

[93] D. E. Spence, P. N. Kean, and W. Sibbett. 60-fsec Pulse Generation from a Self-Mode-Locked Ti:Sapphire Laser. *Opt. Lett.*, **16**, 42 (1991).

[94] F. Salin, J. Squier, and M. Piché. Mode locking of Ti:Al_2O_3 Lasers and Self-Focusing: a Gaussian Approximation. *Opt. Lett.*, **16**, 1674 (1991).

[95] P. F. Moulton. Spectroscopic and Laser Characteristics of Ti:Al_2O_3. *J. Opt. Soc. Am. B*, **3**, 125 (1986).

[96] P. Maine, D. Strickland, P. Bado, M. Pessot, and G. Mourou. Generation of Ultrahigh Peak Power Pulses by Chirped Pulse Amplification. *IEEE J. Quantum Electron.*, **24**, 398 (1988).

[97] C. Fecko, J. Loparo, and A. Tokmakoff. Generation of 45 Femtosecond Pulses at 3 μm with a $KNbO_3$ Optical Parametric Amplifier. *Opt. Commun.*, **241**, 521 (2004).

[98] D. N. Nikogosyan. Beta Barium Borate (BBO). *Appl. Phys. A*, **52**, 359 (1991).

[99] V. Dmitriev, G. Gurzadyan, and D. N. Nikogosyan. *Handbook of Nonlinear Optical Crystals*. Springer, New York (1997).

[100] H. H. Li. Refractive Index of Alkali Halides and its Wavelength and Temperature Derivatives. *J. Phys. Chem. Ref. Data*, **5**, 329 (1976).

[101] H. W. Icenogle, B. C. Platt, and W. L. Wolfe. Refractive Indexes and Temperature Coefficients of Germanium and Silicon. *Appl. Opt.*, **15**, 2348 (1976).

[102] R. A. Kaindl, M. Wurm, K. Reimann, P. Hamm, A. M. Weiner, and M. Woerner. Generation, Shaping, and Characterization of Intense Femtosecond Pulses Tunable from 3 to 20 μm. *J. Opt. Soc. Am. B*, **17**, 2086 (2000).

[103] P. Hamm, R. A. Kaindl, and J. Stenger. Noise Suppression in Femtosecond Mid-Infrared Light Sources. *Opt. Lett.*, **25**, 1798 (2000).

[104] P. J. Kupecek, C. A. Schwartz, and D. S. Chemla. Silver Thiogallate ($AgGaS_2$) - Part I: Nonlinear Optical Properties. *IEEE J. Quantum Electron.*, **10**, 540 (1974).

[105] D. J. Cook and R. M. Hochstrasser. Intense Terahertz Pulses by Four-Wave Rectification in Air. *Opt. Lett.*, **25**, 1210 (2000).

[106] P. B. Corkum. Plasma Perspective on Strong Field Multiphoton Ionization. *Phys. Rev. Lett.*, **71**, 1994 (1993).

[107] T. Fuji, T. Horio, and T. Suzuki. Generation of 12 fs Deep-Ultraviolet Pulses by Four-Wave Mixing through Filamentation in Neon Gas. *Opt. Lett.*, **32**, 2481 (2007).

[108] P. B. Petersen and A. Tokmakoff. Source for Ultrafast Continuum Infrared and Terahertz Radiation. *Opt. Lett.*, **35**, 1962 (2010).

[109] C. R. Baiz and K. J. Kubarych. Ultrabroadband Detection of a Mid-IR Continuum by Chirped-Pulse Upconversion. *Opt. Lett.*, **36**, 187 (2011).

[110] M. Cheng, A. Reynolds, H. Widgren, and M. Khalil. Generation of Tunable Octave-Spanning Mid-Infrared Pulses by Filamentation in Gas Media. *Opt. Lett.*, **37**, 1787 (2012).

[111] C. Calabrese, A. M. Stingel, L. Shen, and P. B. Petersen. Ultrafast Continuum Mid-Infrared Spectroscopy: Probing the Entire Vibrational Spectrum in a Single Laser Shot with Femtosecond Time Resolution. *Opt. Lett.*, **37**, 2265 (2012).

[112] C. Xia, Z. Xu, M. N. Islam, F. L. Terry, M. J. Freeman, A. Zakel, and J. Mauricio. 10.5W Time-Averaged Power Mid-IR Supercontinuum Generation Extending Beyond 4 μm With Direct Pulse Pattern Modulation. *IEEE J. Sel. Top. Quantum Electron.*, **15**, 422 (2009).

[113] I. Kubat, C. S. Agger, U. Møller, A. B. Seddon, Z. Tang, S. Sujecki, T. M. Benson, D. Furniss, S. Lamrini, K. Scholle, P. Fuhrberg, B. Napier, M. Farries, J. Ward, P. M. Moselund, and O. Bang. Mid-Infrared Supercontinuum Generation to 12.5 μm in Large NA Chalcogenide Step-Index Fibres Pumped at 4.5 μm. *Opt. Express*, **22**, 19169 (2014).

[114] C. R. Petersen, U. Møller, I. Kubat, B. Zhou, S. Dupont, J. Ramsay, T. Benson, S. Sujecki, N. Abdel-Moneim, Z. Tang, D. Furniss, A. Seddon, and O. Bang. Mid-Infrared Supercontinuum Covering the 1.4–13.3 μm Molecular Fingerprint Region using Ultra-High NA Chalcogenide Step-Index Fibre. *Nat. Photonics*, **8**, 830 (2014).

[115] S. Ashihara and Y. Kawahara. Spectral Broadening of Mid-Infrared Femtosecond Pulses in GaAs. *Opt. Lett.*, **34**, 3839 (2009).

[116] H. Liang, P. Krogen, R. Grynko, O. Novak, C.-L. Chang, G. J. Stein, D. Weerawarne, B. Shim, F. X. Kärtner, and K.-H. Hong. Three-Octave-Spanning Supercontinuum Generation and Sub-Two-Cycle Self-Compression of Mid-Infrared Filaments in Dielectrics. *Opt. Lett.*, **40**, 1069 (2015).

[117] Y. H. Cheng, J. K. Wahlstrand, N. Jhajj, and H. M. Milchberg. The Effect of Long Timescale Gas Dynamics on Femtosecond Filamentation. *Opt. Express*, **21**, 4740 (2013).

[118] K. Ramasesha. *Dynamics of Water and Aqueous Protons Studied using Ultrafast Multi-Dimensional Infrared Spectroscopy.* Ph.D. thesis, Massachusetts Institute of Technology (2013).

[119] W. H. Strehlow and E. L. Cook. Compilation of Energy Band Gaps in Elemental and Binary Compound Semiconductors and Insulators. *J. Phys. Chem. Ref. Data*, **2**, 163 (1973).

[120] L. Bergé, S. Skupin, C. Köhler, I. Babushkin, and J. Herrmann. 3D Numerical Simulations of THz Generation by Two-Color Laser Filaments. *Phys. Rev. Lett.*, **110**, 1 (2013).

[121] K. Y. Kim, A. J. Taylor, J. H. Glownia, and G. Rodriguez. Coherent Control of Terahertz Supercontinuum Generation in Ultrafast LaserGas Interactions. *Nat. Photonics*, **2**, 605 (2008).

[122] F. Théberge, M. Châteauneuf, G. Roy, P. Mathieu, and J. Dubois. Generation of Tunable and Broadband Far-Infrared Laser Pulses During Two-Color Filamentation. *Phys. Rev. A - At. Mol. Opt. Phys.*, **81** (2010).

[123] O. G. Kosareva, N. A. Panov, R. V. Volkov, V. A. Andreeva, A. V. Borodin, M. N. Esaulkov, Y. Chen, C. Marceau, V. A. Makarov, A. P. Shkurinov, A. B. Savel'ev, and S. L. Chin. Analysis of Dual Frequency Interaction in the Filament with the Purpose of Efficiency Control of THz Pulse Generation. *J. Inf. Mill. Thz. Waves*, **32**, 1157 (2011).

[124] Y. Nomura, H. Shirai, K. Ishii, N. Tsurumachi, A. a. Voronin, A. M. Zheltikov, and T. Fuji. Phase-stable Sub-Cycle Mid-Infrared Conical Emission from Filamentation in Gases. *Opt. Express*, **20**, 24741 (2012).

[125] T. Fuji and Y. Nomura. Generation of Phase-Stable Sub-Cycle Mid-Infrared Pulses from Filamentation in Nitrogen. *Appl. Sci.*, **3**, 122 (2013).

[126] M. Kress, T. Löffler, S. Eden, M. Thomson, and H. G. Roskos. Terahertz-Pulse Generation by Photoionization of Air with Laser Pulses Composed of both Fundamental and Second-Harmonic Waves. *Opt. Lett.*, **29**, 1120 (2004).

[127] I. A. Walmsley and C. Dorrer. Characterization of Ultrashort Electromagnetic Pulses. *Adv. Opt. Photonics*, **1**, 308 (2009).

[128] J. H. Parker Jr., D. W. Feldman, and M. Ashkin. Raman Scattering by Silicon and Germanium. *Phys. Rev.*, **155**, 712 (1967).

[129] S. A. Kovalenko, A. L. Dobryakov, J. Ruthmann, and N. P. Ernsting. Femtosecond Spectroscopy of Condensed Phases with Chirped Supercontinuum Probing. *Phys. Rev. A*, **59**, 2369 (1999).

[130] D. Chandler-Horowitz and P. M. Amirtharaj. High-Accuracy, Midinfrared (450 $\mathrm{cm}^{-1} \leq \omega \leq 4000\mathrm{cm}^{-1}$) Refractive Index Values of Silicon. *J. Appl. Phys.*, **97**, 123526 (2005).

[131] N. Demirdöven, M. Khalil, O. Golonzka, and A. Tokmakoff. Dispersion Compensation with Optical Materials for Compression of Intense Sub-100-fs Mid-Infrared Pulses. *Opt. Lett.*, **27**, 433 (2002).

[132] P. Hariharan. *Basics of Interferometry.* Academic Press, San Diego, 2nd edition (2007).

[133] L. Mertz. Auxiliary Computation for Fourier Spectrometry. *Infrared Phys.*, **7**, 17 (1967).

[134] S. T. Roberts, J. J. Loparo, K. Ramasesha, and A. Tokmakoff. A Fast-Scanning Fourier Transform 2D IR Interferometer. *Opt. Commun.*, **284**, 1062 (2011).

[135] A. Siegman. *Lasers.* University Science Books, Sausalito (1986).

[136] M. K. Yetzbacher, N. Belabas, K. A. Kitney, and D. M. Jonas. Propagation, Beam Geometry, and Detection Distortions of Peak Shapes in Two-Dimensional Fourier Transform Spectra. *J. Chem. Phys.*, **126**, 044511 (2007).

[137] K. C. Jones, Z. Ganim, C. S. Peng, and A. Tokmakoff. Transient Two-Dimensional Spectroscopy with Linear Absorption Corrections Applied to Temperature-Jump Two-Dimensional Infrared. *J. Opt. Soc. Am. B*, **29**, 118 (2012).

[138] R. Bloem, S. Garrett-Roe, H. Strzalka, P. Hamm, and P. Donaldson. Enhancing Signal Detection and Completely Eliminating Scattering using Quasi-Phase-Cycling in 2D IR Experiments. *Opt. Express*, **18**, 27067 (2010).

[139] S.-I. Mizushima, T. Simanouti, S. Nagakura, K. Kuratani, M. Tsuboi, H. Baba, and O. Fujioka. The Structure of N-Methylacetamide. *J. Am. Chem. Soc.*, **72**, 3490 (1950).

[140] T. Miyazawa, T. Shimanouchi, and S.-i. Mizushima. Normal Vibrations of N-Methylacetamide. *J. Chem. Phys.*, **29**, 611 (1958).

[141] H. Torii. Electrostatic Origin of the Cooperative Effect on the CO Bond Lengths and the Amide I Vibrational Frequencies of the N-Methylacetamide Oligomers. *J. Mol. Struct.*, **735-736**, 21 (2005).

[142] S. Ham, J. H. Kim, H. Lee, and M. Cho. Correlation Between Electronic and Molecular Structure Distortions and Vibrational Properties. II. Amide I Modes of NMA-nD_2O Complexes. *J. Chem. Phys.*, **118**, 3491 (2003).

[143] T. La Cour Jansen, A. G. Dijkstra, T. M. Watson, J. D. Hirst, and J. Knoester. Modeling the Amide I Bands of Small Peptides. *J. Chem. Phys.*, **125** (2006).

[144] L. Wang, C. T. Middleton, M. T. Zanni, and J. L. Skinner. Development and Validation of Transferable Amide I Vibrational Frequency Maps for Peptides. *J. Phys. Chem. B*, **115**, 3713 (2011).

[145] M. Reppert, A. R. Roy, and A. Tokmakoff. Isotope-Enriched Protein Standards for Computational Amide I Spectroscopy. *J. Chem. Phys.*, **142** (2015).

[146] R. Jimenez, G. R. Fleming, P. V. Kumar, and M. Maroncelli. Femtosecond Solvation Dynamics of Water. *Nature*, **369**, 471 (1994).

[147] G. R. Fleming and M. Cho. Chromophore-Solvent Dynamics. *Annu. Rev. Phys. Chem.*, **47**, 109 (1996).

[148] W. P. de Boeij, M. S. Pshenichnikov, and D. A. Wiersma. Ultrafast Solvation Dynamics Explored by Femtosecond Photon Echo Spectroscopies. *Annu. Rev. Phys. Chem.*, **49**, 99 (1998).

[149] P. Abbyad, W. Childs, X. Shi, and S. G. Boxer. Dynamic Stokes Shift in Green Fluorescent Protein Variants. *Proc. Natl. Acad. Sci. U. S. A.*, **104**, 20189 (2007).

[150] D. F. Underwood and D. A. Blank. Ultrafast Solvation Dynamics : A View from the Solvent's Perspective Using a Novel Resonant-Pump, Nonresonant-Probe Technique. *J. Phys. Chem. A*, **107**, 956 (2003).

[151] S. Park, J. Kim, and N. F. Scherer. Two-Dimensional Measurements of the Solvent Structural Relaxation Dynamics in Dipolar Solvation. *Phys. Chem. Chem. Phys.*, **14**, 8116 (2012).

[152] G. Otting, E. Liepinsh, and K. Wüthrich. Protein Hydration in Aqueous Solution. *Science*, **254**, 974 (1991).

[153] G. M. Clore, A. Bax, P. T. Wingfield, and A. M. Gronenborn. Identification and Localization of Bound Internal Water in the Solution Structure of Interleukin 1β by Heteronuclear Three-Dimensional ^{1}H Rotating-Frame Overhauser ^{15}N–^{1}H Multiple Quantum Coherence NMR Spectroscopy. *Biochemistry*, **29**, 5671 (1990).

[154] H. Kovacs, T. Agback, and J. Isaksson. Probing Water-Protein Contacts in a MMP-12/CGS27023A Complex by Nuclear Magnetic Resonance Spectroscopy. *J. Biomol. NMR*, **53**, 85 (2012).

[155] L. De Marco, M. Thämer, M. Reppert, and A. Tokmakoff. Direct Observation of Intermolecular Interactions Mediated by Hydrogen Bonding. *J. Chem. Phys.*, **141**, 034502 (2014).

[156] M. Akiyama and T. Ohtani. Hydrogen Bonding of N-Methylacetamide in $CDCl_3$, Solution Studied by NMR and IR Spectra. *Spectrochim. Acta, Part A Mol. Biomol. Spectrosc.*, **50**, 317 (1994).

[157] N. A. Besley. Ab Initio Modeling of Amide Vibrational Bands in Solution. *J. Phys. Chem. A*, **108**, 10794 (2004).

[158] L. P. DeFlores, Z. Ganim, S. F. Ackley, H. S. Chung, and A. Tokmakoff. The Anharmonic Vibrational Potential and Relaxation Pathways of the Amide I and II. *J. Phys. Chem. B*, **110**, 18973 (2006).

[159] M. Barthes. Optical Anomalies in Acetanilide: Davydov Solitons, Localised Modes, or Fermi Resonance? *J. Mol. Liq.*, **41**, 143 (1989).

[160] J. Edler and P. Hamm. Spectral Response of Crystalline Acetanilide and N-Methylacetamide: Vibrational Self-Trapping in Hydrogen-Bonded Crystals. *Phys. Rev. B*, **69**, 214301 (2004).

[161] M. Davies and D. K. Thomas. Energies And Entropies Of Association For Amides In Benzene Solutions. Part II. *J. Phys. Chem.*, **60**, 767 (1956).

[162] L. a. LaPlanche, H. B. Thompson, and M. T. Rogers. Chain Association Equilibria. A Nuclear Magnetic Resonance Study of the Hydrogen Bonding of N-Monosubstituted Amides. *J. Phys. Chem.*, **69**, 1482 (1965).

[163] Y. Liu, M. A. Czarnecki, and Y. Ozaki. Fourier Transform Near-Infrared Spectra of N-methylacetamide: Dissociation and Thermodynamic Properties in Pure Liquid Form and in CCl4 Solutions. *Appl. Spectrosc.*, **48**, 1095 (1994).

[164] I. M. Klotz and J. S. Franzen. Hydrogen Bonds between Model Peptide Groups in Solution. *J. Am. Chem. Soc.*, **84**, 3461 (1962).

[165] S. E. Krikorian. Determination of Dimerization Constants of Cis- and Trans-Configured Secondary Amides Using Near-Infrared Spectroscopy. *J. Phys. Chem.*, **86**, 1875 (1982).

[166] H. Minami and M. Iwahashi. Molecular Self-Assembling of N-Methylacetamide in Solvents. *Int. J. Spectrosc.*, **2011**, 1 (2011).

[167] J. J. Loparo, S. T. Roberts, R. A. Nicodemus, and A. Tokmakoff. Variation of the Transition Dipole Moment Across the OH Stretching Band of Water. *Chem. Phys.*, **341**, 218 (2007).

[168] S. A. Corcelli and J. L. Skinner. Infrared and Raman Line Shapes of Dilute HOD in Liquid H_2O and D_2O from 10 to 90°C. *J. Phys. Chem. A*, **109**, 6154 (2005).

[169] T. Hayashi, W. Zhuang, and S. Mukamel. Electrostatic DFT Map for the Complete Vibrational Amide Band of NMA. *J. Phys. Chem. A*, **109**, 9747 (2005).

[170] W. H. Moore and S. Krimm. Vibrational Analysis of Peptides, Polypeptides, and Proteins. I. Polyglycine I. *Biopolymers*, **15**, 2439 (1976).

[171] S.-H. Lee, N. G. Mirkin, and S. Krimm. A Quantitative Anharmonic Analysis of the Amide A Band in α-Helical Poly(L-Alanine). *Biopolymers*, **49**, 195 (1999).

[172] J. Bandekar. Amide Modes and Protein Conformation. *Biochim. Bophysica Acta*, **1120**, 123 (1992).

[173] J. B. Asbury, T. Steinel, and M. D. Fayer. Vibrational Echo Correlation Spectroscopy Probes of Hydrogen Bond Dynamics in Water and Methanol. *J. Lumin.*, **107**, 271 (2004).

[174] I. V. Rubtsov, J. Wang, and R. M. Hochstrasser. Dual Frequency 2D-IR of Peptide Amide-A and Amide-I Modes. *J. Chem. Phys.*, **118**, 7733 (2003).

[175] H. L. Frisch and G. L. Vidale. Coupled Anharmonic Vibrations as a Cause of Broadening of Spectral Bands: Hydrogen Bonded Systems. *J. Chem. Phys.*, **25**, 982 (1956).

[176] R. G. Snyder and J. R. Scherer. Band Structure in the CH Stretching Region of the Raman Spectrum of the Extended Polymethylene Chain: Influence of Fermi Resonance. *J. Chem. Phys.*, **71**, 3221 (1979).

[177] H. Wolff and E. Wolff. Hydrogen Bonding and Fermi Resonance of n-Propylamine. Comparison of the Results from IR and Raman Measurements. *Spectrochim. Acta*, **44A**, 1273 (1988).

[178] Y. Maréchal. Infrared Spectra of Water. I. Effect of Temperature and of H/D Isotopic Dilution. *J. Chem. Phys.*, **95**, 5565 (1991).

[179] E. Fermi. Über den Ramaneffekt des Kohlendioxyds. *Z. Phys.*, **71**, 250 (1931).

[180] J. Monecke. Theory of Fermi Resonances in Raman and Infrared Spectra. **18**, 477 (1987).

[181] M. Schwartz and C. Wang. Raman study of Fermi resonance, hydrogen bonding, and molecular reorientation in liquid ammonia. *J. Chem. Phys.*, **59**, 5258 (1973).

[182] J. Li, H. Bian, X. Wen, H. Chen, K. Yuan, and J. Zheng. Probing Ion/Molecule Interactions in Aqueous Solutions with Vibrational Energy Transfer. *J. Phys. Chem. B*, **116**, 12284 (2012).

[183] J. Li, H. Bian, H. Chen, X. Wen, B. T. Hoang, and J. Zheng. Ion Association in Aqueous Solutions Probed through Vibrational Energy Transfers among Cation, Anion, and Water Molecules. *J. Phys. Chem. B*, **117**, 4274 (2013).

[184] M. Ji and K. J. Gaffney. Orientational Relaxation Dynamics in Aqueous Ionic Solution: Polarization-Selective Two-Dimensional Infrared Study of Angular Jump-Exchange Dynamics in Aqueous 6M $NaClO_4$. *J. Chem. Phys.*, **134**, 044516 (2011).

[185] I. V. Rubtsov, K. Kumar, and R. M. Hochstrasser. Dual-Frequency 2D IR Photon Echo of a Hydrogen Bond. *Chem. Phys. Lett.*, **402**, 439 (2005).

[186] T. Elsaesser. Two-Dimensional Infrared Spectroscopy of Intermolecular Hydrogen Bonds in the Condensed Phase. *Acc. Chem. Res.*, **42**, 1220 (2009).

[187] A. M. Stingel, C. Calabrese, and P. B. Petersen. Strong Intermolecular Vibrational Coupling through Cyclic Hydrogen-Bonded Structures Revealed by Ultrafast Continuum Mid-IR Spectroscopy. *J. Phys. Chem. B*, **117**, 15714 (2013).

[188] A. Barth and C. Zscherp. What Vibrations tell about Proteins. *Q. Rev. Biophys.*, **35**, 369 (2002).

[189] H. van Amerongen, L. Valkunas, and R. van Grondelle. *Photosynthetic Excitons.* World Scientific Publishing Co., Singapore (2000).

[190] K. Ramasesha, L. De Marco, A. Mandal, and A. Tokmakoff. Water Vibrations have Strongly Mixed Intra- and Intermolecular Character. *Nat. Chem.*, **5**, 935 (2013).

[191] F. Perakis, J. A. Borek, and P. Hamm. Three-Dimensional Infrared Spectroscopy of Isotope-Diluted Ice $\mathrm{I_h}$. *J. Chem. Phys.*, **139**, 014501 (2013).

[192] K.-K. Lee, K.-H. Park, S. Park, S.-J. Jeon, and M. Cho. Polarization-Angle-Scanning 2DIR Spectroscopy of Coupled Anharmonic Oscillators: a Polarization Null Angle Method. *J. Phys. Chem. B*, **115**, 5456 (2011).

[193] T. Miyazawa. Perturbation Treatment of the Characteristic Vibrations of Polypeptide Chains in Various Configurations. *J. Chem. Phys.*, **32**, 1647 (1960).

[194] T. Miyazawa and E. R. Blout. The Infrared Spectra of Polypeptides in Various Conformations: Amide I and II Bands 1. *J. Am. Chem. Soc.*, **83**, 712 (1961).

[195] C. M. Cheatum, A. Tokmakoff, and J. Knoester. Signatures of β-Sheet Secondary Structures in Linear and Two-Dimensional Infrared Spectroscopy. *J. Chem. Phys.*, **120**, 8201 (2004).

[196] L. De Marco, K. Ramasesha, and A. Tokmakoff. Experimental Evidence of Fermi Resonances in Isotopically Dilute Water from Ultrafast Broadband IR Spectroscopy. *J. Phys. Chem. B*, **117**, 15319 (2013).

[197] G. Gale, G. Gallot, F. Hache, N. Lascoux, S. Bratos, and J.-C. Leicknam. Femtosecond Dynamics of Hydrogen Bonds in Liquid Water: A Real Time Study. *Phys. Rev. Lett.*, **82**, 1068 (1999).

[198] S. Knop, T. L. C. Jansen, J. Lindner, and P. Vöhringer. On the Nature of OH-Stretching Vibrations in Hydrogen-Bonded Chains: Pump Frequency Dependent Vibrational Lifetime. *Phys. Chem. Chem. Phys.*, **13**, 4641 (2011).

[199] A. J. Lock, S. Woutersen, and H. J. Bakker. Ultrafast Energy Equilibration in Hydrogen-Bonded Liquids. *J. Phys. Chem. A*, **105**, 1238 (2001).

[200] D. J. Shaw, M. R. Panman, and S. Woutersen. Evidence for Cooperative Vibrational Relaxation of the NH-, OH-, and OD-Stretching Modes in Hydrogen-Bonded Liquids Using Infrared Pump-Probe Spectroscopy. *Phys. Rev. Lett.*, **103**, 1 (2009).

[201] L. P. DeFlores and A. Tokmakoff. Water Penetration into Protein Secondary Structure Revealed by Hydrogen-Deuterium Exchange Two-Dimensional Infrared Spectroscopy. *J. Am. Chem. Soc.*, **128**, 16520 (2006).

[202] A. Nitzan. *Chemical Dynamics in Condensed Phases.* Oxford University Press, New York (2006).

[203] L. Friedman and V. J. Shiner Jr. Experimental Determination of the Disproportionation of Hydrogen Isotopes in Water. *J. Chem. Phys.*, **44**, 4639 (1966).

[204] A. J. Kresge and Y. Chiang. Hydrogen Isotope Disproportionation in Water and its Effect on Isotope-Exchange Equilibrium Constants Measured in Aqueous Solution. *J. Chem. Phys.*, **49**, 1439 (1968).

[205] F. O. Libnau, A. A. Christy, and O. M. Kvalheim. Determination of the Equilibrium Constant and Resolution of the HOD Spectrum by Alternating Least-Squares and Infrared Analysis. *Appl. Spectrosc.*, **49**, 1431 (1995).

[206] M. Wolfsberg, A. A. Massa, and J. Pyper. Effect of Vibrational Anharmonicity on the Isotopic Self-Exchange Equilibria $H_2X+D_2X=2HDX$. *J. Chem. Phys.*, **53**, 3138 (1970).

[207] S. A. Corcelli, C. P. Lawrence, and J. L. Skinner. Combined Electronic Structure/Molecular Dynamics Approach for Ultrafast Infrared Spectroscopy of Dilute HOD in Liquid H_2O and D_2O. *J. Chem. Phys.*, **120**, 8107 (2004).

[208] M. Falk. Frequencies of H-O-H, H-O-D, and D-O-D Bending Fundamentals in Liquid Water. *J. Raman Spectrosc.*, **21**, 563 (1990).

[209] H. J. Bakker and J. L. Skinner. Vibrational spectroscopy as a probe of structure and dynamics in liquid water. *Chem. Rev.*, **110**, 1498 (2010).

[210] H. Graener, G. Seifert, and A. Laubereau. New Spectroscopy of Water Using Tunable Picosecond Pulses in the Infrared. *Phys. Rev. Lett.*, **66**, 2092 (1991).

[211] R. Laenen, C. Rauscher, and A. Laubereau. Local Substructures of Water Studied by Transient Hole-Burning Spectroscopy in the Infrared: Dynamics and Temperature Dependence. *J. Phys. Chem. B*, **102**, 9304 (1998).

[212] S. Woutersen, U. Emmerichs, and H. J. Bakker. Femtosecond Mid-IR Pump-Probe Spectroscopy of Liquid Water: Evidence for a Two-Component Structure. *Science*, **278**, 658 (1997).

[213] S. Woutersen, U. Emmerichs, H.-K. Nienhuys, and H. Bakker. Anomalous Temperature Dependence of Vibrational Lifetimes in Water and Ice. *Phys. Rev. Lett.*, **81**, 1106 (1998).

[214] G. M. Gale, G. Gallot, and N. Lascoux. Frequency-Dependent Vibrational Population Relaxation Time of the OH Stretching Mode in Liquid Water. *Chem. Phys. Lett.*, **311**, 123 (1999).

[215] T. Steinel, J. B. Asbury, J. Zheng, and M. D. Fayer. Watching Hydrogen Bonds Break: A Transient Absorption Study of Water. *J. Phys. Chem. A*, **108**, 10957 (2004).

[216] H.-K. Nienhuys, S. Woutersen, R. A. van Santen, and H. J. Bakker. Mechanism for Vibrational Relaxation in Water Investigated by Femtosecond Infrared Spectroscopy. *J. Chem. Phys.*, **111**, 1494 (1999).

[217] H. J. Bakker, H.-K. Nienhuys, G. Gallot, N. Lascoux, G. M. Gale, J.-C. Leicknam, and S. Bratos. Transient Absorption of Vibrationally Excited Water. *J. Chem. Phys.*, **116**, 2592 (2002).

[218] J. C. Deàk, S. T. Rhea, L. K. Iwaki, and D. D. Dlott. Vibrational Energy Relaxation and Spectral Diffusion in Water and Deuterated Water. *J. Phys. Chem. A*, **104**, 4866 (2000).

[219] Z. Wang, A. Pakoulev, Y. Pang, and D. D. Dlott. Vibrational Substructure in the OH Stretching Transition of Water and HOD. *J. Phys. Chem. A*, **108**, 9054 (2004).

[220] P. Bodis, O. F. A. Larsen, and S. Woutersen. Vibrational Relaxation of the Bending Mode of HDO in Liquid D_2O. *J. Phys. Chem. A*, **109**, 5303 (2005).

[221] J. Stenger, D. Madsen, P. Hamm, E. Nibbering, and T. Elsaesser. Ultrafast Vibrational Dephasing of Liquid Water. *Phys. Rev. Lett.*, **87**, 027401 (2001).

[222] S. Yeremenko, M. S. Pshenichnikov, and D. A. Wiersma. Hydrogen-Bond Dynamics in Water Explored by Heterodyne-Detected Photon Echo. *Chem. Phys. Lett.*, **369**, 107 (2003).

[223] J. Loparo, C. Fecko, J. Eaves, S. Roberts, and A. Tokmakoff. Reorientational and Configurational Fluctuations in Water Observed on Molecular Length Scales. *Phys. Rev. B*, **70**, 180201 (2004).

[224] C. J. Fecko, J. J. Loparo, S. T. Roberts, and A. Tokmakoff. Local Hydrogen Bonding Dynamics and Collective Reorganization in Water: Ultrafast Infrared Spectroscopy of HOD/D_2O. *J. Chem. Phys.*, **122**, 54506 (2005).

[225] J. D. Eaves, J. J. Loparo, C. J. Fecko, S. T. Roberts, A. Tokmakoff, and P. L. Geissler. Hydrogen Bonds in Liquid Water are Broken Only Fleetingly. *Proc. Natl. Acad. Sci. U. S. A.*, **102**, 13019 (2005).

[226] S. T. Roberts, K. Ramasesha, and A. Tokmakoff. Structural Rearrangements in Water Viewed Through Two-Dimensional Infrared Spectroscopy. *Acc. Chem. Res.*, **42**, 1239 (2009).

[227] C. Petersen, A. A. Bakulin, V. G. Pavelyev, M. S. Pshenichnikov, and H. J. Bakker. Femtosecond Midinfrared Study of Aggregation Behavior in Aqueous Solutions of Amphiphilic Molecules. *J. Chem. Phys.*, **133** (2010).

[228] A. A. Bakulin, M. S. Pshenichnikov, H. J. Bakker, and C. Petersen. Hydrophobic Molecules Slow Down the Hydrogen-Bond Dynamics of Water. *J. Phys. Chem. A*, **115**, 1821 (2011).

[229] T. Steinel, J. B. Asbury, S. A. Corcelli, C. P. Lawrence, J. L. Skinner, and M. D. Fayer. Water Dynamics: Dependence on Local Structure Probed with Vibrational Echo Correlation Spectroscopy. *Chem. Phys. Lett.*, **386**, 295 (2004).

[230] R. A. Nicodemus, K. Ramasesha, S. T. Roberts, and A. Tokmakoff. Hydrogen bond rearrangements in water probed with temperature-dependent 2D IR. *J. Phys. Chem. Lett.*, **1**, 1068 (2010).

[231] R. A. Nicodemus, S. A. Corcelli, J. L. Skinner, and A. Tokmakoff. Collective Hydrogen Bond Reorganization in Water Studied with Temperature-Dependent Ultrafast Infrared Spectroscopy. *J. Phys. Chem. B*, **115**, 5604 (2011).

[232] Y. L. A. Rezus and H. J. Bakker. On the Orientational Relaxation of HDO in Liquid Water. *J. Chem. Phys.*, **123**, 114502 (2005).

[233] Y. L. A. Rezus and H. J. Bakker. Strong Slowing Down of Water Reorientation in Mixtures of Water and Tetramethylurea. *J. Phys. Chem. A*, **112**, 2355 (2008).

[234] D. E. Moilanen, E. E. Fenn, Y.-S. Lin, J. L. Skinner, B. Bagchi, and M. D. Fayer. Water Inertial Reorientation: Hydrogen Bond Strength and the Angular Potential. *Proc. Natl. Acad. Sci. U. S. A.*, **105**, 5295 (2008).

[235] S. Park, M. Odelius, and K. J. Gaffney. Ultrafast Dynamics of Hydrogen Bond Exchange in Aqueous Ionic Solutions. *J. Phys. Chem. B*, **113**, 7825 (2009).

[236] K. Ramasesha, S. T. Roberts, R. A. Nicodemus, A. Mandal, and A. Tokmakoff. Ultrafast 2D IR Anisotropy of Water Reveals Reorientation During Hydrogen-Bond Switching. *J. Chem. Phys.*, **135**, 054509 (2011).

[237] A. Rahman and F. H. Stillinger. Molecular Dynamics Study of Liquid Water. *J. Chem. Phys.*, **55**, 3336 (1971).

[238] B. Guillot. A Reappraisal of what we have Learned During Three Decades of Computer Simulations on Water. *J. Mol. Liq.*, **101**, 219 (2002).

[239] H. J. C. Berendsen, J. R. Grigera, and T. P. Straatsma. The Missing Term in Effective Pair Potentials. *J. Phys. Chem.*, **91**, 6269 (1987).

[240] J. Skinner, B. Auer, and Y. Lin. Vibrational Line Shapes, Spectral Diffusion, and Hydrogen Bonding in Liquid Water. In *Adv. Chem. Phys.*, volume 142, 59. John Wiley & Sons (2009).

[241] J. C. Lavalley and N. Sheppard. Anharmonicity of CH_3 Deformation Vibrations and Fermi Resonance between the Symmetrical CH_3 Stretching Mode and Overtones of CH_3 Deformation Vibrations. *Spectrochim. Acta*, **28A**, 2091 (1972).

[242] D. F. Smith Jr. and J. Overend. Anharmonic Force Constants of Water. *Spectrochim. Acta, Part A Mol. Biomol. Spectrosc.*, **28**, 471 (1972).

[243] J. D. Worley and I. M. Klotz. Near-Infrared Spectra of H_2O–D_2O Solutions. *J. Chem. Phys.*, **45**, 2868 (1966).

[244] B. Auer, R. Kumar, J. R. Schmidt, and J. L. Skinner. Hydrogen Bonding and Raman, IR, and 2D-IR Spectroscopy of Dilute HOD in Liquid D_2O. *Proc. Natl. Acad. Sci. U. S. A.*, **104**, 14215 (2007).

[245] H. J. Bakker and H.-K. Nienhuys. Delocalization of Protons in Liquid Water. *Science*, **297**, 587 (2002).

[246] J. R. Fair, O. Votava, and D. J. Nesbitt. OH Stretch Overtone Spectroscopy and Transition Dipole Alignment of HOD. *J. Chem. Phys.*, **108**, 72 (1998).

[247] D. E. Khoshtariya, T. D. Dolidze, P. Lindqvist-Reis, A. Neubrand, and R. van Eldik. Liquid Water (D_2O): A Dynamic Model Emerging from Near-Infrared DOD Stretching Overtone Studies. *J. Mol. Liq.*, **96-97**, 45 (2002).

[248] H. R. Wyss and M. Falk. Infrared Spectrum of HDO in Water and in NaCl Solution. *Can. J. Chem.*, **48**, 607 (1970).

[249] J. Savolainen, S. Ahmed, and P. Hamm. Two-Dimensional Raman-THz Spectroscopy of Water. *Proc. Natl. Acad. Sci.*, **110**, 20402 (2013).

[250] F. Perakis, L. De Marco, A. Shalit, F. Tang, Z. R. Kann, T. D. Kühne, R. Torre, M. Bonn, and Y. Nagata. Vibrational Spectroscopy and Dynamics of Water. *Chem. Rev.*, DOI: 10.1021/acs.chemrev.5b00640 (2016).

[251] S. Woutersen and H. J. Bakker. Resonant Intermolecular Transfer of Vibrational Energy in Liquid Water. *Nature*, **402**, 507 (1999).

[252] A. J. Lock and H. J. Bakker. Temperature Dependence of Vibrational Relaxation in Liquid H_2O. *J. Chem. Phys.*, **117**, 1708 (2002).

[253] A. Pakoulev, Z. Wang, and D. D. Dlott. Vibrational Relaxation and Spectral Evolution Following Ultrafast OH Stretch Excitation of Water. *Chem. Phys. Lett.*, **371**, 594 (2003).

[254] M. L. Cowan, B. D. Bruner, N. Huse, J. R. Dwyer, B. Chugh, E. T. J. Nibbering, T. Elsaesser, and R. J. D. Miller. Ultrafast Memory Loss and Energy Redistribution in the Hydrogen Bond Network of Liquid H_2O. *Nature*, **434**, 199 (2005).

[255] D. Kraemer, M. L. Cowan, A. Paarmann, N. Huse, E. T. J. Nibbering, T. Elsaesser, and R. J. D. Miller. Temperature Dependence of the Two-Dimensional Infrared Spectrum of Liquid H_2O. *Proc. Natl. Acad. Sci. U.S.A.*, **105**, 437 (2008).

[256] J. Lindner, P. Vöhringer, M. S. Pshenichnikov, D. Cringus, D. A. Wiersma, and M. Mostovoy. Vibrational Relaxation of Pure Liquid Water. *Chem. Phys. Lett.*, **421**, 563 (2006).

[257] J. Lindner, D. Cringus, M. S. Pshenichnikov, and P. Vöhringer. Anharmonic Bend-Stretch Coupling in Neat Liquid Water. *Chem. Phys.*, **341**, 326 (2007).

[258] A. Paarmann, T. Hayashi, S. Mukamel, and R. J. D. Miller. Nonlinear Response of Vibrational Excitons: Simulating the Two-Dimensional Infrared Spectrum of Liquid Water. *J. Chem. Phys.*, **130**, 204110 (2009).

[259] M. Yang, F. Li, and J. L. Skinner. Vibrational Energy Transfer and Anisotropy Decay in Liquid Water: Is the Förster Model Valid? *J. Chem. Phys.*, **135** (2011).

[260] J. J. Max and C. Chapados. Isotope Effects in Liquid Water by Infrared Spectroscopy. III. H_2O and D_2O spectra from 6000 to 0 cm^{-1}. *J. Chem. Phys.*, **131**, 0 (2009).

[261] Venyaminov S. Y. and F. G. Prendergast. Water (H_2O and D_2O) Molar Absorptivity in the 1000–4000 cm^{-1} Range and Quantitative Infrared Spectroscopy of Aqueous Solutions. *Anal. Biochem.*, **248**, 234 (1997).

[262] G. E. Walrafen. Raman Spectral Studies of Water Structure. *J. Chem. Phys.*, **40**, 3249 (1964).

[263] C. Rønne, P.-O. Åstrand, and S. Keiding. THz Spectroscopy of Liquid H_2O and D_2O. *Phys. Rev. Lett.*, **82**, 2888 (1999).

[264] F. O. Libnau, O. M. Kvalheim, A. A. Christy, and J. Toft. Spectra of Water in the Near- and Mid- Infrared Region. *Vib. Spec.*, **7**, 243 (1994).

[265] T. L. C. Jansen, B. M. Auer, M. Yang, and J. L. Skinner. Two-dimensional Infrared Spectroscopy and Ultrafast Anisotropy Decay of Water. *J. Chem. Phys.*, **132** (2010).

[266] D. W. Oxtoby and S. A. Rice. On Vibrational Relaxation in Liquids. *Chem. Phys. Lett.*, **42**, 1 (1976).

[267] F. Perakis, S. Widmer, and P. Hamm. Two-Dimensional Infrared Spectroscopy of Isotope-Diluted Ice I_h. *J. Chem. Phys.*, **134**, 204505 (2011).

[268] N. Huse, S. Ashihara, E. T. Nibbering, and T. Elsaesser. Ultrafast Vibrational Relaxation of OH Bending and Librational Excitations in Liquid H_2O. *Chem. Phys. Lett.*, **404**, 389 (2005).

[269] S. Ashihara, N. Huse, A. Espagne, E. Nibbering, and T. Elsaesser. Vibrational Couplings and Ultrafast Relaxation of the OH Bending Mode in Liquid H_2O. *Chem. Phys. Lett.*, **424**, 66 (2006).

[270] O. F. A. Larsen and S. Woutersen. Vibrational Relaxation of the H_2O Bending Mode in Liquid Water. *J. Chem. Phys.*, **121**, 12143 (2004).

[271] K. J. Gaffney, P. H. Davis, I. R. Piletic, N. E. Levinger, and M. D. Fayer. Hydrogen Bond Dissociation and Reformation in Methanol Oligomers Following Hydroxyl Stretch Relaxation. *J. Phys. Chem. A*, **106**, 12012 (2002).

[272] W. M. Haynes. *CRC Handbook of Chemistry and Physics, 95th Edition.* CRC Press (2014).

[273] D. J. Nesbitt and R. W. Field. Vibrational Energy Flow in Highly Excited Molecules : Role of Intramolecular Vibrational Redistribution. *J. Phys. Chem.*, **100**, 12735 (1996).

[274] V. May and O. Kühn. *Charge and Energy Transfer Dynamics in Molecular Systems.* Wiley-VCH, 2nd edition (2004).

[275] P. W. Anderson. Absence of Diffusion in Certain Random Lattices. *Phys. Rev.*, **109**, 1492 (1958).

[276] J. Berges, S. Borsányi, and C. Wetterich. Prethermalization. *Phys. Rev. Lett.*, **93**, 14 (2004).

[277] B. Bertini, F. H. L. Essler, S. Groha, and N. J. Robinson. Prethermalization and Thermalization in Models with Weak Integrability Breaking. *Phys. Rev. Lett.*, **115**, 1 (2015).

[278] P. Hamm and G. Stock. Vibrational Conical Intersections as a Mechanism of Ultrafast Vibrational Relaxation. *Phys. Rev. Lett.*, **109**, 173201 (2012).

[279] P. Hamm and G. Stock. Nonadiabatic Vbrational Dynamics in the $HCO_2^- \cdot H_2O$ Complex. *J. Chem. Phys.*, **143** (2015).

[280] P. Hamm and G. Stock. Vibrational Conical Intersections in the Water Dimer. *Mol. Phys.*, **111**, 2046 (2013).

[281] S. T. van der Post, C.-S. Hsieh, M. Okuno, Y. Nagata, H. J. Bakker, M. Bonn, and J. Hunger. Strong Frequency Dependence of Vibrational Relaxation in Bulk and Surface Water Reveals Sub-Picosecond Structural Heterogeneity. *Nat. Commun.*, **6**, 8384 (2015).

[282] S. Imoto, S. S. Xantheas, and S. Saito. Ultrafast Dynamics of Liquid Water: Frequency Fluctuations of the OH Stretch and the HOH Bend. *J. Chem. Phys.*, **139** (2013).

[283] R. Nandkishore and D. A. Huse. Many-Body Localization and Thermalization in Quantum Statistical Mechanics. *Annu. Rev. Condens. Matter Phys.*, **6**, 15 (2015).

[284] J. T. King, C. R. Baiz, and K. J. Kubarych. Solvent-Dependent Spectral Diffusion in a Hydrogen Bonded “Vibrational Aggregate”. *J. Phys. Chem. A*, **114**, 10590 (2010).

[285] V. V. Volkov, D. J. Palmer, and R. Righini. Heterogeneity of Water at the Phospholipid Membrane Interface. *J. Phys. Chem. B*, **111**, 1377 (2007).

[286] L. Piatkowski, K. B. Eisenthal, and H. J. Bakker. Ultrafast Intermolecular Energy Transfer in Heavy Water. *Phys. Chem. Chem. Phys.*, **11**, 9033 (2009).

[287] L. De Marco, W. Carpenter, R. Biswas, H. Liu, J. M. Bowman, and A. Tokmakoff. Differences in the Vibrational Dynamics of H_2O and D_2O: Observation of Symmetric and Antisymmetric Stretching Vibrations in Heavy Water. *J. Phys. Chem. Lett.*, **7**, 1769 (2016).

[288] B. Chen, I. Ivanov, M. L. Klein, and M. Parrinello. Hydrogen Bonding in Water. *Phys. Rev. Lett.*, **91**, 215503 (2003).

[289] A. K. Soper and C. J. Benmore. Quantum Differences Between Heavy and Light Water. *Phys. Rev. Lett.*, **101**, 1 (2008).

[290] J. H. Choi and M. Cho. Computational IR Spectroscopy of Water: OH Stretch Frequencies, Transition Dipoles, and Intermolecular Vibrational Coupling Constants. *J. Chem. Phys.*, **138**, 174108 (2013).

[291] A. C. Belch and S. A. Rice. The OH Stretching Spectrum of Liquid Water: A Random Network Model Interpretation. *J. Chem. Phys.*, **78**, 4817 (1983).

[292] J. G. Davis, K. P. Gierszal, P. Wang, and D. Ben-Amotz. Water Structural Transformation at Molecular Hydrophobic Interfaces. *Nature*, **491**, 582 (2012).

[293] M. G. Sceats and S. A. Rice. The Intramolecular Potential of Water Molecules Engaged in Hydrogen Bonding from Analysis of the Overtone Spectrum of Ice I. *J. Chem. Phys.*, **71**, 973 (1979).

[294] H. Torii. Time-Domain Calculations of the Polarized Raman Spectra, the Transient Infrared Absorption Anisotropy, and the Extent of Delocalization of the OH Stretching Mode of Liquid Water. *J. Phys. Chem. A*, **110**, 9469 (2006).

[295] A. Paarmann, T. Hayashi, S. Mukamel, and R. J. D. Miller. Probing Intermolecular Couplings in Liquid Water with Two-Dimensional Infrared Photon Echo Spectroscopy. *J. Chem. Phys.*, **128**, 191103 (2008).

[296] D. Cringus, T. L. C. Jansen, M. S. Pshenichnikov, and D. A. Wiersma. Ultrafast Anisotropy Dynamics of Water Molecules Dissolved in Acetonitrile. *J. Chem. Phys.*, **127**, 084507 (2007).

[297] Y. Wang and J. M. Bowman. Ab Initio Potential and Dipole Moment Surfaces for Water. II. Local-Monomer Calculations of the Infrared Spectra of Water Clusters. *J. Chem. Phys.*, **134**, 154510 (2011).

[298] H. Liu, Y. Wang, and J. M. Bowman. Quantum Local Monomer IR Spectrum of Liquid D_2O at 300 K from 0 to 4000 cm^{-1} is in Near-Quantitative Agreement with Experiment. *J. Phys. Chem. B*, **120**, 2824 (2016).

[299] Y. Wang, X. Huang, B. C. Shepler, B. J. Braams, and J. M. Bowman. Flexible, Ab Initio Potential, and Dipole Moment Surfaces for Water. I. Tests and Applications for Clusters Up to the 22-mer. *J. Chem. Phys.*, **134**, 094509 (2011).

[300] Y. Wu, H. L. Tepper, and G. A. Voth. Flexible simple point-charge water model with improved liquid-state properties. *J. Chem. Phys.*, **124**, 024503 (2006).

[301] M. J. Frisch, G. W. Trucks, H. B. Schlegel, G. E. Scuseria, M. A. Robb, J. R. Cheeseman, G. Scalmani, V. Barone, B. Mennucci, G. A. Petersson, H. Nakatsuji,

M. Caricato, X. Li, H. P. Hratchian, A. F. Izmaylov, J. Bloino, G. Zheng, J. L. Sonnenberg, M. Hada, M. Ehara, K. Toyota, R. Fukuda, J. Hasegawa, M. Ishida, T. Nakajima, Y. Honda, O. Kitao, H. Nakai, T. Vreven, J. A. Montgomery Jr, J. E. Peralta, F. Ogliaro, M. J. Bearpark, J. Heyd, E. N. Brothers, K. N. Kudin, V. N. Staroverov, R. Kobayashi, J. Normand, K. Raghavachari, A. P. Rendell, J. C. Burant, S. S. Iyengar, J. Tomasi, M. Cossi, N. Rega, N. J. Millam, M. Klene, J. E. Knox, J. B. Cross, V. Bakken, C. Adamo, J. Jaramillo, R. Gomperts, R. E. Stratmann, O. Yazyev, A. J. Austin, R. Cammi, C. Pomelli, J. W. Ochterski, R. L. Martin, K. Morokuma, V. G. Zakrzewski, G. A. Voth, P. Salvador, J. J. Dannenberg, S. Dapprich, A. D. Daniels, Ö. Farkas, J. B. Foresman, J. V. Ortiz, J. Cioslowski, and D. J. Fox. Gaussian 09 (2009).

[302] C. M. Leavitt, A. F. DeBlase, C. J. Johnson, M. Van Stipdonk, A. B. McCoy, and M. A. Johnson. Hiding in Plain Sight: Unmasking the Diffuse Spectral Signatures of the Protonated N-terminus in Isolated Dipeptides Cooled in a Cryogenic Ion Trap. *J. Phys. Chem. Lett.*, **4**, 3450 (2013).

[303] K. Modig, B. G. Pfrommer, and B. Halle. Temperature-Dependent Hydrogen-Bond Geometry in Liquid Water. *Phys. Rev. Lett.*, **90**, 075502 (2003).

[304] W. Kauzmann. Some Factors in the Interpretation of Protein Denaturation. *Adv. Protein Chem.*, **14**, 1 (1959).

[305] D. Eisenberg and A. D. McLachlan. Solvation Energy in Protein Folding and Binding. *Nature*, **319**, 199 (1986).

[306] C. Tanford. Hydrophobic Free Energy, Micelle Formation and the Association of Proteins with Amphiphiles. *J. Mol. Biol.*, **67**, 59 (1972).

[307] J. N. Israelachvili, D. J. Mitchell, and B. W. Ninham. Theory of Self-Assembly of Hydrocarbon Amphiphiles into Micelles and Bilayers. *J. Chem. Soc. Faraday Trans. 2*, **72**, 1525 (1976).

[308] J. Israelachvili and H. Wennerström. Role of Hydration and Water Structure in Biological and Colloidal Interactions. *Nature*, **379**, 219 (1996).

[309] D. Chandler. Interfaces and the Driving Force of Hydrophobic Assembly. *Nature*, **437**, 640 (2005).

[310] R. B. Loftfield, E. A. Eigner, A. Pastuszyn, T. N. Lövgren, and H. Jakubowski. Conformational Changes During Enzyme Catalysis: Role of Water in the Transition State. *Proc. Natl. Acad. Sci. U. S. A.*, **77**, 3374 (1980).

[311] M. M. Teeter. Water-Protein Interactions: Theory and Experiment. *Annu. Rev. Biophys. Biophys. Chem.*, **20**, 577 (1991).

[312] M. Colombo, D. Rau, and V. Parsegian. Protein Solvation in Allosteric Regulation: a Water Effect on Hemoglobin. *Science*, **256**, 655 (1992).

[313] F. Zhu and G. Hummer. Pore Opening and Closing of a Pentameric Ligand-Gated Ion Channel. *Proc. Natl. Acad. Sci. U. S. A.*, **107**, 19814 (2010).

[314] M. O. Jensen, D. W. Borhani, K. Lindorff-Larsen, P. Maragakis, V. Jogini, M. P. Eastwood, R. O. Dror, and D. E. Shaw. Principles of Conduction and Hydrophobic Gating in K^+ Channels. *Proc. Natl. Acad. Sci. U. S. A.*, **107**, 5833 (2010).

[315] J. Ostmeyer, S. Chakrapani, A. C. Pan, E. Perozo, and B. Roux. Recovery from Slow Inactivation in K^+ Channels is Controlled by Water Molecules. *Nature*, **501**, 121 (2013).

[316] S. K. Pal, J. Peon, and A. H. Zewail. Biological Water at the Protein Surface: Dynamical Solvation Probed Directly with Femtosecond Resolution. *Proc. Natl. Acad. Sci. U. S. A.*, **99**, 1763 (2002).

[317] B. Halle. Protein Hydration Dynamics in Solution: a Critical Survey. *Philos. Trans. R. Soc. Lond. B. Biol. Sci.*, **359**, 1207 (2004).

[318] N. Nandi and B. Bagchi. Dielectric Relaxation of Biological Water. *J. Phys. Chem. B*, **101**, 10954 (1997).

[319] A. Barth. Infrared Spectroscopy of Proteins. *Biochim. Biophys. Acta*, **1767**, 1073 (2007).

[320] S. Krimm and J. Bandekar. Vibrational Spectroscopy and Conformation. *Adv. Protein Chem.*, **38**, 181 (1986).

[321] J. Safar, P. P. Roller, G. C. Ruben, D. C. Gajdusek, and C. J. Gibbs. Secondary Structure of Proteins Associated in Thin Films. *Biopolymers*, **33**, 1461 (1993).

[322] W. F. Wolkers, M. G. Van Kilsdonk, and F. A. Hoekstra. Dehydration-Induced Conformational Changes of Poly-L-Lysine as Influenced by Drying Rate and Carbohydrates. *Biochim. Biophys. Acta - Gen. Subj.*, **1425**, 127 (1998).

[323] A. Xie, A. F. G. van der Meer, and R. H. Austin. Excited-State Lifetimes of Far-Infrared Collective Modes in Proteins. *Phys. Rev. Lett.*, **88**, 18102 (2001).

[324] A. Striolo, A. Favaro, N. Elvassore, A. Bertucco, and V. Di Noto. Evidence of Conformational Changes for Protein Films Exposed to High-Pressure CO_2 by FT-IR Spectroscopy. *J. Supercrit. Fluids*, **27**, 283 (2003).

[325] G. Shanmugam and P. L. Polavarapu. Vibrational circular dichroism of protein films. *J. Am. Chem. Soc.*, **126**, 10292 (2004).

[326] M. Rozenberg and G. Shoham. FTIR Spectra of Solid Poly-L-Lysine in the Stretching NH Mode Range. *Biophys. Chem.*, **125**, 166 (2007).

[327] M. D. Fayer. *Ultrafast Infrared Vibrational Spectroscopy.* CRC Press, Boca Raton (2013).

[328] G. Shanmugam and P. L. Polavarapu. Concentration- and Dehydration-Dependent Structural Transitions in Poly-L-Lysine. *J. Mol. Struct.*, **890**, 144 (2008).

[329] P. M. Cowan and S. McGavin. Structure of Poly-L-Proline. *Nature*, **176**, 501 (1955).

[330] S. Arnott and S. D. Dover. The Structure of Poly-L-Proline II. *Acta Crystallogr. Sect. B Struct. Crystallogr. Cryst. Chem.*, **24**, 599 (1968).

[331] A. A. Adzhubei and M. J. Sternberg. Left-Handed Polyproline II Helices Commonly Occur in Globular Proteins. *J. Mol. Biol.*, **229**, 472 (1993).

[332] B. Schuler, E. A. Lipman, P. J. Steinbach, M. Kumke, and W. A. Eaton. Polyproline and the "Spectroscopic Ruler" Revisited with Single-Molecule Fluorescence. *Proc. Natl. Acad. Sci. U. S. A.*, **102**, 2754 (2005).

[333] R. L. York, G. J. Holinga, and G. A. Somorjai. An Investigation of the Influence of Chain Length on the Interfacial Ordering of L-Lysine and L-Proline and Their Homopeptides at Hydrophobic and Hydrophilic Interfaces Studied by Sum Frequency Generation and Quartz Crystal Microbalance. *Langmuir*, **25**, 9369 (2009).

[334] I. Reva, S. Stepanian, A. Plokhotnichenko, E. Radchenko, G. Sheina, and Y. Blagoi. Infrared Matrix Isolation Studies of Amino Acids. Molecular Structure of Proline. *J. Mol. Struct.*, **318**, 1 (1994).

[335] L. Ackels, P. Stawski, K. E. Amunson, and J. Kubelka. On the Temperature Dependence of Amide I Intensities of Peptides in Solution. *Vib. Spectrosc.*, **50**, 2 (2009).

[336] E. B. Dunkelberger, M. Grechko, and M. T. Zanni. Transition Dipoles from 1D and 2D Infrared Spectroscopy Help Reveal the Secondary Structures of Proteins: Application to Amyloids. *J. Phys. Chem. B*, **119**, 14065 (2015).

[337] I. R. Piletic, D. E. Moilanen, D. B. Spry, N. E. Levinger, and M. D. Fayer. Testing the Core/Shell Model of Nanoconfined Water in Reverse Micelles Using Linear and Nonlinear IR Spectroscopy. *J. Phys. Chem. A*, **110**, 4985 (2006).

[338] D. Urry, T. Trapane, and H. Sugano. Sequential Polypeptides of Elastin: Cyclic Conformational Correlates of the Linear Polypentapeptide. *J. Am. Chem. Soc.*, **103**, 2080 (1981).

[339] D. W. Urry, T. L. Trapane, and K. U. Prasad. Phase-Structure Transitions of the Elastin Polypentapeptide-Water System within the Framework of Composition-Temperature Studies. *Biopolymers*, **24**, 2345 (1985).

[340] J. Lee, C. W. Macosko, and D. W. Urry. Mechanical Properties of Cross-Linked Synthetic Elastomeric Polypentapeptides. *Macromolecules*, **34**, 5968 (2001).

[341] K. Lum, D. Chandler, and J. D. Weeks. Hydrophobicity at Small and Large Length Scales. *J. Phys. Chem. B*, **103**, 4570 (1999).

[342] A. A. Bakulin, C. Liang, T. la Cour Jansen, D. A. Wiersma, H. J. Bakker, and M. S. Pshenichnikov. Hydrophobic Solvation: A 2D IR Spectroscopic Inquest. *Acc. Chem. Res.*, **42**, 1229 (2009).

[343] L. N. Johnson. The Early History of Lysozyme. *Nat. Struct. Biol.*, **5**, 942 (1998).

[344] C. Blake, D. Koenig, G. Mair, A. North, D. Phillips, and V. Sarma. Structure of Hen Egg-White Lysozyme: A Three-Dimensional Fourier Synthesis at 2 Å Resolution. *Nature*, **206**, 757 (1965).

[345] J. Wang, M. Dauter, R. Alkire, A. Joachimiak, and Z. Dauter. Triclinic Lysozyme at 0.65 Å Resolution. *Acta Crystallogr. Sect. D Biol. Crystallogr.*, **63**, 1254 (2007).

[346] P. McBride-Warren and D. D. Mueller. Hydrogen-Deuterium Exchange of Lysozyme. I. Rate Constants and pH Dependence. *Biochemistry*, **11**, 1785 (1972).

[347] D. M. Leitner, M. Havenith, and M. Gruebele. Biomolecule Large-Amplitude Motion and Solvation Dynamics: Modelling and Probes from THz to X-Rays. *Int. Rev. Phys. Chem.*, **25**, 553 (2006).

LUIGI DE MARCO
1719 E 55th St. #1
Chicago, IL; 60615-5913
Tel.: (617) 999-4593
Email.: ldemarco@mit.edu

Education

Massachusetts Institute of Technology
2010 - 2016 Cambridge, MA, USA
PhD in physical chemistry.
Advisor: Andrei Tokmakoff

McGill University
2007 - 2010 Montreal, QC, Canada
BSc with first class honours (gpa 3.97)
Honours chemistry, minor physics

Research Experience

The University of Chicago
2013 - 2016 Chicago, IL, USA
Non-degree visiting student in the group of Prof. Andrei Tokmakoff. Designed an ultrafast laser laboratory and engineered a broadband multidimensional IR spectrometer with several orders of magnitude decrease in acquisition time and increase in signal to noise ratio. Research concerned the molecular dynamics of hydrogen-bonding systems, with a special emphasis on liquid water.

Massachusetts Institute of Technology
2010 - 2013 Cambridge, MA, USA
Graduate research assistant in the group of Prof. Andrei Tokmakoff. Research focused on the development of a novel plasma-based source of ultrashort broadband IR pulses for use in two-dimensional IR spectroscopy experiments.

McGill University
2009-2010 Montreal, QC, Canada
Undergraduate research assistant in the group of Prof. Pat Kambhampati. Research primarily involved writing LabVIEW software for an acousto-optic pulse shaper to perform multidimensional electronic spectroscopy on CdSe quantum dots.

Teaching Experience

Massachusetts Institute of Technology
2010 - 2011 Cambridge, MA, USA

5.38 Physical Chemistry Laboratory, Spring 2011
Teaching assistant. Responsibilities included guiding ~20 undergraduate students through time-resolved fluorescence experiments on tagged biomolecules to explore their dimerization kinetics and hydrodynamic volume, as well as lecturing and grading.

5.60 Thermodynamics & Kinetics, Fall 2010
Teaching assistant. Responsibilities included giving four recitation lectures per week to over 30 students and preparing and grading problem sets and exams. Topics included thermal and statistical physics, kinetics of chemical reactions, and energy and its relation to the environment.

McGill University
2009-2010 Montreal, QC, Canada
McGill Chemistry Student Society Tutor. Gave tutorial lectures to junior and sophomore students on physical chemistry subjects. Topics included kinetic theory of gases, thermodynamics, statistical mechanics, quantum mechanics, and molecular spectroscopy.

Honours and Awards

2015	IR Systems Development Outstanding Poster Award
2013	ACS Oustanding Student Poster Award
2012	NSERC Postgraduate Scholarship (3 yr.)
2011	MIT Department of Chemistry Teaching Award
2010	Society of Chemical Industry Merit Award
2010	R.F. Robertson Prize in Chemistry
2010	NSERC A. G. Bell Canada Graduate Scholarship
2010	NSERC Undergraduate Student Research Award
2009	Canadian Society for Chemistry Silver Medal
2009	John M. Walkley Jr. Memorial Award
2009	AstraZeneca Scholarship
2009	NSERC Undergraduate Student Research Award
2008	Herbert J. Brennen Scolarship

Publications

8. L. De Marco, W. Carpenter, H. Liu, R. Biswas, J. M. Bowman, and A. Tokmakoff. Differences in the Vibrational Dynamics of H_2O and D_2O: Observation of Symmetric and Antisymmetric Vibrations in Heavy Water. *J. Phys. Chem. Lett.* **7**, 1769 (2016).
7. F. Perakis, L. De Marco, A. Shalit, F. Tang, Z. Kann, et al. Vibrational Spectroscopy and Dynamics of Water. *Chem. Rev.* DOI: 10.1021/acs.chemrev.5b00640
6. M. Thämer, L. De Marco, K. Ramasesha, A. Mandal, and A. Tokmakoff. Ultrafast 2D IR spectroscopy of the excess proton in liquid water. *Science.* **350**, 78 (2015).

5. L. De Marco, M. Thämer, M. Reppert, and A. Tokmakoff. Direct observation of intermolecular interactions mediated by hydrogen bonding. *J. Chem. Phys.* **141**, 034502 (2014).
4. A. Mandal, K. Ramasesha, L. De Marco, and A. Tokmakoff. Collective vibrations of water-solvated hydroxide ions investigated with broadband 2DIR spectroscopy. *J. Chem. Phys.* **140**, 204508 (2014).
3. K. Ramasesha,* L. De Marco,* A. Mandal, and A. Tokmakoff. Water vibrations have strongly mixed intra- and intermolecular character. *Nature Chem.* **5**, 935 (2013).
2. L. De Marco, K. Ramasesha, and A. Tokmakoff. Experimental evidence of Fermi Resonances in Isotopically Dilute Water from Ultrafast Broadband IR Spectroscopy. *J. Phys. Chem. B.* **117**, 15319 (2013).
1. K. Ramasesha, L. De Marco, A. D. Horning, A. Mandal, and A. Tokmakoff. A phenomenological approach to modeling chemical dynamics in nonlinear and two-dimensional spectroscopy. *J. Chem. Phys.* **136**, 134507 (2012).

Oral Presentations

6. Observation of Water–Protein Interaction Dynamics with Broadband Two-Dimensional Infrared Spectroscopy. *APS March Meeting 2016.* Baltimore, MD. March 18, 2016.
5. Ultrafast IR spectroscopy of vibrational dynamics in water. *Time resolved vibrational spectroscopy 2015.* Madison, WI. June 26, 2015.
4. Vibrational dynamics of water investigated with broadband two-dimensional infrared spectroscopy. *Water –the most anomalous liquid, Nordic Institute for Theoretical Physics.* Stockholm, Sweden. November 27, 2014. (Invited.)
3. Direct observation of hydrogen-bond-mediated interactions with multidimensional infrared spectroscopy. *McGill University.* Montreal, Canada. October 14, 2014. (Invited.)
2. Studying vibrational dynamics in water using nonlinear time-resolved broadband spectroscopy. *MIT Department of Chemistry Student Seminar.* Cambridge, MA. March 1, 2013.
1. Ultrafast broadband spectroscopy of neat and isotopically dilute water. *Water & Aqueous Solutions Gordon Research Seminar.* Holderness, NH. August 11, 2012.

Poster Presentations

5. Direct observation of intermolecular interaction with broadband 2D IR spectroscopy. *Time Resolved Vibrational Spectroscopy.* Madison, WI. June 2015. (Received IR Systems Development Outstanding Poster award.)
4. Direct observation of intermolecular interactions with broadband 2D IR spectroscopy. *Coherent Multidimensional Spectroscopy.* Eugene, OR. July 2014.
3. Ultrafast broadband spectroscopy of neat and isotopically dilute water. *American Chemical Society.* Indianapolis, IN. September 2013. (Received ACS Outstanding Student Poster award.)

2. Ultrafast broadband spectroscopy of neat and isotopically dilute water. *Water & Aqueous Solutions Gordon Research Conference.* Holderness, NH. August 2012.
1. Generation of pulsed broadband mid-IR light for two-dimensional vibrational spectroscopy. *Coherent Multidimensional Spectroscopy.* Berlin, Germany. July 2012.

References

Andrei Tokmakoff, University of Chicago, tokmakoff@uchicago.edu, (773) 834-7696
Robert Field, Massachusetts Institute of Technology, rwfield@mit.edu, (617) 253-1489
Gregory Engel, University of Chicago, gsengel@uchicago.edu, (773) 834-0818
Francesco Paesani, UC San Diego, fpaesani@ucsd.edu, (858) 822-3383
Keith Nelson, Massachusetts Institute of Technology, kanelson@mit.edu (617) 253-1423